UNIVERSITY OF OSLO
Department of Physics

On the Possible Causes and Forecast of the GPS-Satellite Outages during the Super Storm on November 20, 2003

Master thesis

Heidi Cathrine Ege

29.04.2014

Kartverket

UNIVERSITAS OSLOENSIS
MDCCCXI

Front cover: View of Scandinavia from the International Space Station (ISS). Photo by: André Kuipers, ESA/NASA. (*http://www.flickr.com/photos/astro_andre/6859089586/)*

Logo: Kartverket,(*http://www.kartverket.no/Om-Kartverket/Presse/Logo/*)

Foreword

When I applied for admission to the MS - program in Physics in the winter of 2009, I wanted to write a thesis on a subject which would have an obvious and direct relevance to the society. I was intrigued by the research field of space weather and on the consequences felt here on Earth. Thus I chose the subject on satellite communication outage, and I did not hesitate to contact Professor Jøran Moen to get started. The project was in collaboration with the Norwegian Mapping Authority (NMA), and in January 2009 Moen and I went to see Oddgeir Kristiansen, Anna Jensen and Mohammed Ouassou at the NMA main office in Hønefoss. We had a long meeting where we talked about their challenges with ionospheric disturbances and GNSS-services. Jensen and Ouassou had worked with ionospheric modelling for quite some time and were happy to assist me on finding a decent event to work with. We ended up with the superstorm event from November 20, 2003 where their receiver stations suffered from poor reception from the afternoon and throughout the day.

There have been times I did regret choosing this topic, though. I have pondered whether it would have been easier to work with an instrumental task instead and focus on one problem instead of trying to get a general overview of so many topics. On the other hand, I feel I have gained a greater understanding of how different phenomena are related, by choosing this task. The one thing I have found most challenging though, was not being able to spend more time with my fellow students, supervisors and scientists at Blindern and NMA. I have truly missed having the opportunity to stop by their office for a talk, or discuss different topics. Having that said, my supervisors, and PIs I have been in contact with, have always taken the time to respond and provide guidance and tips.

Today, five years have passed. I have been busy taking my courses, working my full time job as a high school teacher, raising my children and gathering so much data I have forgotten, or have not had time, to look into half of it. Still, the geomagnetic storm from a decade ago has ‘haunted’ the back of my head through all these years. Hence it felt like an immense relief when I finally started writing it down one and half years ago. I hope that the result could shed some light on what happened during the event and the possible causes, and what chances were of being prepared for such an event then, now- and in the future.

Eidsvoll, April 2014

Heidi C. Ege

Acknowledgements

I want to thank the Department of Physics, University of Oslo and the Norwegian Mapping Authority for granting me the opportunity to write this thesis. In this respect, my sincere and heartfelt gratitude goes to my supervisors Professor Jøran Moen (UIO) and Knut Stanley Jacobsen (NMA). Although we have barely had time to meet in person, you have always been available when I have needed your feedback and advice. And you have always given me constructive response to my work. I could not have done this without your competent supervision. A special thanks to you, "Super- Knut", for all your assistance with MATLAB codes and plots from NMA.
I also want to thank Anna Jensen, former employee at NMA and Mohamed Ouassou (NMA) for providing me with data sets and valuable information on processing them.
I want to thank my fellow students in the Plasma and Space physics group for great fun, inspiration and motivation throughout all these years. A special thanks to Yvonne Dåbakk for her inspiring lectures in FYS 3610 (and fabulous lecture notes) that gave me the confidence to embark on this journey. A warm thanks to Grete Stavik Døvle and the student counselors for guidance and help with forms and course administrations.
I gratefully acknowledge the following persons and facilities for providing data, granting permissions and contributing with helpful tips and guidance:
The OVATION project at JHU/APL for AO-maps and spectrograms, and the providers of the original data sets used as source material , here under SuperDARN, DMSP, AFRL, UVI, NOAA and University of Alaska. The OVATION project is supported by NSF grants ATM-0222411 (P. Newell) and ATM-0004365 (T. Sotirelis). The Finnish Meteorological Institute, the PIs, and all who contribute to maintain the IMAGE magnetometer network and providing data. "The IMAGE magnetometer data are collected as a joint European collaboration" (*http://www.geo.fmi.fi/image/*). The ACE Science Center at Caltech for providing the ACE-data, [Garrard et al., 1998], (*http://www.srl.caltech.edu/ACE/ASC/*)
The WDC Kyoto for providing the data sets for hourly Dst index, and the facilities contributing to the geomagnetic data at: *http://wdc.kugi.kyoto-u.ac.jp/wdc/obslink.html*.
The SST for sun spot photo: "The Swedish 1-m Solar Telescope is operated on the island of La Palma by the Institute for Solar Physics of the Royal Swedish Academy of Sciences in the Spanish Observatorio del Roque de los Muchachos of the Instituto de Astrofísica de Canarias" (*http://www.solarphysics.kva.se/*). To GSFC for SYM-H data: "The OMNI data were obtained from the GSFC/SPDF OMNIWeb interface at (*http://omniweb.gsfc.nasa.gov")*
QinetiQ Radio Science and Propagation Group, (PI Dr. Paul S. Cannon), for providing the Tromsø ionograms (*www.qinetiq.com*).
The William B. Hanson Center for Space Sciences at the University of Texas, Dallas (*http://cindispace.utdallas.edu/DMSP/),* and the US Air Force for providing the DMSP data: "The DMSP particle detectors were designed by Dave Hardy of the Air Force Research Laboratory, and the Auroral Boundary/Hemispheric Power Indices are provided with permission from the Space Vehicle Directorate, Air Force Research Laboratory, Kirtland AFB, NM 87117, via the Cedar Database at the National Center for Atmospheric Research which is supported by the National Science Foundation" (http*://cedarweb.hao.ucar.edu/wiki/index.php/DMSP:Main*).
A special thanks to Doug Bisecker and Rodney Viereck at National Oceanic and Atmospheric Administration (NOAA) for information on ACE real time services available in 2003 and the POES data. Credit to the NOAA Space Weather Prediction Center, Boulder, Co: NOAA is an agency under the US Dept. of Commerce *(http://www.swpc.noaa.gov/*).
I also thank Bernhard Fleck, Pål Brekke (NRS) and Svein-Vidar H. Haugan (ITA) for information on SOHO real time services in 2003. "The SOHO/LASCO data used here are produced by a consortium

of the Naval Research Laboratory (USA), Max-Planck-Institut fuer Aeronomie (Germany), Laboratoire d'Astronomie (France), and the University of Birmingham (UK)". Also credit to the GSFC for providing EIT images, Stanford University for providing the MDI images. SOHO is a project of international cooperation between ESA and NASA [Scherrer et al., 1995] (*http://sohodata.nascom.nasa.gov).*
Many thanks to Urban Brändström at IRF for permission to use the all sky images, and to IRF Kiruna for operating and providing data (*www.irf.se/allsky*). Credit to Giorgana DeFranceschi at INGV for information on the ISACCO and ESWUA projects and scintillation forecast (*www.eswua.ingv.it/ingv/*).
A warm thank you to Dr. John C. Foster at Millstone Hill, MIT, for kindly answering all my questions, and to Dr. Anthea J. Coster, for permission to use TEC-maps from the World-Wide GPS Receiver Network. Coster's work is supported by NSF grant number 0856093. (*http://www.haystack.mit.edu*).
A credit to Ingemar Häggström at EISCAT for permission to use the quick look plots from the UHF radar in Tromsø. "EISCAT is an international association supported by research organizations in China (CRIRP), Finland (SA), Japan (NIPR and STEL), Norway (NFR), Sweden (VR), and the United Kingdom (NERC)" *(www.eiscat.se)*. Thanks to Ethan Miller (JHU/APL), and Lasse Clausen (UiO), for help with SuperDARN data. "SuperDARN is an international collaboration involving scientists and funding agencies of over a dozen countries [Chisham et al., 2007 and references therein] A special thanks to the Wallops Island radar, JHU/APL, for providing all convection plots. The US SuperDARN is supported by the National Science Foundation, with grant number AGS-0946902 (*superdarn.jhuapl.edu*).
I will especially thank Prof. Bodo W. Reinisch (LDI) for kind help with ionograms and for providing the Sondrestrom ionograms. The Lowell GIRO datacenter and DIDbase is based on data sharing infrastructure administered by the University of Massachusetts, Lowell [Reinisch and Galkin, 2011; *http://spase.info/SMWG/Observatory/GIRO ;* Reinisch et al., 2005] (*http://giro.uml.edu*/). Thanks to Dr. Anja Strømme, PI at Sondrestrom ISR, for tips on real time service and providing the summary plots. The Sondrestrom Upper Atmospheric Research Facility is operated by SRI International and supported by the NSF Cooperative Agreement AGS-0836152, and Denmark's Meteorological Institute (*http://isr.sri.com*). I would also like to thank David Themens at CHAIN for info on the CADI data. Canadian Advanced Digital Ionosonde is a part of the Canadian High Arctic Network (CHAIN). "Infrastructure funding for CHAIN is provided by the Canada Foundation for Innovation and the New Brunswick Innovation Foundation. CHAIN operation is conducted in collaboration with the Canadian Space Agency" [Jayachandran et al., 2009].
Thanks to the Libraries at University of Oslo for providing, more or less, all the literature used as source material in this thesis.
Last, but definitely not least, I want to thank my dearly beloved family for their love and support. Especially my sons, Andreas and Julian, thank you for having had such incredible patience with me through this process. You are my inspiration, pride and joy- always. ❤

Abbreviations/Acronyms

ACE	Advanced Composition Explorer
AFB	Air Force Base
AFRL	Air Force Research Laboratory
AE	Auroral Electrojet
AIA	Atmospheric Imaging Assembly
AL	Auroral Lower (electrojet)
AR	Active Region
ARTEMIS	Automatic Recognition of Transient Events and Marseille Inventory from Synoptic maps
AO	Auroral Oval
AU	Auroral Upper (electrojet)
BBF	Bursty Bulk Flow
BEAR	Baltic Electromagnetic Array Research
C/A	Coarse Acquisition
CACTus	Computer Aided CME Tracing
CADI	Canadian Advanced Digital Ionosonde
CALTECH	California Institute of Technology
CCD	Charge Coupled Device
CD	Current Disruption
CHAIN	Canadian High Arctic Ionospheric Network
CHAMP	Challenging Minisatellite Payload
CEDAR	Coupling,Energetics and Dynamics of Atmospheric Regions
CEM	Channel Electron Multiplier
CIR	Co-rotating Interaction Regions
CNES	Centre National d'Etude Spatiales
CME	Coronal Mass Ejection
CONUS	Continental US
CORS	Continuous Operating Reference Station
CPCP	Cross Polar Cap Potential
CRAND	Cosmic RayAlbedoNeutral Decay
CRIRP	China Research Institute of Radio Propagation
CSR	Coherent Scatter Radar
DARN	Dual Auroral Radar Network
DASC	Digital All Sky Camera
DGPS	Differential GPS
DIDbase	Digital Ionosonde Database
DLR	Deutsche zentrum führ Luft und Rauhmfart
DMSP	Defence Meteorological Satellite Program
DOP	Dilution of Presicion
DPS	Dessler Parker Sckopke
DSN	Deep Space Network
Dst	Disturbance storm time
EEJ	Eastward Electro Jet
EGNOS	European Geostationary Navigation Overlay System
EISCAT	European Incoherent Scatter
EIT	Extreme ultraviolet Imaging Telescope
EOG	Earth Observation Group
ESA	European Space Agency
ESFRI	European Strategy Forum on Research Infrastructures
ESW	East South West
ESWUA	Electronic Space Weather Upper Atmosphere
EUV	Extreme Ultra Violet

FAC	Field Aligned Current
FAST	Fast Auroral SnapshoT explorer
FCE	Flow Channel Event
FMI	Finnish Meteorological Institute
F.O.V.	Field of View
FTE	Flux Transfer Event
FUS	Fast Update Synchronization
GBAS	Ground Based Augmentation System
GDI	Gradient Drift Instability
GDOP	Geometrical Dilution of Presicion
GI	Geophysical Institute (Alaska)
GIM	Global Ionospheric Model
GIRO	Global Ionospheric Radio Observatory
GISTM	GNSS Ionospheric Scintillation & TEC Monitor
GIVE	Grid Ionospheric Vertical Error
GNSS	Global Navigation Satellite System
GLONASS	Global'naya Navigatsinaya Sputnikovaya Sistema
GOES	Geostationary Operational Environmental Satellite
GPS	Global Positioning System
GRACE	Gravity Recovery and Climate Experiment
GRIMS	GPS Real time Ionospheric Mapping System
GSC	Geologic Survey Canada
GSE	Geocentric Solar Elliptic coordinate system
GSFC	Goddard Space Flight Center
GSM	Geocentric Solar Magnetospheric coordinate system
GUISDAP	Grand Unified Incoherent Scatter Design and Analysis Package
HAFv2	Hakamada-Akasofu-Fry version 2
HDOP	Horizontal Dilution of Presicion
HEO	Highly Eliptical Orbit
HF	High Frequency
HLBL	High Latitude Boundary Layer
ICI-2	Investigation of Cusp Irregularities 2
ICME	Interplanetary CME
IDA3D	Ionospheric Data Assimilation 3D
IGS	International GNSS Service
IMAGE	International Monitor for Auroral Geomagnetic Effects
IMF	Interplanetary Magnetic Field
INGV	Istituto Nazionale de Geofisica eVulcanologia
INVERT	INVERse problems and Tomography
IPP	Ionospheric Pierce Point
IPS	Ionospheric Prediction Service
IRF	Institutet för Rymdfysik
IRI	International Reference Ionosphere model
IRNSS	Indian Regional Navigational Satellite System
ISACCO	Ionospheric Scintillation Arctic Campaign Coordinated Observation
ISEE	International Sun Earth Explorer
ISP	Institute of Solar Physics (Uni Stockholm)
ISPM	Interplanetary Shock Propagation Model
ISR	Incoherent Scatter Radar
ISRIM	Incoherent Scatter Radar Ionospheric Model
ITA	Institutt for Teoretisk Astrofysikk
JHU/APL	John Hopkins University Applied Physics Laboratory
JPL	Jet Propulsion Laboratory
KH/KHI	Kelvin Helmholtz Instability
L1	L-band frequency 1

L1*	Lagrange point 1
LANL	Los Alamos National Laboratory
LAS	Laboratoire d'Astronomie Spatiale
LASCO	Large Angle Spectrometic Coronagraph
LDI	Lowell Digisonde International
LEO	Low Earth Orbit
LF	Low Frequency
LLBL	Low Latitude Boundary Layer
LOS	Line Of Sight
MAPe	Max Planck institut für Aeronomi
MC	Magnetic Cloud
MDI	Michelson Doppler Imager
MEO	Medium Earth Orbit
MF	Medium Frequency
MHD	Magneto-Hydro Dynamics
MI-coupl.	Magnetospher-Ionosphere coupling
MIDAS	Multi Instrument Data Analysis System
MIDAS*	Millstone Incoherent Data Acquisition System
MISA	Millstone Hill Steerable Antenna
MIT	Massachusetts Institute of Technology
MLAT	Magnetic Latitude
MLT	Magnetic Local Time
MP	Magnetopause
MS	Magnetosheath
MSFC	Marshall Space Flight Center
MSP	Meridian Scanning Photometer
NASA	National Aeronautics and Space Administration
NAV-msg.	Navigation message
NENL	Near Earth Neutral Line
NERC	National Environmental Research Council
NFR	Norges Forskningsråd (Research Council of Norway)
NGDC	National Geophysical Data Center
NIF	Normal Incidence Frame
NIPR	National Institute of Polar Research
NMA	Norwegian Mapping Autority
NOAA	National Oceanic Atmospheric Administration
NPCC	North East Power Coordinating Council
NRL	Naval Research Laboratory
NRS	Norsk Romsenter (Norwegian Space Center)
NSF	National Science Foundation
O/C Boundary	Open/Closed Boundary
OTF	On-The-Fly
OVATION	Oval, Variation, Assessment, Tracking, Intensity and Online Nowcasting
PDOP	Positional Dilution of Presicion
P-code	Presicion Code
PEJ	Polar Electro Jet
PI	Principal Investigator
PLL	Phase Lock Loop
PMAF	Poleward Moving Auroral Form
POES	Polar-orbiting Operational Environmental Satellites
PRN	Pseudo Random Noise
PSBL	Plasma Sheet Boundary Layer
QZSS	Quazi Zenith Satellite System
R1	Region 1 currents
R2	Region 2 currents

RFE	Reversed Flow Events
RIMS	Ranging and Integrity Monitoring Stations
RINEX	Receiver Independent Exchange Format
ROT	Rate of TEC
ROTI	Rate of TEC Index
RTD	Residence Times Difference
RTK	Real Time Kinematic
RTIM	Real Time Ionospheric Monitor
RTIS	Real Time Ionospheric Scintillation (monitor)
SA	Scientific Association (EISCAT Finland)
SAMNET	(UK) Sub Auroral Magnetometer Network
SAPS	Sub Auroral Polarization Streamers
SATCOM	Satellite Communication
SATREF	SATellitt-basert REFeransesystem
SBAS	Satellite Based Augmentation System
SCW	Stormtime Current Wedge
SEC	Space Environment Center
SED	Storm Enhanced Density
SEEDS	Solar Eruptive Event Detection System
SEP	Solar Energetic Particles
SI	Sudden Impulse
SIDC	Solar Influences Data Center
SLM	Single Layer Model
SIM	SATREF Ionospheric Model
SNR	Signal to Noise Ratio
SMC	Space andMissile systems Center
SOHO	Solar and Heliospheric Observatory
SOI	Solar Oscillations Investigation
SPDF	Space Physics Data Facility
SRI	Stanford Research Institute
SSC	Storm Sudden Commencement
SSC*	STEREO Science Center
SSIES	Special Sensor Ions Electrons and Scintillation
SSJ	Special Sensor Precipitating Electron and Ion Spectrometer
SSM	Special Sensor Magnetometer
SST	Swedish Solar Telescope
STARE	Scandinavian Twin Auroral Radar Experiment
STD	Solar Terrestrial Dispatch
STEC	Slant Total Electron Content
STEL	Solar Terrestrial Environment Laboratory
STEREO	Solar Terrestrial Relations Observatory
SuperDARN	Super Dual Auroral Radar Network
SVD	Space Vehicles Directorate
SW	Solar Wind
SWEPAM	Solar Wind Electron Proton and Alpha Monitor
SWPC	Space Weather Prediction Center
SWOOPS	Solar Wind Observations Over the Poles of the Sun
SXI	Solar X-ray Imager
SYM	Symmetric component of Geomagnetic field
TCV	Travelling Convection Vortices
TDOP	Time Dilution of Presicion
TEC	Total Electron Content
TECU	Total Electron Content Unit
THEMIS	Time History of Events and Macroscale Interactions during Substorms
TID	Travelling Ionospheric Disturbances

TGO	Tromsø Geophysical Observatory
TOI	Tongue Of Ionization
TRACE	Transition Region And Coronal Explorer
UAF	University of Alaska Fairbanks
UHF	Ultra High Frequency
UIO	Universitetet I Oslo (University of Oslo)
UMLCAR	University of Massachusetts Lowell Center for Atmospheric Research
UT	Universal Time
UVI	Ultra Violet Imager
VDOP	Vertical Dilution of Presicion
VHF	Very High Frequency
VR	Vetenskapsrådet (Swedish Research Council)
VRS	Virtual Reference Station
VT	Virginia Tech (Virginia Polytechnic Institute and State University)
VTEC	Vertical TEC
WAAS	Wide Area Augmentation System
WDC	World Data Center
WEJ	Westward Electro Jet
WGS	World Geodetic System

Content

1 Introduction

This thesis seeks to shed light upon the cause of the GPS-satellite outage the Norwegian Mapping Authority experienced on November 20, 2003. A number of articles on the storm have laid the foundation for understanding the development of the storm, as well as the phenomena being plausible candidates for the loss of satellite communication in the afternoon. Supporting data from the NMA have been studied in order to establish an understanding of the dynamics in the ionosphere above the mainland of Norway.

1.1 Motivation

The challenge of predicting space weather has become one of the most important issues in space physics during the last years. Especially communication and navigation satellites suffer from deteriorating performance during enhanced solar activity and plasma instabilities in the ionosphere.

In this thesis I have studied the super storm event that took place on November 20, 2003 with respect to the ionospheric response that severely limited the positioning services in Norway. The Norwegian Mapping Authority (NMA/Kartverket) was using their SATREF-system to monitor the delay-meter calculated from the total electron content (TEC) measured at five different GPS ground stations in southern parts of Norway. During this storm event the network lost lock of several satellites in the afternoon, and it lasted throughout the whole day and night. This resulted in too few satellites to tri-laterate positions and therefore a limited service. Needless to say, this could have led to challenges for clients who are relying on high precision positioning service and navigation.
The direct cause is a distortion of the electromagnetic signals as the radio wave encounter plasma irregularities (structures in the electron populations) as it propagates through the ionosphere. The electron density gradients affect the refractive properties of the ionosphere and therefore split the plane wave into multiple paths. This phenomenon is called scintillation and is always present in the ionosphere to a certain degree, but is enhanced under solar storm conditions [e.g. Alfonsi et al., 2008; Kintner et al., 2007]. Figure 1.1-1a) illustrates the scintillation effects on the satellite signal traversing the ionosphere. The so-called satcom outage regions are presented in Figure 1.1-1a). They are the polar caps due to solar wind forcing, and then around the Equator due to the equatorial spread F [Kintner et al., 2007]. Here we will focus on the northern hemisphere polar regions.
We do know a lot about what happens in the Earth's ionosphere and what causes deteriorated radio signals. But how can we monitor and forecast events with enhanced scintillation?

For years space scientists and geophysicists have studied the interaction between the interplanetary magnetic field (IMF) and the geomagnetic field. We also know a lot about the Sun and the 11 year solar cycle, the massive outbursts of hot plasma that propagates towards the Earth, and what happens when this plasma is infused into our upper atmosphere. However it is very difficult to precisely predict when and what will happen. The November storm of 2003 has been thoroughly studied and there are several established facts on how it developed. It turned out to be one of the strongest geomagnetic storms during the 23d solar cycle, showing unusual behavior and duration of approximately 24 hours [e.g. Gopalswamy et al., 2005a; Yizengaw et al., 2006].

a) 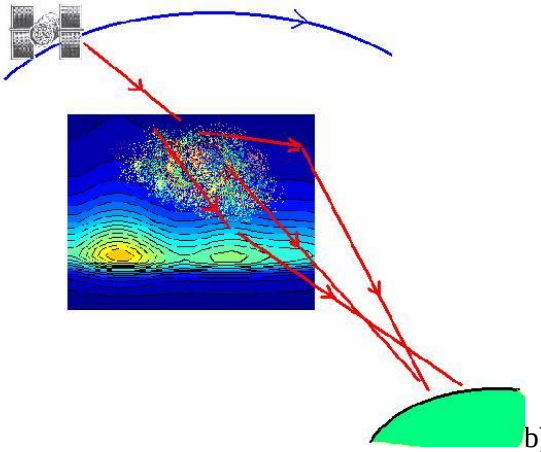 b) 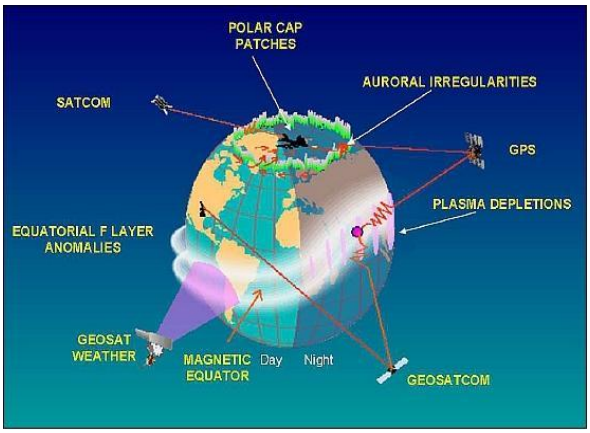

Figure 1.1-1:Scintillation: the plasma irregularities in the ionosphere diffract and refract radio waves. Figure from:(*http://roma2.rm.ingv.it/en/themes/11/ionospheric_scintillation.)* b) Typical regions where satellite communication is compromised due to ionospheric effects. Adapted from: Bekkeng, T.A. [2009]

The solar activity can be monitored by satellites, and we can extract key parameters such as solar wind speed, proton density and temperature, pressure etc. that may help us predict what is in store. Shock arrival forecasts are not very accurate (prediction error >9 hours) [Cho et al., 2003], but in time improved techniques probably will make them more reliable. Solar wind parameters and measurements of the interplanetary magnetic field (IMF) are available in real time from the ACE-satellite [Zwickl et al., 1998]. Calculated arrival times based on these measurements are more accurate, but the timeline is less than 1 hour, which could be too short. However the coupling between the IMF and the magnetosphere both during quiet conditions and storm enhanced conditions are more difficult to forecast. During the November storm solar extreme ultra violet (EUV) ionization occurred over the American continent and created high density plasma in the upper atmosphere. This cold plasma formed a tongue of ionization (TOI) which drifted across the polar cap during the storm, adding more "fuel" to the already enhanced densities in the ionosphere [e.g. Foster et al., 2005]. This was most probably a partial source of the severe scintillation effect the NMA experienced.
If this is the case, such TOIs will form over the American continent due to EUV-ionization and storm enhanced densities [Foster et al., 1993; 2005]. A TOI will drift across the pole adding to the plasma convection in the F-layer and cause instabilities and irregularities. Using GPS receivers to monitor the enhanced TEC during this formation, and tracking the dense regions across the pole with GPS and radars [Oksavik et al. 2010; and e.g. Foster et al.,2005] we can be able to pinpoint a more precise forecast for the NMA. Research has shown that patch drift velocities are in the range from 300-1000 kms^{-1} [Weber et al., 1984], which means that these patches can travel across the polar cap within a couple of hours. Thus, for our part in Norway, we have increased the prediction accuracy by narrowing the timeline down to within a few hours after formation of the patch.

What is the scenario for Norway?

Since the auroral oval covers Svalbard in the daytime and the mainland in the night, Norway is vulnerable to geomagnetic and ionospheric disturbances. This affects both radio communications for aviation and ship traffic, as well as navigation. Having a lot of off-shore industry that relies strongly on precise positioning, it is crucial that NMA can forecast accurate predictions to their clients [e.g. Norwegian Space Center, 2013].
As the patches of plasma form on the dayside over the American continent, it is obvious that it is the mainland of Norway that will encounter the most perturbed ionosphere in the evening when patches exit the polar cap and join the return flow [Crowley et al., 2000]. In addition, because we are situated underneath the the auroral oval during nighttime, auroral precipitation and electro jets contribute to scintillation effects [Aarons, 1982; Jacobsen and Schafer, 2012]

Could the NMA have been notified in advance?

The simple answer is yes. The scientific community had the knowledge and data, and ability to provide estimates and predictions to the public or subscribing clients in 2003. However; the details and timelines of the disturbance development, called for a more thorough understanding of the scenario in general- and on NMA's behalf. This thesis will shed some light upon the causes of the satcom outage and the possibilities concerning forecasting them.

2 Background

In this chapter I will establish some of the theoretical basis for an understanding of the origin of the space weather related disturbances. I have chosen to begin with the solar source and solar wind and from thereon continue with a description of the Earth's magnetic field and ionosphere. In the last section I give a short introduction to GNSS and the NMA (Kartverket).

2.1 The Sun and the solar wind

The Sun is the source of the violent eruptions that cause geomagnetic storms. During the 11 year cycle (Schwabe cycle) it undergoes, the solar activity varies, but there is always emission of solar particles, the solar wind. I will begin with a brief outline on the Sun, solar wind and the interplanetary magnetic field.

2.1.1 The Sun

The Sun is a large sphere of hot ionized gas. The main constituents are hydrogen and helium, but also some heavier elements. As all main sequence stars, the Sun is also fueled by nuclear fusion of hydrogen in the core. These reactions can occur due to high density and temperature in the core and contribute to balance the gravitational force and maintain hydrostatic and thermal equilibrium. [Friedman and Kauffmann III, 2001]

A closer look at the Sun reveals that it has a zonal structure. The Sun's interior can be divided in to three zones in which different processes take place (see Figure 2.1-1). The innermost zone is the core. It extends approximately 2500000 km from the center of the Sun and the temperature here is about 15 million K. The high temperature combined with the high particle density makes nuclear fusion possible. There are several conversion chains leading to the energy production, but the most important is the PP-chain, where four protons are converted into helium and energy through multiple stages. The energy flux from the interior is transported throughout the core and through the next zone, which is called the radiative zone. This zone extends from 250 000 km to about 500 000 km and the heat is transported via random movement of the photons. The mean free path of a photon is very short and despite travelling at the speed of light in vacuum, a photon's escape time is more than 100 000 years. The constant re-absorption and re-emitting of the photons lead to decreased temperature and energy as more photons are created radially throughout the radiative zone [Prölss, 2004].

The mean temperature at a distance about 500000 km from the solar center is approximately 2 million K. At this low temperature protons and electrons can form atomic hydrogen under absorption of photons. This inhibits the outward radiation of free photons and therefore the energy flux has to be transported in a different manner [Friedman, and Kauffmann III, 2001].

The third layer of the Sun's interior is also part of the solar surface. This zone is called the convection zone and is due to the convective energy transport. As the temperature and pressure drops towards the edge of the radiative zone, it leads to an expansion of the gas. The closer to the surface, the more rapid it drops, and parcels of cooler gas from the upper layers becomes heavier and drops down as warmer gas will rise. This circulative motion is called convection and it transports the energy flux from within the Sun to its surface. The convection cells give rise to the granulated surface look. The temperature on the surface is approximately 5800 kelvin. Some of the main physical properties of the Sun are summarized in Table 2.1-1.

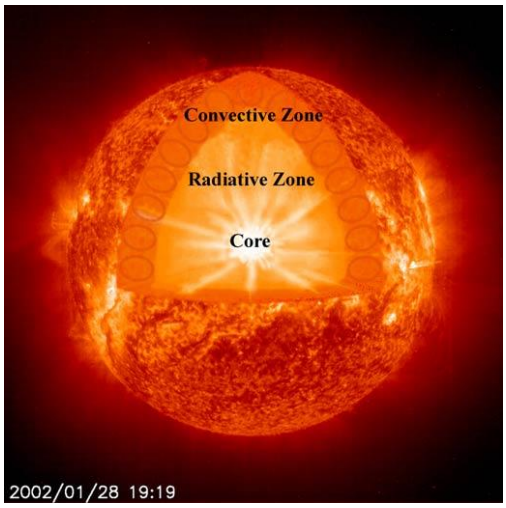

Figure 2.1-1: The different layers in the Sun's interior. The solar surface is granulated due to the convection cells in the uppermost layer. Photo: NASA/SOHO (*http://sunearthday.nasa.gov/2007/multimedia/gal_004.php)*

Radius R_S	$6.96 \cdot 10^8\, m$
Mass M_S	$1.99 \cdot 10^{30} kg$
Composition (mass fraction)	72% H, 26% He, 2% other
Mass density (mean)	$1.41 \cdot 10^3\ kgm^{-3}$
Mass density (center)	$1.5 \cdot 10^5 kgm^{-3}$
Luminosity	$3.86 \cdot 10^{26} W$
Temperature (effective)	5800K

Table 2.1-1: The physical properties of the Sun. Adapted from: Prölss [2004].

What makes the solar surface look like a sharply defined sphere is the lowest of three layers constituting the solar atmosphere. This is a thin layer of gas called the photosphere from which the visible light is emitted [Friedman and Kauffmann III, 2001]. The photosphere is about 500 km thick and the temperature decreases radially outwards from 6400 K to 4200 K (which is visualized by limb darkening) allowing the hydrogen and helium to exist in neutral form, see Figure 2.1-2a). Above the photosphere is the next layer, the chromosphere. It has its name due to the strong emission of H_α -line at wavelength 656.5 nm and violet CaII-lines providing it with a magenta color seen through H_α – filter. The chromosphere is not visible unless the solar disk is completely covered such, as during a total eclipse. Then it is recognized by filaments and red gas jets (spicules) which are ejected from the supergranules (convection cells) on the solar surface (Figure 2.1-2b)). The temperature in the chromosphere is radially increasing outwards throughout the 2000 km width. At the top, it may well reach 25000K [Prölss, 2004; Friedman, and Kauffmann III, 2001].
Above the chromosphere we find the last layer, the corona. The corona is an ultra- thin gas layer that

extends from about 3000 km height to several solar radii ($6R_S$). Despite the decreasing density, the coronal temperature is well above one to two million K, enough to ionize the gas into a fine plasma of H^+, He^{2+} and electrons. The corona is easily visualized during an eclipse as a dim glowing tenuous structure surrounding the solar disk (Figure 2.1-2c)). Apart from this light, the corona emits extreme ultra violet radiation (EUV), X-rays as well as radio waves (thermal). Viewing the Sun in these ranges provide a good understanding of the distribution of the different types of coronal features, such as coronal holes and active regions (Prölss, 2004).

a) 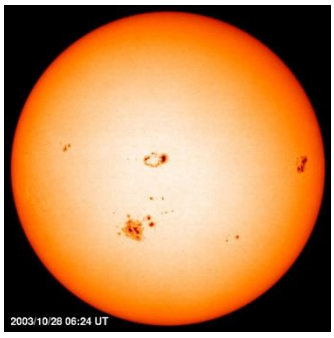

b) 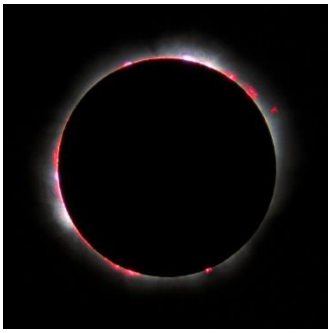
c) 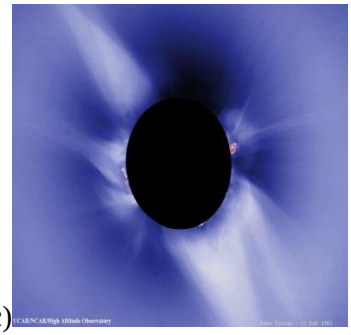

Figure 2.1-2: a) The photosphere of the Sun with large sunspots. Photo: NASA/SOHO (*http://sohowww.nascom.nasa.gov/gallery/images/large/mdi20031028_prev.jpg)*. b) The magenta colored chromosphere during the 1999 total eclipse. Photo: Luc Viatour (*http://www.kis.uni-freiburg.de/index.php?id=513&L=1&id=513)* c) The dim lit solar corona. Photo: UCAR/High Altitude Observatory (*http://solarscience.msfc.nasa.gov/images/Ecl1991a.jpg)*

2.1.2 The Solar Magnetic Dynamo and Sunspots.

It is believed that the Sun's magnetic field originate from a transition layer between the radiative and the convective zones, the so-called tachocline [e.g. Garaud, 2001]. Several models have tried to explain the dynamics of the magnetic field and still more advanced models are required to get the full picture [Vecchio et al. 2012]. In this outline I will only give a simple description of the solar dynamo and the interplanetary field.

The main explanation of the dynamo effect are the ω-and α- effects first suggested by E.N. Parker in 1955and H.W. Babcock in 1961 [Vecchio et al. 2012; Friedman and Kauffmann III, 2001; Hood and Hughes, 2011]. This provides an explanation to the photospheric global field and the solar cycle. In the ω-effect, the magnetic field is dominated by the poloidial component in the North-South direction at solar minimum. With time the poloidial field lines becomes twisted and stretched down and along the equatorial latitudes, see Figure 2.1-3a). This happens due to differential rotation and velocity shears arising from the transition between the slow-rotating radiation zone, and the faster rotating convection zone. After approximately 11 years, the field is dominated by a toroidal component in the East-West direction [Vecchio et al. 2012; Friedman and Kauffmann III, 2001; Mackay, 2011].The α-effect is the dynamo's ability to change the toroidal field back to poloidal with the reversed polarity [Hood and Hughes, 2011]. It is the Coriolis force that twists the field lines in a certain manner that makes the toroidal flux transform into poloidal flux and therefore reverse the field [Kivelson and Russell, 1995]. See Figure 2.1-3b).

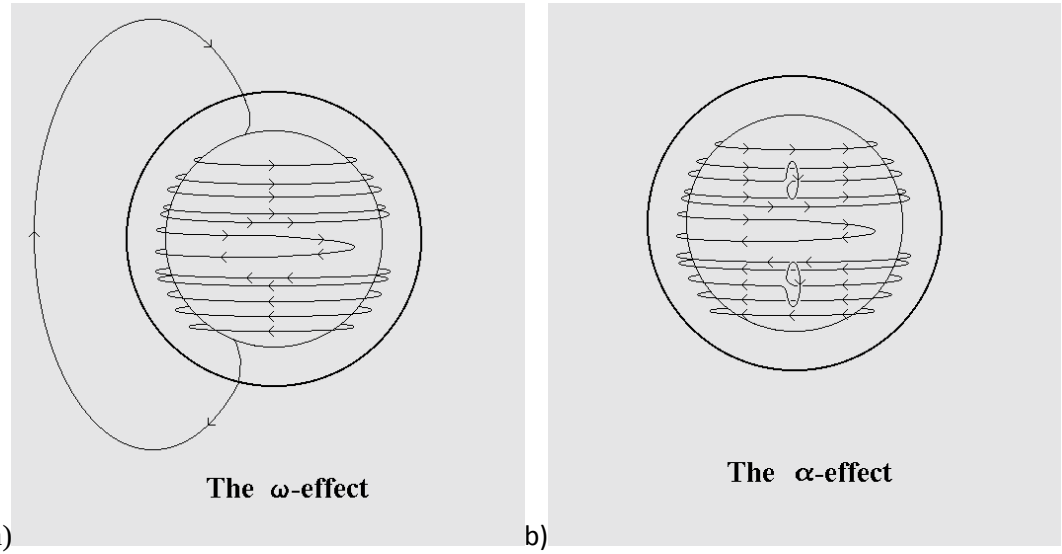

a) b)

Figure 2.1-3: a) The ω- effect showing how the poloidal fieldlines are wrapped around the Sun in an toroidal direction. b) The α-effect showing how the field lines twist and reverse the polarity of the field. Both figures from: *http://solarscience.msfc.nasa.gov/dynamo.shtml*

2.1.3 The Sunspots and the Spörer – diagram.

The visual display of the twisted magnetic field is the sunspots. The first knowledge of sunspots date back to the fourth century B.C [Priest, in Kivelson and Russell, 1995], and the first recorded sunspot observation in Europe was in 1610 [Prölss, 2004]. However, the source of these spots was not explained until 1908, when American astronomer G.E. Hale studied the spectral lines from the sunspots. He discovered that the spectral lines were split into several lines. This could be explained by the Zeeman effect, in which spectral lines split when the atom is subjected to a magnetic field The explanation to where the sunspots originated from was clear, it had to be areas with strong magnetic field. The color is due to magnetic deflection of hot surface plasma, and therefore the spots are cooler and appear darker than the ambient photosphere, see Figure 2.1-4 [Friedman and Kauffmann III, 2001].

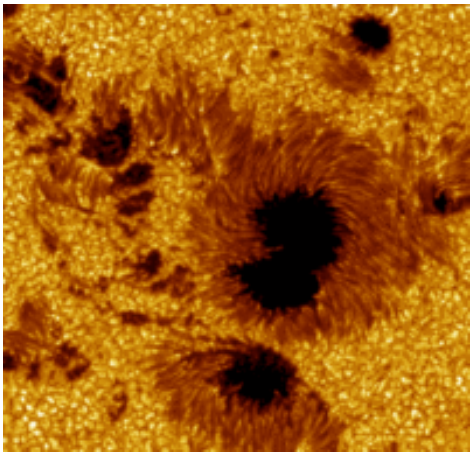

Figure 2.1-4: Photo taken, at visible wavelength, of sunspots occurring in the photosphere showing the dark umbra surrounded by the lighter penumbra. Photo: SST, Scharmer,G. and Löfdahl,M., ISP, 15 Jul 2002. (*http://www.solarphysics.kva.se)/*

The ω-effect is displayed by the sunspots. During the Schwabe cycle, the sunspots appear at 35º latitude on either side of the equator and slowly migrate down towards the equator. This motion gives rise to the Spörer diagram, or butterfly diagram as it resembles butterfly wings, in Figure 2.1-5a). The sunspots appear in pairs where the leading spots have opposite polarities in opposite hemispheres throughout the whole cycle. Although this bipolar behavior, the field inside a sunspot can be very complex, due to the twisted field lines. The sunspots may appear dull on the surface, but in reality they are very active regions playing an important role in the development of loops and prominences (Figure 2.1-5b)), [Mackay, 2011; Priest in Kivelson and Russell, 1995].

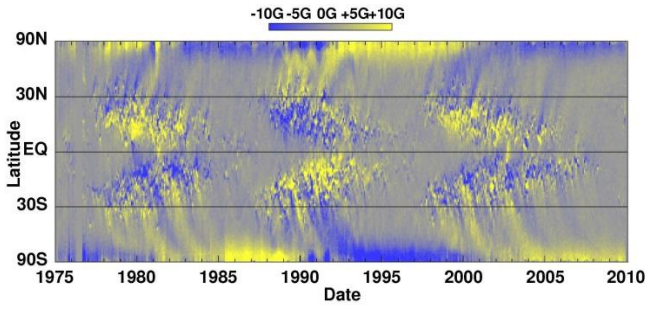

a)

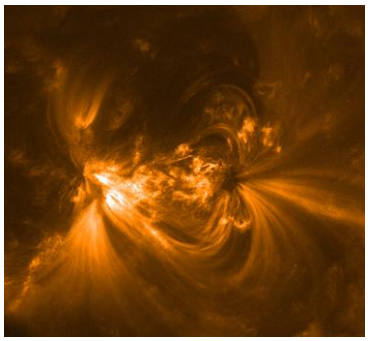

b)

Figure 2.1-5: a) The Spörer- , or butterfly diagram. The magnetic flux on both hemispheres, approach the equator during the 11 year cycle. Photo: NASA/MSFC/David Hathaway (*www.nasa.gov/topics/solarsystem/features/solar_plasma.html*). b) A magnetic active region where a flux rope is connected to two sunspots. Image is taken at 171Å wavelength, revealing a lot more of the true nature of sunspots. Photo: NASA/TRACE, *(http://trace.lmsal.com/POD/images/T171_0602_14UT.gif)*

2.1.4 The Coronal Field and the Interplanetary Magnetic Field

This field varies also throughout the solar cycle, with the strongest magnetic fluxes situated near the equatorial regions during solar maximum. In the higher latitudes, the magnetic field is weaker and the field lines are open and extend into space. This gives rise to a complex magnetic field with both closed flux at low latitudes and open flux at higher latitudes [Hood and Hughes., 2011]. Figure 2.1-6 shows resulting images of two models on the evolution of the coronal field adapted from Yeates et al. [2010]. The coronal features that are normally seen at lower latitudes, are helmet streamers. These magnetic loops form above sunspots and so-called active regions with intense radiation. At higher latitudes, open field lines contribute to coronal holes. They appear less bright and have low density due to the outward flow of plasma along the field lines. At solar maximum coronal holes also emerge closer to the equator as the general field is distorted. Although the coronal field is complex, it tends to be radial beyond a distance of roughly $3R_S$. Since the Sun rotates, the radial field lines are swept along, and form Archimedean spirals (Parker spirals). The solar magnetic field is not a real dipole field, but it has a dipole component.

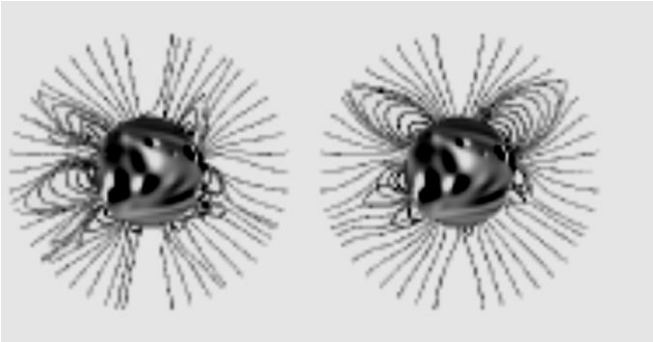

Figure 2.1-6: Both models show the photospheric surface field and the fieldlines of the coronal field. Notice the open flux towards the poles. Adapted from: Yeates et al., [2010].

The solar equator is inclined approximately 7º with respect to the ecliptic and thus the direction of the field is sometimes directed towards the Sun and sometimes away from the Sun (a couple of times during a solar rotation) according to the hemispheric polarization. A neutral current sheet divides the two magnetic directions. This neutral sheet is part of the heliospheric current sheet which produces an additional field superposed to the original field. The current flows towards the Sun in logarithmic spirals which are perpendicular to the magnetic field lines, Figure 2.1-7 [Prölss, 2004].

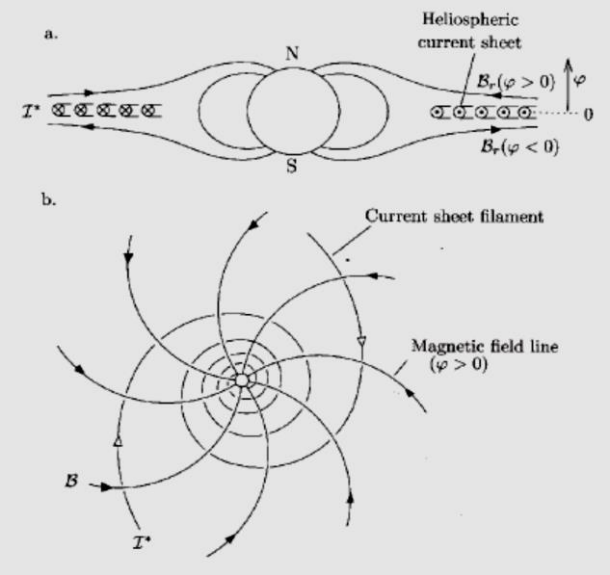

Figure 2.1-7: Top : meridional cross section of the heliospheric current sheet and the dipole field. Bottom: The interplanetary field seen from above the north pole of the Sun. By Alfvèn (1981) taken from Prölss [2004], p. 309.

This current sheet is a circumsolar disk with an inclination with respect to the ecliptic, and hence the Earth will find itself above or below the sheet during the Sun's rotation period. As mentioned above, this affects the observed direction of the magnetic field. In addition to that, the sheet is warped in the azimuth direction due to uneven distribution of coronal holes. Deformations also occur in the radial direction. The warping of the current sheet is often referred to as a ballerina skirt, see Figure 2.1-8, [Prölss, 2004].

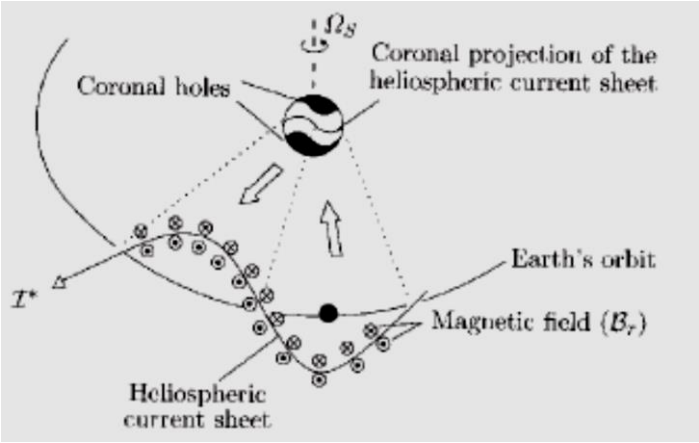

Figure 2.1-8: The warping of the heliospheric current sheet. Adapted from: Prölss [2004], p.311.

2.1.5 The Solar Wind and Magnetic Clouds

The solar wind is plasma emitted from the Sun. As mentioned before, plasma escape through coronal holes along the open magnetic field lines. In addition, the disruption of helmet streamers, contribute to eject large amounts of plasma into the interplanetary space.
The solar wind is separated into two types based upon its origin. The solar wind originating from lower latitudes, where the field lines are closed, is characterized as "slow". Whereas the solar wind from higher latitudes is "fast". Table 2.1-2 summarizes main features of the two types at 1AU.

Solar wind	Velocity (u)	Proton density (n_p)	Proton temperature (T_p)
Slow (closed flux)	$300\ kms^{-1}$	$8\ cm^{-3}$	$0{,}3 \cdot 10^5\ K$
Fast (open flux)	$700\ kms^{-1}$	$2-3\ cm^{-3}$	$2 \cdot 10^5\ K$

Table 2.1-2: Parameters of solar wind from different origins. From Prölss [2004]

The solar wind can be modeled by gas dynamic models, however; since it is a magnetized plasma, ideal magneto-hydrodynamics (MHD) is more appropriate. I will return to that in section 2.2.2. Whenever the plasma obeys ideal MHD, its movement is perpendicular to the magnetic field, and the field lines are frozen in inside the plasma. Therefore the interplanetary field and solar wind jets originating from different solar regions are coinciding Archimedean spirals. The overall structure of the solar wind and the jet lines is governed by the differences in velocities. Since the plasma is frozen to the magnetic field lines from a certain location, it will stay on that field line and is prohibited from penetrating to neighboring field lines (jet lines). Slow solar wind spirals will either be accelerated by fast solar wind from behind and the jet lines becomes compressed. Or the slow solar wind cannot keep up with fast solar wind ahead, and a rarefaction region is formed, (Figure 2.1-9) [Prölss, 2004].
Both coronal holes and active regions have lifetimes exceeding more than one solar rotation period (25 days). This means that they are periodic structures, often referred to as co-rotating interaction regions (CIR), although it is not an accurate term. CIRs are actually quazi-periodic features. The most prominent structures in the solar wind arise from eruptions of helmet streamers and solar filaments leading to flares and coronal mass ejections (CMEs). CMEs occur one to three times a day during solar maximum [Lepping et al., 2003].

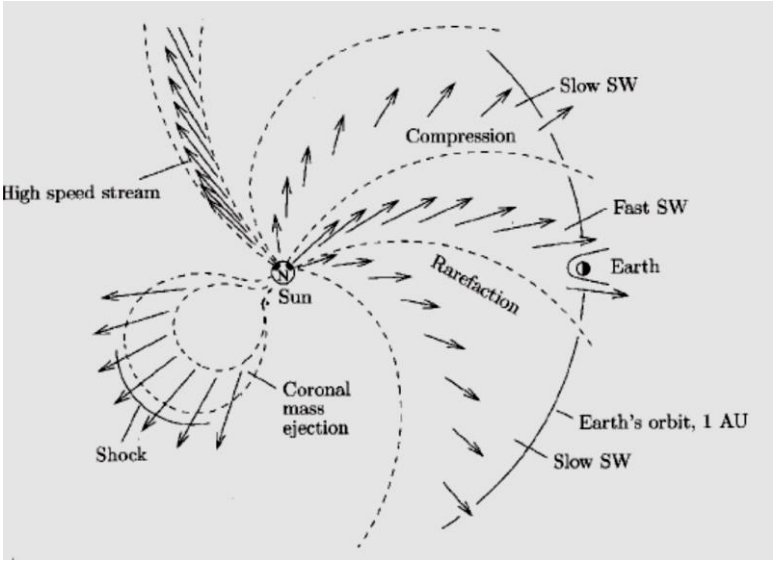

Figure 2.1-9 :The arrows indicate compressed and rarefied jet lines due to different velocities. Adapted from: Prölss [2004]. p.299.

A CME is a violent eruption where the Sun ejects a large portion of its own mass into space. The dynamics of CMEs are complex and beyond the scope of this outline, however I will give a general and brief description. The twisted magnetic field lines along the equatorial region of the Sun form flux ropes. These intertwined field lines are anchored in the photosphere and magnetically bipolar. Plasma is frozen into the field providing the bright high density dome, see Figure 2.1-10. Sometimes the anchorage may break due to instabilities and the flux rope loosens, hence expanding the CME outwards. When it happens; plasma is drained into space along open field lines. Afterwards the open field lines reconnect and a new helmet streamer is developed [Low, 2001]. Many reconnection processes in the corona lead to flares. More on reconnection will be treated in section 2.3.3. The dynamics of solar flares are too extensive to discuss here, so I will only give a short introduction. Flares are commonly associated with a rapid release of large amounts of excess energy in coronal loops. This results in strong radiation from radio wavelengths to x-ray and gamma rays. The most characteristic emissions are x-rays and hydrogen alpha [Priest in Kamide and Chian, 2007]. Flares are classified by the maximum x-ray flux emitted. The classes are A,B,C, M and X. A and B are weak flares with fluxes from $1.0 \cdot 10^{-8}$ -$9.9 \cdot 10^{-7}$ Wm^{-2}.

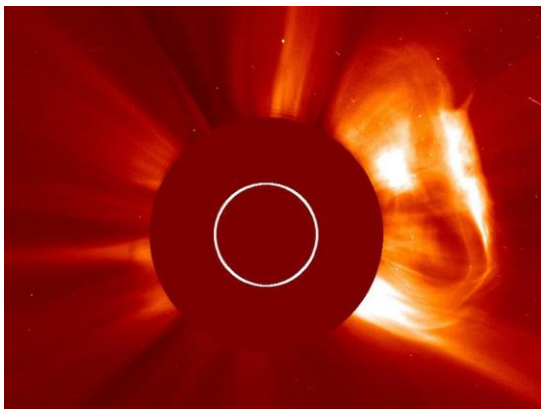

Figure 2.1-10: A CME erupting from the Sun's limb. Notice the bright dome of dense plasma in the front. Photo: NASA/SOHO *(http://www.nasa.gov/images/content/611128main_cme-112611_full.jpg*)

The letters C, M and X stand for "common", "medium" and "extreme". The associated fluxes are listed in Table 2.1-1 below. An x-ray flux of $3.2 \cdot 10^{-5}$ Wm^{-2} is classified as a M3.2-flare. [Rowlett, 2003].

Class	A_n	B_n	C_n	M_n	X_n
Flux (Wm^{-2})	$n \cdot 10^{-8}$	$n \cdot 10^{-7}$	$n \cdot 10^{-6}$	$n \cdot 10^{-5}$	$n \cdot 10^{-4}$

Table 2.1-3: The maximum X-ray flux classification of solar flare intensity. For X-flares, n >9. Adapted from Rowlett [2003] (*http://www.unc.edu/~rowlett/units/scales/solar_flares.htm*)

In the interplanetary field, large transient ejecta from the Sun propagate towards the Earth. One of these, are so called magnetic clouds (MCs). They are believed to originate from field structures that overlay CMEs. MCs have helical flux rope structures, which orientation play an important role in interaction with the geomagnetic field and give rise to long lasting periods with southward interplanetary magnetic field Bz-component (IMF B_z), Figure 2.1-11a).

When a MC has a flux rope Bz- component that is right handed, the axial inclination of the field could be directed from south to north or north to south. This leads to either trailing or leading southward IMF Bz, resulting in reversal of the field during MC-passage. Other configurations are also possible, see Figure 2.1-11b). The rope polarity is also related to the solar cycle and the polarity of sunspots [Lepping et al., 2003]. The MC that was formed during the superstorm on November 20, 2003, had a right hand (RH) east-southwest (ESW) inclination according to Huttunen et al [2005]. This suggests that the Bz-component was southwards during the entire passage of the MC.

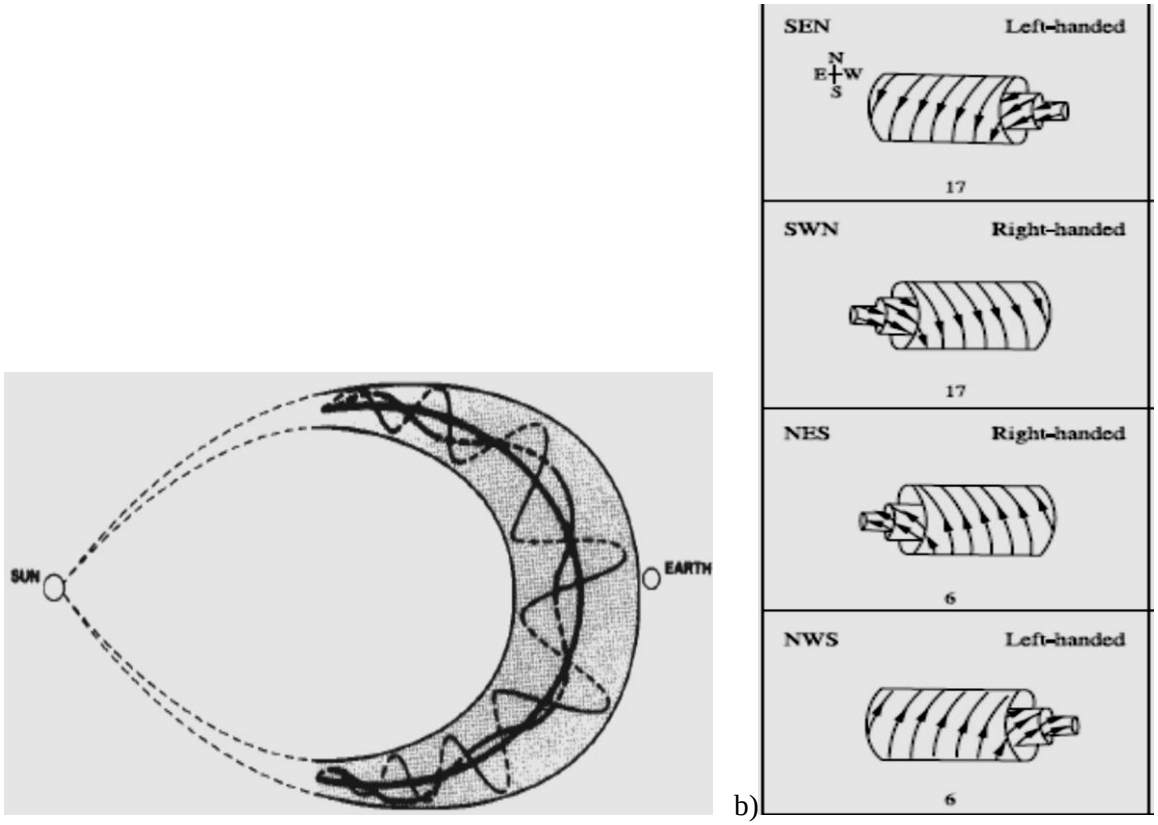

Figure 2.1-11: a) The flux rope of a magnetic cloud. Adapted from: Burlaga and Lepping [1990]. b) The various orientations of the axial fields of magnetic clouds. Adapted from: Bothmer and Schwenn [1998].

Sometimes it is not the MC itself which causes the southward turning of the IMF Bz. So called sheath fields in front of the MC may be strong enough to trigger geomagnetic storms. The ram pressure of the solar wind is capable of pushing the Earth's magnetopause earthwards about 5 Earth radii (R_E). The initial compression of the MC, contributes to interplanetary shocks or pressure pulses that pushes the magnetopause earthwards and trigger geomagnetic storms [Lepping et al., 2003]. When the solar wind pressure suddenly increases and the magnetopause is compressed, and the magnetopause current is intensified along with the geomagnetic field. This is called a sudden impulse (SI). If a geomagnetic storm follows, it is called a storm sudden commencement (SSC), [Huges in Kivelson and Russell, 1995]. The MC-velocity does also play a role in how the storm intensity develops. Large velocities are associated with enhanced ring current and depressed Dst-index [Lepping et al., 2003].

I have very briefly outlined some of the features of the Sun and the solar wind that contribute to the interaction between the interplanetary field and the geomagnetic field. Before I treat the magnetosphere, I will return to MHD under the following section.

2.2 Magnetohydrodynamics

The solar wind is not a neutral gas, but consisting of charged particle in a magnetic field. It is a dilute gas we treat it as a collisionless magnetoplasma. In order to describe the behavior of the solar wind and the interplanetary field we introduce magnetohydrodynamics (MHD) which accounts for the currents arising from charged particle motion. With MHD, the magnetic plasma can be treated as a single hydrodynamic fluid that is subjected to electric and magnetic forces [Prölss, 2004].

2.2.1 Derivation of MHD-equations with Quasi - neutral Approximation

The subscripts "i" and "e" stand for ions and electrons. Vector identities are written in bold. Assume a quasi- neutral gas where the particles have same densities, temperature and velocities and no production or loss processes occur. Assume charge density and relative velocities $n_i \simeq n_e = n$ and $\boldsymbol{u}_i \neq \boldsymbol{u}_e$. The density balance equation for the plasma is derived with neglect to production and loss processes.

$$\frac{\partial n_i}{\partial t} = -\nabla(n_i \, \boldsymbol{u}_i) \qquad (2.1)$$

and

$$\frac{\partial n_e}{\partial t} = -\nabla(n_e \, \boldsymbol{u}_e) \qquad (2.2)$$

Letting

$$\rho = (\rho_i + \rho_e) \qquad (2.3)$$

and

$$\boldsymbol{u} = \frac{(\rho_i \boldsymbol{u}_i + \rho_e \boldsymbol{u}_e)}{\rho} \qquad (2.4)$$

we get the *density balance equation* for an ionized plasma (with no production or loss):

$$\frac{\partial \rho}{\partial t} = -\nabla(\rho \, \boldsymbol{u}) \qquad (2.5)$$

where ρ stands for net charge density and $\boldsymbol{u}$ is the velocity.

The *current contiuity equation* is given by:

$$\frac{\partial \rho}{\partial t} + \nabla \cdot \boldsymbol{j} \ = 0 \qquad (2.6)$$

Where $\boldsymbol{j}$ is the current density given by

$$\boldsymbol{j} = nq(\boldsymbol{u}_i - \boldsymbol{u}_e) \qquad (2.7)$$

where q is the charge.

However; since $\frac{\partial \rho}{\partial t} < \nabla \cdot \boldsymbol{j}$, we can simplify (2.6) to

$$\nabla \cdot \boldsymbol{j} \ = 0 \qquad (2.8)$$

The derivation of the moment balance equation inside a closed volume with no in-or-out flow requires a lot more work and will not be accounted for here. For further reading see Prölss [2004] or Kivelson and Russell [1995]. The Lorentz force on charged carriers from the magnetic field is given by:

$$\frac{\partial (mn\boldsymbol{u})}{\partial t} = nq(\boldsymbol{E} + \boldsymbol{u} \times \boldsymbol{B}) \qquad (2.9)$$

where m stands for mass, $\boldsymbol{E}$ and $\boldsymbol{B}$ are the electric and magnetic field vectors respectively. With the aid of the plasma pressure gradient that is closely related to the motion of particles, and eq. (2.7), the momentum balance equation for a single fluid plasma eventually is obtained:

$$\rho \frac{D\boldsymbol{u}}{Dt} = \rho(\frac{\partial \boldsymbol{u}}{\partial t} + (\boldsymbol{u} \cdot \nabla)\boldsymbol{u} = \sigma \boldsymbol{E} + \boldsymbol{j} \times \boldsymbol{B} - \nabla p \qquad (2.10)$$

If the conductivity is small, the electric force $\sigma \boldsymbol{E}$ may be omitted and the quasi neutral approximation of the *momentum balance equation* becomes

$$\rho \frac{D\boldsymbol{u}}{Dt} = -\nabla p + \boldsymbol{j} \times \boldsymbol{B} \qquad (2.11)$$

Since we are dealing with a magnetized plasma, we must include a set of Maxwell equations to deal with the electromagnetic quantities.

$$\nabla \cdot \boldsymbol{E} = \frac{\rho}{\varepsilon_0} \qquad (2.12)$$

$$\nabla \times \boldsymbol{E} = -\frac{\partial \boldsymbol{B}}{\partial t} \qquad (2.13)$$

$$\nabla \cdot \boldsymbol{B} = 0 \qquad (2.14)$$

$$\nabla \times \boldsymbol{B} = \mu_0 \boldsymbol{j} + \frac{1}{c^2}\frac{\partial \boldsymbol{E}}{\partial t} \qquad (2.15)$$

where $\boldsymbol{E}$ is the electric field strength, $\boldsymbol{B}$ is the magnetic flux density, $\boldsymbol{j}$ is the current density, ρ is the charge density and ε_0 and μ_0 are the electric permittivity and magnetic permeability of free space respectively. Eq. (2.12) is Gauss' law which states that electrical charges are sources of electrical

fields. Eq. (2.13) is Faraday's induction law which basically says that time varying magnetic fields induces rotational electric fields, with strength proportional to the intensity and rate of change in the magnetic field. The next equation (2.14) is Gauss' law for magnetic fields, which state that there are no magnetic monopoles. The last equation (2.15) is a form of Ampere's law, which says that stationary current densities and time-varying electric fields produce rotational magnetic fields. The strength of the field is proportional to the intensity and rate of change in the electric field and the strength of the current density [Prölss, 2004].

Equation (2.10) can be written as

$$\nabla \cdot (\varepsilon_0 \boldsymbol{E}) = \sigma \tag{2.16}$$

where σ is the conductivity. Also (2.15) can be simplified with the exclusion of the displacement current term $\frac{1}{c^2}\frac{\partial \boldsymbol{E}}{\partial t}$. This lead to the general form of Ampere's law:

$$\nabla \times \boldsymbol{B} = \mu_0 \boldsymbol{j} \tag{2.17}$$

We also infer a generalized form of Ohm's law:

$$\boldsymbol{E} + \boldsymbol{u} \times \boldsymbol{B} = \eta \boldsymbol{j} + \frac{\boldsymbol{j} \times \boldsymbol{B} - \nabla \rho}{nq} \tag{2.18}$$

where η is the resistivity, $\nabla\rho$ is the charge density gradient and q is charge. If we assume that the gyro radius is very small compared to the scale length of the fluid motion, the last term in (2.18) may be omitted. This gives the simplified generalized Ohm's law.

$$\boldsymbol{E} + \boldsymbol{u} \times \boldsymbol{B} = \eta \boldsymbol{j} \tag{2.19}$$

If we now assume infinite conductivity, so $\sigma \to \infty,\ \eta \to 0$,which is a legitimate assumption, since resistivity is relatively small in hot plasma, eq. (2.19) can be simplified even more:

$$\boldsymbol{E} \simeq -\boldsymbol{u} \times \boldsymbol{B} \tag{2.20}$$

2.2.2 Ideal MHD

The simplified form of Ohm's law eq. (2.20) relates the plasma state parameters and electromagnetic quantities providing a new set of equations that enable us to describe the plasma motion. It basically tells us that when we focus on induced electric fields, the conductivity along the magnetic field lines is of such a magnitude, that only electric fields perpendicular to the magnetic field is of importance. This means that all plasma motion is perpendicular to both the electric and the magnetic field, resulting in an ambipolar $\boldsymbol{E} \times \boldsymbol{B}$ –drift motion.

In section 2.1.5, I stated that the plasma obeyed ideal MHD whenever the plasma motion was perpendicular to the magnetic field. Then the magnetic field lines are frozen in to the plasma motion, so that all plasma elements are constrained to that explicit field line [Prölss, 2004].

The frozen in approximation can only be used if the magnetic Reynolds number, $R_m \gg 1$.

The magnetic Reynolds number is given by

$$R_m = \mu_0 \sigma u L \tag{2.21}$$

where μ_0 is the permeability of free space, σ is the conductivity, u is the flow velocity and L is a scale length for the field and flow. Characteristic lengths in solar phenomena are beyond $10^6 m$ [Priest in Kivelson and Russell, 1995]. The set of ideal MHD-equations are summarized in Table 2.2-1.

Plasma density equation (2.5)	$\frac{\partial \rho}{\partial t} = -\nabla(\rho \boldsymbol{u})$
Plasma velocity equation (2.22)	$\rho \frac{D\boldsymbol{u}}{Dt} = -\nabla p + \rho \boldsymbol{g} + \boldsymbol{j} \times \boldsymbol{B}$
Current velocity equation (2.17)	$\nabla \times \boldsymbol{B} = \mu_0 \boldsymbol{j}$
Plasma pressure equation (2.23)	$p = \alpha \rho^{\gamma^*}$
Faraday (Removed E-field) equation (2.24)	$\frac{\partial \boldsymbol{B}}{\partial t} = \nabla \times (\boldsymbol{u} \times \boldsymbol{B})$
Ohm (infinite conductivity) (2.25)	$\boldsymbol{E} + \boldsymbol{u} \times \boldsymbol{B} = 0$

Table 2.2-1: summarizes the ideal MHD equations, where $\boldsymbol{\rho} = (\boldsymbol{\rho_i} + \boldsymbol{\rho_e}), \boldsymbol{u} = \frac{(\boldsymbol{\rho_i u_i} + \boldsymbol{\rho_e u_e})}{\boldsymbol{\rho}}$, $\boldsymbol{p} = (\boldsymbol{p_i} + \boldsymbol{p_e})$, and $\boldsymbol{j} = \boldsymbol{nq}(\boldsymbol{\rho_i u_i} + \boldsymbol{\rho_e u_e})$. $\boldsymbol{\gamma}^*$ is the polytropic index and α is a constant composite factor [Prölss, 2004].

2.2.3 Charged Particle Motion in the Geomagnetic Field

We consider a charged particle with mass *m* and charge *q* in a collision less plasma. We ignore friction and interaction with other particles in the medium as well as. The forces acting upon *m* are the inertial force, the

$$\boldsymbol{F}_i = m\frac{d\boldsymbol{u}}{dt} \qquad (2.26)$$

Lorentz force

$$\boldsymbol{F}_B = q(\boldsymbol{u} \times \boldsymbol{B}) \qquad (2.27)$$

and forces other external forces, $\boldsymbol{F}_{ext}$. This provides the equation of motion:

$$m\frac{d\boldsymbol{u}}{dt} = q(\boldsymbol{u} \times \boldsymbol{B}) + \boldsymbol{F}_{ext} \qquad (2.28).$$

To evaluate the solution, we separate it into velocity components parallel and perpendicular to the magnetic field, giving:

$$m\frac{d\boldsymbol{u}_\parallel}{dt} = \boldsymbol{F}_{ext_\parallel} \qquad (2.29)$$

and

$$m\frac{d\boldsymbol{u}_\perp}{dt} = \boldsymbol{F}_{ext_\perp} + q(\boldsymbol{u}_\perp \times \boldsymbol{B}) \qquad (2.30).$$

The solution to (2.29) is straightforward, but (2.30) depends on the orientation of the magnetic field and whether external forces are present. For further reading on this topic, see e.g. Prölss [2004].

It is common to study the following five special cases for eq. (2.30):

I. Gyromotion $\boldsymbol{F}_{ext_\perp} = 0,\ \boldsymbol{B}\ uniform$

In this case, the charged particles will be accelerated by the magnetic field in a direction perpendicular to both the magnetic field and the direction of motion. This forces the charged particles to orbit the magnetic field line in a circular motion. The charge of the particle decides the direction of the circular motion. For a right hand system, ions will gyrate clockwise and electrons will gyrate counter - clockwise, see Figure 2.2-1a). The gyro radius is given by:

$$r_B = \frac{mu_\perp}{|q|B} \qquad (2.31)$$

and the gyro frequency is:

$$\omega_B = \frac{|q|B}{m} \qquad (2.32).$$

The gyrating charges are producing electric current, resulting in a dipole field opposite of the background field. The dipole field strength is:

$$\boldsymbol{M}_g = -\frac{E_\perp \boldsymbol{B}}{B^2} \qquad (2.33)$$

The velocity component parallel to the magnetic field line, slide along it, resulting in a helical trajectory around the field line. See Figure 2.2-1b).

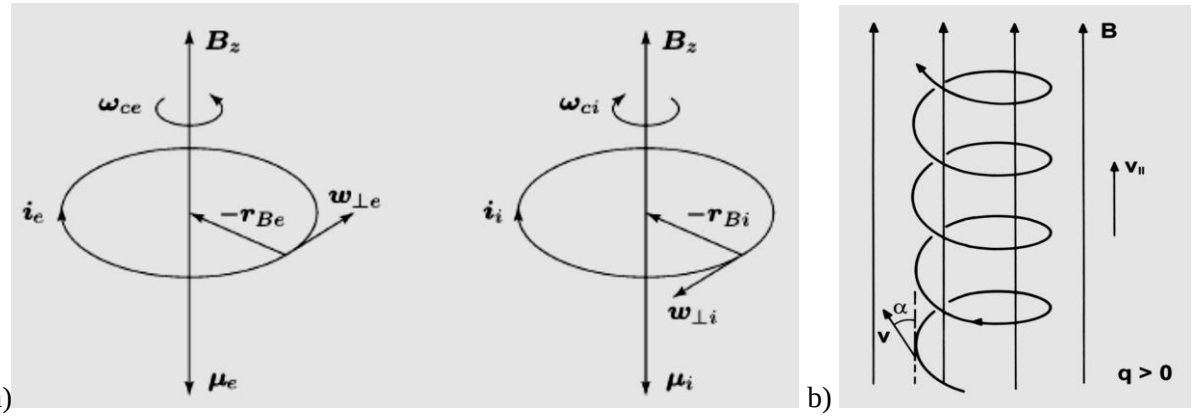

Figure 2.2-1: a) The gyro motion of electrons and ions in a uniform magnetic field. From: Moisan and Pelletier [2012], (*www.springer.com/cda/content/.../cda.../9789400745575-c2.pdf*). b) The helical trajectory of an ion gyrating along the magnetic field. From Bittencourt [2004]. (*www.springer.com/cda/content/.../cda.../9780387209753-c1.pdf*)

II. Oscillatory bounce motion $\boldsymbol{F}_{ext_\perp} = 0,\ \nabla \boldsymbol{B} \parallel \boldsymbol{B}$

Gyrating charges bounce back and forth between the magnetic poles due to a magnetic intensity gradient parallel to the magnetic field, see Figure 2.2-2.
The geomagnetic field lines are converging at the magnetic poles. The increasingly smaller separation, lead to enhanced field strength which affect the trajectory of the charged particles in such a fashion that every time the charges approach the poles, they are decelerated to a halt by the magnetic intensity

gradient force, before they are accelerated back. Reversal occurs when the pitch angle of the helical trajectory becomes 90º, in so called mirror points. The magnetic field strength at mirror point is obtained by:

$$B_{mirror} = \frac{B_0}{sin^2\alpha_0} \qquad (2.34)$$

where $\boldsymbol{B}_0$ is the magnetic field strength at apex of the guiding center field line, and α_0 is the apex point. The typical helical trajectory path length is about 2Earth radii [Prölss, 2004].

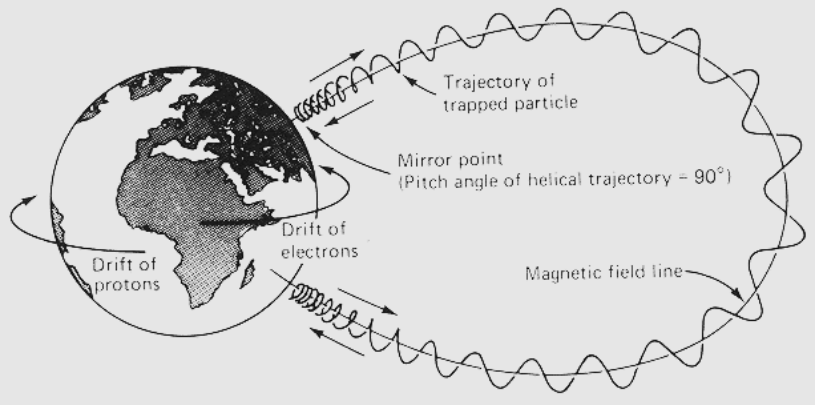

Figure 2.2-2: Showing the trapped particle motion along geomagnetic field line.
Adapted from: *http://www-ssg.sr.unh.edu/tof/Smart/Students/lees/periods.html*

III. Gradient drift motion $\boldsymbol{F}_{ext_\perp} = 0, \quad \nabla \boldsymbol{B} \perp \boldsymbol{B}$

When the gradient is perpendicular to the magnetic field, the charges feel discontinuities in the field strength perpendicular to their direction of motion. This affect the gyro motion in such a manner that the gyro radius becomes smaller in vicinity of stronger field, and larger in vicinity of weaker fields as demonstrated in Figure 2.2-3.

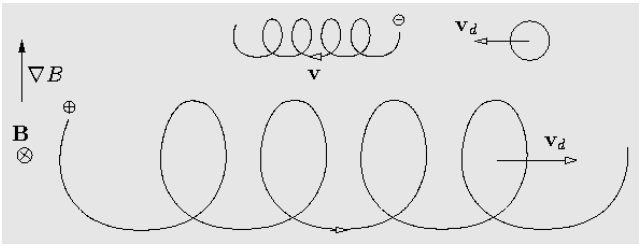

Figure 2.2-3: Showing the gradient drift motion of the charge carriers. From Hutchinson [2001], (*http://silas.psfc.mit.edu/introplasma/chap2.html)*

IV. External force drift in uniform field $\boldsymbol{F}_{ext_\perp} \neq 0, \ \boldsymbol{B}\ uniform$

Let the external force be charge independent and perpendicular to the magnetic field. Let the charges be at rest initially. When the particles feel the external force, they will be accelerated towards it. However, the magnetic force from the magnetic field is forcing the moving charges into a gyro motion around the field lines. As soon as the charges move in the opposite direction of the external force they

are decelerated and they fall back to rest. Figure 2.2-4 illustrates how the cycloid drift motion develops sideways and perpendicular to both the external force and the magnetic field. Particles with opposite sign move in opposite directions, contributing to a current flow along the ion drift direction.

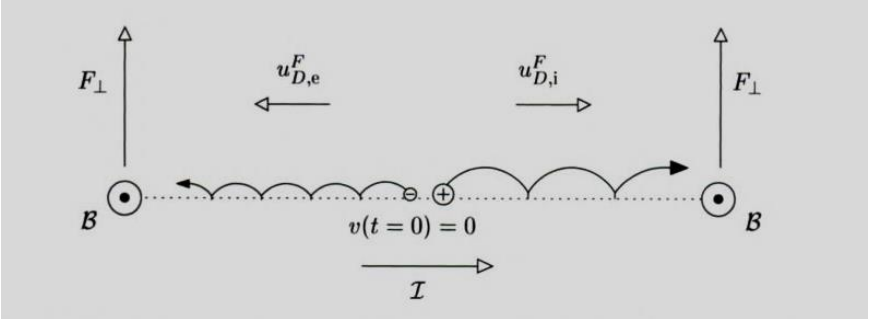

Figure 2.2-4: The charged particle motion under appliance of an external force. Electrons and ions drift in opposite directions. Figure adapted from: Prölss [2004], p. 231.

V. Ambipolar $\boldsymbol{E} \times \boldsymbol{B}$-drift $\quad \boldsymbol{F}_{ext_\perp} = q\boldsymbol{E}_\perp \quad \boldsymbol{B}\ uniform$

This is the last case of particle motion I will treat in this section, but it is one of the most important for further applications. When an electric field is present, the electric force accelerates the charges as in case IV, but the opposite charges cancel and they drift together in the *same* direction (Figure 2.2-5). The drift motion is perpendicular to both the electric and the magnetic field with velocity:

$$\boldsymbol{u}_D^E = \frac{\boldsymbol{E}_\perp \times \boldsymbol{B}}{B^2} \qquad (2.35)$$

The $\boldsymbol{E} \times \boldsymbol{B}$-drift play an important role in the plasma convection in the ionosphere.

Another drift motion is the curvature drift which is associated with the ring current [Prölss, 2004].

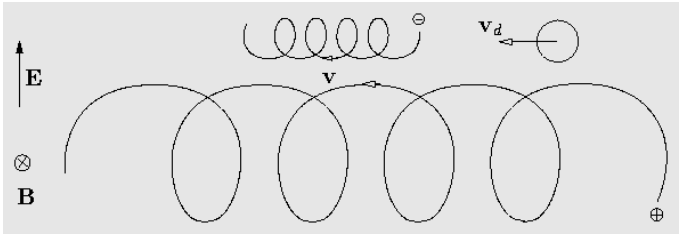

Figure 2.2-5: ExB-drift. Both negatively and positively charged particles drift in the same direction perpendicular to the electric and magnetic fields. From Hutchinson [2001], (*http://silas.psfc.mit.edu/introplasma/chap2.html)*

2.3 The Magnetosphere

The melted interior inside the Earth combined with its rotation, contributes to a dynamo magnetic field similar to the Sun's. However the Earth's magnetic field is a time stable dipole with only small variations.

The direction of the field, as of present day, is with the magnetic south located near the geographic north pole, and is referred to as the boreal pole. This means that the magnetic field lines are directed from the geographic south towards geographic north, in other words the field points northwards. The austral pole is therefore the Earth's magnetic north pole. The magnetic inclination poles are drifting, so the declination is varying a lot, but the magnetic dip equator is fairly aligned with the geographic equator, with some exceptions. Figure 2.3-1a) presents the main features of the geocentric dipole field. Because of the constant interaction with the solar wind (SW) and the interplanetary magnetic field (IMF) the geomagnetic field is not a perfect dipole, but rather compressed on the dayside facing the sun, and elongated into a tail on the nightside, see Figure 2.3-1b). The magnetotail extends more than two hundred Earth radii away from the Earth's center [Prölss, 2004].

a) 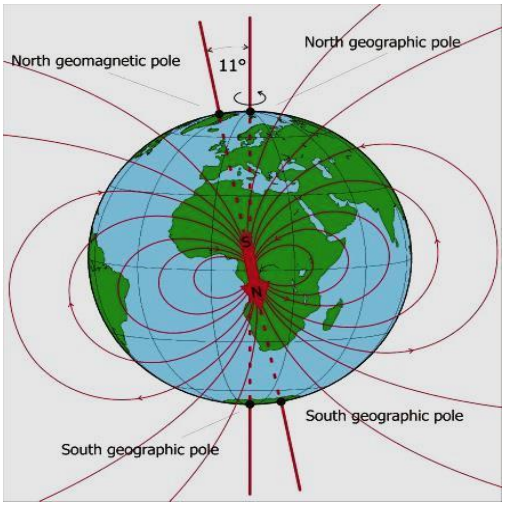

b) 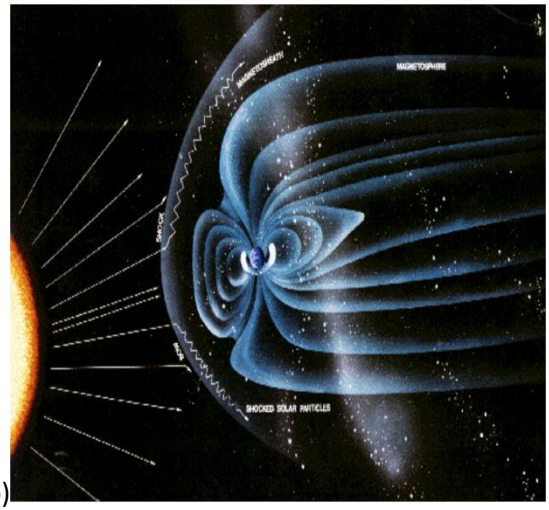

Figure 2.3-1: a) The geocentric dipole field. The magnetic field is tilted 11.7º away from the axis of rotation. Figure from: *http://roma2.rm.ingv.it/en/themes/7/the_earth-s_main_field.*
b) The magnetosphere showing the field lines of the geomagnetic field. Figure from: *http://www.igpp.ucla.edu/public/THEMIS/SCI/Pubs/Nuggets/FTE_nugget/first_figure%5B1%5D.bmp*

The nearly 11 º tilt of the geomagnetic field causes variations in the field strength with latitude, which has an impact on the longitudinal plasma flow [Pfaff,2012]. The field is strongest where the field lines converge at the magnetic poles, approximately twice the value as the dip equator value of $B_0 \simeq 31\ \mu T$. The internal magnetic field can be approximated as a geocentric dipole where the position is expressed in terms of the distance from the center of the Earth, R, and the geomagnetic latitude, λ_M. At the geomagnetic equator $\lambda_M = 0°$. The magnetic dipole-moment, M_E is directed along the dipole axis, which is declined 11º away from the rotation axis as shown in Figure 2.3-1a).The magnetic field strength of a field line, $\mathcal{B}$, can be described in terms of the vector components $\mathcal{B}_{\lambda_M}$ and $\mathcal{B}_R$ where R and λ_M are defined as above. This gives us the horizontal component:

$$\mathcal{B}_{\lambda_M} = \mathcal{B}_0 \left(\frac{R}{R_E}\right)^3 \cos\lambda_M \qquad (2.36)$$

where R_E is the Earth's radius and $\mathcal{B}_0$ is the field strength at magnetic dip equator. The vertical component can be written as:

$$\mathcal{B}_R = -2\mathcal{B}_0 \left(\frac{R}{R_E}\right)^3 \sin\lambda_M \qquad (2.37)$$

The angle between a field line and the Earth's surface is the inclination and is expressed as:

$$I = \tan^{-1}(2tan\,\lambda_M) \qquad (2.38)$$

[Prölss, 2004].

In 1961 presented C .E. McIlwain a coordinate system which enabled him to map the trajectories of the trapped particles in the magnetosphere. He introduced the shell parameter L which designates the relationship between the geocentric distance at magnetic equator R, and the radius of the Earth R_E. For a given field line we get the field line equation:

$$R = L\,R_E\,cos^2\lambda_M \qquad (2.39)$$

Thus L =1 is the surface of the Earth at the magnetic dip equator [McIlwain, 1961]. This allows us to determine the magnetic latitude of a foot print at a given height h above the Earth:

$$\lambda_M(R_E + h) = \cos^{-1}\sqrt{\frac{R_E + h}{R_E\,L}} \qquad (2.40)$$

In Cartesian coordinates, it is custom to define the internal dipole field as shown in Figure 2.3-2a). In positive direction $\hat{x}$ points towards geographic north, $\hat{y}$ points towards east and $\hat{z}$ points into the center of the Earth. The horizontal component of the magnetic field is expressed with the parameter, H, where

$$H = \sqrt{\hat{x}^2 + \hat{y}^2} \qquad (2.41)$$

so that the field strength is given by:

$$\mathcal{B}^2 = H^2 + z^2 \qquad (2.42)$$

The field strength expressed in terms of the shell parameter L:

$$\mathcal{B}(field\ line) = \frac{\mathcal{B}_0}{L^3}\sqrt{\frac{1 + 3sin^2\lambda_M}{cos^6\lambda_M}} \qquad (2.43)$$

Figure 2.3-2b) shows the definition of the field in Cartesian coordinates.

a)

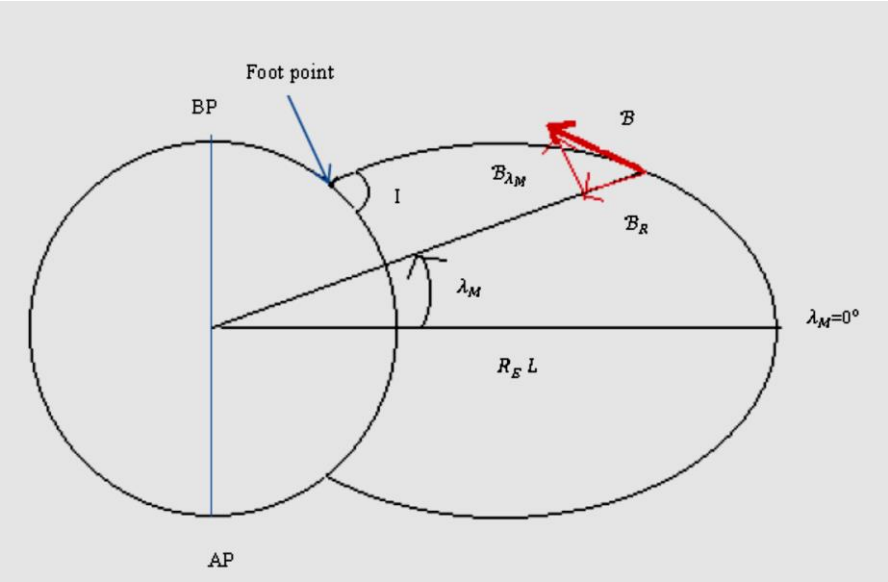

b)

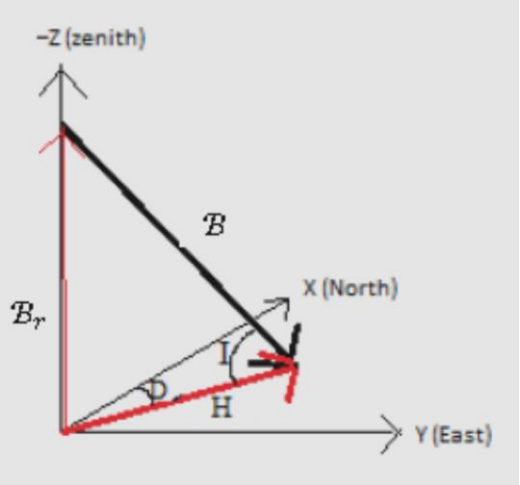

Figure 2.3-2: a) Showing the geocentric dipole approximation. The field vector on a field line in a distance r from the Earth's center. b) The field vector in Cartesian coordintes. Both figures are adapted freely from: Prölss [2004].

The distant Earth field is subject to the solar wind and interactions with it. Therefore the dipole approximation gives a poor description of the far field. Instead the Geocentric Solar Magnetospheric (GSM) coordinate system is more applicable from a space view. Figure 2.3-3 shows the definition of the GSM-coordinate system. The x-axis points radially towards the Sun (sub solar), the y-axis is perpendicular to the magnetic dipole axis and positive towards dusk. Finally; the z-axis is positive towards north, in the same sense as the northern magnetic pole. The interplanetary magnetic field (IMF) is also described by this coordinate system. Also it is custom to use magnetic local time (MLT) in order to describe phenomena in the magnetosphere/ionosphere. Magnetic noon is pointed sunwards along the GSM x-axis, whereas dawn points towards East (-y) and dusk towards west.

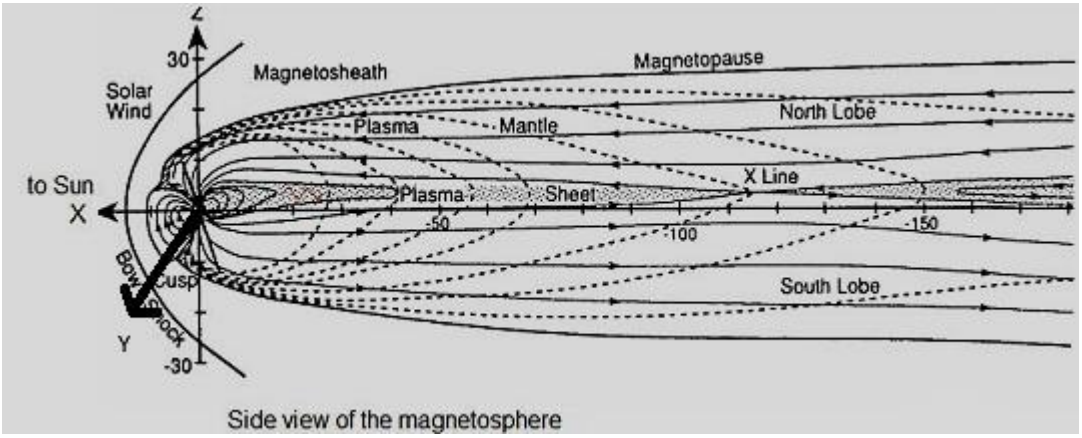

Figure 2.3-3: shows the magnetosphere and the GSM coordinate system for the magnetic field. Adapted from Christine Gabrielse at: *(http://www.igpp.ucla.edu/public/THEMIS/SCI/Pubs/Nuggets/gabrielse/gabrielse.html)*

2.3.1 The Near Earth Field

The Near Earth field is confined within approximately 6 Earth radii (R_E) from the Earth's center. The inner magnetic field is the closed dipole field below 60º magnetic latitude (MLAT). The dipole seems to co-rotate with the Earth and plasma is constrained to the field lines. A co-rotation electric field that originates in the dynamo layer, is directed towards the Earth, and is responsible for the E x B-drift of the charged particles. This region within the closed field is referred to as the plasmasphere and is an extension of the ionosphere stretching out from 2 R_E to about 4 R_E. Beyond this range, the plasma density drops sharply giving rise to the so called plasmapause. The plasma is relatively dense and cool and differs from the lower ionosphere by having atomic hydrogen as primary ion constituent [Pfaff, 2012; Prölss, 2004]. The main characteristics are summarized in Table 2.3-1, and Figure 2.3-4 shows the dominant particle motions.

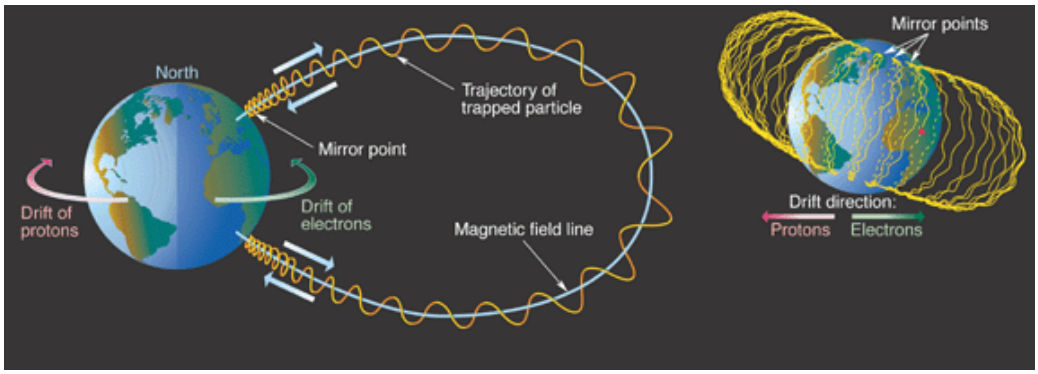

Figure 2.3-4: The motion of the trapped particles in the inner magnetosphere. The particles gyrate around the field lines, bounce between mirror points and drift in separate directions according to their charge.*(http://www.propagation.gatech.edu/ECE6390/project/Fall2011/group5/website/ssp/sat/env/res/FigureE5.gif).*

There are more charged particles confined within the region of the inner magnetic field overlapping the plasmasphere as shown in Figure 2.3-5. In a region located at approximately 2 R_E, we find the so called radiation belts (Van Allen belts) consisting of high energetic protons up to tens of MeV. It is believed that these particles are produced in a process of neutron decay, called CRAND (Cosmic Ray Albedo Neutron Decay). Cosmic high energy particles collide with the denser upper atmosphere and

subsequently neutrons are released. When these neutrons decay, they give rise to high energetic electrons and protons that becomes trapped within the magnetic field. The particles gyrate and bounce along the field lines and have a remarkably high drift velocity, but due to low density the current contribution is negligible. However; the high energy radiation can damage satellite instruments and possibly outdo a health risk for astronauts [Prölss, 2004].

Population	Ion temperature	Electron temperature	Particle density/flux	Composition	L-shell	Particle motion
Radiation Belts	1-100MeV	50keV-10Mev	$< 10^8$ m^{-2} s^{-1} (50MeV protons)	H^+, e^-	1.2-2.5	Gyration, bouncing, drift
Ring Current	1-200 keV	<10 keV	$< 10^6$ m^{-3}	H^+, O^+, He^+, e^-	3-6	Gyration, bouncing, drift
Plasmasphere	< 1 eV	< 1eV	$> 10^8$ m^{-3}	H^+, (O^+), e^-	1.2-5	Gyration, corotation

Table 2.3-1: The main properties of the particle populations in the inner magnetosphere. Adapted freely from Prölss [2004].

Outside the radiation belts (~3-6 R_E) we find a population of particles which azimuthal drift is of great importance. This is the ring current where positive charge carriers drift westwards and negative eastwards. The particle energy is in the keV-range and the mean density is $10^{\,6}\ m^{-3}$ and its main ion constituents are protons under solar quiet conditions. During solar disturbed conditions, the oxygen ion content increase due to infusion from the plasmasheet. The ring current sets up a magnetic field that disturbs the geomagnetic field at low latitudes. During disturbed conditions, charged particles from the solar wind penetrate the magnetosphere and they will enhance the ring current so that the magnetic disturbance increases. This relation between the ring current and magnetic disturbance is referred to as the Dessler-Parker-Sckopke (DPS) relation or theorem. This disturbance is described by the Dst index (Disturbance storm index) which illustrate the negative depression in the horizontal component of the geomagnetic field [Prölss, 2004]. It is believed that electric penetration fields are the cause of the Dst-enhancements and there are different models that describe this relation [Burke et al., 2007]. I will return to the Dst index in section 2.4-4, although the disturbances from the ring current are mostly of concern for lower latitudes. The DPS-theorem adapted from Burke et al.[2007] is given by:

$$\frac{Dst^*(t)}{B_0} = \frac{2E_{RC}}{3E_M} \qquad (2.44)$$

Where Dst^* is the Dst value corrected for the Chapman-Ferraro current at the magnetopause, B_0 is the magnetic field strength at magnetic equator. E_{RC} and E_M are the energies in the ring current and the magnetic field separately.

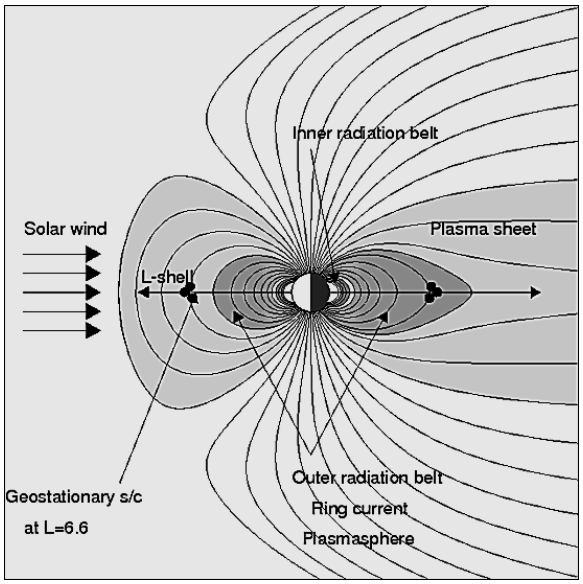

Figure 2.3-5: The main populations within the plasmasphere (dark grey region). Here the distances are described with the shell parameter L. Figure from: (*http://solarphysics.livingreviews.org/Articles/lrsp-2007-1/fig_4.html*).

2.3.2 The Distant Earth Field

The outer field is closely coupled to the interplanetary magnetic field (IMF). In order to describe this interaction, it is custom to separate the outer magnetic field into the dayside facing the Sun, and the nightside facing away from the Sun.

The dayside is subject to the effects of the solar wind (SW) and acts like a shield that prevents the solar wind from reaching the Earth. The barrier between the Earth's magnetosphere and the IMF is called the magnetopause (MP). The frozen-in solar wind plasma is unable to penetrate the magnetosphere perpendicular to the magnetic field, due to the Lorentz force (see Figure 2.3-6). Thus the magnetopause is said to form a tangential discontinuity and instead the supersonic plasma is deflected, and produces a bow shock allowing the plasma to flow around the magnetosphere. The shock contributes to heating of the plasma which is confined in the region between the magnetosphere and the bow shock. This region is referred to as the magnetosheath (MS) [Paschmann, 1991].

The magnetopause is located at roughly 10 R_E (subsolar), but it varies with the velocity of the solar wind. The geocentric stand-off distance can be calculated from the pressure balance between the solar wind kinetic pressure and the magnetic pressure at the magnetopause.

Let the solar wind kinetic pressure:

$$P_{SW} = 2nmu_{SW}^2 \qquad (2.45)$$

where *n* is the number density, *m* is the particle mass and u_{SW} is the solar wind speed. The magnetic pressure at the magnetopause can be written as:

$$P_{MP} = \frac{B_{MP}^2}{2\mu_0} \qquad (2.46)$$

where μ_0 is the vacuum permeability and B_{MP} is the field strength at the magnetopause given as:

$$B_{MP} = 2\mathcal{B}_0 \left(\frac{R_E}{R_{MP}}\right)^3 \qquad (2.47)$$

Here R_{MP} is the geocentric distance to the magnetopause at the noon meridian and $\mathcal{B}_0$ is the field strength at equator. The pressure balance becomes:

$$2nmu_{SW}^2 = \frac{2\mathcal{B}_0^2}{\mu_0}\left(\frac{R_E}{R_{MP}}\right)^6 \qquad (2.48)$$

which provides the stand-off distance:

$$R_{MP} = R_E \left(\frac{\mathcal{B}_0^2}{\mu_0 nmu_{SW}^2}\right)^{\frac{1}{6}} \qquad (2.49)$$

For practical calculations, a simplified version of eq. (2.49) is given by:

$$R_{MP} = R_E(107.4(n_{SW}u_{SW}^2))^{-\frac{1}{6}} \qquad (2.50)$$

where n_{SW} is the proton density number and the u_{SW} is the solar wind bulk velocity [Kivelson and Russell, 1995].

The deformation of the dipole field on the dayside is caused by local magnetic fields which are induced by surface currents. These fields are parallel with the dipole field line on the earthward side of the magnetopause current, and anti-parallel on the sunward side. The anti-parallel field cancels the dipole field on the outside, but the parallel field enhances the dipole field on the inside. This is the reason why the field strength at the MP is approximately twice the dipole strength. The surface current at the MP is often called Chapman-Ferraro current and is caused by charge separation due to the Lorentz force and gyro motion (in opposite directions) along the field lines (see Figure 2.3-6). The magnetic Lorentz force prevents the particles to complete at full gyro cycle, and the particles are reflected back into the solar wind after half a cycle [Prölss, 2004]. The gyro radius provides the approximate MP-thickness, which has to be above 50 km [Paschmann.1991]. The protons are deflected eastwards creating an eastward current which flows in closed loops perpendicular to the magnetic field. The protons have larger inertia than electrons, and penetrate further into the MP. It is believed that this generates an electric polarization field directed towards the Sun, which accelerates the electrons and increasing their gyro radius and likewise decelerate the protons and decrease their gyro radius. Thus the main charge carriers in the MP-current are electrons [Prölss, 2004].

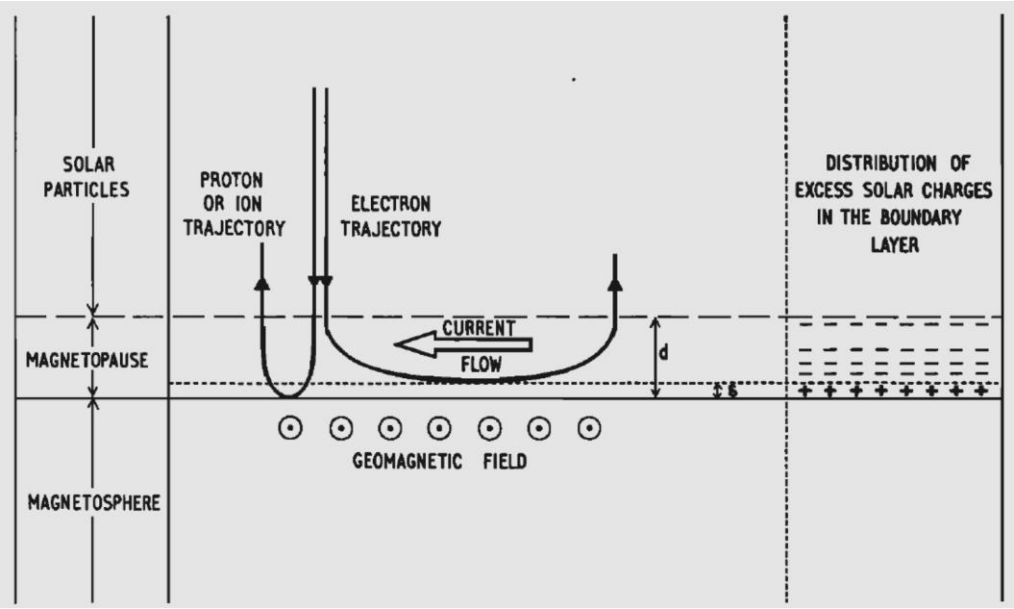

Figure 2.3-6: Seen from above: the solarwind arrives from top and the charged particles are deflected in either direction upon encountering the MP boundary layer. The polarization electric field points up (towards the Sun), and the magnetic field points out of the paper plane. Figure is adapted from: Willis [1971].

The current responds to changes in the solar wind dynamic pressure. Sudden increase in the SW-pressure leads to an increase in the geomagnetic field intensity. This is often referred to as a sudden impulse (SI) [Kievelson and Russell, 1995]. Whenever the IMF Bz – component is directed southwards, the magnetopause changes into a rotational discontinuity. This means that the MP is no longer a barrier, but is open to the IMF. The frozen-in theorem breaks down within a little area called the x-line where IMF-field lines and geomagnetic field lines merge together allowing SW-particles to flow into the magnetosphere [Paschmann, 1991]. I will return to the dynamics of magnetic reconnection in section 2.3.3.There are several transfer models, however I will only describe the Dungey cycle. Figure 2.3-7 illustrates the so-called Chapman-Ferraro current system of the magnetopause and associated field aligned (Birkeland) currents.
The region in the magnetopause where the field lines separate into dayside and nightside is a cleft with low magnetic field pressure [Paschmann, 1991]. This region is called the cusp and is located within invariant latitudes $\Lambda 77^{o}$ - 81^{o} in the northern hemisphere. This is the approximate location of Svalbard. The cusp is sensitive to changes in the IMF. During periods of southwards IMF, the cusp moves equatorward as more field lines opens in the MP. In addition; strong negative By-component pushes the cusp towards the morning MLT. Likewise a strong positive By-component pushes it back towards afternoon MLT. The plasma in the cusp is magnetosheath-like with energies in the range from tens to hundreds of electron volts [Russell, 2000]. The MP-current flows around the cusp, contributing to the funnel shape [Prölss, 2004]. The By –distortion of the cusp also affect the neighboring regions causing a westwards (northern hemisphere) flow of field aligned current sheets [Cowley, 2000].

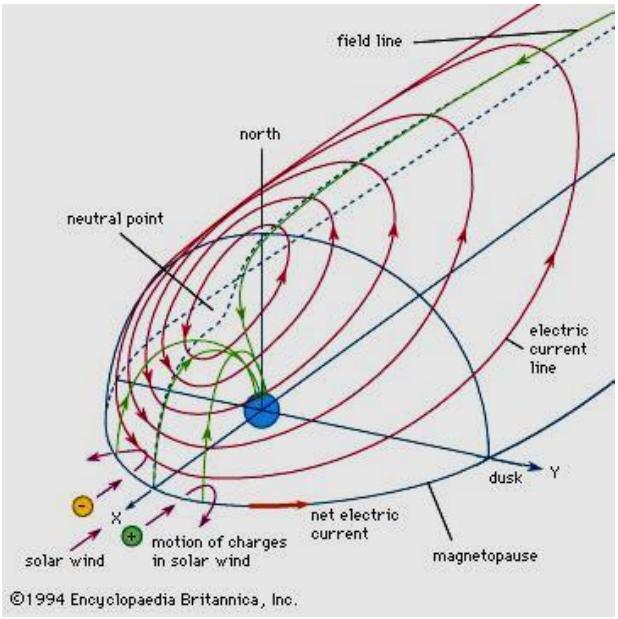

Figure 2.3-7: illustrates the magnetopause current system. The charged particles drift in separate directions causing the Eastwards current. The surface currents flow in circles perpendicular to the magnetic field. The cusp is shown as the neutral point. Figure from: *http://global.britannica.com/EBchecked/topic/106159/Chapman-Ferraro-current-system*

On the nightside, the magnetic field lines are stretched into a long tail, see Figure 2.3-8. The tail is separated into two segments with opposite magnetic polarity. Between these segments, along the x-axis, the Bx –components of the segments are anti-parallel, and thus cancel each other. This gives rise to a neutral sheet with only a weak Bz –component. A westward current flows within the neutral sheet which induces a second magnetic field. The resultant of this field and the Bz –component is tilted with respect to the neutral sheet. The tilt is steepest closest to the Earth and decrease with distance tailwards. This is the reason why the nightside dipole field is distorted.

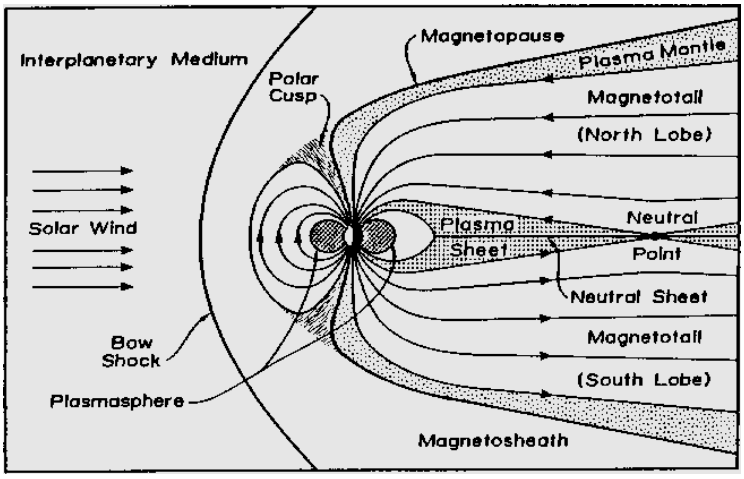

Figure 2.3-8: The magnetosphere viewed from dusk. Figure from: *http://www-ssc.igpp.ucla.edu/personnel/russell/papers/magsphere/msphere06.gif*

The current within the neutral sheet close the MP-current loop. The result is two solenoidal circuits which are joined together within the mid-plane as shown in Figure 2.3-9a). The mid-plane of the tail corresponds to the plasmasheet. The particle population main constituents are oxygen ions, protons and electrons, originating from the ionosphere, boundary layers and the solar wind. The mean temperatures are within a few keVs, and mean densities are about 10^5-10^6 m^{-3}; decreasing tailwards. The plasmasheet field lines maps the latitudes between 68º and 72º in an oval ring around both poles. This is what is referred to as the polar or auroral ovals, see Figure 2.3-9b). Thus the loss process in the plasmasheet is partially via aurora precipitation, and plasmoids [Prölss, 2004]. Also the plasmasheet boundary layer (PSBL) maps down in the ovals. The PSBL is the transition layer between the plasmasheet and the tail lobes [Kivelson and Russell 1995]. Inside the tail lobes the plasma has lower densities and temperature at low altitudes, and is in fact the weakest population in the tail. At higher altitudes, the density increases due to infusion from the plasma mantel (high latitude boundary layer) further down the tail. The lobes maps the polar caps and electron precipitation (> 100 keV) is the cause of different phenomena. At low altitudes, the precipitation is connected to the direction of the IMF Bz – component. Whereas southward IMF causes polar rain, a northward IMF-component causes polar showers and polar cap arcs. There are different models which describe the dynamics of the entry mechanisms of the plasma. For instance Fairfield and Scudder proposed a modified direct entry model in 1985, and another is the internal barrier model by Foster and Burrows from 1976-77. Evidence does not favor one of them, but they seem to supplement each other [Gussenhoven, 1989].
Just inside the magnetopause we find the outermost particle populations. These are the magnetospheric boundary layers that surround the magnetosphere. At the thinnest it is merely a few thousand kilometers at the sub solar point, but in the tail the thickness is several Earth radii thick. It is custom to distinguish between the different layers [Prölss, 2004].

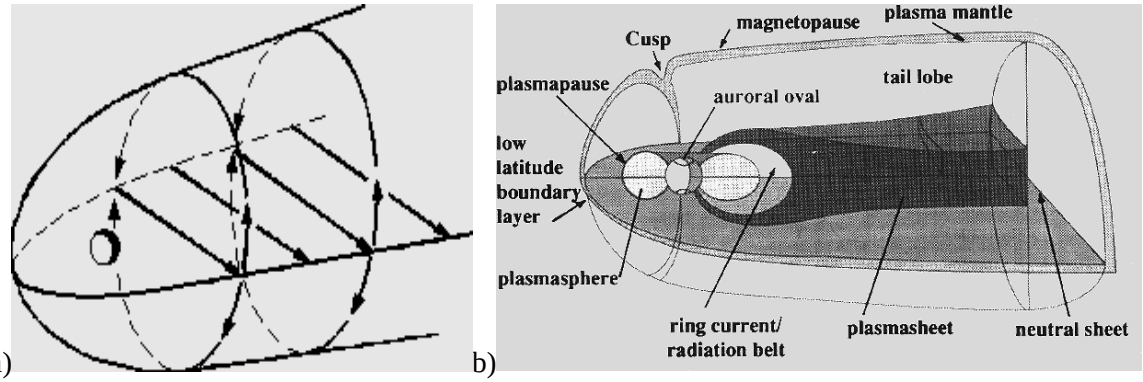

Figure 2.3-9: a) The magnetotail current loop. Estimated current at 20 R_E tailward using formula for solenoidal magnetic field is about four mega ampere [Prölss, 2004]. Figure from Stern [2001], *(http://www-spof.gsfc.nasa.cov/Education/wtail.html*). b) The different plasma populations in the distant tail. The plasma sheet maps down in the auroral oval. Figure from Cravens [1997] found at: *(http://www.physics.usyd.edu.au/~cairns/teaching/lecture14/node4.html)*

The entry layer is located on the dayside high altitude cusp region in the northern hemisphere. It contains magnetosheath – plasma which enters directly via open field lines through the MP, and ionospheric plasma that evaporates and follows field lines from the polar cap. The plasma mantel, also associated with the high latitude boundary layer (HLBL), is located tailwards of the cusp. It consists of plasma originated from the solar wind and the magnetosheath, which enters via open field lines. The plasma flow is tailwards and the density drops with increasing geocentric distance. At lower latitudes, the HLBL merges with the low latitude boundary layer (LLBL). The LLBL maps within the cusp region where the plasma enters on open, or partially open, field lines. It is believed that magnetic reconnection plays a role in the formation of the LLBL [Kivelson and Russell, 1995; Prölss, 2004].

Both HLBL and LLBL are responsible for the convection cell formation in the polar cap ionosphere [Siscoe et al., 1991]. I will return to plasma convection in section 2.4.2. Table 2.3-2 gives an overview of the main features of the particle populations in the distant Earth field.

Population	Ion temperature	Electron temperature	Particle Density	Composition	Location	Magnetic footprints
Plasmasheet	5 keV	1 keV	$\sim 10^5$ m^{-3}	H^+ , e^-	Central mid-tail plane	Nightside Auroral oval
Lobes	-	200 eV (2keV)	$<\sim 10^4$ m^{-3}	H^+ , e^-	Tail lobes	Polar cap
Boundary Layers	~ 3 keV	0.2 keV	$\sim 10^6$ m^{-3}	H^+ , e^-	Inside MP	Cusp region

Table 2.3-2 summarizes some of the properties at 30 R_E. Adapted freely from: Prölss [2004].

2.3.3 Magnetic Reconnection

Magnetic reconnection involves merging of magnetic field lines. According to MHD, plasma is frozen-in on field lines convecting through the magnetosphere. This means that the particles are constrained to their field line and cannot mix across to the next. There are thin current sheets which act as boundaries between different plasma populations preventing diffusion of particles. The adjacent magnetic field components are tangential to these current sheets, thus forming a tangential discontinuity. However; MHD may break down within the current sheet and we have a rotational discontinuity. In short; magnetic reconnection is the breakdown of the frozen – flux theorem in MHD. This corresponds to the magnetic Reynolds number R_M reaches unity [Prölss, 2004].
In driven reconnection, plasma diffusion through the current sheet requires both inflow and out flow of magnetic flux in the diffusion region. Introducing a small diffusion region in the mid-plane of the tail called a neutral x-line, as depicted in Figure 2.3-8, we allow magnetic field lines to convect towards and through this point from both hemispheres. Inside the x-line, the opposite field lines lose their identity and are allowed to merge together so that plasma can transfer from one field line to the next. The reconnected field lines aid restoring the dipole field. This process is called dipolarization. Figure 2.3-10 illustrates the x – line reconnection site. The field lines flow into the neutral point from both sides, where they merge together and dipolarize. The horizontal arrows indicate the direction of jets that arise from the reconnection process.

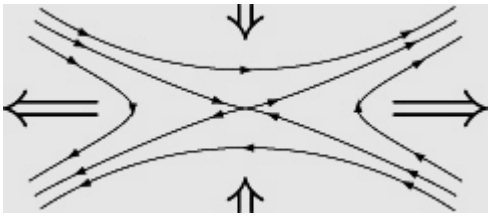

Figure 2.3-10: schematic illustration of the reconnection x- line. Taken from: *http://plasma.physics.swarthmore.edu/ssx/faq.html*

In1961, Dungey, J.W., became the first to propose the occurrence of magnetic reconnection in the magnetosphere; however the purpose was to explain the convection patterns. Sweet, P. and Parker, E.E. came up with MHD – solutions to the phenomenon independently in the late 1950-ies. These were modified by Petschek, H. in 1964, Sonnerup, B.U. in 1970 and by Priest, E. and Forbes, T. in 1986-87. Also explanations based upon particle behavior were introduced by e.g. Harris, E.G. in 1962

and Cowley, S.W.H. in 1986 [Kivelson and Russell, 1995]. The models are somewhat limited. The simplifications are fairly applicable in the tail, but describe the magnetopause dynamics poorly. The role of the current sheet is omitted, and it is questioned whether instabilities in the current sheet can give rise to spontaneous reconnection at onset of a geomagnetic storm [Kivelson and Russell, 1995; Prölss, 2004].

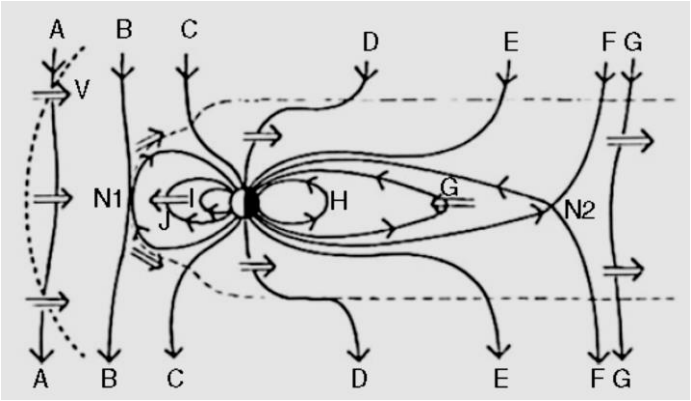

Figure 2.3-11: Illustrates the Dungey – cycle where the field lines convect in steps from A to G. At N1 and N2 we find the x – lines where reconnection occurs. Notice the dipolarization in steps G-J. Figure adapted from: Zarka, P. [2011].

As mentioned; Dungey, proposed an explanation to the convection patterns in the polar ionosphere n 1961. The model is a simple and general description that surveys a steady state convection of frozen-in flux. The convection is driven by the reconnection in the magnetopause and magnetotail [Kivelson and Russell, 1995]. Assuming southward IMF Bz the field lines are anti-parallel at the magnetopause and a rotational discontinuity forms in an x-line at the magnetopause. Reconnection between IMF-field and the geomagnetic field opens the magnetosphere and allows solar wind plasma diffusion. The reconnected field line continues to convect tailwards across the polar cap, giving rise to the convection pattern in the polar caps (anti-solar E x B – drift). Tailwards, the field lines are heavily extended and the tension adds stress to the field line, which desires to return Earthwards. Instead they are drawn towards the x – line in the mid-plane, also called the near Earth neutral line (NENL), located ~30 R_E [Kivelson and Russell, 1995; Prölss, 2004]. Corresponding field lines from northern and southern hemisphere reconnect, and due to the tension, the reconnected field lines are "fired" towards Earth. The Earthward traveling field line may give rise to so called bursty bulk flows (BBF's) which are the main contributors to the plasmasheet plasma, and thus directly coupled to the precipitation in the auroral ovals and auroral streamers during geomagnetic storms [Sergeev et al. ,2004]. A consequence of this dipolarization is the formation of plasmoids which travel tailwards, whereas plasma is lost from the magnetosphere [Prölss, 2004]. For further reading see e.g. Pandey and Lakshina [2001].
Figure 2.3-11 illustrates the Dungey – cycle with open magnetosphere and dipolarization.
The dayside reconnection during southwards IMF is described by various transfer models as mentioned earlier. The reconnection process in the Dungey model is steady state, however also time dependent reconnection may occur. This transient, pulsed reconnection at the MP involves consecutive time intervals where the reconnection is completely shut off [Smith, 1994].
The shear angle between the IMF and the MP influence the reconnection occurrence [Prölss, 2004]. Reconnection in the MP may still occur when the IMF is northwards, but not at the sub solar point. When IMF Bz is northwards, and parallel to the geomagnetic field, the IMF- field lines wrap around the magnetosphere, giving rise to new merging sites closer to the poles. In 1981 and 1983, Cowley, S.W.H. classified the magnetospheric topology during northwards IMF, and described different scenarios based upon the dipole tilt (Summer/Winter hemisphere) [Crooker,1992] , see Figure 2.3-12.

Crooker [1992] modified the model and inferred a dormant merging site. Reconnection during northwards IMF gives rise to reversed convection cells in the polar ionosphere. Reversed convection is often associated with velocity shears and auroral arcs or theta aurora [Crooker, 1992; Chisham , 2004]. These phenomena are closely related to scintillation and I will address them in section 2.4.3.2.

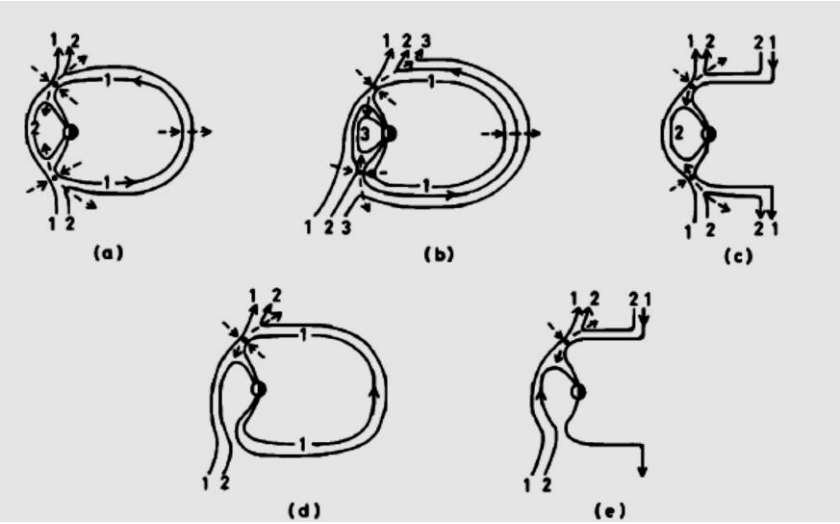

Figure 2.3-12: illustrates Cowley's catalogue for northward IMF reconnection. Adapted from: Crooker [1992].

2.4 The Ionosphere

The ionosphere is a part of the upper atmosphere stretching from approximately from 100 to 1000 km above the Earth's surface. It is divided into four main layers based upon the dominant species residing there, and the electron content. The ionosphere consists of weak plasma which enables currents to flow within it [Prölss, 2004]. I will return to the currents in section 2.4.2, and start with a short outline of the composition.

2.4.1 Characteristics of the Ionosphere

Treating the ionosphere as a quasi – neutral mixture of charge carriers above 90 km altitude, it is possible to assume that the total density of positive ions is approximately the same as the electron density. However the densities are varying with altitude, providing the layered structure of the ionosphere. It is custom to infer the parameter h_m as the maximum (peak) heights of the layers. Also the maximum ionization density n_m and the column density N_e of electrons are useful parameters.The densities also undergo diurnal and seasonal variations in addition to variations caused by the solar cycle. Figure 2.4-1a) illustrates the density profile of electrons during day and night at mid-latitudes. Figure 2.4-1b) shows the ionopheric composition during the day at mid-latitudes. It is clear from these figures that the layers have different compositions. The production and loss processes in the various layers are important, but too extensive in detail to be accounted for here. I will only mention the most important formation processes in the following, under their "residential" layer.

a)

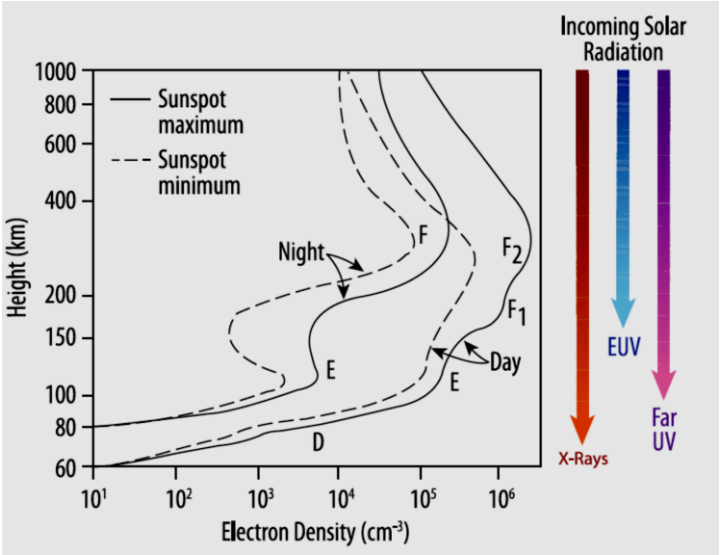

b)

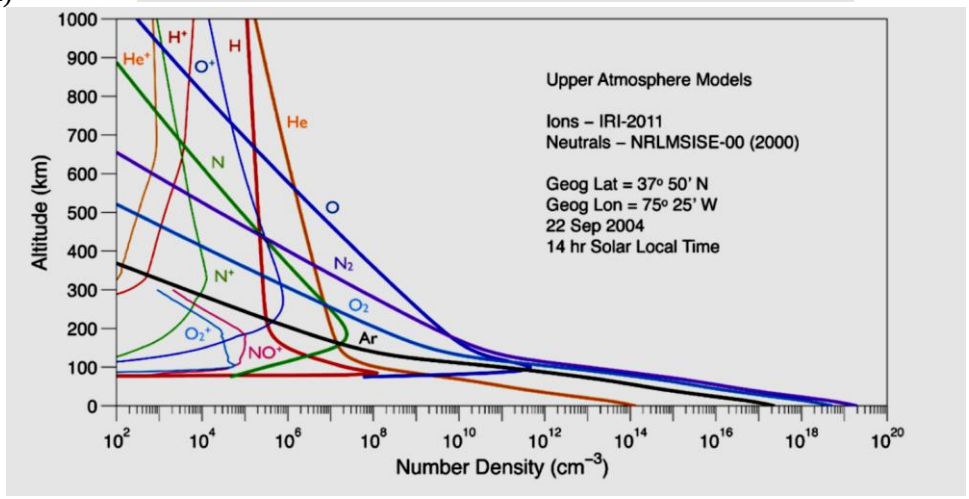

Figure 2.4-1: a) The diurnal variation in electron density. The colored arrows indicate how deep into the ionosphere the solar radiation penetrates. b) The ion content in the ionosphere during daytime at mid-latitudes. Both figures adapted from: Pfaff [2012].

The D-layer is located at altitudes from h_m = 50- 90 km. This region consists of negative ions and cluster ions such as NO_3^- and $H_3O^+ \cdot (H_2O)_n$ clusters [Prölss, 2004]. The D-layer is dense with high collision rate. Also electron densities can become extreme during winter due to solar ionization of nitric oxide. The D-layer contributes to radio wave absorption in MF and HF radio signals due to the density, but also changes in the LF/VLF reflection height [Rishbeth, 2003].

Above the D-layer are the E-layers. The normal E-layer occupies altitudes from h_m= 90 km to 170 km and consists dominantly of O_2^+ and NO^+. The most important of these is NO^+ which is produced primarily from charge-exchange with other ions and atoms, dissociative recombination and from photo-ionization by soft X-rays.

From approximately h_m = 100-120 km we have another E-layer, called the Sporadic E-layer (Es). These are heavy ion layers created by neutral wind shears by distributions of long lived metallic ions (Mg^+ and Fe^+) created in impact ionization by meteoroids. They are common in both day and night at mid-latitudes. They are often so dense that they affect the HF radio waves propagating through the ionosphere [Prölss, 2004; Pfaff, 2012; Rishbeth, 2003].

The F-layer is stretching from h_m =170-1000 km. During daytime, it is split into two regions, where the F1-region is the lower part and the F2-region is the upper part. The dominating ion in the F1 – layer is O^+ which has it peak density at h_m = 170 km. The O^+ is produced by extreme ultra violet (EUV) solar radiation. In the F2-layer O^+ also dominates, but also secondary ions are present such as H^+ and He^+,which have entered from the plasmasphere (above 700 km). The electron content in the F2 –region is larger than the F1-layer.

Whereas the F1-layer follows a Chapman layer model where we assume a photochemical equilibrium, the F2-region follows diurnal, seasonal and annual variations [Prölss, 2004; Rishbeth, 2003; Kivelson and Russell, 1995]. During magnetic disturbances the h_m F2 peak elevates up to hundreds of kilometers (e.g. Yin et al. [2006]), due to thermospheric expansion and changes in the neutral gas composition [Crowley et al., 2006].

In the high latitudes and polar region, the ionosphere is open to the IMF and the main ionization is due to impacts between solar wind and neutral gas. Magnetospheric E- fields contribute to **E** x **B**-drift (cross polar convection) which drives neutral winds. At mid- and- low-latitudes neutral winds set up polarization electric fields that drive currents e.g. the equatorial electrojets. Here vertical charge separation result in horizontal **E** x **B**-drift. The **E** x **B**-drift along the magnetic equator is also responsible for the Fountain effect [Pfaff, 2012]. At high latitudes plasma instabilities cause small scale irregularities which in turn cause radio wave scintillation and fading. These patches will be discussed in section 2.4.3.

Critical plasma frequency, which is the angular frequency of the electron oscillation, is given by

$$f_0F_2 = 80.6N_m \simeq 9\sqrt{N_m} \qquad (2.51)$$

where N_m is the maximum electron density. This formula provides the maximum frequency for which the radio waves are reflected. In order to transmit radio waves through the ionosphere, the radio frequency has to be larger than the critical frequency. The background plasma frequency is within the HF- spectrum (3-30MHz) [Rishbeth, 2003; Prölss, 2004].

2.4.2 Ionospheric Currents and Convection

A part of the most important current system is located in the E – layer at about 125 km. Below this altitude, the conductivity is too low due to the increased collision frequency and low ionization. In the upper ionosphere, above 250 km, the conductivity is also too low for any currents to form, instead we have **E** x **B –** drift.

The transversal conductivities and currents in the E – layer forms due to electric fields. In the polar cap, the anti-sunward plasma flow and the magnetic field are perpendicular. This configuration along with the tidal motion of the Earth [Farley, 1963] gives rise to a right hand electric field from dawn to dusk. In the polar ovals, the plasma return flow is sunwards and thus the electric field is directed from dusk to dawn, see Figure 2.4-2a). Initially the collision less plasma flows with an **E** x **B –** drift, according to MHD. However; in the E-layer in the presence of the electric field, the ions are forced to drift parallel with the field. This results in the Pedersen current. Electrons are not influenced that strongly, and flow perpendicular to the electric field. This is the Hall current. At h~125 km the current densities of these currents are approximately equal. The Hall current flows sunwards across the polar cap (-**E** x **B**) and anti-sunwards in the polar ovals. The latter flow is also referred to as the auroral electrojets, due to strong enhancements during geomagnetic disturbances. The Hall currents overlap in the Harang-discontinuity region in the midnight sector. In addition the Hall current sets up a perturbation magnetic field which has a direct impact on the geomagnetic horizontal component. The eastward electrojet in the dusk sector contribute to increased magnetic field strength, whereas the westward jet weakens it (field components are anti-parallel). Apart from this, the Hall currents deposits no energy into the ionosphere, while the $\mathbf{j}_p$ x **B** –force applied on the neutral gas from the Pedersen current, provides Joule heating [Prölss, 2004; Cowley, 2000].

The energy and momentum in the ionosphere are transferred from the magnetosphere and the solar wind. The downward Poynting flux during a magnetic storm main phase can exceed 600 GW [Burke et al., 2007]. The particles flow down into the ionosphere along the magnetic field lines. Thus they are so called field aligned currents (FAC's), or Birkeland currents. In the ionosphere the Pedersen currents close the Birkeland currents, whereas the magnetopause current closes them in the magnetosphere. All this contribute to the steady state current pattern shown in Figure 2.4-2a). The conductivities are given by:

$$\sigma_P = \frac{eN_e}{B}\left[\frac{\omega_e \cdot \nu_{e,n}}{\omega_e^2 + \nu_{e,n}^2} + \sum_j P_{ij}\frac{\omega_{ij} \cdot \nu_{ij,n}}{\omega_{ij}^2 + \nu_{ij,n}^2}\right] \tag{2.52}$$

$$\sigma_H = \frac{eN_e}{B}\left[\frac{{\omega_e}^2}{\omega_e^2 + \nu_{e,n}^2} - \sum_j P_{ij}\frac{{\omega_{ij}}^2}{\omega_{ij}^2 + \nu_{ij,n}^2}\right] \tag{2.53}$$

where *j* designates the ion species, *e* is the electron charge (C), N_e is the electron number density (m^{-3}), *B* is the magnetic field strength (Wbm^{-2}), ω_e, ω_{ij} are the gyro frequencies of electrons and ions, $\nu_{e,n}$, $\nu_{ij,n}$ are the collision frequensies with neutrals and P_{ij} is the relative number density of ion species *j* [Brekke and Moen, 1993]. For altitudes above 200 km, the Birkeland conductivity can be approximated as:

$$\sigma_B = \frac{e^2 N_e}{m_e \nu_{e,i}} \tag{2.54}$$

where m_e is the electron mass and $\nu_{e,i}$ is the collision frequency between electrons and ions. The conductivities are related to the current density by Ohm's law [Prölss, 2004]. Height integrated conductivities (conductance) and current densities provide important information about the ionospheric currents.

The twin cells are the plasma convection cells that originate in steady state reconnection process (Dungey cycle). The flow is anti-sunward in the polar cap and sunwards in the polar ovals.
As shown in Figure 2.4-2b), the Birkeland currents enter and escape the ionosphere in two regions. Region 1 (R1) is located at high latitudes on the boundary between open and closed field lines (o /c – boundary). Region 2 (R2) is located at sub-polar latitudes. In the dawn sector, the Birkeland currents in R1 are downwards, and the R2-currents are directed downwards. The opposite occurs in the dusk sector. R1-currents close Pedersen currents in the ionosphere, and are stronger than the R2-currents which close in partial ring current [Cowley, 2000].

a) 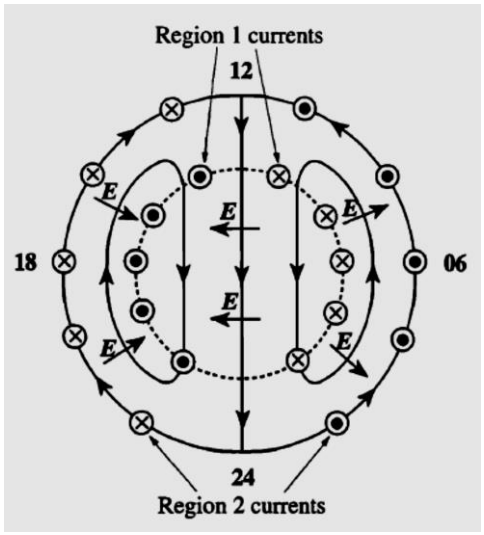

b) 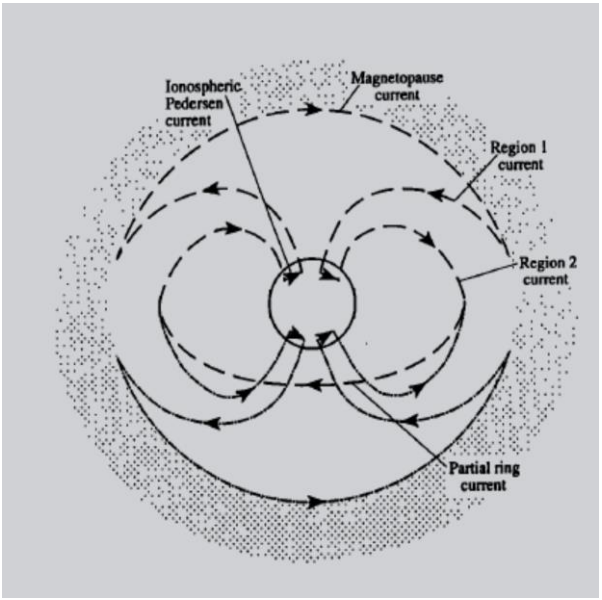

Figure 2.4-2: a) the ionospheric currents seen from above the polar cap. The dotted line marks the o/c-boundary. Notice the electric field directions. The Pedersen currents flow along the electric fields between the R1- and R2- currents. The Hall currents flow along the cell pattern. b) The closure of R1- and R2- currents. Figures are adapted from Cowley [2000].

The polar/auroral oval is a ring that surrounds the polar caps in which the plasmasheet maps down in the ionosphere. The poleward boundary of the oval coincides with the o/c-boundary in the night side, whereas the particles enter on open field lines through the cusp on dayside. The solar wind driven convection in the high latitude ionosphere assumes steady state reconnection in both dayside and nightside. However; the plasma flow is often non steady, and reconnection in dayside and nightside are two separate processes [Cowley and Lockwood, 1992; Provan, 2004]. A negative IMF Bz – component leads to dayside reconnection around noon MLT. The o/c-boundary will expand equatorwards as more flux opens. The anti-sunward flow of incompressible plasma generates a twin cell convection pattern in the noon sector. This is what that is referred to as a flux transfer event (FTE), see Figure 2.4-3a). The flux transfer rate (voltage) is largest in the merging gap and decrease to zero towards midnight sector [Cowley and Lockwood, 1992]. During a substorm the dayside reconnection corresponds to the growth phase where open flux is produced. This flux propagates across the polar cap to the tail. As the tail receives more flux, it becomes unstable and reconnection is initiated in the tail. This corresponds to the storm time expansion phase. The timegap from the onset of the storm, to the reconnection begins in the nightside is approximately 20-50 minutes [Provan, 2004]. Since nightside reconnection involves closure of field lines, the o/c-boundary in the nightside will shift polewards and lead to a contraction of the o/c-boundary, see Figure 2.4-3b). According to Cowley and Lockwood, the total flow is the sum of the two separate processes. Steady state convection occurs when the flux transfer rates are equal in both sectors (Figure 2.4-3c) [Cowley and Lockwood, 1992].

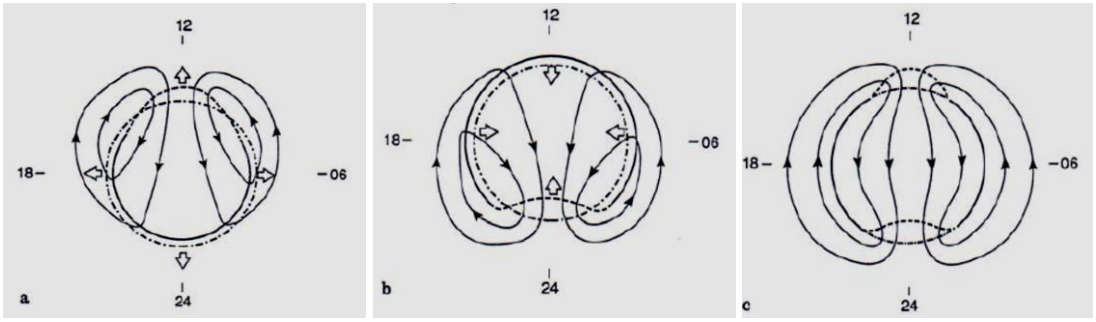

Figure 2.4-3: a) unbalanced dayside reconnection with expanded merging gap. b) Unbalanced nightside reconnection. c) Steady state reconnection. Adapted from: Cowley and Lockwood [1992].

The voltage difference measured across the polar cap from dawn to dusk is the cross polar cap potential, (CPCP), Φ_{PC} :

$$\Phi_{PC} = \int v_{\perp} B dl \qquad (2.55)$$

where $v_{\perp}$ is the anti-sunward component of the plasma flow, B is the polar cap magnetic field strength and l is the cross polar diameter from dawn to dusk. The Φ_{PC} is a direct measure of the flux transfer rate in the polar cap. According to Provan [2004], the average Φ_{PC} is $53 \pm 9\ kV$, and in the lower latitudes (ovals), it is $36 \pm 7\ kV$. When the IMF turn northwards, the Φ_{PC} drops from > 100 kV to ≥ 10 kV [Paschmann 1991]. There are also differences in the potential between the cells due to different flow velocities. The average plasma flow velocities are 200 ms^{-1} in the polar cap and 600 ms^{-1} in the polar ovals. The dawn cell has a positive electric potential, and the dusk cell has a negative potential [Provan,2004; Prölss, 2004; Weimer, 1995].

IMF By –components tend to rotate the IMF, giving rise to asymmetric convection patterns [Cowley and Lockwood, 1992]. A positive By-component will draw the flux tube towards dawn, whereas a negative By-component will draw it towards dusk [Southwood, 1987]. If both Bz - and By-component of the IMF are negative, the dusk cell becomes elongated (banana) and the dawn cell becomes rounder (orange). The anti-sunward flow and midnight sector flow are stronger when the By-component is negative. If the By-component is positive (still negative Bz), the dawn cell becomes the elongated cell and the dusk cell round. The flow will increase in the dawn/dayside sector under these circumstances [Provan, 2004]. See Figure 2.4-4a) for different configurations. Effects of the Bx –component corresponds to a tilt in the IMF with respect to the magnetosphere [Chisham, 2004]. When both Bz and Bx –components are negative, the cusp in the northern hemisphere is "open" to the solar wind, resulting in dayside cusp aurora [Valladares et al., 2002].

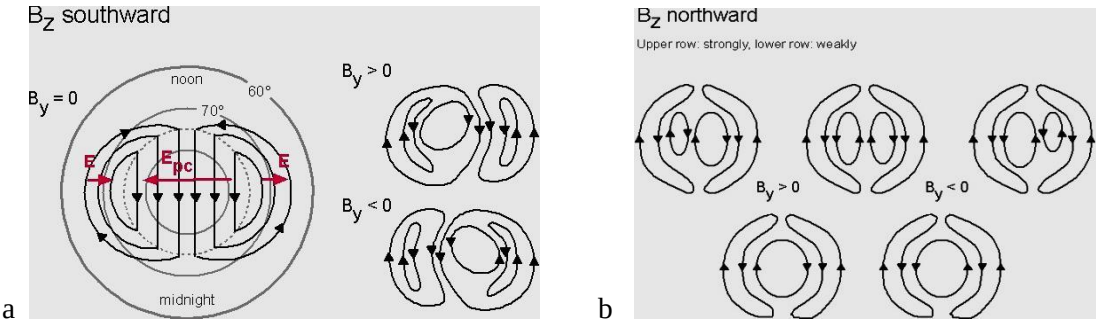

a b

Figure 2.4-4:a) For a negative IMF, showing the asymmetric cell patterns stemming from the B_y-component. b) Different reversed convection patterns for a northwards IMF and B_y-components. Figures by: Reijo Rasinkangas,(*https://wiki.oulu.fi/display/SpaceWiki/Ionospheric+convection)*

When the IMF is northwards, the convection patterns are dramatically different. Reconnection tailwards of the cusp, gives rise to four reverse convection cells. The two negative may merge together leaving a total of three cells. Those cells that contribute to closed flux (o/c-boundary), are merging cells. Cells located on open field lines are lobe cells (polar cap). Crooker [1992] linked the reverse convection to formation of velocity shears and theta aurora during northwards IMF (Weimer, 1995; Crooker, 1992; Chisham, 2004]. Figure 2.4-4b) illustrates some of the reverse convection cell configurations.
Another type of convection vortices are so called traveling convection vortices (TCV's). They are westwards propagating disturbances located at high latitudes, associated with Birkeland currents. They appear in pairs with mutual reverse convection which is defined by the direction of the Birkeland currents. TCV's are the response to sudden changes in the solar wind [Cowley, 2000]. TCV's may explain irregular spikes in ground magnetometer measurements [Friis-Christensen, 1988]. Many TCV's may transit across the polar cap resembling patch like structures associated with increased polar cap potentials and plasma depletion zones around the vortices [Valladares et al., 1999].

2.4.3 Plasma Patches and Irregularities

There are different kinds of irregularities in plasma, driven by various mechanisms. I will only address the most important irregularities and phenomena that cause scintillation of radio waves in which is the central topic of this thesis. The dominating features of the polar F-region are polar cap patches and sun aligned arcs [Buchau et al.,1983]. I will give a brief outline on patches first and then a short description of arcs.

2.4.3.1 Plasma patches and Tongue of Ionization (TOIs)

The first observations of patches were made by G.E. Hill in 1963 [Tsunoda, 1988] and there has been a lot of research on patches during the last three decades concerning formation mechanisms and morphology. In general; patches are large scale high density plasma structures which have a horizontal scale size extent of 100-1000 km and electron densities that are five to ten times as high as the background plasma. The maximum values are around 10^{12} m^{-3} (10^{6} cm^{-3}) - typical for daytime in mid – latitudes [Weber et al., 1986; Carlson et al., 2006; Oksavik et al., 2006]. The patches emerge in the dayside and follow the anti-sunward convection pattern across the polar cap. The typical velocity is about 300 -1000 ms^{-1} [De Franceschi et al. 2008]. The drift velocity can vary with changes in the IMF, and studies have shown that the drift velocity caused by the IMF By-component is delayed with respect to the Bz-component [Oksavik et al., 2010; Hosokawa et al., 2006].
The patch occurrence is associated with southwards IMF Bz-conditions and the plasma within the patches is either solar produced at low latitudes equatorward of the dayside cusp [Buchau et al., 1985], or by precipitation of soft electrons in the cusp [Walker et al., 1999]. Patches are present in the polar cap in both summer and winter, during solar maximum as well as solar minimum [Rodger et al., 1994.]
In 1959 T.Sato suggested that plasma was transported from low latitudes on the dayside into a tongue of ionization (TOI) by a storm time electric field [Knudsen, 1974]. Direct evidence of such transport was found by Kelley and Vickrey [1984] when they found no increase in electron temperature as would have occurred for precipitation. Foster and Doupnik [1984] confirmed the presence of an eastward electric field along with high density F-region plasma convecting through the cusp. Knudsen [1974] found that the convection time in the cusp were about 5 minutes and the ionization added was about $1\text{-}2\cdot10^{6}$ cm^{-3}, which is a significant enhancement in wintertime when the background density is low. Hosokawa et al. [2010] studied the time development of a TOI during a magnetic storm and found that in order for a TOI to develop, there must be an expansion of the high latitude convection

pattern and a build-up of plasma in mid -latitudes in advance. During geomagnetic storms, storm enhanced densities (SEDs) are formed in the nightside sector from eroded plasmasphere/plasma boundary layer and carried to the dayside (American sector) by a subauroral disturbance electric field, so called sub auroral polarization streams (SAPS) (e.g [Foster and Vo, 2002; Foster and Burke 2002]). In addition SEDs are formed in the post noon sector due to stagnation of plasma. When the storm time convection pattern expands during substorms, the dusk cell is pronouncedly shifted equator wards (due to offset of geographic and magnetic poles) and the plasma along the equatorward boundary is decelerated by co-rotating plasma (in Earths reference frame). The result is a narrow SED which can co-rotate or even stagnate before it is convected back to the cusp region [Foster 1993]. Figure 2.4-5a) is a 2D-image of the polar cap during the superstorm event described in this thesis. Notice the enhanced tongue that extends across the pole and the SAPS that flow along the flanks. Figure 2.4-5 b) is a global TEC-map with projected cross tracks of DMSP F12 and F15 which register the anti – sunward flow velocity. The enhancements correspond to the SAPS.

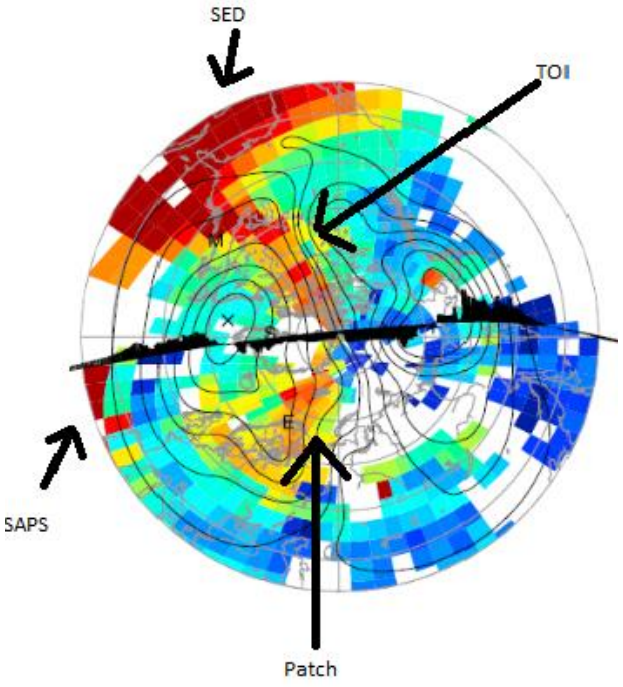

a)

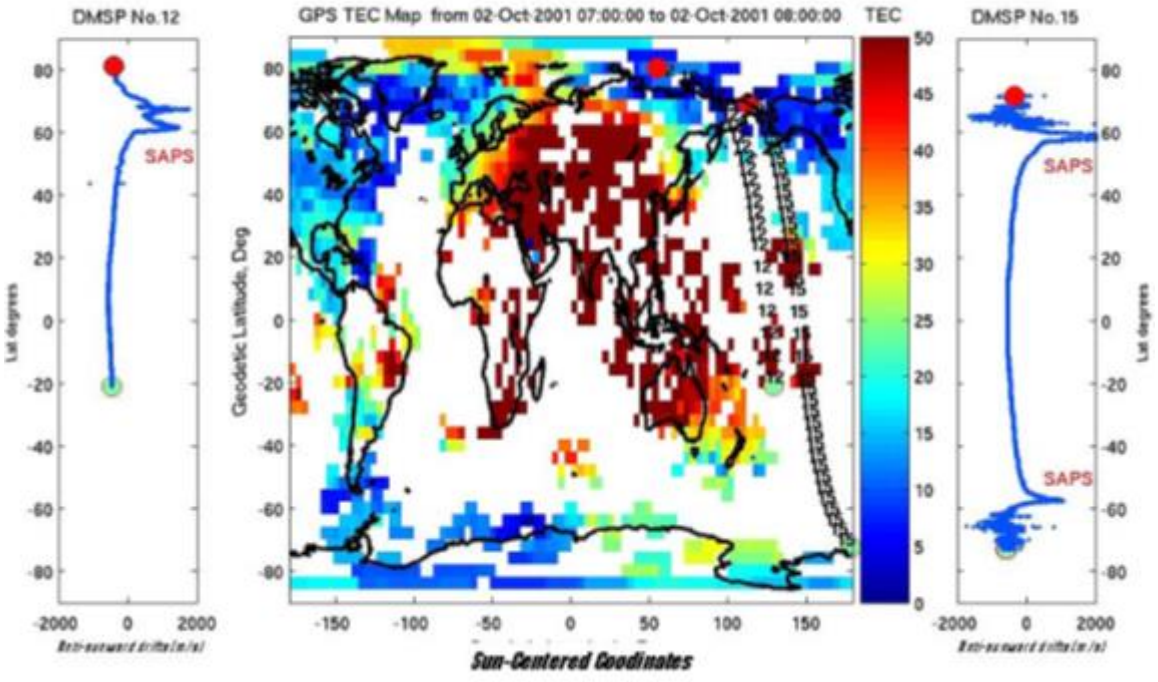

b)

Figure 2.4-5: a) A TEC-map showing the enhanced regions in the northern hemisphere. The SED is located over the American continent on top, the TOI extends across the polar cap with an isolated patch over Scandinavia. The SAPS is the enhancement equatorward of the trough. Figure adapted from Foster et al. [2005]. b) Global TEC map with enhanced TEC over the European/Asian sector. The trajectories of DMSP-satellites are projected onto the TEC-map. The side plots illustrate the SAPS flow velocities as enhancements in the anti-sunward flow.
Figure adapted from Coster et al.[2006]

The SED plume is a plausible source of TOI-formation [Foster et al., 2005; Coster et al,. 2006]. Yizengaw et al.[2006b] have also reported observing a similar density plume over Europe, but it is more infrequent due to the low geomagnetic tilt of the European sector.

There are several suggestions on how the patches form, but a plausible mechanism is segmentation of the TOI due to transient reconnection in the dayside [Moen et. al 2006, Carlson 2012]. Lockwood and Carlson [1992] suggested that a flux transfer event (FTE) in the dayside magnetopause is a likely mechanism for patch formation. A TOI represents a continuous flow of plasma, consistent with steady state reconnection, whereas patches are isolated segments of enhanced density which can form when the reconnection is transient. Figure 2.4-6 shows a cartoon of the formation process of a patch due to an FTE. A similar mechanism was proposed by Anderson et al. in 1988, but not in terms of FTEs. Instead; patches are formed when the whole convection pattern expands during southward IMF and solar produced plasma is entrained into the flow pattern. As the convection patterns contracts, the high density plasma drifts polewards [Anderson et al.,1988]. Tsunoda [1988] suggested that consecutive changes in the Bz and By- components of IMF could chop the TOI into separate pieces. The By – component is of importance concerning patch formation, since it dictates the MLT-location of the reconnection site. When the expansion is directed into regions of denser plasma, the probability of

patch formation increases [Zhang et al.,2011]. Foster [1984] found that the region plasma enters is within 3-4 hours around MLT noon.

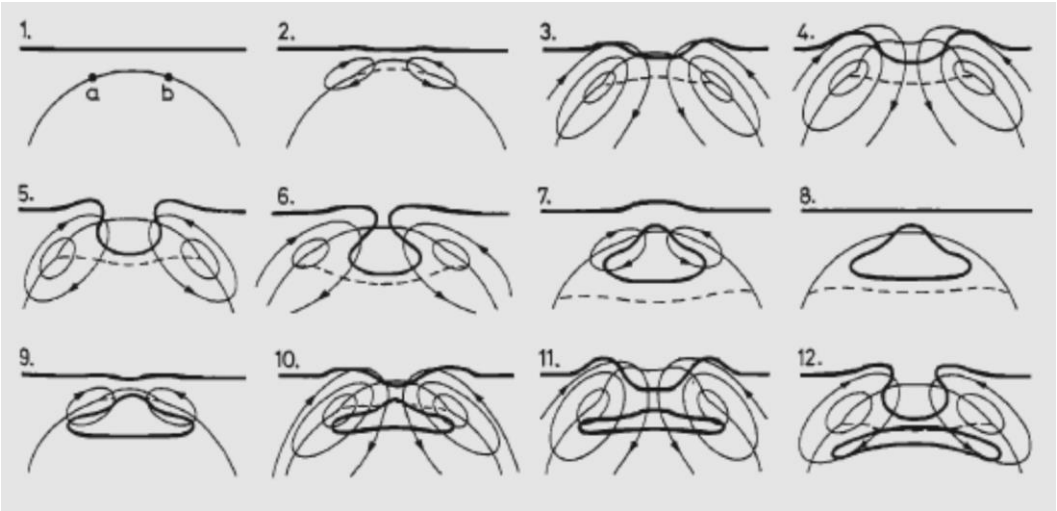

Figure 2.4-6: A cartoon showing formation of a patch with 2.5 minutes intervals. The merging gap (ab) with convection cells expands equatorwards and the enhanced plasma (solid line) is entrained within the convection, as long as the reconnection is ongoing. When it stops, the merging gap withdraws and a 10-15 minutes relaxation time occurs before a new reconnection burst starts. The patches are formed when reconnection stops and convected polewards in a step-like motion. Figure by: Cowley et al. 1991, in Lockwood and Carlson [1992]

Patches can also form rapidly in association with plasma jets [Valladares et al., 1996; Rodger et al., 1994]. So called flow channel events are short lived plasma jets with velocities around 2 kms^{-1} can disrupt the convection in association with fast changes in the By-component. FCEs are located within the cusp footprints. The jet flow causes perturbations because the background convection speed is slowed by a weak return flow adjacent to the FCE. Joule heating and field aligned currents associated with the FCE depletes the FCE and making it act as a separatrix between plasma enhancements. The poleward enhanced region becomes the new patch and can form in less than 3 minutes if the ion velocity is high. The newly formed patch drifts polewards with the **E**x**B**-convection. It is worth mentioning that patches can only form from FCEs with contribution of By-reversals [Rodger et al., 1994]

An important contribution of strong By –component is the draping of field lines from the flanks across the magnetopause. This leads to shifted patch origins and the following drift motion is both zonal and anti-sunwards as the field line is stretched out. Also the speed across the polar cap is influenced by the By-component. The anti- sunward flow is confined within a narrow channel with the highest flow speed in the center. Outside this channel the speed is slower. Patches aligned within the center of the channel will drift faster across the pole than patches outside the channel. If a patch is located partially inside the flow channel, it will rotate or change velocity. This means that the leading edge of a patch can become the trailing edge, or the first patch that enters can stagnate or exit last. Also; a non-uniform electric field can alter the shape of the patches [Oksavik et al., 2010].

The By-component is of importance e.g. regarding the localization of the patches. Bowline et al. [1996] modeled the By –dependence of TOIs in order to predict the visibility of patches from ground. Moen et al. [2007] found that the patches are evenly distributed around midnight MLT, with a peak around 23:35 MLT recorded at Ny-Ålesund. Another peak density occurs in the dayside at noon [Moen et al. 2008; Hosokawa et al. 2010]. Dandekar and Bullett [1999] showed a diurnal behavior of

the patch occurrence (and strength) and found the peak within the timeframe of 22:00-02:00 UT, corresponding well with the result of Moen et al. [2007, 2008]. Figure 2.4-7 illustrates the patch drift direction according to the By-polarity. A negative By –component corresponds to an inflow region in the pre-noon MLT, and post-noon for a positive By-component.

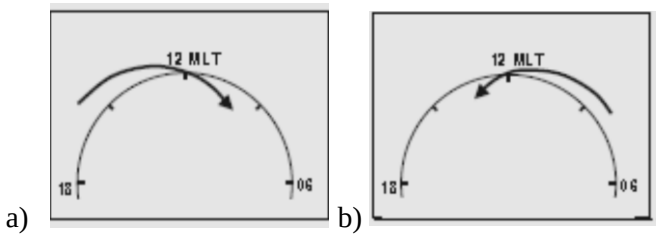

Figure 2.4-7: Schematic illustration on how the inflow is affected by the By-component. a) post-noon for positive By and b) pre-noon for negative By. Adapted from: Moen et al. [2008].

Moen et al. [2006] have also observed patches that formed on closed field lines at sub-auroral latitudes. These patches are segmented by current sheets at the border of the pulsed return flow as illustrated in Figure 2.4-8.

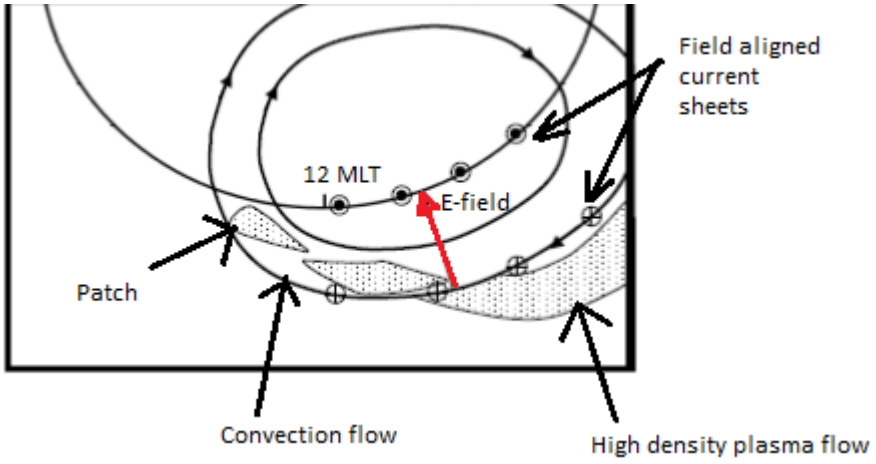

Figure 2.4-8: Sub-auroral patches are created by the downward current sheet along the flow border. The red arrow is the electric field vector. Figure adapted from: Moen et al. [2006].

Lorentzen et al. [2010] used both ground based optical and radar data in addition to measurements from the ICI-2 sounding rocket to study poleward moving auroral forms (PMAF) and patch formation mechanisms. They suggested a model that unifies the existing formation theories. In Figure 2.4-9 the temporal development of a patch is illustrated. The first picture at t_0 reveals precipitation in the cusp and EUV-ionization, but no PMAFs. At t_1 a reconnection burst occurs accompanied by an FCE depletion-region separating the PMAF and the cusp. At t_2 and t_3 the enhanced plasma is beginning to drift polewards and frictional Joule heating from the increased Birkeland and Pedersen conductivity causes an upwelling of plasma. At t_4 the patch is formed when the density is high enough in the F-region altitude. At t_5 the procedure starts over again. In this process patches are viewed as a continuation of PMAFS and clearly incorporate the most important formation mechanisms.

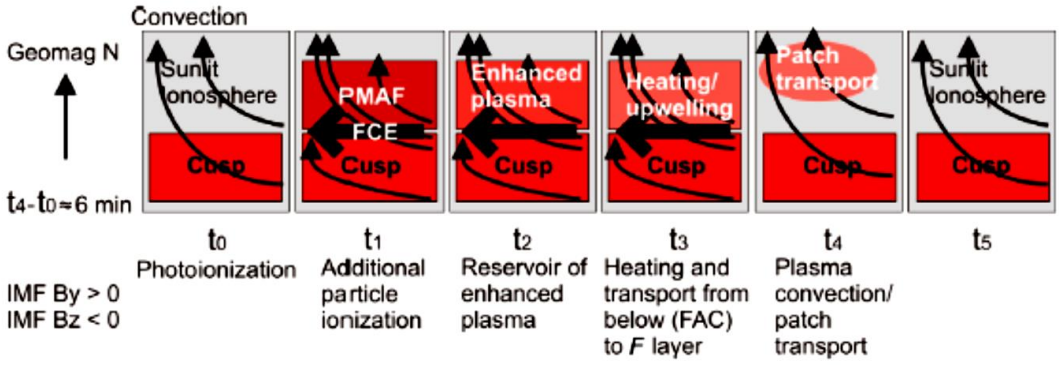

Figure 2.4-9: Formation of patches from PMAFS in a 6 minute time interval. Adapted from: Lorentzen et al. [2010].

Another kind of flow in the cusp region are so-called reversed flow events (RFEs) which are flow channels where the flow direction is opposite of the By-tension. They are found in association with large scale plasma flows [Rinne et al., 2007]. On the edges of the flow, shear driven instabilities contribute to rapid formation of decameter irregularities [Oksavik et al., 2011]. It is not certain how the RFE phenomenon is related to patches [Carlson 2012].
When the patches exit the polar cap into the nightside auroral oval, they are referred to as blobs [Crowley et al., 2000]. Here, they can return to the dayside with the sunward flow [Crowley et al., 2000; Oksavik et al. 2010]. One can distinguish between three types of blobs; the boundary blobs, auroral blobs and sub-auroral blobs [Tsunoda, 1988]. The boundary blobs are narrow, elongated (longitudinally extended) plasma features with long lifetimes. They are dominated by convection and located along the equatorward boundary of the auroral oval. The cross sectional area is approximately the same as for polar cap patches, and the low electron temperature indicate that they are reconfigured polar cap patches, although some precipitation can occur in the midnight sector [Tsunoda 1988; Pryse et al., 1996, 2006]. The sub-auroral blobs resemble the boundary blobs, but are located in the trough-region equatorward of the boundary blobs. They are believed to originate from boundary blobs which have been transported equatorwards with the expansion of the auroral oval during substorms and stagnated in lower latitude in the recovery phase. Sub-auroral blobs are less extended than boundary blobs. The auroral blobs are found in the nightside auroral oval. They can either stem from sun aligned arcs that have exited the polar cap or from particle precipitation [Tsunoda, 1988, Pryse et al., 1996]. Burns and Hargreaves [1996] classified blobs in the auroral zone with respect to their altitude. Type 1 and type 2 blobs were located in altitudes between 250 km and 400 km. They were characterized by their intense fluctuations in electron density, especially at the edges of the blobs. The intensity increased with solar activity, but was not influenced by geomagnetic activity. The plasma temperature indicated that it was not produced locally; however type 2 blobs differed from type 1 due to ongoing precipitation in the E-region. Type 3 blobs were found at altitudes below 250 km and contained hotter plasma due to precipitation. The intensity in these blobs increased with geomagnetic activity.

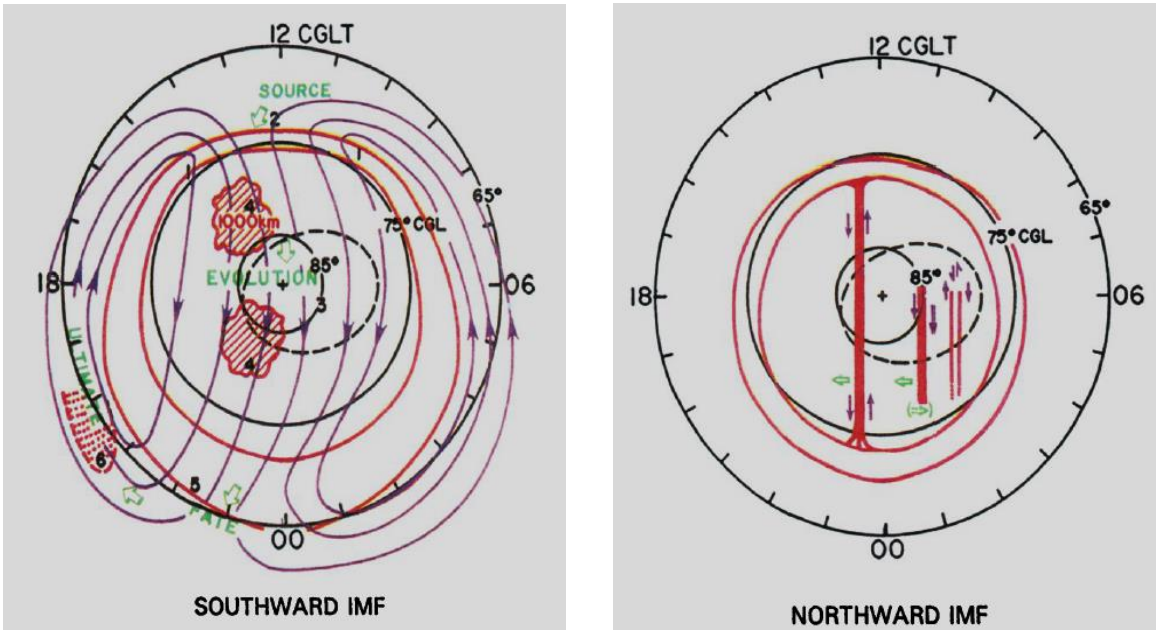

a) b)

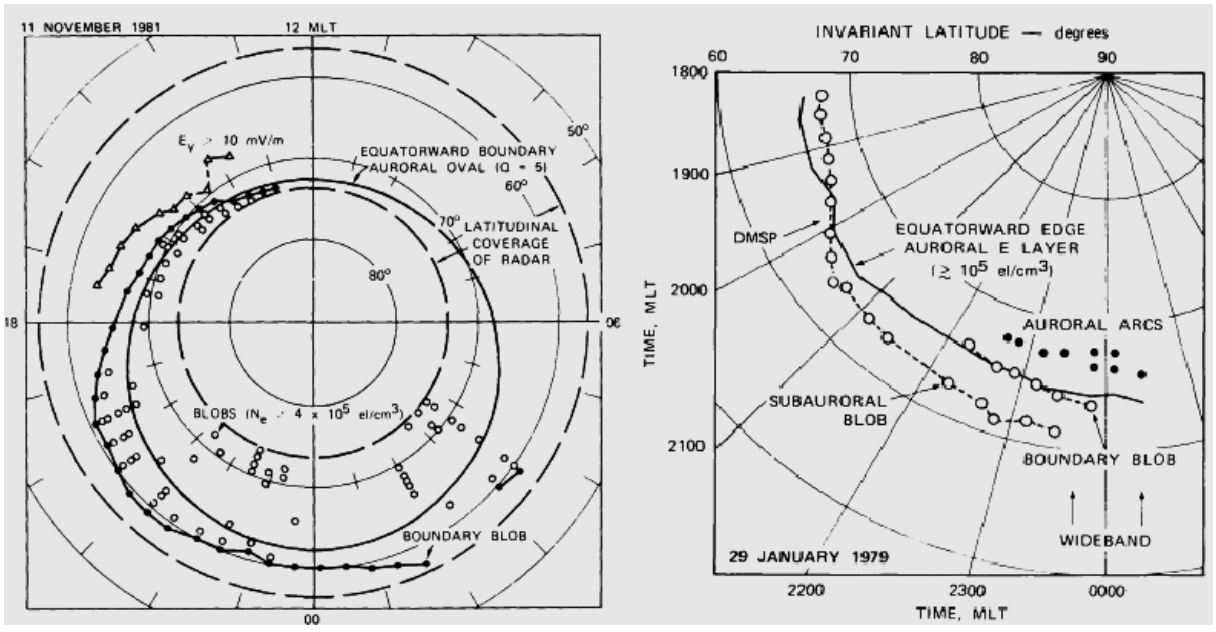

c) d)

Figure 2.4-10:a) The life and fate of a polar cap patch. b) Sun-aligned arcs drifting in dusk-dawn direction during northward IMF. Both figures are taken from Carlson [1994]. c) Location of auroral blobs and boundary blobs in the nighttime MLT. d) Location of boundary blob and sub-auroral blob in E-region. Both figures are adapted from Tsunoda [1988].

Crowley et al. [2000] conducted a study of a patch and its trajectory across the polar cap and through the Harang discontinuity (transition region between anti-sunward and sunward flow). They found that the patch became narrowed in latitude and elongated in longitude upon entering this region, and evolved into a blob with extension into both dawn and dusk. The calculated trajectories were sensitive to the location of the enhanced regions and the convection pattern. Changes in the convection pattern led to the formation of a boundary blob and a sub-auroral blob. The time interval of this study was ~4h, indicating that entry and exit of the polar cap is less than this time. Although patches change their orientation and velocity, a patch can cross the polar cap in ~2 h [Oksavik et al., 2010]. Figure 2.4-10a) shows a schematic evolution of the patch into a blob. Figure 2.4-10b) shows the features of the polar

cap when the IMF is northwards and will be treated later in this section. Figure 2.4-10 c and d) shows how the different blobs are distributed on two occasions according to Tsunoda [1988].
When patches exit the polar cap in the nightside, they can only escape through the o/c-boundary by tail reconnection. The high electron density within the patch excites neutral oxygen creating intense airglow, which in this case brightens the boundary. This is an indication of ongoing tail reconnection [Lorentzen et al. 2004]. The 630.0 nm airglow from the patches can be optically tracked by photometers on the ground. The patches are not really aurora, but due to excitation and recombination of oxygen caused by the high electron densities, the patches glow red with brightness about 100 Rayleighs [Steele and Cogger, 1996; Lorentzen et al. 2004; Sandholt, Carlson and Egeland, 2002]. In Figure 2.4-11, 630.0 nm airglow images show patches (2.4-11a) and a TOI (2.4-11b). The images are taken with an all-sky imager in Resolute Bay on two separate occasions.

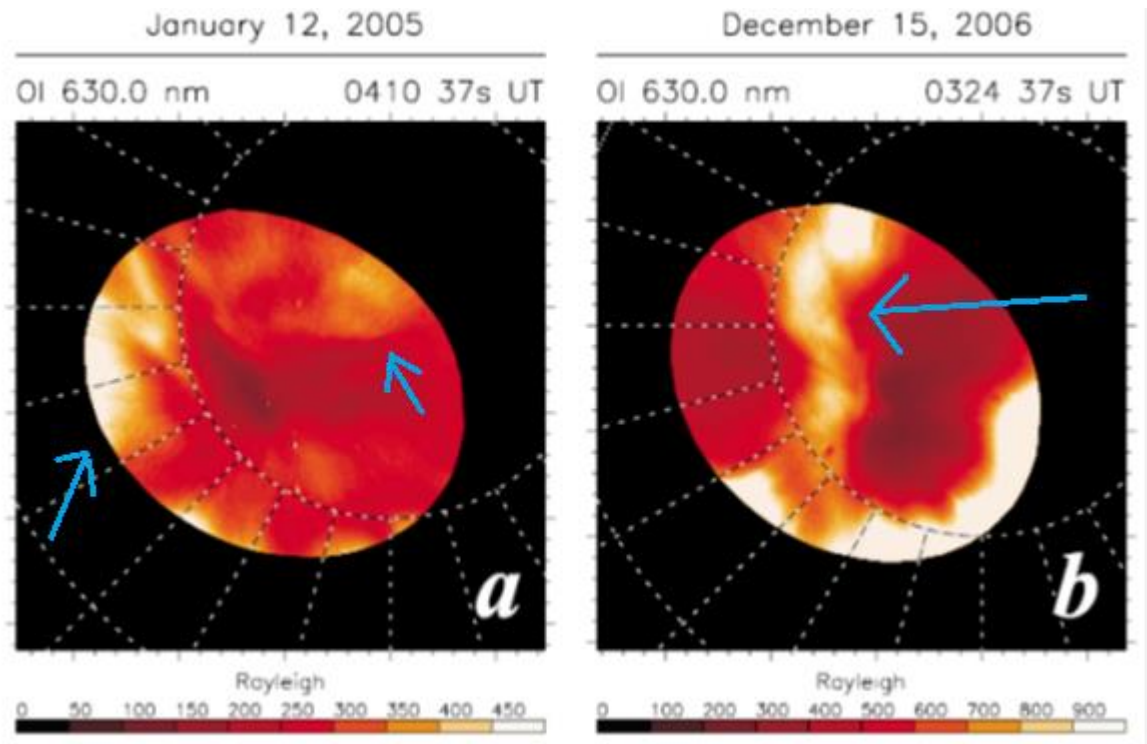

Figure 2.4-11: a) Air glow image of polar cap patches drifting over Resolute Bay. b) A TOI imaged over Resolute Bay during a magnetic storm. Adapted from: Hosokawa et al. [2010]

2.4.3.2 Irregularities and Instabilities

Large scale plasma features such as patches and blobs are associated with kilometer scale irregularities [Tsunoda, 1988]. Further structuring of the patches leads to smaller scale irregularities, which give rise to radio wave scintillation. The structuring is driven by plasma instability mechanisms [e.g. Weber et al., 1984].

Plasma instabilities are enhancements in the amplitude of the plasma waves caused by deviations from equilibrium conditions [Kivelson and Russell, 1995]. In order to drive the instability process, there must be a source of free energy to set the turbulence in motion. Such sources can be electrons or ions streaming in field aligned current sheets, such as in the cusp region [Curtis et al., 1982].There are several mechanisms which cause different kinds of instabilities in plasma, and it is far too extensive to discuss them here. However; there are two mechanisms which are of importance; the gradient drift instability (GDI) and the shear driven instability, loosely called Kelvin-Helmholtz instability (KHI) [Kintner and Seyler, 1985] The GDI is associated with steep density gradients and is a convective mechanism, also referred to as **E**x**B**-instability. It favors scale sizes less than 10 km and shorter wavelengths. The irregularities are distributed within the patch with maximum in the trailing edge of the patch [e.g. Tsunoda, 1988]. In the F-region, GDI develops if there is a density gradient perpendicular to both the magnetic field and the background electric field, $\mathbf{E_0}$. Along the perturbation line of the irregularity the ions and electrons drift with different velocities inducing a polarization electric field, $\mathbf{E_p}$, due to the charge separation. This results in an $\mathbf{E_p}$x**B**-drift in along the direction of the density gradient, which displace the perturbation line into regions with a different density. Figure 2.4-12 illustrates this scenario. The perturbation lines are the curved lines along the y-axis. This is the direction of the background **E**-field and the Pedersen drift direction. The density gradient is along the x-axis. The electrons lag behind the ions causing the polarization E-field to develop. The result is a **E**x**B**-drift of the perturbation in the Hall-direction along the density gradient. The irregularities are enhanced if they drift into an area with larger density [Tsunoda, 1988; Schiffler, 1996]. This instability is often said to be responsible for convecting plasma irregularities such as patches and blobs [Basu et al. 1990], but it seems that it is too slow to explain the growth of irregularities. There must be other mechanisms in addition to it [Carlson et al., 2008; Oksavik et al. 2010; Carlson 2012].

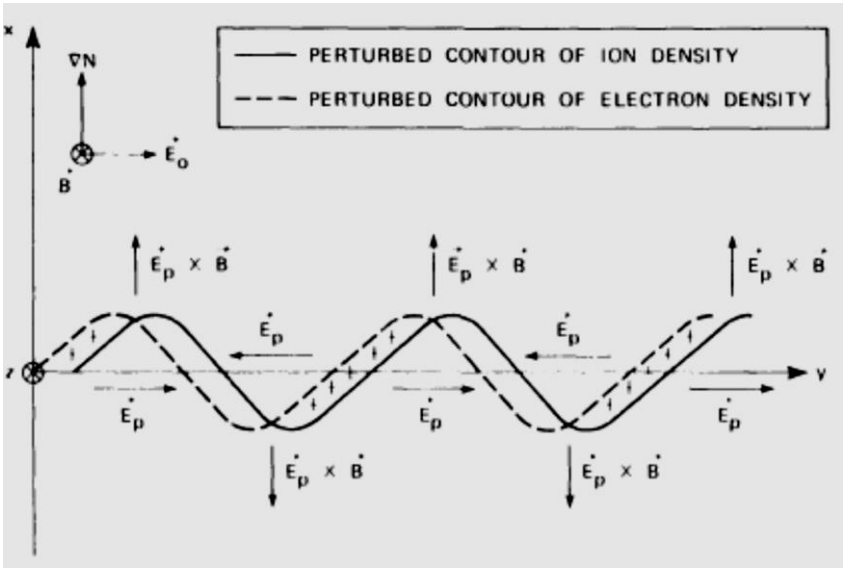

Figure 2.4-12: The GDI illustrated by Tsunoda [1988]. The Pedersen drift is in the y-direction, the density gradient in the x-direction and the magnetic field points into the paper. The perturbed regions are transported into areas of larger/lesser density by the ExB-drift.

The Kelvin-Helmholtz instability, which arises when there are differences in flow velocities viewed from the rest frame of the neutral gas, is a suitable candidate. Carlson et al. [2008] suggested that both gradient drift and shear instabilities cooperate in structuring plasma irregularities. The dominant patch formation mechanism is the transient reconnection model of Lockwood and Carlson [1992]. The reconnection dominated pulsation of the o/c-boundary (merging gap) allows magnetic flux tubes with different plasma densities to become entrained within the poleward drift of the merging gap when reconnection is shut off. The poleward accelerated flow is associated with flow shears. Injection velocity of dense plasma is ~1-2kms^{-1}, (to the east if By <0, west; By>0) as long as reconnection is taking place. Later, the anti-sunward drift begins with a velocity ~half of the injection speed. The shear driven instability begins to structure the plasma along the sides of the plasma jet at the onset of reconnection, whereas the GDI starts to feed off the primary irregularity at the trailing edge as the anti-sunward drift takes over when the patch enters the polar cap. This explains why the irregularity maximum is observed at the trailing end. Dahlgren et al. [2012] have also shown that irregularities are present throughout the whole patch. This could be due to rotation and re-shaping of the patch. Figure 2.4-13 illustrates the development of the two instability mechanisms. Typical growth time of GDI is about 10 minutes, whereas it is less than a minute for KHI [Carlson et al., 2008]. From in situ measurements with the ICI-2 (Investigation of Cusp Irregularities) sounding rocket in 2002, Moen et al. [2012] found that GDI growth times were in the order of tens of seconds for sufficiently steep density gradients.

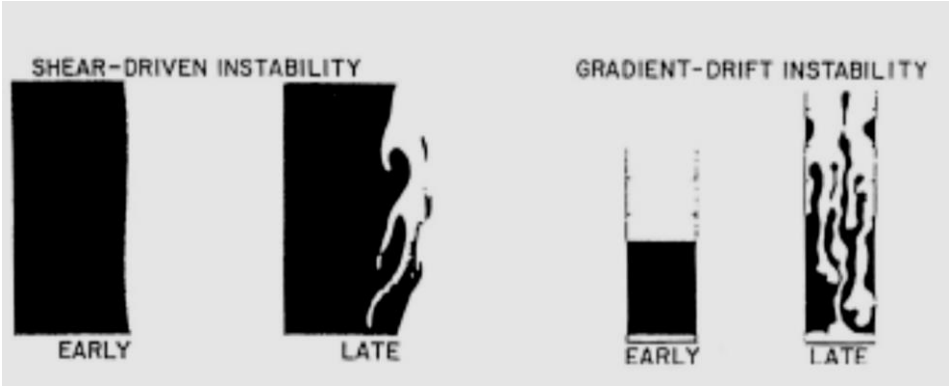

Figure 2.4-13: The development of KHI and GDI. Figures are originally from Keskinen et al. [1988] and Keskinen and Ossakow [1983] found in Carlson et al. [2008].

Another irregularity structure arises mainly due to shear instabilities during northwards IMF. These are the so called arcs. They emerge in the edge of the auroal oval at dawn or dusk and drift across the polar cap with velocities around 100 -200 ms^{-1}. For a positive IMF By , the arcs drift towards dusk, and towards dawn when By is negative. The arcs mark the boundary between flow channels in the polar cap with different velocities or directions. Reconnection of open field lines may produce flow cells in the polar cap with reversed flow. This may lead to a boundary with flows in opposite directions. The anti-sunward flow on the dusk side is slower than on the dawn side, leading to a velocity gradient along the flow. The collisions with neutral gas produce a Pedersen current perpendicular to the shear boundary that in turn is closed by a Birkeland current sheet. The Pedersen current decreases from dawn to dusk, likewise; the sunward plasma drift decreases in the same direction, see Figure 2.4-14a) and b). The electrons precipitating down along the Birkeland sheet are soft, in the 0.1 – 1 keV –range, and contribute to the emission of 630 nm from O^1D and 427.8 nm from N_2^+ , but are not of visible intensity.

a) 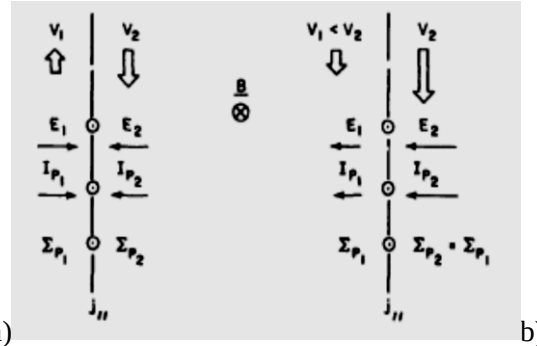

b) 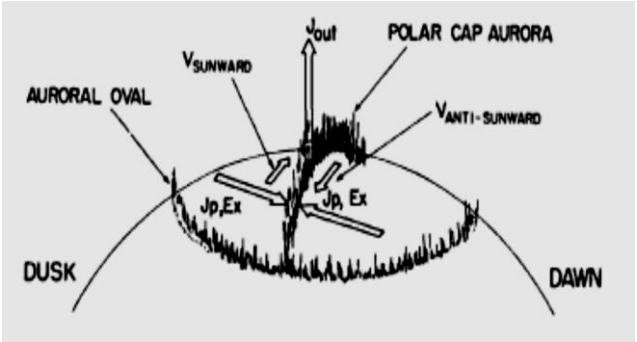

Figure 2.4-14: a) The flow configurations of sun aligned arcs. To the left velocity reversal, and to the right velocity gradient. b) The formation of a sun aligned arc. Both figures are adapted from: Carlson [1990].

During solar maximum, the density in the F-region above the arcs is denser and strong scintillation is associated with arcs [Sandholt, Carlson and Egeland, 2002].
Both polar cap patches and polar cap arcs are occurring simultaneously in the polar cap. After reversal of the IMF Bz from southwards to northwards, found Valladares et al. [1998a,b] evidence of coexistence of patches that still were lingering in the polar cap and sudden emerging polar cap arcs from reconnection. There has also been reported that patches can form on lobe cells during northward IMF [Oksavik et al. 2010], and that ionization blobs drawn around the polar cap are the northward IMF's counterpart of a TOI [Middleton et al., 2005].
It was long believed that GDI dominated the patch structuring during southward IMF, and KHI dominated the formation of arcs during northward IMF. As we have seen this is not entirely accurate, but it is evident that GDI is responsible for the further structuring of the patches [Carlson et al., 2008].

2.4.4 Geomagnetic Disturbances

I will not distinguish between storms and substorms, but give a general overview of the mechanisms. During a passage of a magnetic cloud or enhanced solar wind dissipation, the magnetosphere is subjected to disturbances, which exceeds the regular fluctuations during solar quiet conditions.
When a magnetic cloud reaches the magnetosphere, the magnetopause is compressed by the shock which is felt by the geomagnetic field causing a sudden increase. This sudden impulse (SI) marks the onset of the storm. As the IMF is southwards, reconnection occurs in the dayside magnetopause. It is custom to distinguish between the growth phase, expansion phase and recovery phase of the storm. During the growth phase, particles are injected which are enhancing the ring current and tail-current, and magnetic flux accumulates in the tail lobes. The increased magnetic pressure compresses the plasmasheet and stretches the field lines. The increased current strength and the associated earthward **j** x **B**-force makes the tail and plasmasphere shift closer to the Earth. The polar current system, along with the electro jets also intensifies. The expansion phase is characterized by the sudden release of magnetic energy in the tail lobes. It is believed that the tail current is partially disrupted in the neutral sheet giving rise to a current wedge of ascending and descending Birkeland currents allowing particles to infuse the polar ovals when tail reconnection occurs, see Figure 2.4-15.Descending electrons along these currents excite the neutral gas giving rise to the auroral display [Prölss, 2004]. Figure 2.4-16 shows a time development of an auroral substorm with brightening in the auroral oval midnight sector. The auroral electrojets are intensified during the expansion. The recovery phase is recognized by the diminishing of disturbed conditions and may last for days [McPherron in Kivelson and Russell, 1995].

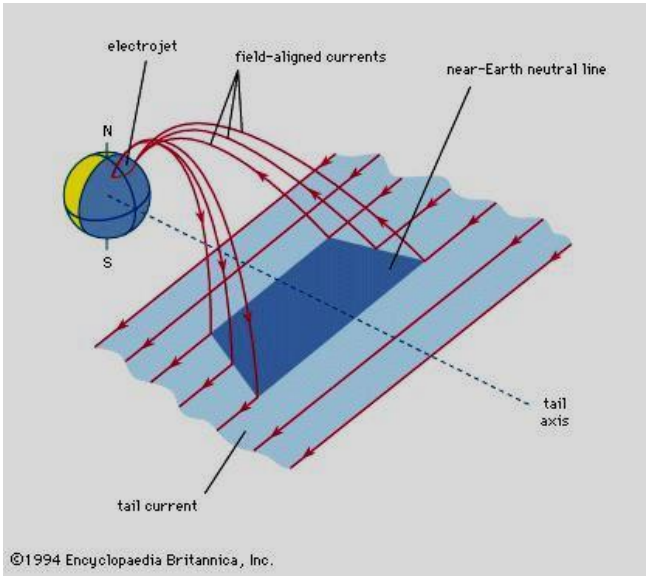

Figure 2.4-15: The storm time current wedge that forms during tail reconnection. Figure from: *http://www.britannica.com/EBchecked/media/1171/The-substorm-wedge-current-is-a-field-aligned-current-system*

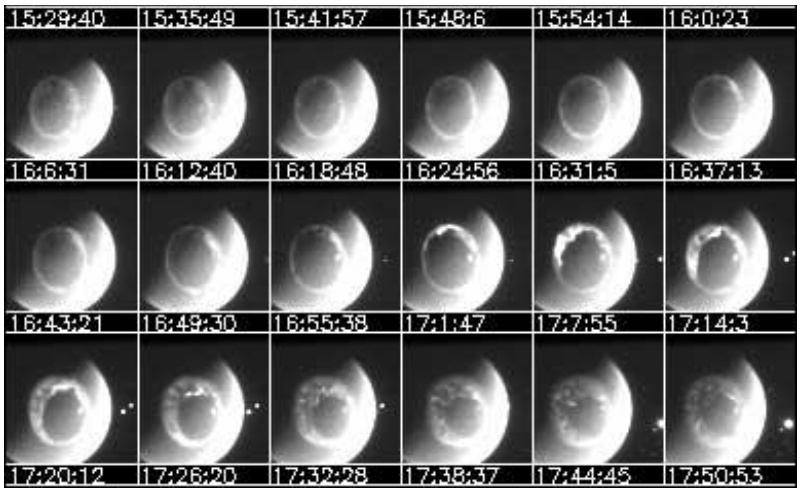

Figure 2.4-16: The time development of an auroral substorm viewed in UV-spectrum. Notice the brightening in the oval in the midnight sector and the enhanced electrojets around 16:30 UT . Photo: NASA,(*http://www.nasa.gov/mission_pages/themis/auroras/substorm_history.html)*

2.4.4.1 The Aurora

Aurora is produced by precipitating particles which deposit energy into the ionosphere. The de-excitation of the neutral gas provides the colorful light display in the sky. Different kinds of aurorae can be distinguished by their particle energy and location [Pfaff, 2012; Akasofu, 1963]. As mentioned earlier, the aurora is commonly confined to an oval surrounding the polar cap. The morphology of the auroral oval (AO) has been studied since the 1860-ies, and is well documented [Akasofu, 1963 and references therein]. Feldstein and Starkov [1967] made a thorough study of the width and location of the AO with respect diurnal differences and magnetic activity. I refer to the Feldstein oval later, which is a model based on their work. Figure 2.4-17 is a schematic representation of the AO for different

scales of magnetic activity made by Feldstein and Starkov [1967]. Also Akasofu [1963,1976] investigated the auroral morphology. He studied dynamics and auroral forms and their motion in the polar sky. Figure 2.4-18 a) illustrates the distribution of auroral forms in the AO based on photographies taken by satellites in 1974-75. Newer studies have been performed by authors as e.g. Elphinstone et al. [1993] or Milan et al. [2009].

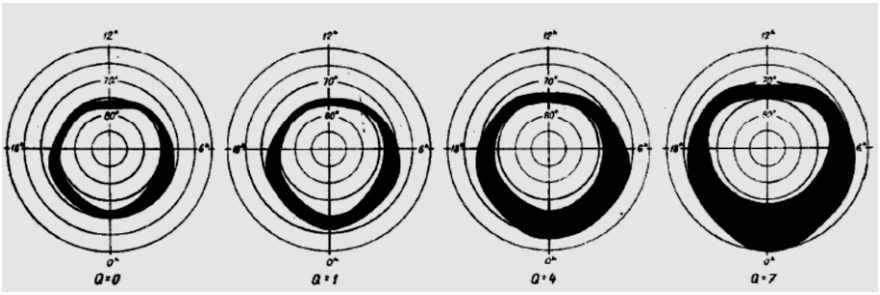

Figure 2.4-17:The location and widths of the auroral oval for different scales of magnetic activity. From quiet on the left, to disturbed conditions on the right. Adapted from Feldstein and Starkov [1967].

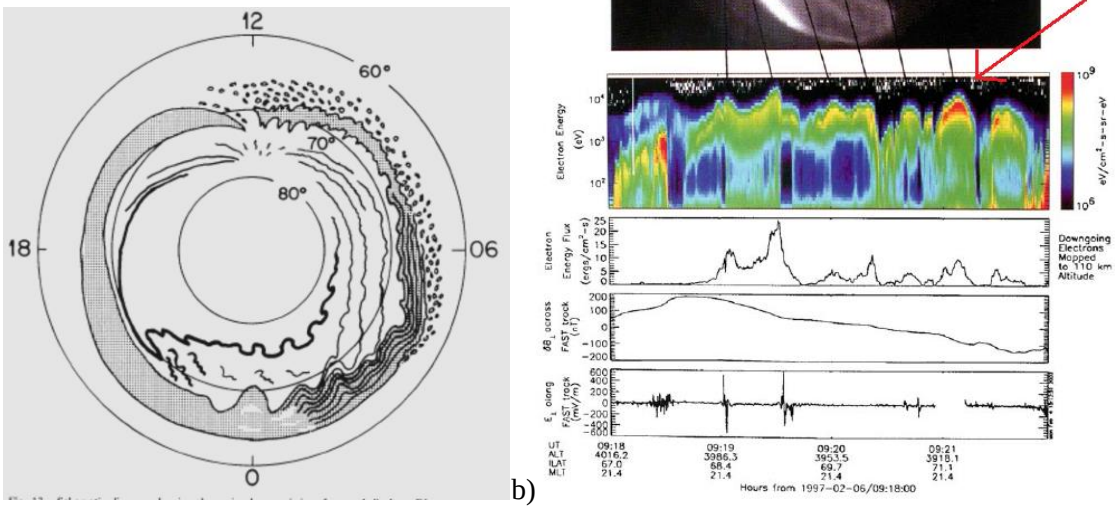

a) b)

Figure 2.4-18: a) In this schematic sketch of the auroral forms, the shaded region in the dusk sector is the diffuse aurora. The solid lines are discrete arcs and bands. Adapted from: Akasofu [1976]. b) Discrete auroral arcs in the top, photographed with and all-sky camera. The dotted line is the track of the FAST satellite which performed the measurements in the lower panels. The red arrow points to one of the inverted-Vs in the electron energy spectrum, which coincide with the spikes in the electron flux in the panel underneath. The two lowest panels reveal the magnetic and electric field disturbances. Figure originally by Stenbeck-Nielsen et al.,[1998] adapted from: [Heltquist in Kamide and Chian,2007]

Aurorae can be divided into three main groups; discrete, Alfvénic and diffuse. The discrete aurora is the visible aurora associated with arcs, bands and veils. The higher energy of the electrons is within the range from 100s of eV to a few 10s of keV. The maxima in the energy spectrum are characterized by inverted V-shapes, as illustrated by the red arrow in Figure 2.4-18b) [Pfaff, 2012]. Bands, like the omega bands, are folds within the AO associated with bursty bulk flows. Hornlike structures as reported by Akasofu [1976] are undulation effects, likely caused by SAPS [Henderson et al. 2002, 2010]. The discrete aurora is prevalent on the dayside and in the pre-midnight of the AO, however the largest energy deposit is in the dusk region (post-noon/pre-midnight) [Pfaff, 2012]. The discrete aurora can also be located within the region of diffuse aurora [Kamide, 1982]. Inverted-Vs are also associated with black aurora, which is produced by upgoing electrons in the same energy range. The black aurora emits no visual light, because there are no neutrals to interact with at higher altitudes. Alfvén aurora and/or oscillating aurora are present in dayside and nightside, but deposit most of the energy in the pre-midnight sector. This wave-particle interaction is due to oscillation in the E-field of the waves, which causes a counter-stream of electrons up and down the field lines. The energy spectrum contains inverted –Vs for the highest energies and it ranges from 10s of eV to ~1keV. This type of aurora is responsible for one third of the energy input during magnetic activity. The last, but not least type is the diffuse aurora. This latitudinal wide and faint aurora is located in post-midnight and morning region of AO. The electrons have energies slightly lower than plasmasheet electrons (100 eV) and are pitch angle scattered into a loss cone. This is the reason for the dimmer glow. In spite of the faintness, diffuse aurora dominates the total electron flux input in the ionosphere in high latitudes. The diffuse aurora is prevalent in the dayside cusp, and the ion aurora peaks here. In the post-midnight sector, the diffuse aurora can pulsate with periods up to a half minute [Pfaff, 2012]. Theta aurora that occurs in the polar cap is treated before. Other forms of polar cap precipitations are polar rain and showers caused by strahl electrons [Prölss, 2004; Gussenhoven, 1989]. The dayside/cusp aurorae are associated with convection and precipitation. The aurora moves poleward from the cusp in a pulsating manner, due to pulsed reconnection and are often referred to as poleward moving auroral forms (PMAFs) [Sandholt et al., 1993] Figure 2.4-19 illustrates the distribution of auroral forms and their number fluxes for high and low solar activity during the years from 1988 to 1998.

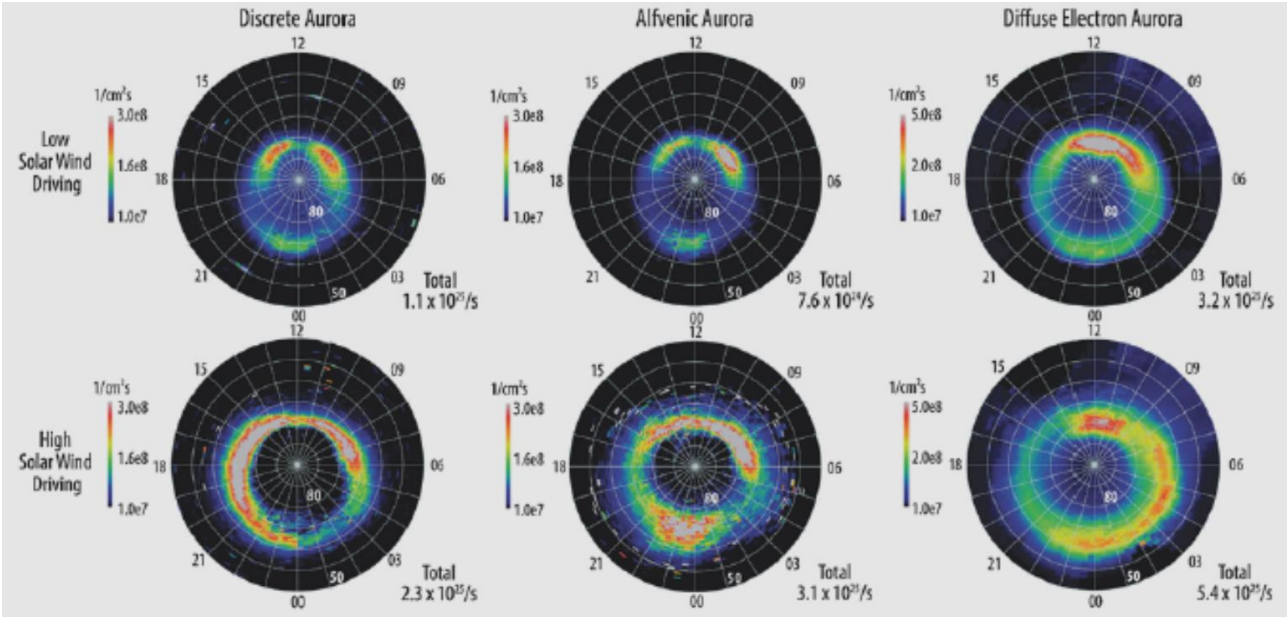

Figure 2.4-19: Electron number fluxes for all three main types of aurorae for high solar activity (upper), and low solar activity (lower). Figure by Newell et al., 2009, adapted from Pfaff [2012].

The maximal Hall conductivity is within an altitude range from 125-150 km. The E-layer electrojets coincide approximately with the AO, and are the result of particle precipitation [Prölss, 2004; Xu, 2009; Gullikstad Johnsen, 2013]. There are three electrojets associated with the AO. The polar electrojet (PEJ) is located at the polar boundary of the AO, near magnetic noon where the dayside cusp maps down in the ionosphere. The eastward electrojet (EEJ) is located within the zone of the diffuse aurora. The lowest latitudinal boundary is in late afternoon sector (15-17 MLT), and highest in post-noon and pre-midnight [Feldstein et al., 2007]. Both electrojets in the flanks are controlled by the convection E-field [Xu., 2009], and the weaker EEJ is mapped by the Alfvén layer in the ionosphere [Feldstein et al., 2007]. The Alfvén layer is the separatrix between the open and closed convection stream lines in the dusk sector [Wolf et al., 2007]. In the midnight sector, the Harang discontinuity separates the EEJ and the WEJ (westward electrojet). The Harang discontinuity is the region of the flow reversal. The WEJ penetrates into the dusk region and is slightly poleward of the EEJ [Rostoker et al., 1975; Gjerloev et al., 2003; Feldstein et al., 2007]. WEJ is stronger than EEJ [Wang et al., 2008] and it can be divided into a morning part and a midnight part [Xu., 2009]. The morning part is located in the AO, and close to the poleward boundary at ~10 MLT. The midnight part of the WEJ overlap with EEJ in the dusk region, and is close to the poleward boundary at ~18MLT [Feldstein et al., 2007]. During substorms, the substorm current wedge (SCW) contributes to an enhancement of the midnight WEJ [Xu, 2009]. The central plasma sheet maps the ionospheric footprint of the WEJ. Figure 2.4-20 shows the auroral precipitation distribution and electrojets as illustrated in Feldstein et al., [2007]. The EEJ is located in dusk region, the WEJ in dawn. The PEJs are the grey and brown lines in noon sector. The magenta colored bands in noon and midnight are soft diffuse precipitation regions, the yellow zone is the diffuse auroral zone, and the green is the auroral oval precipitations zone.

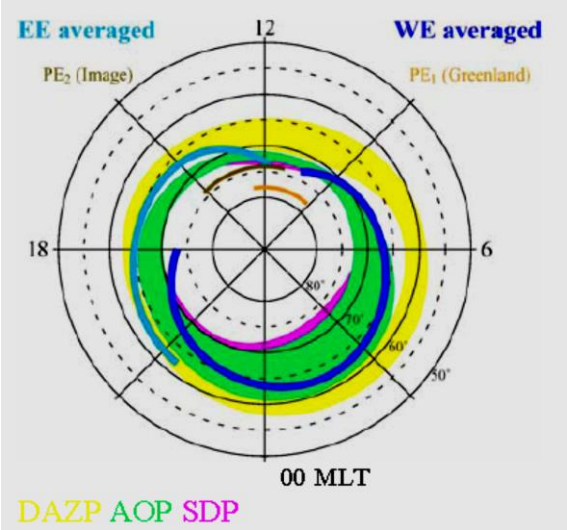

Figure 2.4-20: The high latitude electrojets and auroral precipitation zones.
Adapted from: Feldstein et al., [2007].

Although the electrojets are closely related to the AO, the location varies with local time, season and magnetic activity [Feldstein et al., 2007]. The conductivity depends on the ionization grade (both precipitation and solar zenith angle). When conductivity increases, the electrojets can become wider than the actual auroral oval [Gullikstad Johnsen, 2013] and models like the Feldstein oval, does not necessarily cover the diffuse aurora zone [Kamide, 1982]. The ability to pinpoint the position of the AO, and the electrojets is important in order to forecast associated scintillation effects on GPS and communication [Gullikstad Johnsen, 2013; Sigernes et al.,2011a, 2011b; Jacobsen and Schaeffer, 2012].

2.4.4.2 Disturbance Indices

There are different indices that illustrate geomagnetic disturbances. The most common are summarized in Table 2.4-1).

Latitude	Index	Magnitude	Description
Low latitudes	Dst	50 - 150 nT (moderate) 150 - 300 nT (storm) 300-500 nT (superstorm)	Negative depression in magnetic field due to enhanced ring current
Mid-latitudes	K_p	0-9 (0= very quiet) (9=very disturbed)	Enhanced ring current and contribution from field aligned currents
High latitudes	AE (= AU-AL)	200-2000nT	Distortion of geomagnetic H-component by polar electro jets

Table 2.4-1: Summary of the common indices used for describing geomagnetic disturbances. Information from: Kivelson and Russell [1995]), Prölss [2004] and *http://wdc.kugi.kyoto-u.ac.jp/index.html*.

The Dst-index are provided by magnetic observatories located in the vicinity of the magnetic dip equator and calculated by the World Data Center in Kyoto. Negative depressions correspond to disturbed conditions as the ring current increases [http://wdc.kugi.kyoto-u.ac.jp/dstdir/dst2 /onDstindex.html; Prölss,2004]. In high latitudes the magnetometer chain observatories are placed in a circle around the pole. They measure disturbances in the H-component of the geomagnetic field and derive the intensity of the westward (AL) and eastward (AU) electrojets. The AE index is the difference in the two intensities [http://wdc.kugi.kyoto-u.ac.jp/aedir/ae2/onAEindex.html]. The K-index for mid-latitudes provides a simple scaling of the disturbance and solar wind energy dissipation [Kivelson and Russell, 1995]. A global version of the K-index is the planetary Kp-index, which is an average from 13 stations. The three hour K_p index is provided by the Helmholtz center in Potsdam [http://www-app3.gfz-potsdam.de/kp_index/description.html, 2013]. The Kp-index is a very common classification of the geomagnetic activity, but at high latitudes the Q-index is more appropriate. The Q-index is a 15 minute index which measures deviations in H- and D- components of the magnetic field. It has one common scale for all high latitude stations with ranges from 0 to 11 [Rourke, 1965; Lehtoranta, 1997]. The last indices worth mentioning are the ASY and SYM indices. They measure both asymmetric (ASY) and symmetric longitudinal disturbances in the H-and D- components. ASY H and ASY D correlate well with the AE-index, whereas the SYM H is practically the same as the hourly Dst-index [Wanliss and Showalter, 2006].

Heating of the atmosphere by energy dissipation within the current systems, causes perturbations in the global thermosphere. Although these perturbations have an important impact on the density distribution in the atmosphere, I will not address them further here. The thermospheric winds however; are the predominant cause of so called positive ionospheric storms. In a positive ionospheric storm, the ionization layer of the ionosphere, h_mF2, and the peak ionization density N_mF2, are elevated, giving rise to increased densities. This is due changes in the $[O]/[N_2]$ ratio, which is linked to production and recombination. When $[O]>[N_2,]$, ionization is increased leading to increased electron content [Prölss, 2004; Crowley et al., 2006]. When the density decreases during a storm, it is classified as a negative ionopheric storm [Prölss, 2004]. The superstorm on November 20, 2003, was indeed a positive ionospheric storm with increased densities and consequent disturbances.

2.5 GNSS and The Norwegian Mapping Authority (NMA)

In the following sections I will briefly present information on the global navigation satellite system with emphasis on GPS, and introduce the Norwegian Mapping Authority (NMA), also referred to as "Kartverket" in Norwegian.

The acronym GNSS stands for Global Navigation Satellite System and is a collective term for the different satellite positioning systems and augmentations. Currently there are two fully operational systems, GLONASS and GPS, but Galileo is under steady development and scheduled to be operational by the end of 2020-ies [http://www.gsa.europa.eu/, 2013]. Also, other countries have regional systems, such as the Japanese QZSS, the Indian IRNSS and the Chinese Beidou/Compass (global) system [Hofmann-Wellenhof, Lichtenegger and Wasle, 2008].

GLONASS (Global'naya Navigatsinaya Sputnikovaya Sistema) was developed in the nineteen seventies under military management in the former Soviet Union. Later; it became available to civilian users and is now operated the Russian Space Forces and the Ministry of Defence of the Russian Federation [Xu, 2007; Hofmann-Wellenhof, Lichtenegger and Wasle, 2008]. The concept of GLONASS is roughly as follows. The system consists of 29 satellites confined in three orbital planes with an equal spacing of 45º and ascending node separation of 120º. The inclination is 64.8º. The orbit is nearly circular with a period of 11h and 16 min. All ground control segments are located in former Soviet territory [Xu, 2007; http://glonass-iac.ru, 2013].

Galileo is being developed by the EU and ESA (European Space Agency). It differs from GLONASS and GPS, as it is an independent civilian system. The first test-satellite was launched in 2005 and currently there are four in operation. When fully operational capability is reached, there will be 30 satellites in three orbital planes with equal spacing (40º) and a 120º ascending node separation. The orbit is nearly circular with an inclination of 56º and a period of 14h and 4min. [Xu, 2007; Hofmann-Wellenhof, Lichtenegger and Wasle, 2008; http://www.gsa.europa.eu/, 2013]. The ground control segments are globally distributed, as Galileo also is an international co-operation project [http://www.gsa.europa.eu/, 2013]. GPS (Global Positioning System) was also developed in the nineteen seventies by US military and Department of Defence. It reached full operational capability in the mid-nineties and is also augmented for civilian users. Today there are 31 satellites in six orbital planes with a 60º ascending node separation, near circular orbit with a 55º inclination and a period of 11h and 58 min. The ground control segments are globally distributed. It is a goal that the different GNSSes are interoperable to increase accuracy and integrity. Since the systems are developed and operated independently, they have different coordinate-and-time reference systems and carrier frequencies, see Table 2.5-1. However, they are convertible and thus the different systems are compatible providing a reliable performance for all users [Xu, 2007 and Hofmann-Wellenhof, Lichtenegger and Wasle, 2008]. Figure 2.5-1 illustrates some characteristics of the three different systems.

GPS		GLONASS	Galileo	Interoperable
Carrier (MHz)	Code	Carrier (MHz)	Carrier (MHz)	
L_1=1575.420	C/A P	G_1 =1602.000	E_1 = 1575.420	GPS, Galileo
L_2 =1227.600	P (Y)	G_2 =1246.000	E_6 =1278.750	
L_5 = 1176.450		G_3 = 1204.704*	E_5 = 1191.795	GPS, Galileo (center frequency)

Table 2.5-1: Overview of the carrier frequencies. Adapted freely from:Hofmann-Wellenhof, Lichtenegger and Wasle [2008].

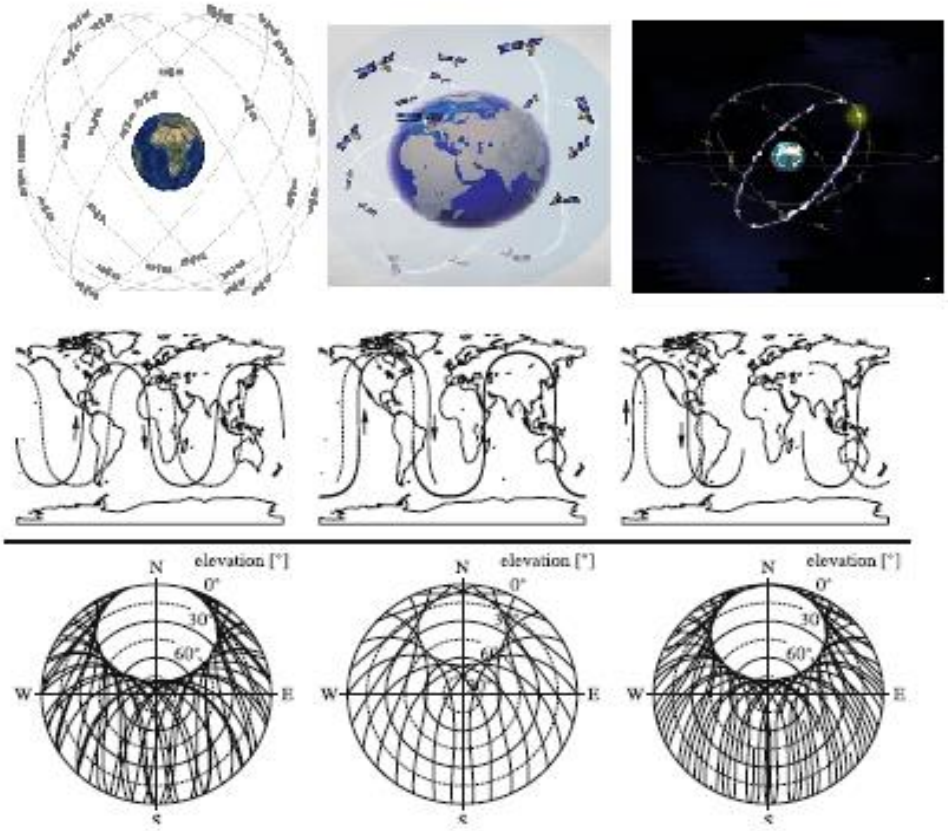

Figure 2.5-1: Upper panel from left: Satellite constellations of GPS, GLONASS and Galileo. All inclinations are chosen so that there will always be at least five satellites in view from every position on Earth. Figures from: *http://www.faa.gov/about/office_org/headquarters_offices/ato/service_units/techops/navservices/gnss/gps,http://glonass-iac.ru/en and http://spaceinimages.esa.int/Images/2000/12/Galileo*. Middle panel: Ground track plot of the three systems. Bottom panel: Sky plot of azimuth and elevation over 24 h from user postion Graz, Austria 47.1ºN, 15.5ºE and altitude 400m. Figures are adapted from: Hofmann-Wellenhof, Lichtenegger and Wasle [2008].

In order to meet user requirements in accuracy and integrity, the augmentation systems have been developed. These can either be ground based augmentation systems (GBAS), such as differential systems or reference stations, or space based (SBAS). An example of SBAS is the European augmentation system EGNOS (European Geostationary Navigation Overlay System), which uses three geostationary satellites to complement the navigation satellites. Ground segments (RIMS) receive signals from the navigations satellites and send them to the master stations which uplink corrections to the geostationary satellites. The geostationary satellites transmit the improved information back to the user receivers, see Figure 2.5-2. [Nordian, 2005; Hofmann-Wellenhof, Lichtenegger and Wasle, 2008; http://www.egnos-portal.eu/, 2013].

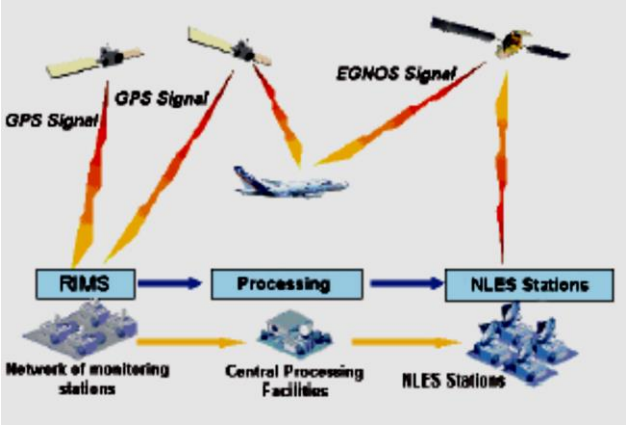

Figure 2.5-2: illustration of the EGNOS infrastructure. Reference stations dispatch downlinked information from GPS-satellites to a processing central. Next; the processed and corrected information is uplinked to a geostationary satellite which complements the GPS-signals in the plane's receiver. Figure from: *http://www.egnos-portal.eu/*

2.5.1 The principle of GPS

The whole GPS-system with the infrastructure and signal processing is too extensive to address here, but I will give a simple description. For further reading, see e.g. Xu [2007] or Hofmann-Wellenhof, Lichtenegger and Wasle [2008].

GPS determines the position via trilateration (triangulation). A simple explanation follows:

Assume four satellites are fixed in space and each sends a signal to a receiver on the ground. The receiver has a clock that can measure the time of arrival for all four satellites and multiply it with the propagation velocity (c) , which gives the distances the signals have travelled. The signals propagate from each satellite in spherical shells. When these four shells intersect in the exact same point, we have the position of the receiver. Figure 2.5-3a) illustrates the principle of trilateration. Figure 2.5-3b) shows the WSG-84 ellipsoid reference system the GPS is using to provide the position on Earth in the more familiar longitude/latitude format.

a) 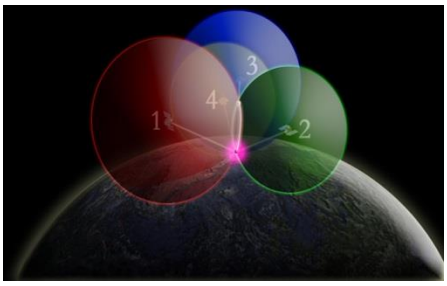

b) 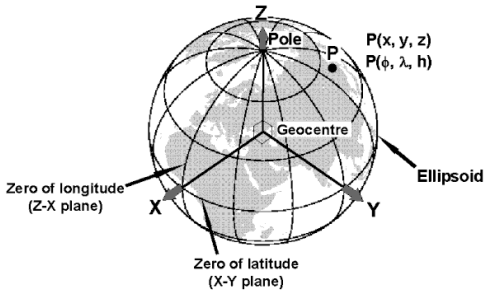

Figure 2.5-3a) The intersection of the four ranges marks the point. Figure from: *http://oceanservice.noaa.gov/education/kits/geodesy/media/supp_geo09b4.html* b) The WGS-84 ellipsoid reference system. Figure from: *http://www.gpspassion.com/pics/geoideb.gif*

The trilateration requires that the receiver knows the position of the satellites, and that the clocks inside the receiver and satellites are synchronized. Also; in order for the receiver to acquire the signals from all satellites simultaneously, it must have multiple channels to track all the satellites in view. The signals (and satellite vehicles) are distinguished by their pseudo random noise (PRN) codes, which are binary pulses generated by the maser clock on board the satellite [Nordian, 2005; Xu, 2007]. The receiver is able to reconstruct the signal and generates a reference signal to synchronize it with the received signal, which enables it to measure the time shift and calculate the pseudo range [Hofmann-Wellenhof, Lichtenegger and Wasle, 2008; Trimble, 2013]. Satellites have atomic clocks, but the receiver has not. There is a discrepancy in the time of arrival measurements, which leads to inaccurate position. This is what is called clock-bias (δ) and must be accounted for. When calculating a position, the precision depends on whether the receiver uses the code pseudo range or the phase pseudo range. Phase pseudo range is more accurate, because it is calculated from phase differences in the received and generated carrier frequency. However there is a phase ambiguity involved which makes this method a bit more challenging to resolve. If the satellite signal is interrupted, the cycle counting has to start over again and this affects the next carrier phase. These cycle slips may occur due to signal obstructions in the atmosphere or multipath. A simple formula of calculating the pseudo range is:

$$R = \varrho + c\delta \qquad (2.56)$$

where R is the pseudo range, ϱ is the range, c is the speed of light and δ is the clock bias. [Xu, 2007 ; Hofmann-Wellenhof, Lichtenegger and Wasle, 2008]. Figure 2.5-4 illustrates the geometry for the calculation of pseudo range.

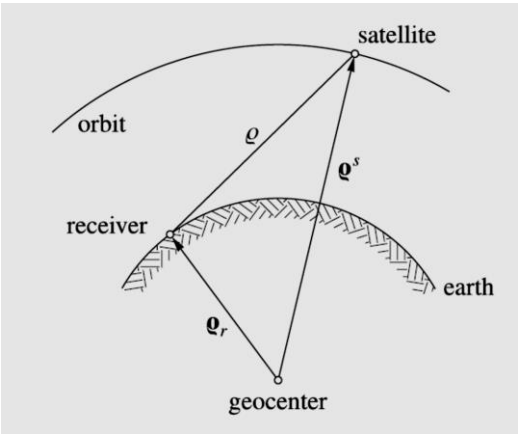

Figure 2.5-4: The simple geometric principle of determining pseudo range for one satellite. Figure from: Hofmann-Wellenhof, Lichtenegger and Wasle [2008].

There are different ranging code signals modulated onto the carrier frequencies. In L_1 there are coarse/acquisition (C/A) code and the P-code. C/A-code is the standard positioning code for civilian users, and P is the precision positioning code for authorized users and the military. The accuracy on P-code is about 3-5 meters, whereas the C/A code has an accuracy of 5-15 meters [Kintner et al., 2007]. L_2 have a P-code and a new code for civilian users; the L_2C-code, as well as an M-code for military. In addition to the code signals, a low - frequency navigation (NAV) message is modulated onto the signal. This NAV- message contains health status, ephemerides and clock corrections, and is repeated every 12 minutes. The ground segments and augmentation systems constantly monitor the performance of the satellites in view in order to consecutive update and correct errors [Nordian, 2005]. Despite signal processing and modeling, there are certain factors that must be taken into account, such as multipath and atmospheric disturbances. Multipath can be resolved by using a dual frequency receiver, which uses the first arrived signal for processing [Trimble, 2013]. The encrypted P(Y) code on the L_1 and L_2 are used in dual frequency receivers and cross correlation of the two signals can contribute to measurements of the refractive properties of the ionospheric medium, such as the electron content (see next section) enabling removal of errors. In order to do so, the receiver should be stationary [Kintner et al., 2007].

An option to correct errors is use of differential GPS, DGPS. This is a relative positioning method which determines the unknown position's coordinates with respect to a known permanent reference station (stationary) along a baseline vector. Remote receivers; either fixed (static) or mobile (kinematic) receivers (rovers), get precise positions with respect to the reference station. The reference station corrects the pseudo range and range rate (velocity) in the retransmitted signal. To further improve accuracy and coverage one uses a network of reference stations including the master station which monitors the network and distribute corrections them. To compensate for long distances between the reference station and the rover, range corrections can be dispatched via a virtual reference station (VRS). The VRS uses the data from the closest permanent reference stations to determine its own position. For roving receivers, the kinematic relative positioning rely on a permanent reference station or VRS to transmit ranges for arbitrary epochs. Figure 2.5-5 illustrates the simple concept of relative positioning. The receivers are located in A and B connected by a baseline vector $\mathbf{b}_{AB,}$ between them. Relative positioning requires simultaneous observation of both receivers and satellites involved. Triple differencing between satellites, receivers and time tags contributes to cancellation of the ambiguity effect, so that the accuracy is improved. Corrections are transmitted from the permanent receiver to the rover, e.g. from A to B. There is a small time delay in the signal due to the communication back and forth, however the signals travel so fast that the data can be considered as real time data [Hofmann-Wellenhof, Lichtenegger and Wasle, 2008].

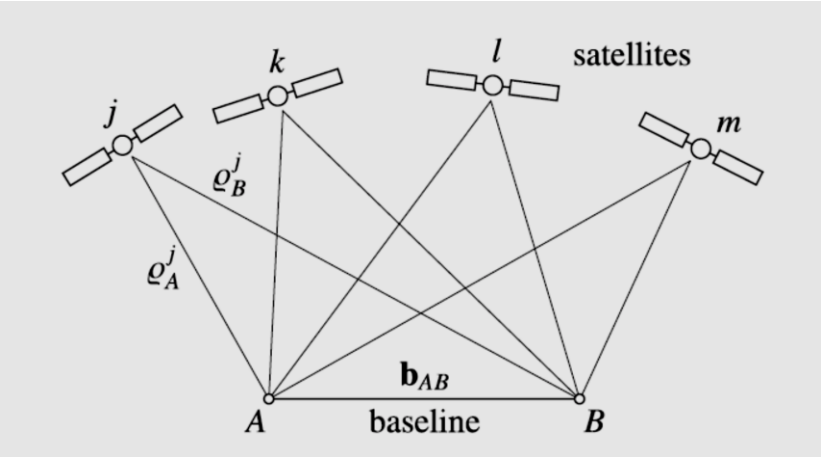

Figure 2.5-5; Schematic illustration of relative positioning. The two receivers A and B lies along the baseline vector, $\mathbf{b}_{AB}$, and all satellites transmit to both stations. The permanent receiver in position A sends corrected data to the rover in B, enabling it to calculate its precise position. Figure adapted from Hoffman-Wellenhof, Lichtenegger and Wasle, [2008].

2.5.2 Total Electron Content (TEC)

The disturbing properties of the ionosphere depend on the number density of electrons. As mentioned earlier, polar patches are 100-1000 km islands of high electron density. GDI operates on the trailing edge of the patch producing irregularities which may lead to disturbances in the radio wave signal, so called scintillation (explained in the next section). The electron density in the ionosphere is commonly measured in TEC (Total Electron Content).

If we consider a vertical column, with one square meter cross-sectional area, and length equal to the path length R, then the total electron content is the integrated number density of electrons within that column.

Total electron content is given by the curvilinear integral:

$$TEC = \int_{rec}^{sat} NdR \qquad (2.57)$$

where *N* is the number of electrons along the path length *R* between the receiver and the satellite. For a zenith path TEC can vary between 10^{16} to10^{19} electrons m^{-2}.

For simplicity one can use TEC-units (TECU) as a measure of TEC where:

$$1\,TECU = 10^{16}\,\frac{electrons}{m^2} \qquad (2.58)$$

e.g. [Saunders and Aragón-Zavala,2007;Tiwari et al., 2009; Brunini et al., 2011].

If the line of sight (LOS) is vertical, (2.57) is referred to as vertical TEC (VTEC). If the LOS is oblique, then (2.57) is called slant TEC (STEC). So it is obvious that this expression depends on the zenith angle and the higher elevation, the less multipath and loss effects affects the radio wave propagation [Brunini et al.,2011; Zhang et al., 2003]. VTEC is modeled from STEC via mapping techniques and signal processing. Many of the models involve using the simple single-layer model (SLM) for conversion to VTEC. Here the total electron content is confined within an infinitesimal thin layer at a height h_m. The ionospheric pierce point (IPP or IP), is located in this layer. The zenith angles z_0 and z' follows the relation:

$$secz' = \frac{1}{\sqrt{1 - \left(\frac{R_E}{R_E + h_m}\right)^2 sinz_0}} \qquad (2.59)$$

and constitute the mapping function, thus:

$$STEC = secz' \cdot VTEC \qquad (2.60)$$

Figure 2.5-6 illustrates the SLM-geometry. The disadvantage with this model is that the layer height $h_{m,}$ may influence the VTEC estimation. TEC is dependent on diurnal, seasonal and latitudinal variations, and the ionosphere is in fact layered. The single layer height is commonly selected to be between 350 and 450 km [Brunini et al., 2011; Zhang et al. 2003; Karslioğlu and Durmaz,2012].

The refractive index of the ionosphere depends on the number density of electrons, the magnetic field and the frequency and polarization of the radio waves. As a radio wave propagates through the ionosphere, the velocity and phase of the wave is changed due to the variations in the refractive index. This gives rise to group delay, which is a phase shift of the radio wave relative to the phase shift expected from the physical path length. The phase of a wave propagating through the ionosphere is advanced by the same amount the group velocity is delayed [Saunders and Aragón-Zavala, 2007; Dyrud et al., 2007].

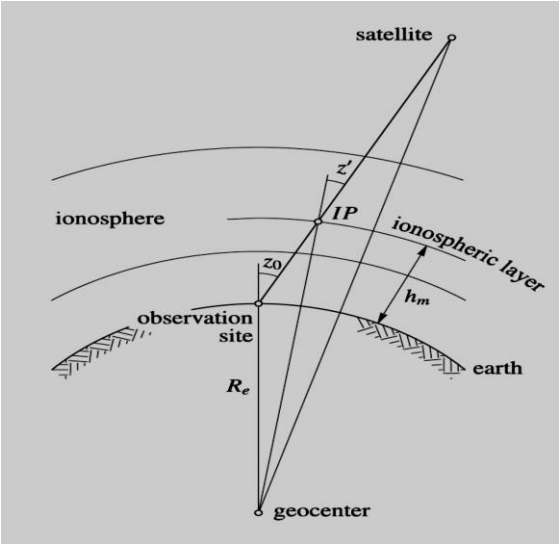

Figure 2.5-6: The geometry of single layer model. Figure from: Hofmann-Wellenhof, Lichtenegger and Wasle [2008].

The Dual frequency receivers, operating with both L_1 and L_2, can estimate the TEC from group delay and carrier phase advance on the two carriers.

The group delay is proportional to the TEC-value and inversely proportional to the carrier frequency:

$$\Delta t = \frac{40.30}{cf^2} \cdot TEC \qquad (2.61)$$

where c is the speed of light, f is the carrier frequency and Δt is the time delay in seconds equivalent to the difference in path length [Carrano, 2008].

There are two ways of deriving TEC; the first approach is based on using the difference in measured pseudo ranges on L_1 and L_2. The other is based on differences in the carrier phases on L_1 and L_2.

The code derived TEC is absolute, but contains noise and code differential biases. The absolute code derived TEC can be expressed as:

$$TEC_p = \frac{\rho_{L1} - \rho_{L2}}{0.104\, m\, TECU} \qquad (2.62)$$

where ρ_{L1} and ρ_{L2} are the pseudo ranges on L_1 and L_2 in meters. On L_1; 1 TECU corresponds to a delay of 0.163m, and 0.267m on L_2.

The phase derived TEC is smoother, but ambiguous due to the unknown integer number of cycles between the satellite and receiver. The carrier phase derived TEC can be expressed as:

$$TEC_\phi = \frac{-\phi_{L1} + \phi_{L2}}{0{,}104 m\, TECU} \qquad (2.63)$$

where ϕ_{L1} and ϕ_{L2} are the phases (in meters) of both carriers. To get an absolute TEC value with low noise, these two equations are combined by some fitting procedure, e.g. as:

$$TEC_{final} = TEC_\phi - TEC_{offset} \qquad (2.64)$$

where the last term is an estimate of the differential code offset between the relative phase TEC and the absolute code TEC.

The receivers are designed to provide a precise position, and leveling and smoothing techniques that will enhance the performance, produce errors in derivation of TEC. Therefore it is important that the receiver is calibrated to measure the differential code bias, instead of estimating it [Dyrud et al.,2007]. After removal of noise and biases, the VTEC can be modeled from the slant TEC.

There are several methods to model VTEC, and it is too extensive to describe them here. For further reading, see e.g. Brunini et al. [2011] Zhang et al. [2003], Karslioğlu and Durmaz [2012] or Burrell et al. [2008].

Once the VTEC is constructed for every IPP, it can be used to create global TEC maps, see Figure 2.5-7. A common method is tomography which uses algebraic reconstruction techniques to reconstruct ionospheric densities along a two-dimensional grid, based upon differential Doppler measurements. Other models are assimilation models, which combine measurements from different instruments, such as e.g. MIDAS (Multi Instrument Data Analysis System) [Mitchell and Spencer, 2003; Schunk et al., 2003; Yin et al., 2004].

The number of electrons along the path is not constant. The fluctuations in TEC are therefore accounted for in using the rate of TEC (ROT), which is the distributive variation of TEC over time. It can be obtained by measuring the time rate of differential phase of the signal [Tiwari et al., 2009; Pi et al., 1997]. Tiwari et al. [2009] expresses the ROT as the time derivative of TEC:

$$ROT = \frac{TEC_k^i - TEC_{k-1}^i}{(t_k - t_{k-1})} \qquad (2.65)$$

where *i* is the satellite in view and *k* is the time of the epoch. The unit is TECU/min.

At high latitudes, the ROT can be used as a measurement of irregularities with scale sizes of tens of kilometers. For smaller irregularities, the rate of TEC index, ROTI, provides a better presentation of the TEC-fluctuations. ROTI is the standard deviation of ROT over five minutes, of TEC sampled every thirty seconds, and is given by:

$$ROTI = \sqrt{\langle ROT^2 \rangle - \langle ROT \rangle^2} \qquad (2.66)$$

During low solar activity, ROTI usually reaches a maximum of 0.5, but during strong geomagnetic storms, it may be 10 times higher (5 or more). A ROTI >0.5 indicates irregularities with a few kilometers scale lengths. It has been observed during high ROTI conditions that GPS receivers have lost lock to satellites due to irregularities causing scintillation [Pi et al., 1997; Alfonsi et al., 2011a; Carrano and Groves, 2007]. Alfonsi et al. [2011] used the ROT mean and ROT mean square as parameters to describe irregularities from relative TEC measurements during solar minimum (high latitudes). The absolute value of ROT was associated with electron density gradients in irregularities of a few to tens of kilometers. They found that combinations of ROT and ROT mean square (ROT_{RMS}) gave rise to different scintillation scenarios (see next section). An advantage of using ROT or ROTI, is that they are not affected by phase ambiguities [Alfonsi et al., 2011; Tiwari et al.,2009].

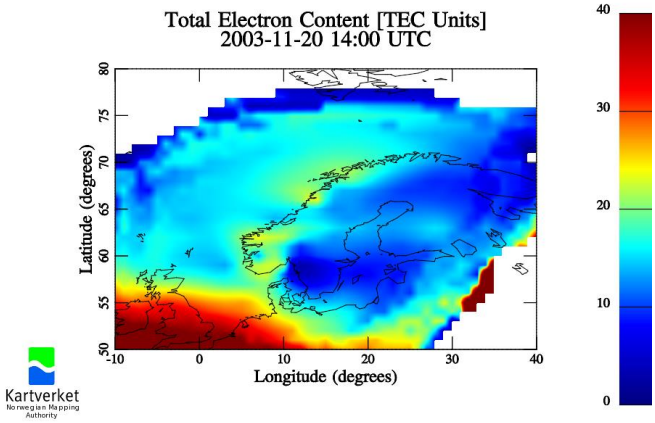

Figure 2.5-7: VTEC map over Scandinavia. The TEC is presented in TECU in color scale from blue to red, where dark blue represents low TEC. Credit: Jacobsen, K.S. , Kartverket 2013

2.5.3 Scintillation

The ionosphere makes up a dispersive medium that will change the properties of electromagnetic waves when electric and magnetic forces act upon them [Prölss,2004]
Interactions with free electrons will interfere with the waves and they will suffer from different phenomena such as scattering, polarization, refraction and diffraction. An electromagnetic wave can have a phase velocity given by:

$$v_p = \lambda f \qquad (2.67)$$

where λ is the wavelength and *f* is the frequency of the signal. GPS-signals are modulated, so it will have a group velocity, which is a superposition of different waves with different frequencies. The group velocity can be expressed as:

$$v_g = v_p - \lambda \frac{dv_p}{d\lambda} \qquad (2.68)$$

where v_p is the phase velocity, λ the wavelength and $\frac{dv_p}{d\lambda}$ the velocity dispersion of the phase velocity [Seeber,2003; Xu, 2007].
The density or concentration of free electrons in the ionosphere vary with height and extent and has a proportional relation with the ionospheric refractive index, *n* [Saunders and Aragón-Zavala, 2007]. The phase refractive index and group refractive index can be expressed as:

$$n_p = 1 - \frac{40.3N}{f^2} \qquad (2.69)$$

and

$$n_g = 1 + \frac{40.3N}{f^2} \qquad (2.70)$$

where *N* is the electron content and *f* is the carrier frequency [Seeber, 2003]. This provides us with two new expressions for the group-and-phase velocities:

$$v_p = \frac{c}{1 - \frac{40.3N}{f^2}} \qquad (2.71)$$

and

$$v_g = \frac{c}{1 + \frac{40.3N}{f^2}} \qquad (2.72)$$

Carrier phases are affected by the phase velocity, and code signals are affected by the group velocities [Seeber, 2003]. Recalling that the delay in propagation can be written as in (2.63), it should be clear that the carrier phase advance is of same magnitude as the group delay, but with opposite signs; when the phase velocity increases, the group velocity slows down [Xu,2007; Seeber,2003;Carrano,2008]. When the radio wave encounter enhanced density regions, such as patches, it can either suffer from refraction or diffraction [Kintner et al.,2007]. Refraction is associated with larger scale irregularities (hundreds of meters to a few kilometers, [Spogli et al., 2009]) which cause phase shifts due to changing group and phase velocities as the wave traverse the irregularity region. Diffraction occurs when the signal propagates through smaller scale irregularities - (smaller than the Fresnel radius which is about 100 m for L_1). Along the signal path the wave is scattered and the phases shifts. The resulting interference means that phases may add constructively or destructively contributing to fluctuations in amplitude and phase, so-called scintillation [Kinter et al.,2007; 2009].
The easiest approach to approximate wave propagation through an irregular medium was presented in 1950-51 by Booker et al. and Hewish et al. [Kintner et al., 2007]. This so called phase screen approximation method treats the irregular medium as a thin screen in which an incident radio wave experiences phase perturbations. When the wave exits the phase screen, the perturbations evolve into phase and amplitude scintillation as the wave propagates forward [Kinter et al. 2007]. Other models are single scatter theory for weak scintillation and multiple scatter theory for strong scintillation. For further reading, see e.g. Yeh and Liu [1982] and Crane [1977].

2.5.3.1 Scintillation Indices

The strength of scintillation is commonly characterized by scintillation indices. For amplitude scintillation, the S_4-index, originally introduced by Fremouw et al. in 1978, is the most common. It is the ratio of the standard deviation of the signal power to the mean signal power computed over one minute [Kintner et al., 2007; Manucci et al., 1999]:

$$S_4 = \sqrt{\frac{\langle I^2 \rangle - \langle I \rangle^2}{\langle I \rangle^2}} \qquad (2.73)$$

The S_4-index is unit less. According to Skone et al. [2005], typical ranges are between 0-1, but is usually lower at high latitudes (see next section).The intensity of scintillation can be distinguished as in Figure 2.5-8a). The graph shows the amplitude scintillation in Darwin, Australia, on an arbitrary day.
The phase fluctuations are measured with another index; the σ_ϕ-index. This is the standard deviation of the phase ϕ, (eq. 2.63) measured in radians [Kintner et al.,2007; Mushini et al., 2012]:

$$\sigma_\phi = \sqrt{\langle \phi^2 \rangle - \langle \phi \rangle^2} \qquad (2.74)$$

The intensity values range from 0.05 rad for weak scintillation, to 1.0 rad for strong scintillation, but can also reach 1.5 rad for severe conditions in high latitudes. A σ_ϕ~0.5 is considered moderate, nevertheless; even moderate scintillation can cause tracking errors at high latitudes [Skone et al., 2005]. Many authors have used 0.5 rad as a threshold value in studies concerning phase scintillation and cycle slips [Aquino et al., 2006; Béniguel et al. 2009; Prikryl et al., 2010,2013]. An example of the sigma-phi index is shown in Figure 2.5-8b) from Taloyoak in Canada.

As mentioned in the previous section; Alfonsi et al. [2011] used ROT and ROT_{RMS} when they investigated bipolar scintillation climatology during solar minimum. |ROT| can be viewed as an indication of TEC-gradients in the plasma, and ROT_{RMS} is associated with the variation of ROT. Combinations of these parameters provided an overview of the different scale sizes and their related scintillations. They found that phase scintillations were associated with irregularities of all scale sizes, amplitude scintillations with irregularity scale sizes of hundreds of meters, and finally ROT were related to scale sizes of a few kilometers [Alfonsi et al.,2011; Moen et al., 2013]. Table 2.5-2 reproduces the table from Alfonsi et al. [2011].

a)

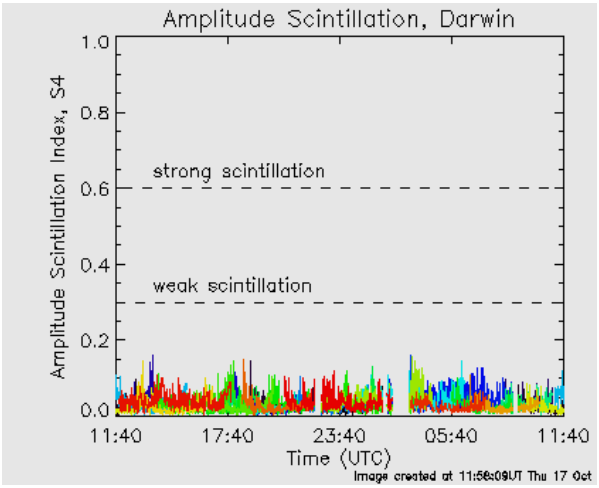

b)

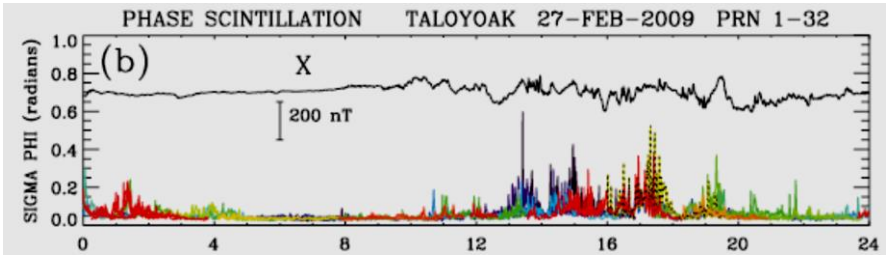

Figure 2.5-8: a) Amplitude scintillation index S_4 in Darwin, Australia. The threshold may vary in different articles depending on selected method of investigation.
Credit: *http://www.ips.gov.au/Images/Satellite/Ionospheric%20Scintillation/dwn_S4_latest.png*
b) Phase scintillation above the arctic circle in Canada. Figure adapted from: Prikryl et al. [2011].

|ROT|	ROT_{RMS}	Scale size	Scintillation
High	High	All scales	σ_ϕ, S_4
High	Low	Few kilometers (predominant)	Predominant σ_ϕ
Low	High	All scales	σ_ϕ, S_4
Low	Low	Few kilometers (little)	Not defined

Table 2.5-2: Combinations of scale sizes, scintillation and ROT. Adapted from: Alfonsi et al. [2011].

To determine whether scintillation may take place, we revisit some previous theory. Both the refractive index (eq. 2.69 and 2.70) and the plasma frequency (eq. 2.51) depend on the TEC in the ionosphere. The refractive index also depends on the carrier frequency f, which must be above the plasma frequency to penetrate the ionosphere. This means that dense plasma and variations in TEC, may cause strong irregularities and associated density gradients that produce scintillations at even high

frequencies [e.g. Kintner et al., 2007]. The relationship between electron density and plasma peak frequency can be used to characterize the patch strength in terms of peak frequency, see Table 2.5-3 below [e.g. Dandekar and Bullett, 1999 or Buchau et al., 1985].

Strength of patch	f_0F_2 (MHz)	N_e (m^{-3})
Weak	3.0	$1.0 \cdot 10^{11}$
Moderate	6.0	$4.5 \cdot 10^{11}$
Strong	9.0	$1.0 \cdot 10^{12}$

Table 2.5-3: The strength of polar cap patches characterized by peak frequency and electron number density.

2.5.3.2 Scintillation Distribution

Scintillation is most severe in the nighttime in the equatorial region. Due to the fountain effect irregularities and consequent scintillation are produced in two zonal bands approximately at ± 10º GMLAT [Skone et al., 2001; Alfonsi et al., 2011a]. However; strong scintillation is also present at high latitudes, in the auroral region which is located at 65º-75º GMLAT, and in the polar cap >85º GMLAT [Skone et al., 2001]. In the mid-latitudes scintillations may occur due to traveling ionospheric disturbances (TIDs), SAPS and geomagnetic activity when the auroral oval is shifted equatorwards [Kintner et al., 2007; Spogli et al., 2009]. See Figure 2.5-9 for distribution.
In the nighttime at high latitudes scintillation is pronounced due to auroral precipitation and large scale plasma structures such as patches and blobs [e.g. Kersley and Chandra, 1988]. In the daytime, scintillation is associated with patches and cusp precipitation [e.g. Prikryl et al., 2010; Moen et al., 2013]. For all cases; scintillation is associated with smaller scale irregularities due to steep TEC gradients and plasma instabilities [e.g. Tsunoda 1988; Prikryl et al., 2013].

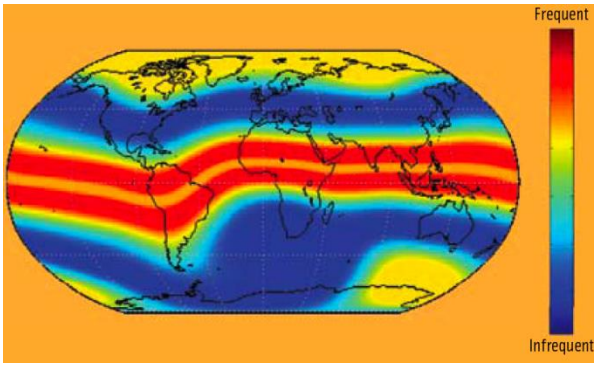

Figure 2.5-9: Global distribution of scintillation. Adapted from: Kintner et al. [2009].

High latitude scintillation varies with respect to season, solar cycle, local time and geomagnetic activity (IMF-orientation) [Buchau et al., 1985; Aarons, 1997; Shagimuratov et al., 2009; Li et al., 2010; Prikryl et al., 2010, 2011]. Scintillation is a local winter time phenomenon meaning that the highest occurrence is distributed from fall equinox to spring equinox. Although ionization is higher during summer, the scintillation occurrence is low because the higher conductivity decelerates the instability growth [Buchau et al., 1985; Wernik et al., 2003; Aarons, 1997]. During solar maximum, both arcs and patches contribute to scintillation in the polar cap [Buchau et al., 1985], but the amplitude scintillation occurrence is lower than the phase scintillation occurrence. Even during magnetic activity the amplitude scintillation is low in the polar cap, and is mostly confined to magnetic noon and midnight auroral oval boundaries [Spogli et al., 2009]. This is also the case at solar minimum, but then only patches are responsible for scintillation in the polar cap [Buchau et al., 1985;

Alfonsi et al., 2011]. Phase scintillation is always present in the polar cap, both in winter and summer, and for solar maximum and minimum [Spogli et al., 2009; Alfonsi et al., 2011]. On disturbed days during solar maximum, the phase scintillation follows the TEC-gradients at the auroral oval boundaries and therefore shifts equatorwards with it. In magnetic noon the phase scintillation is associated with the auroral cusp and in nighttime it favors the afternoon and pre-midnight [Spogli et al. 2009]. This asymmetry around magnetic midnight is supported by Moen et al., [2007] concerning the patch distribution, and by Li et al., [2010]. In solar minimum the phase scintillation is strongest in the cusp and in auroral brightening in nighttime [Spogli et al., 2009; Prikryl et al.,2010].
Aarons [1997] defined the irregularity oval as a modified auroral oval with a slightly broader extent which houses the scintillations. Scintillation incidences for a certain location can be associated with the irregularity oval, as the ground enters the region underneath it. This correlation is confirmed for instance in a statistical study from Li et al. [2010]. In their paper they investigate the impact of the By-component on the scintillation distribution when Bz is southwards. For a negative By-component they found that the scintillation preferred the late afternoon and post-midnight, whereas a positive By-component revealed a weak occurrence in noon and pre-midnight. Figure 2.5-10 illustrates the different occurrence distributions for solar maximum and minimum. Figure 2.5-10a) reveals the percentage occurrence of phase scintillation for winter and summer. The black lines represent the Feldstein oval during quiet magnetic activity, while the red lines are for disturbed days. Underneath are the amplitude scintillation maps for the same period. Notice how modest this occurrence is compared to that of phase scintillation. All these figures are from an article on the bi-polar climatology of high latitude scintillations during solar minimum by Alfonsi et al. [2011]. Figure 2.5-10b) are scintillation occurrence maps for the fall of 2003, covering the superstorm event this thesis is concerned with. The grey lines represent the Feldstein oval during magnetic quiet days, and the red; magnetic disturbed days. The upper row displays the sigma phi index, and the lower; the S_4 [Spogli et al., 2009]. The modest occurrence of amplitude scintillation is evidently a feature of the high latitudes.

a)

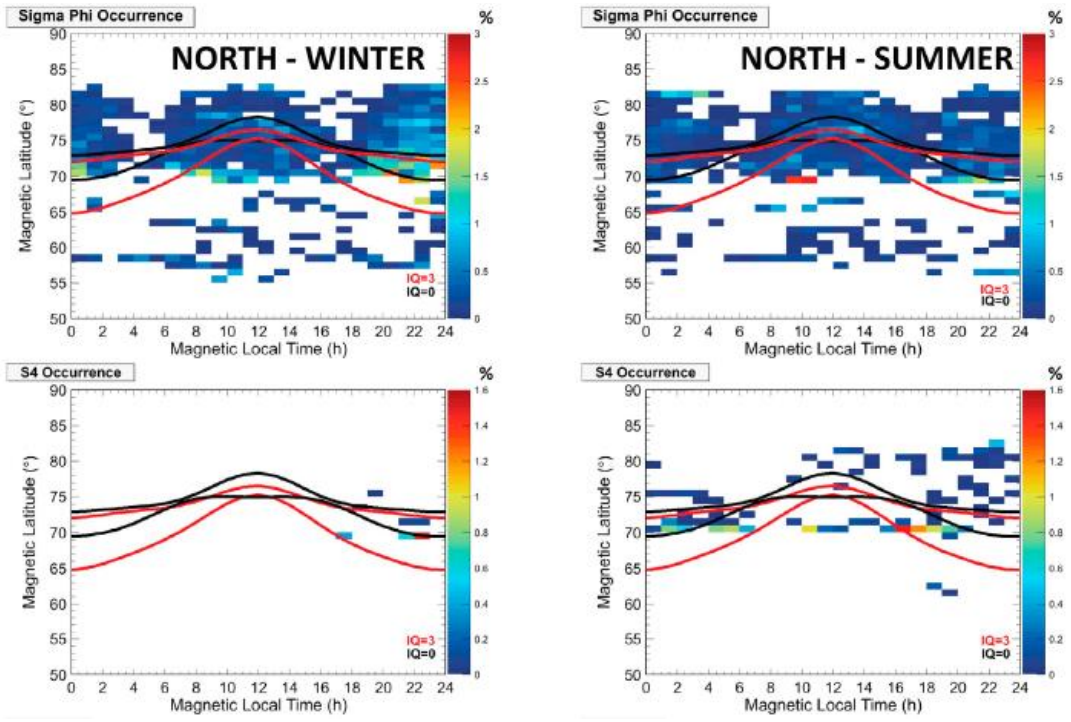

b)

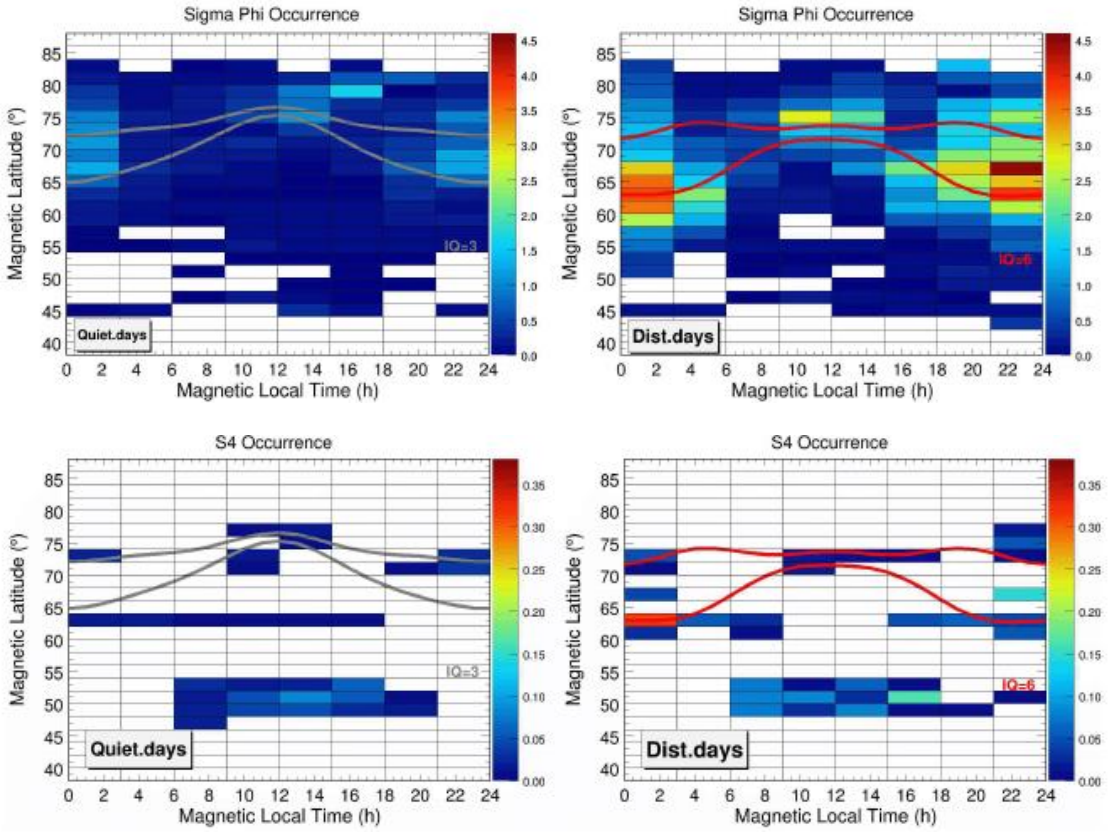

Figure 2.5-10: a) The percentage occurrence of phase scintillation (top) and amplitude scintillation (bottom) for winter and summer during solar minimum. Adapted from: Alfonsi et al. [2011]. b) The percentage of occurrence of phase scintillation (top) and amplitude scintillation (bottom) for quiet (grey Feldstein oval) and disturbed (red Feldstein oval) days during fall and winter at solar maximum. Adapted from: Spogli et al.[2009].

In order to minimize errors in positioning and velocity data, there are different filtering techniques applied to the signal within the GPS-receiver. Normally, a 6-th order Butterworth filter with 0.1 Hz cut-off is used to remove the low frequency parts of the carrier signal [Niu et al., 2012]. However; several authors have pointed out that the phase scintillation sigma-phi index is too sensitive to de-trending [e.g. Beach, 2006; Mushini et al., 2012, Prikryl et al., 2011,2013]. At high latitudes the Butterworth filter has a tendency to overestimate the phase scintillation in comparison with amplitude scintillation. Since phase scintillation may take place for irregularities of all scale sizes, there should be additional amplitude scintillation present when irregularities are small, that will correlate well with the phase fluctuations. According to observations, this is not the case. On the contrary it is common to register phase scintillation without amplitude scintillation. This phenomenon might be caused by a poor de-trending, rather than too weak scattering [Mushini et al., 2012]. By using a higher cut –off frequency and a wavelet filter instead of the Butterworth filter. Mushini et al., [2012] managed to improve the sigma-phi index and the correlation between the phase scintillation and amplitude scintillation indices. Other authors have also introduced alternative indices to complement the sigma-phi index for the same purpose [see e.g. Forte in Béniguel et al., 2009 or Prikryl et al., 2013].

a) 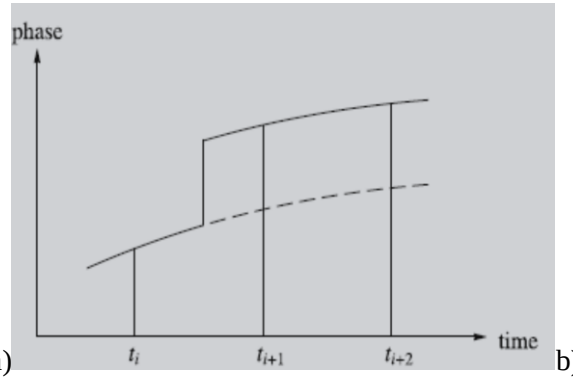

b) 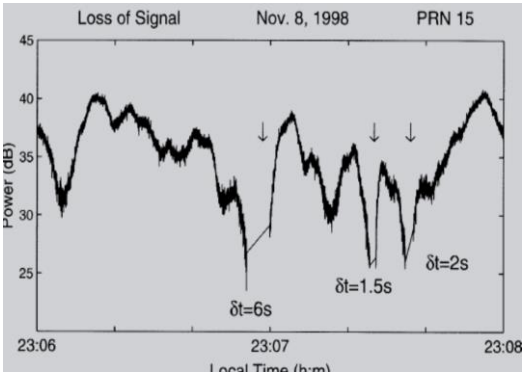

Figure 2.5-11: a) A schematic illustration of cycle slip. Carrier phase makes a sudden jump over one or more cycles depending on accumulated phase. Figure taken from: Hofmann-Wellenhof, Lichtenegger and Wasle [2008]. b) Power fades in GPS signal from satellite PRN 15. The deep fades cause loss of lock. From Kintner and Ledvina [2005].

Consequences of scintillations are related to the performance of the communication between satellite and receiver. Amplitude scintillation can cause deep fades in the signal power, even below the receiver threshold [Alfonsi et al., 2011]. Consequently; the receiver may lose lock on the satellite, because the signal power is too weak (high signal to noise ratio, SNR). In order to track the satellites, the receiver must acquire the broadcasted signal on one or both carrier bands. L_2 has a lower power than L_1, which makes it harder to track. If a power fade happens during acquisition, the whole process must start over. For short fades re-acquisition is easier, because previous data may be used as the navigation message is valid for a couple of hours. The receivers use tracking loops to measure variations in amplitude and phase of the carrier. A phase lock loop (PLL) with a variable bandwidth is capable of tracking both phase and carrier for even weak signals. This is an advantage in high latitudes because a permanent low bandwidth, although it is better to prevent loss of lock, causes an under-sampling of the phase fluctuations [Skone et al., 2005; Kintner et al., 2007]. Figure 2.5-11b) illustrates signal power fades that cause loss of lock on satellite signal over a two minute interval. The deepest fade (> 10dB) lasted for six seconds, which is harmless in most cases [Kintner and Ledvina, 2005].
In section 2.5.1 cycle slips were mentioned. Cycle slips are usually dealt with in signal processing, however scintillation is difficult to account for [Hoffman-Wellenhof, Lichtenegger and Wasle, 2008]. In the scintillation case, cycle slips take place when the receiver fails to detect the rapid fluctuations in the carrier phase. Thus in severe situations the receiver may completely lose lock on the satellite signal. The carrier phase jumps over one or more cycles, as illustrated in Figure 2.5-11a) [Seeber, 2003]. When the PLL fails to detect a phase shift it can also result in a half-cycle slip [Humphreys et al., 2010]. The time of exposure to scintillations is of great importance as well. If the receiver is influenced by long perturbation time scales, it is more likely to lose lock. Moving receivers are more sensitive to this than stationary because the ionospheric disturbances may drift along with the receiver motion and prolong the effect of the perturbation exposure. Alternatively; the satellite can "follow" the patch. Figure 2.5-12 can illustrate this scenario. Actually this figure depicts a method of determining the drift velocity of the scintillation intensity pattern on the ground by comparing the drift speed of the ionosphere and the IPP of the satellite signal [Kintner et al., 2001].

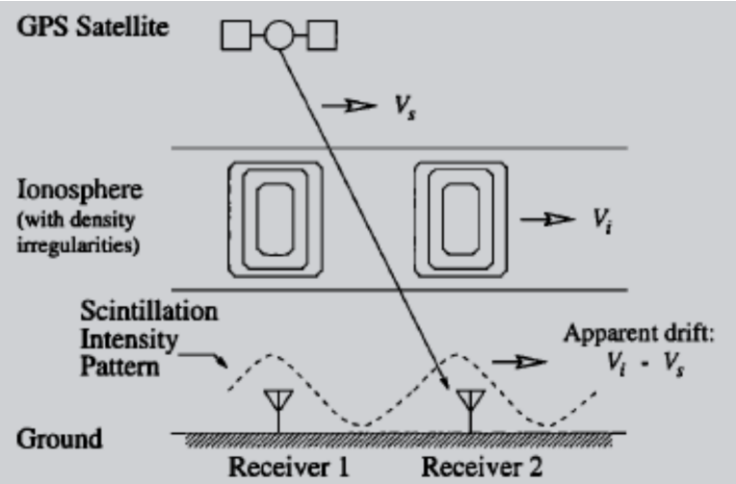

Figure 2.5-12: The apparent drift of the scintillation intensity pattern on ground is the difference in satellite IPP speed and ionospheric drift speed. This figure also illustrates that either the satellite IPP or a mobile receiver on ground can drift along with the ionosphere (patch) prolonging the scintillation effect. Figure adapted from: Kintner et al. [2001].

To summarize what we have learned so far, the ionospheric irregularities form in boundary regions between higher and lower TEC, which can be caused by patches, blobs or precipitation. Drift mechanisms and gradients contribute to instabilities and further structuring of the dense plasma. These smaller scale irregularities lead to refraction and diffraction of the radio waves which propagate through the medium. The interference cause rapid fluctuations in the amplitude and phase of the diffracted wave, so-called scintillation. The consequences are positioning errors and, in the worst case, loss of signal and eventual tracking.

2.5.4 The Norwegian Mapping Authority (NMA)

The Norwegian Mapping Authority (NMA) dates back to 1773 and it is responsible for administration, development and surveillance of geodetic data in Norway. The Geodetic Division runs the positioning service CPOS from the control center at the main office in Hønefoss (~60ºN, 10ºE). Among the tasks of the control center are production and distribution of correction data to reference stations and users, and performance monitoring with respect to technical issues and space weather [www.kartverket.no, 2013]. The GNSS reference stations are located on stable bedrock or concrete and distributed in a network all over Norway including Svalbard and Iceland. This network is called SATREF (Satellite based Reference system) and has been in operation since 1989. As of today there are 160 permanent geodetic stations with a typical interstation distance of 50-60 km. They are used for determination, maintenance and contribution of the reference frame. The raw data is transmitted to the control center in Hønefoss which re-distributes and archives it for post processing [Jensen et al., 2007, 2008; Jacobsen and Schäfer, 2012]. Figure 2.5-13a) is a map over the SATREF reference stations in Norway. In Figure 2.5-13b) the stations with the orange circles are the stations concerned in this thesis.

a) 

b) 

Figure 2.5-13: a) Overview of the reference stations in Norway. Station on Iceland is omitted. b) The five reference stations in Southern Norway used in this thesis are encircled. In addition the control center in Hønefoss is encircled. It is located within the circle north west of Oslo. Figures are adapted from: *www.Kartverket.no.*

From 1999 the NMA began providing real time kinematic (RTK) services [Jensen et al., 2007, 2008]. RTK-positioning uses both code-and-phase measurements, either separately or in combination [Seeber, 2003]. As we recall, phase measurements are more accurate than code, but they are more sensitive to multipath and so-called dilution of precision (DOP). The visibility of the satellites is defined as "the unobstructed line between receiver and satellite" [Hoffman-Wellenhof, Lichtenegger and Wasle, 2008]. Since roving receivers and satellites are moving relative to one another, the geometric constellation, and hence the visibility, are constantly changing. The instantaneous geometry is called the dilution of precision [Hoffman-Wellenhof, Lichtenegger and Wasle, 2008]. DOP is the ratio between the standard deviation of the range, σ_r, and the standard deviation of positioning, σ_p.

$$DOP = \frac{\sigma_r}{\sigma_p} \qquad (2.75)$$

Geometric DOP (GDOP) is a combination of position and time, given by:

$$GDOP = \sqrt{(PDOP)^2 + (TDOP)^2} \qquad (2.76)$$

PDOP consists of horizontal and vertical dilution of precision, HDOP and VDOP, and is therefore used in 3D-postioning [Seeber, 2003]. Since phase based measurements are the most sensitive to variations in visibility and signal strength, the PDOP has to be smaller than 4.0. A PDOP larger than 8.0 gives poor accuracy, while a PDOP in the range between 4.0 and 8.0 is acceptable [STD-SAT, 2009].

The RTK- service CPOS is based on phase measurements to provide centimeter accuracies. DPOS is a similar RTK-service which delivers decimeter accuracies. The lesser requirements in accuracy, allows the use of code based measurements instead of phase measurements, hence the service is less sensitive

to multipath and scintillation effects [STD-SAT, 2009; Jacobsen and Schäfer, 2012; www.kartverket.no, 2013].

Ionospheric models are not necessarily accurate enough to estimate disturbances in high latitudes. For instance, the international reference ionosphere model by Bilitza, D. from 2001 (IRI2001), does not account for the patch drift in polar latitudes [Moen et al., 2008 and references therein]. In 2007 Jensen et al. [2007, 2008] developed a regional ionosphere model based on the SATREF network. This model gives the delay on L_1 as output for a distinct location or for a grid network. The aim of the model was to monitor the ionospheric activity at high latitudes along with the EGNOS ionosphere model performance at high latitudes. The EGNOS model has a poor availability in high latitudes during geomagnetic storms [Jacobsen and Schäfer, 2012]. The SATREF model was also compared to the IGS Global Ionosphere Model (GIM), and it proved that for high latitudes the SATREF ionosphere model was slightly more accurate [Jensen et al., 2008].

The work on improving models continues, and now the NMA has developed a real time ionosphere monitor (RTIM) to improve the ionospheric surveillance at high latitudes. The RTIM monitors the ionospheric activity based on received dual frequency code and phase measurements from the whole SATREF network, and the NMA provides data plots of VTEC, ROTI and large scale gradients with a five minute resolution. [Jacobsen and Schäfer, 2012; sesolstorm.kartverket.no, 2013].

Jacobsen and Schäfer [2012] studied the CPOS performance during a geomagnetic storm on October 24-25; 2011.They found that the RTK-service was strongly affected by the increased ionospheric activity, especially in latitudinal localized region. This proved to be co-located with the auroral electrojets, which had moved equatorwards during the ongoing disturbance. Other regions thus remained unaffected. This is illustrated in Figure 2.5-14 which shows the plots made by the RTIM and the Trimble software. As we can see, the increased VTEC and ROTI plots correlate well with the red dotted SATREF stations where the CPOS service was affected.

The RTIM makes surveillance in high latitudes much easier, and with the installation of a scintillation receiver network (RTIS), the ability to monitor ionospheric TEC variation also at scintillation causing scales. The scintillation receivers will be integrated in 2013 and 2014 [Hanssen, 2013].

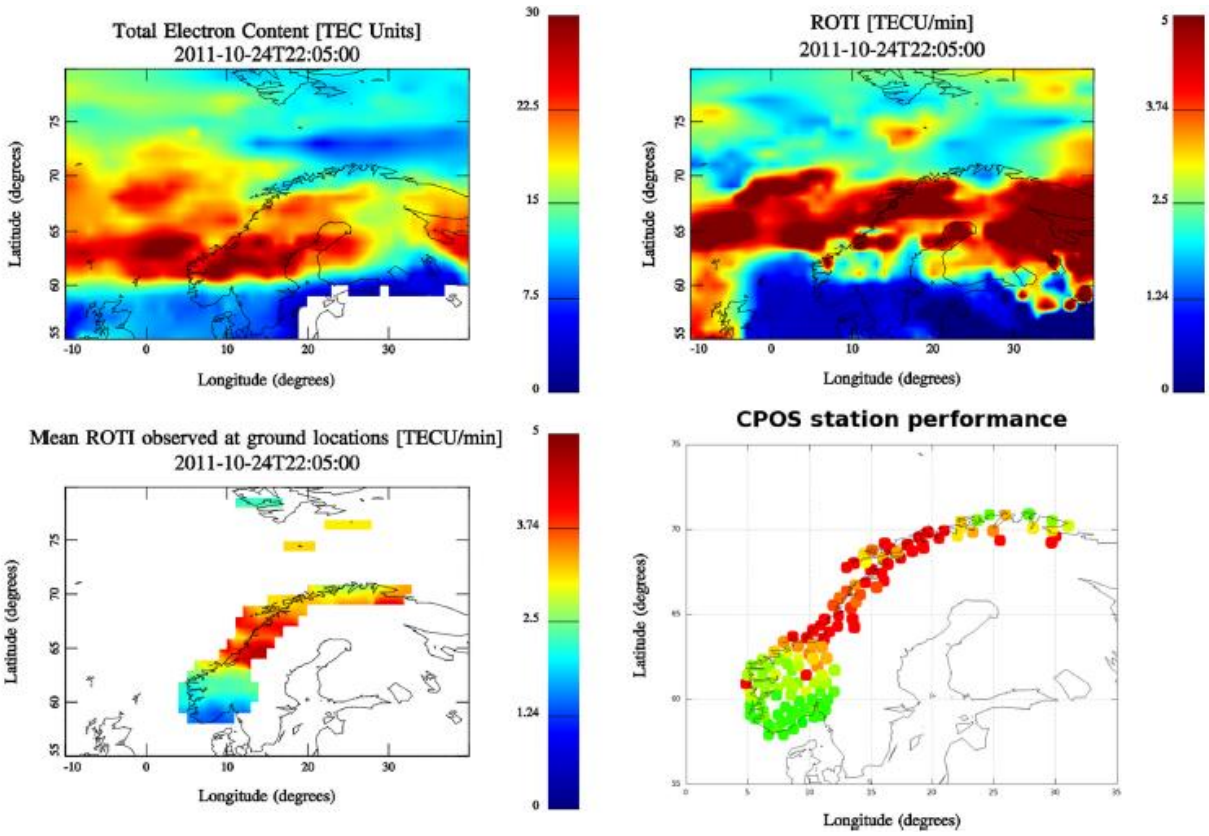

Figure 2.5-14: Top row: illustrates the ionospheric VTEC and ROTI at 350 km altitude. The irregularities are concentrated in a latitudinal belt over Mid-Norway. Bottom row: reveals the ROTI on ground and the CPOS performance. The red dots in the CPOS plot reveal the strongest affected stations, and correlate with the disturbed regions in the RTIM plots. Figure adapted from: Jacobsen and Schäfer [2012].

3 Instruments and methods

The superstorm event on November 20, 2003 has been investigated by several authors and the instrumentation and methods they have used would be too extensive to describe. Thus I will only give an overview of some of the most important instruments concerning forecasting, and the instruments I have used data from. In the next sections I distinguish between space based measurements and ground based measurements. In the last section I will give a brief outline on the work done in MATLAB.

3.1 Satellites

Satellites which are used for studying the Sun and solar wind are placed in orbits in the upstream solar wind path between the Sun and the Earth. In order to maintain a space craft in a stable position, it has to be placed in one of the so-called Lagrangian points. These positions are named after the French-Italian mathematician Joseph Louis Lagrange, who in 1772 showed that there must exist five libration points within the joint gravity field of a two-body system. A third body, if its mass is comparably smaller than the mass of the two other objects, can be held in a stable position within this gravitational equilibrium region (aka a restricted three body problem). Three of the Lagrangian points, designated L1, L2 and L3, lie along the straight line conjoining the massive objects. The last two are co-linear quazi-stable points located on either side of the line making up two equilateral triangles with the two massive bodies. Figure 3.1-1 shows the geometry of the Lagrangian points of the Sun-Earth system. In 1964 Farquhar, R. suggested that L1 could be an ideal location for a space solar observatory; however this did not become a reality before the initiation of the ISEE-program (International Sun-Earth Explorer) in 1972. There are two satellites situated in L1 that have provided data for the studies in this thesis; the SOHO-satellite which was launched into a halo-orbit around L1 in 1996 and the ACE satellite which was launched in 1997 (Lissajous-orbit) [Dunham and Farquhar in Gomez, Lo and Masdemont, 2003]. Note: The distance between the Sun and Earth is 1AU, $\sim 1.5 \cdot 10^8$km. The distance between L1 and the Earth is $\sim 1.5 \cdot 10^6$km. The distance between L1 and the Earth is so much smaller in comparison with the distance to the Sun, thus the location of L1 is sometimes approximated to be at 1AU.

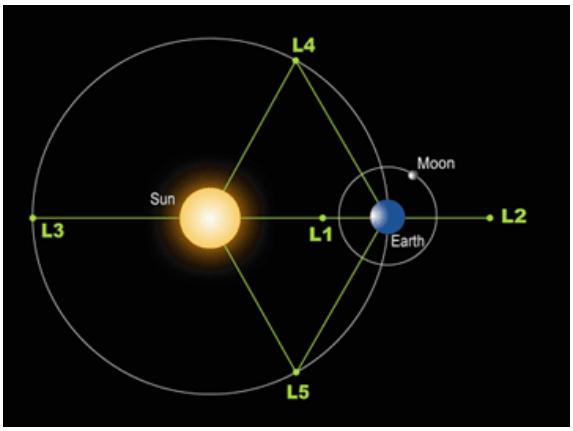

Figure 3.1-1: The five libration points of the Sun-Earth system. Image from: *http://www.onr.navy.mil/focus/spacesciences/satellites/orbit2.htm*

Satellites used for observations of the Earth, are placed in orbits around the Earth. The altitude of the satellite dictates the rotation period and thus the choice of satellite orbit depends on the purpose of the satellite mission. Satellites with the highest altitudes are often so-called geostationary (GEO) satellites. These orbits have an altitude of ~36,000km and a period of 24 hours enabling to co-rotate with the

Earth and continuously observe the same location. Medium Earth orbits (MEO) have an altitude of approximately 20,000 km and roughly 12 hour orbital period. The GPS-satellites are an example of MEO-satellites. Low Earth orbits (LEO) are mainly used for Earth observations. They occupy an altitude around 800 km and have orbital periods of ~100 min. LEOs are often in sun synchronous polar orbits, which allows them to pass over a location at the same local time every day. Polar orbits are either in noon-midnight or dawn-dusk directions. The ground coverage for polar orbits increases with increasing latitude, making it ideal for Earth observation at higher latitudes. In addition to altitude, orbits are also classified by their eccentricity and inclination with respect to the equatorial plane [Weydahl,D.J., 2009]. GPS-satellites have a 55º inclination in order to ensure coverage of the polar regions [e.g.Hofmann-Wellehof, Lichtenegger and Wasle, 2008]. Highly elliptical orbits (HEO) have large inclinations, thus a satellite in apogee will look down on a fixed position for a long period of time. This could be an advantage over LEOs in the polar region [Trishchenko and Garand, 2012]. Figure 3.1-2 illustrates different types of satellite orbits around the Earth.

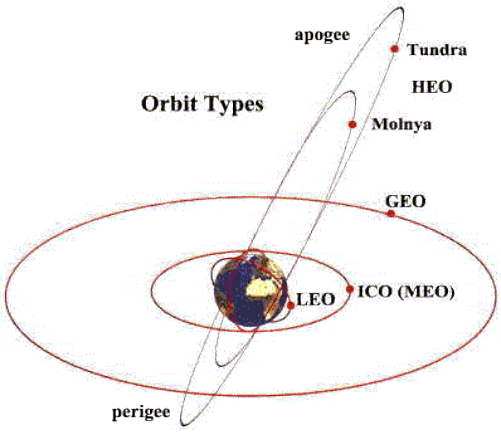

Figure 3.1-2: Different orbits used for satellites orbiting the Earth. Tundra and Molnya are HEO orbits, while the others are circular orbits with different altitudes above the Earth's surface. Image from : *http://www.geo-orbit.org/sizepgs/geodef.html*

3.1.1 Satellites in L1-SOHO and ACE

The Solar and Heliospheric Observatory (SOHO) is an international collaboration project between the European Space Agency (ESA) and the National Aeronautics and Space Administration (NASA) with the mission objective to study the Sun. SOHO was launched in December 1995 and is still operative. All the original12 instruments on board were developed by US and European scientists and investigations are led by Principals Investigators (PIs) from US and Europe [http://sohowww.nascom.nasa.gov/about/about.html, 2014].
Three of the instruments onboard SOHO were used by authors who investigated the solar source of the superstorm, e.g. Gopalswamy et al. [2005a]. These instruments provide measurements which enabled them to study the development and parameters of magnetic and coronal features.

3.1.1.1 Michelson Doppler Imager (MDI)

The MDI-probe used for observation and investigation of the Solar Oscillations Investigations (SOI) project at the Stanford University, USA until 2011 [soi.stanford.edu, 2014]. The MDI-probe consists of a refractive telescope with cascading narrow filters. Two tunable Michelson interferometers filters light with a 94mÅ bandpass, allowing only light centered five wavelengths around the Ni 6768Å

absorption line to be recorded. The images are captured by a 1024x1024 pixel CCD-camera. The MDI instrument makes measurements of the Doppler velocity and the magnetic field in the photosphere. Helioseismic studies help shed light upon the development of the solar cycle, the convective flows and active regions. Every minute, during its operation, the MDI made Doppler velocity and continuum intensity images of the entire solar disk, which were downloaded and investigated by SOI [Scherrer et al. 1995; soi.stanford.edu, 2014]. Figure 3.1-3 shows a magnetogram and an intensitygram from the morning of October 28, 2003. The white spots in the magnetogram shows magnetic structures of positive polarity, whereas the black, are magnetic structures with a negative polarity. In the intensitygram (without limb darkening), the sunspots are visible on the solar disk.

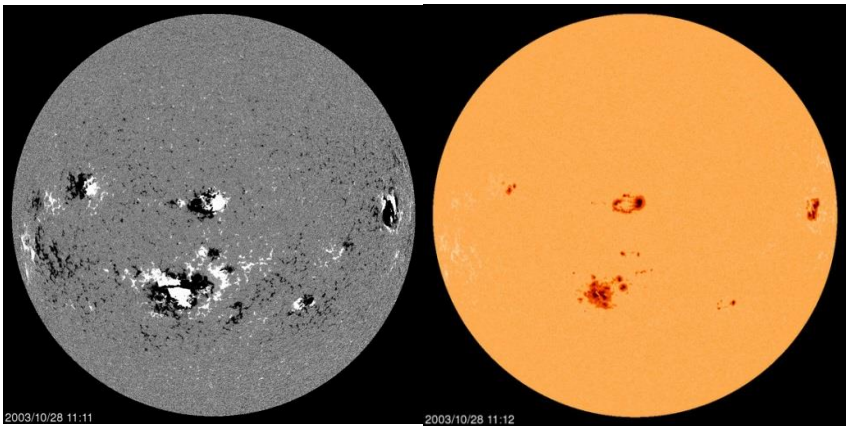

Figure 3.1-3 Left: A magnetogram revealing magnetic structures of opposite polarities. Right: An intensitygram showing sunspots on the solar disk. Both images are taken with the MDI-instrument onboard SOHO on October 28, 2003. Credit: SOHO/NASA/ESA.
(*http://sohodata.nascom.nasa.gov/cgi-bin/data_query)*

3.1.1.2 Large Angle Spectrometric Coronagraph (LASCO)

This instrument was built by collaboration of four European and US institutions, where three of them were responsible for each of the coronagraphs. LASCO consists of three coronagraph telescopes with overlapping field of view (f.o.v.) to ensure capture of the whole corona (both inner E-corona and outer K-corona)[1]. A coronagraph has an occulting disk in the focal plane, thus the f.o.v. are divided into concentric annular rings. C1 is the inner mirror version of the Lyot coronagraph with internal occultation and a Fabry-Perot interferometer. The f.o.v. of C1 covers the solar corona from 1.1-3.0 solar radii. The interferometer provides monochromatic spectrograms by scanning the wavelength in vicinity of the spectral lines of Fe XIV,X, Ca XV, Na I, Hα and white light. The interferometer is used as a 0.07nm bandpass filter which can block each of the spectral lines, but the selected one. The line profiles are used to derive bulk velocities, Doppler shifts and magnetic field configurations. Max Planck Institut für Aeronomi (MAPe), Germany was responsible for the design of C1 [Brueckner et al.,1995; lasco-www.nrl.navy.mil,2014]. Unfortunately, the C1 coronagraph stopped working after the incident with loss of contact with SOHO in 1998 [David, L., 1999].
The C2 and C3 coronagraphs make up the outer annular rings of the telescope. They both have external occulter and their f.o.v. overlap. The C2 has a f.o.v. covering 2.0-6.0 solar radii and C3 overlaps from 3.7-32 solar radii. The Laboratoire d'Astronomie Spatiale (LAS), France, was

[1] E-corona is the inner part of the corona recognized by ion emission lines, whereas the K-corona is due to scattering of light by free electrons, which gives a continuous spectrum. F-corona is scattered light due to dust particles and gives rise to the Fraunhofer absorbtion lines. (http://science.gsfc.nasa.gov/671/staff/bios/cs/Nelson_Reginald/Chapter1.pdf)

responsible for the C2 coronagraph, and The Naval Research Laboratory (NRL), US, was responsible for the C3 coronagraph and the interferometer, and is the PI-institution. In addition, the University of Birmingham contributed to the design and building of the telescope. All three coronagraphs use the same 1024x1024 CCD camera for recording images [Brueckner et al., 1995; lasco-www.nrl.navy.mil, 2014]. Figure 3.1-4 shows images taken by the C2 and C3 coronagraphs in the afternoon October 28, 2003.

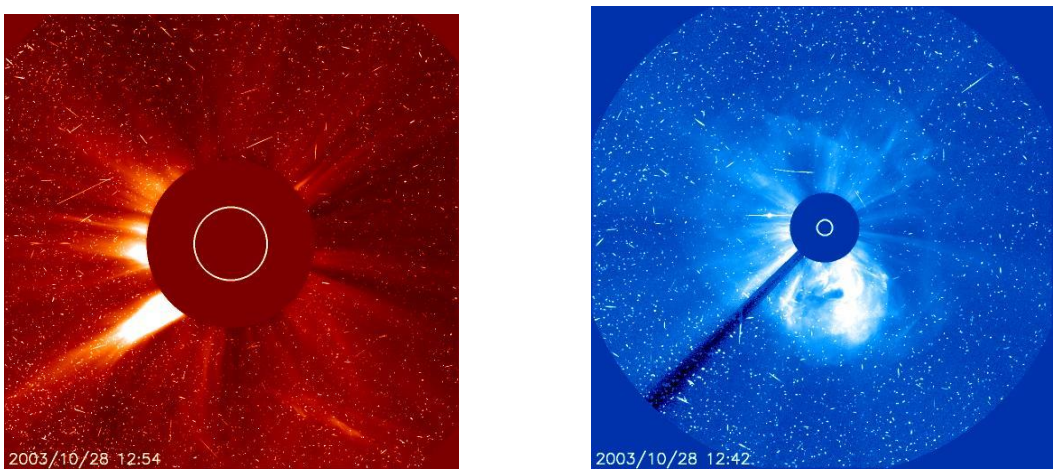

Figure 3.1-4 Left: Image taken with the C2 camera of the solar corona in the afternoon October 28, 2003. Right: image taken with the C3 camera from the same day. Notice the different sizes of the occultating disks in the two images. Credit: SOHO/NASA/ESA, (*http://sohodata.nascom.nasa.gov/cgi-bin/data_query).*

3.1.1.3 Extreme Ultraviolet Imaging Telescope (EIT)

This telescope provides full disk images of the solar transition region and inner solar corona to ~1.5 solar radii. The aim of this instrument is to better understand the coronal heating mechanisms and the acceleration of the solar wind. The telescope optics is a Ritchey Chretien design and has multilayered coatings applied on the telescope mirrors to select distinct emission lines. The f.o.v. is divided into 45x45 arc minute quadrants making it possible to tune in the coatings of each quadrant into desired wavelengths in order to derive the temperature range. Each quadrant forms a full image on the 1024x1024 CCD. Table 3.1-1 lists the EIT spectral lines and their associated temperature ranges along with their characteristic features. EIT shares the electronic and computer compartment with LASCO, thus the three LASCO telescopes and EIT are operationally viewed as a single instrument package [Delaboudinière et al., 1995]. EIT was designed by the consortium of five French and Belgic institutions along with three from the US. EIT was operated by the NASA Goddard Space Flight center (NGSFC) until 2010 when its role was replaced by the Solar Dynamics Observatory (SDO) Atmospheric Imaging Assembly (AIA). Fortunately for LASCO; the whole telemetry bandwidth is now available to improve the capacity [http://umbra.nascom.nasa.gov/eit/,2014]. Figure 3.1-5 shows the same image taken at different wavelengths by the EIT on October 28, 2003.

Spectral ion	Wave length (Å)	Temperature (K)	Features
He II	304	$8 \cdot 10^4$	Chromospheric network, coronal holes
Fe IX, X	171	$1.3 \cdot 10^6$	Corona/transition region boundary, structures inside coronal holes
Fe XII	195	$1.6 \cdot 10^6$	Corona outside holes, quiet corona
Fe XV	284	$2.0 \cdot 10^6$	Active regions

Table 3.1-1 The EIT bandpasses with their associated wavelength and temperature. Adapted from: Delaboudinière et al. [1995].

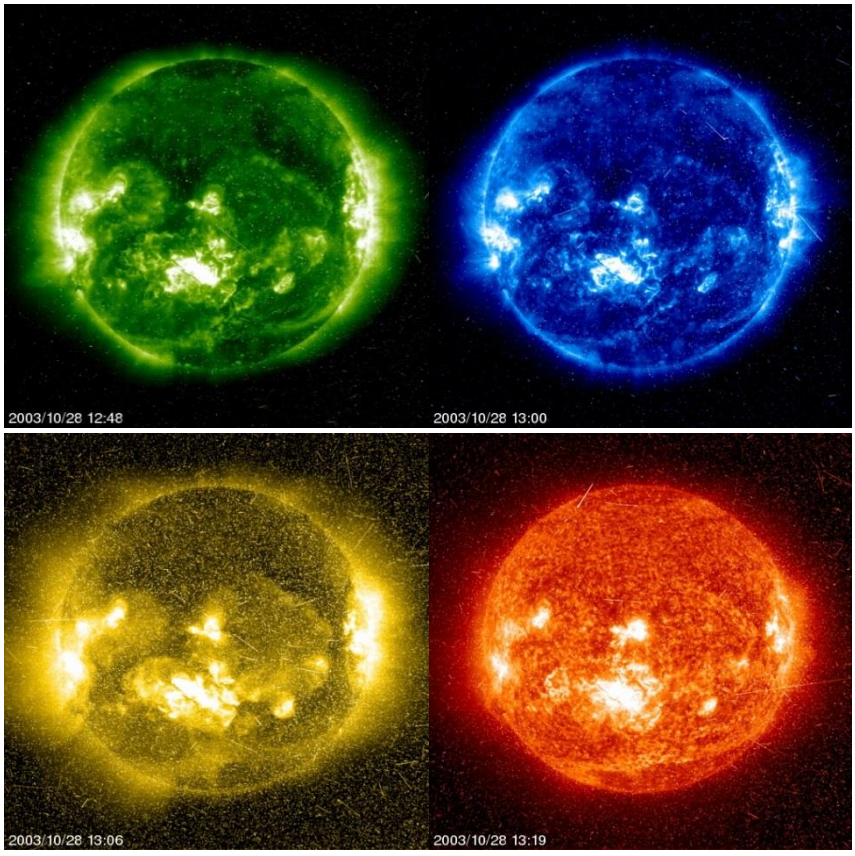

Figure 3.1-5: Images taken with different filters. The green image is the 195Å band, revealing the quiet corona, whereas the blue image is taken in the 171Å band. This image reveals the structures within the corona. The yellow image is the 284Å band and highlights the active regions in the solar disk. The final image is the 304Å band which shows the locations of the coronal holes. All images are taken around noon on the October 28, 2003. Credit: SOHO/NASA/ESA

All the SOHO-data is downlinked to the Deep Space Network (DSN) which is a worldwide antenna network used for communication with space probes. This network has a busy schedule, thus SOHO has not a 24 hour contact with Earth. This means that during the time of contact both the stored data and the real-time data is downloaded instantly. The data is handled chronologically starting with the oldest stored data, therefore the real-time data has a latency of about 3 hours including the one hour telemetry buffer [Haugan, S.V.H., private communication, 2014; lasco-www.nrl.navy.mil, 2014].

3.1.1.4 The Advanced Composition Explorer (ACE)

In addition to SOHO, the ACE-satellite is also placed in orbit around L1. It was developed by the John Hopkins University Applied Physics Laboratory (JHU/APL) and launched in 1997 with the aim to study the parameters of particles of solar and galactic source including the interplanetary environment. ACE carries 6 high resolution spectrometers and 3 monitoring instruments which are available in near real time. The spectrometers measure particle parameters from galactic/cosmic rays as well as the solar wind. The instruments monitors the state of the interplanetary medium hereunder the IMF. Thus the ACE satellite is ideal for monitoring the solar wind and IMF with respect to forecast space weather. The National Oceanic and Atmospheric Administration (NOAA), utilizes the satellite data from ACE for this purpose and has a 24 hour contact with the satellite to access real time data. Data is downlinked to a worldwide NOAA-operated network of antennas for approximately 21 hours a day in addition to the 3 hours of contact with DSN. NOAA Space Weather Operations in Boulder, Colorado process and uploads the real time data on their forecast website (http://www.swpc.noaa.gov/ace/) continuously [Stone et al. 1998; Chiu et al., 1998; Zwickl et al., 1998].
In this thesis I have used data from ACE SWEPAM and MAG to plot the solar wind and IMF parameters, and compute the propagation delay of the solar wind to the magnetopause.

3.1.1.5 Solar Wind Electron Proton Alpha Monitor (SWEPAM)

The aim of the SWEPAM experiment is to conduct measurements of the solar wind composition in the studies of solar wind phenomena [McComas et al.,1998].There are two monitors; the SWEPAM-I and SWEPAM-E and their associated sensors and housekeeping. The energy per charge analyzers provide plasma measurements of solar wind particles in three dimensions with a 64s time resolution. In the SWEPAM-I analyzer, ions arriving at all polar angles as the spacecraft spins, are bent with a 5º polar angle separation (to maximum 105º) in order to measure their energy per charge. There are 16 channel electron multiplier (CEM) detectors which counts the different ions in their energy ranges from 260 eV -36 keV. The SWEPAM-E has a similar analyzer with a maximum bending angle of 120º. Electrons entering at different polar angles normal to the space craft's spin axis, are counted in 7 CEM detectors within the range of 160 eV -1350keV. The SWEPAM instruments are enhanced spares from the SWOOPS instrument from the Ulysses mission. In e.g. the electronics are enhanced in order to provide real time telemetry of the particle distributions [McComas et al.1998; www.srl.caltec.edu/ACE, 2014].

3.1.1.6 MAG

The MAG instrument was built by collaboration of the Bartold Research Institute, University of Delaware and the Laboratory for Extraterrestrial Physics at GSFC. It consists of a pair of tri-axial Fluxgate magnetometers located on each boom of the space craft. They continuously measure the vector magnetic field of the IMF as the space craft rotates within the interplanetary medium. The measurements are provided to NOAA with a 1s time resolution. The aim of the MAG experiment is to shed more light upon the temporal variations in the IMF [Smith et al.,1998; http://www.ssg.sr.unh.edu/mag/ACE.html]. Figure 3.1-6 illustrates the exploded view of the ACE spacecraft with indexed instruments.

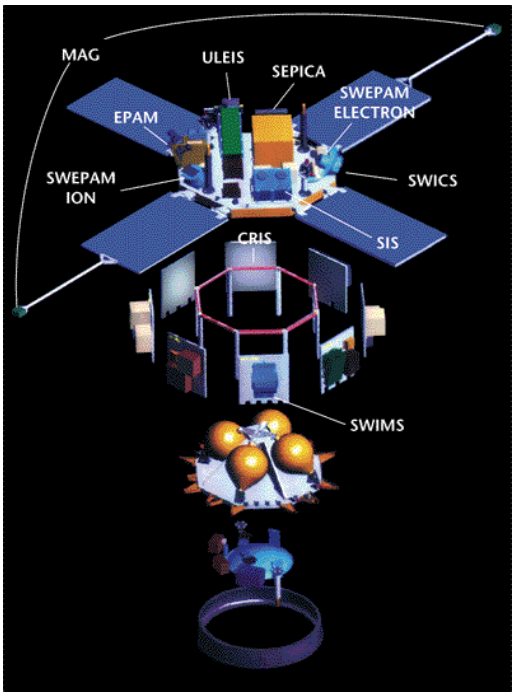

Figure 3.1-6: The exploded view of the ACE spacecraft. The SWEPAM monitors are located on either side of the centerpiece, the magnetometers are located on each end of the space craft booms. Image from: *http://www.ssg.sr.unh.edu/mag/ACE.html*

3.1.2 Earth Orbiting Satellites

In this section I will only give a brief description of the DMSP-satellites which instruments have, and still contribute to the space weather research.

3.1.2.1 Defense Meteorological Satellite Program (DMSP)

The DMSP is a Department of Defense program which was initiated in 1965. Its primary goal was to provide meteorological observations and forecasts for military purposes. Today it is managed by the US Air Force Space and Missile Systems Center (SMC) at Los Angeles Air Force base, and controlled by the NOAA National Geophysical Data Center (NDGC) Earth Observation Group (EOG) [www.losangeles.af.mil, 2014; ngdc.noaa.gov/eog/dmsp, 2014].The instruments onboard the DMSP-satellites provides global meteorological and oceanographic data, as well as solar-terrestrial data All the satellites are LEOs with a mean altitude of ~830 km and an orbital period of 101minutes. The orbits are sun-synchronous near polar orbits with a 3000 km swath footprint which ensures global coverage twice each day. There are at least two satellites in operation at any given time and they are either in a dusk-dawn or day-night directed orbit [ngdc.noaa.gov/eog/dmsp, 2014; cindispace.utdallas.edu/dmsp, 2014]. Since the beginning, there have been several satellites within the program, and all satellites from each block are successive numbered from F1. Today block 5D is in operation [space.jpl.nasa.gov/msl/Programs/dmsp, 2003].

The space environment research instruments onboard the satellites are designed to measure plasma composition, densities, drift velocities and magnetic field. The SSIES (Special Sensor-Ions, Electrons and Scintillation), is an instrument package built by the Center for Space Sciences at University of Texas. It consists of a scintillation monitor, drift meter, Langmuir probe and potential analyzer, and the objective is to measure the particle densities, plasma temperature and plasma flow. The SSJ4 is built by the US Air Force Research Laboratory, Space Vehicles Directorate (SVD). It is a spectrometer which measures the flux of precipitating ions and electrons in the energy range from 30

eV to 30 keV. SSM is a tri-axial fluxgate magnetometer built by SVD and the NASA GSFC. Its purpose is to measure the variations in the geomagnetic field and ionospheric currents. There are more instruments that have been incorporated in the latest satellites along with updated versions of the mentioned sensors, but I will not describe them further [ngdc.noaa.gov/eog/dmsp, 2014; cindispace.utdallas.edu/dmsp, 2014].

The DMSP-data have been widely used in space weather research. In this thesis, I refer to the work of Foster et al. [2005] who used the DMSP cross track plasma drift to emphasize the flow direction of the plasma (see Figure 3.1-7)). The OVATION maps in section 4.3.2 are based on particle fluxes from the SSJ4 instruments to derive the boundaries of the auroral oval [e.g. Sotirelis et al., 1998]. Figure 3.1-7b) shows a spectrogram of the particle flux and temperature which can be used to determine the precipitation boundaries. Data from the SSIES-instruments are available from the homepage of University of Texas Coupled Ion Neutral Dynamics Investigation group (cindispace.utdallas.edu). Data from the SSJ4/5 are available at the homepage of the Coupling, Energetics and Dynamics of Atmospheric Regions (CEDAR), (http://cedarweb.hao.ucar.edu/wiki/index.php/Main_Page) or from the OVATION homepage (http://sd-www.jhuapl.edu/Aurora/spectrogram/spectrogram_displays.html).

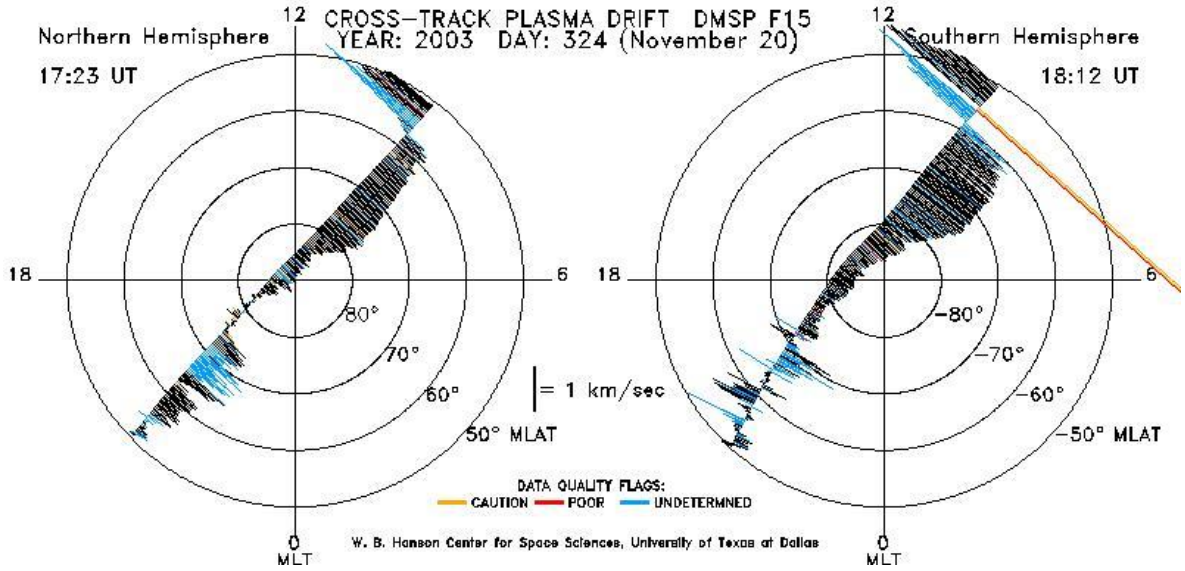

a)

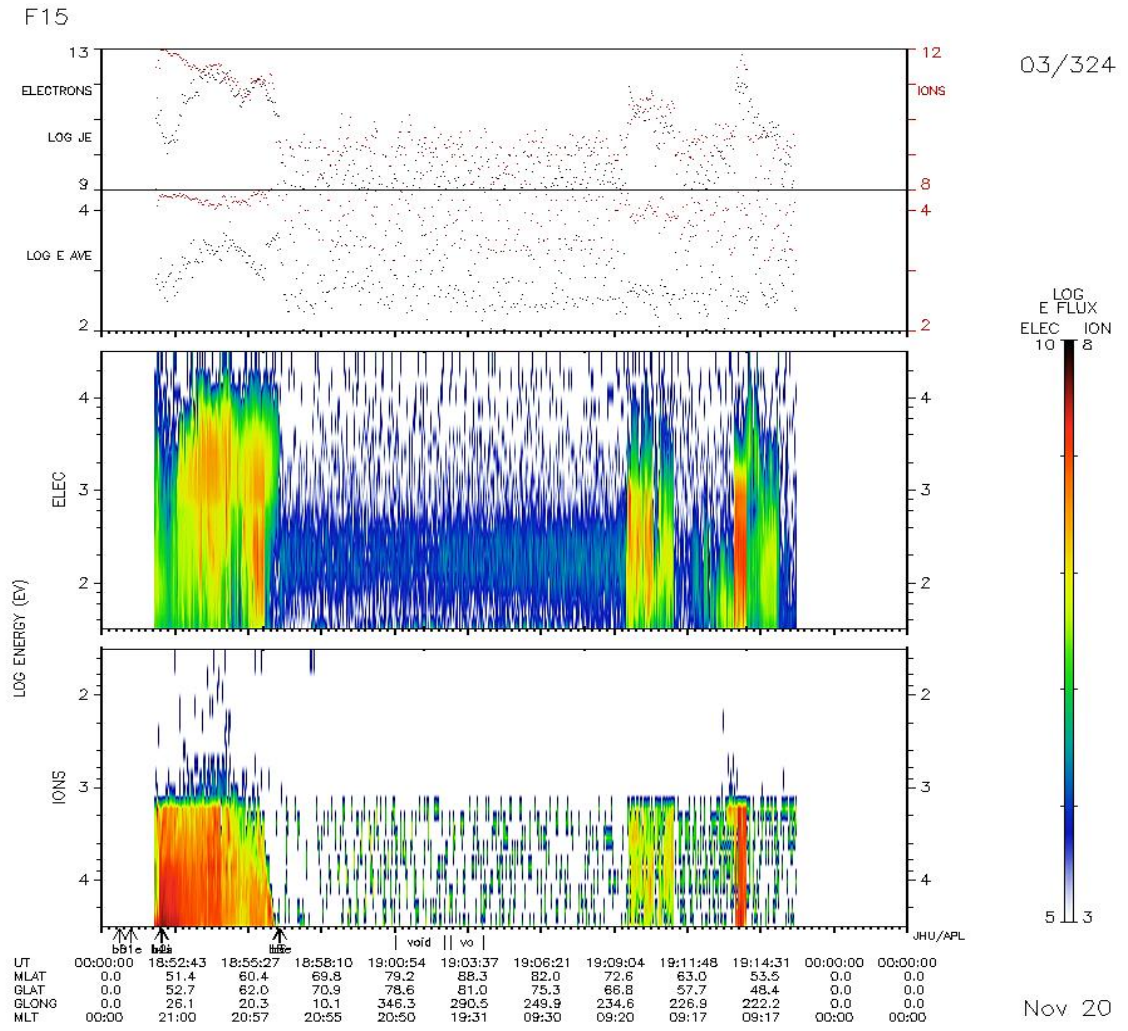

b)

Figure 3.1-7: DMSP-plots: a) Cross track ion drift measured by the F-15 satellite on its pass in the evening Nov. 20, 2003. b) spectrogram showing the electron and ion energy flux at the precipitation boundaries. Plot a) is downloaded from *cindispace.utdallas..edu*, plot in b) is downloaded from the OVATION homepage at *sd-www.jhual.edu/Aurora/spectrograms*.

3.1.3 OVATION

The (Auroral) Oval Variation Assessment, Tracking, Intensity and Online Now casting tool is meant for quick determination of the location of, and the precipitation intensity within the auroral oval. This is one of many models for locating the auroral oval boundaries and was developed through a collaboration project between scientists from John Hopkins University/ Applied Physics Laboratory (JHU/APL), the Air Force Research Laboratory Hanscom AFB, and the University of Alaska Fairbanks (UAF).Instruments and data used for determination and cross calibration of the auroral boundaries are SuperDARN convection data in e.g. for identifying the reversal boundary, NASA Polar UVI-images and the UAF meridian scanning photometer for confirmation of the actual location and the particle data measured by the DMSP SSJ/4 and SSJ/5 sensors on their boundary crossings [Newell et al., 2002].

The techniques for determining the boundaries and shape of the oval are based on the Automated Boundary Routine described by Newell et al. [1991] which was an automated online database on auroral oval parameters (back to 1983!). It provides the morphology of the auroral oval as it classifies the different boundaries corresponding to different particle energies and hence their source. See also Sotirelis et al.[1998] for determination of the shape of the polar cap and Sotirelis and Newell [2000] for precipitation modelling.
In general; the o/c boundary is set to be the poleward boundary of the oval, whereas the equatorward boundary is the zero energy electron boundary corresponding to the plasmapause [Newell et al.,2002]. The latter choice has one drawback because not all instruments are sensitive enough to measure these energies, besides the DMSP sensors [Newell et al.,2002]. Thus this substantiates how valuable the DMSP satellites are for particle measurements. Figure 3.1-8 shows an OVATION map from a random day. The auroral oval moves with time in a fixed geographic frame. The perpendicular axes correspond to longitudes with a 45º separation, whereas the circular are latitudes with 20º separation. The F-12 satellite track is marked by the black line and the crosses marks the boundaries as measured by the satellite particle data. The color code inside the oval corresponds to the logarithmic current density.

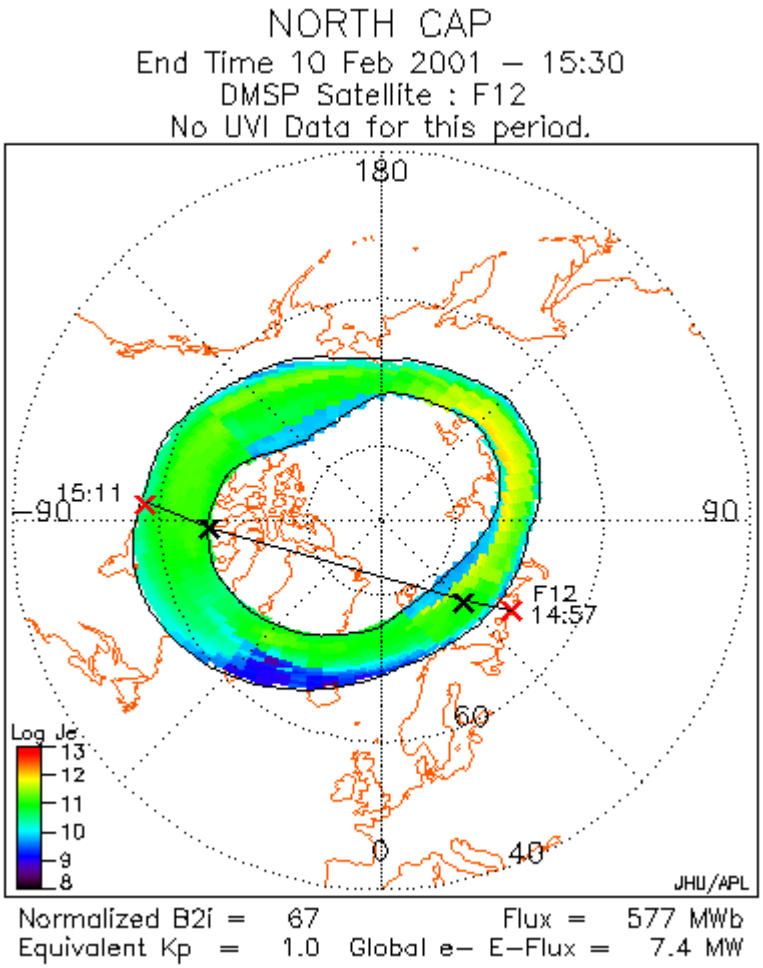

Figure 3.1-8: OVATION auroral oval map . The actual boundaries are marked by the crosses from the DMSP particle data. Credit: OVATION/JHU/APL

3.2 Radars

Both coherent scatter radars (CSR) and incoherent scatter radars (ISR) are used to study plasma irregularities in the ionosphere. Radars are sensitive to irregularities with wavelengths equal to one half of the radar wavelength [Greenwald et al., 1995]. For CSRs in the HF-band, this is consistent with irregularities of decameter scales [Ruohoniemi et al., 2012]. For wavelengths used by VHF and UHF - ISRs, this corresponds to irregularity wave lengths of 0.2-3meters [Greenwald et al., 1995].
It is worth mentioning, that for ISRs the wavelength must be larger than the Debye-length. The Debye length is given by:

$$\lambda_D \simeq 69\sqrt{\frac{T_e}{n_e}} \qquad (3.1)$$

where Te and ne is the electron temperature and density, respectively. The relationship between the radar wave and the Debye length (Debye cut-off) is given by: $(\lambda_D/\lambda_{radar})^2 \ll 1$ where λ_{radar} is the radar wave length. From eq. (3.1) it becomes obvious that the Debye-length increase with increasing altitude and must be taken into account to achieve incoherent scattering [Strømme, 2006]. The simple radar basics can be explained as follows; the radar sends out a sequence of radio pulses into the ionosphere. As the signal ray intercepts electrons in the plasma, a pulse echo is transmitted back to the radar antenna. The time between the transmission of the pulse and the reception of the echo is used to determine the distance to the target, and the Doppler shift of the echo determines the movement of the target. Electrons scatter the radio waves, thus the strength of backscatter is a measure of the number density of the electrons [e.g. Levanon, N., 1988]. Figure 3.2-1 is a simple illustration of the radar concept.

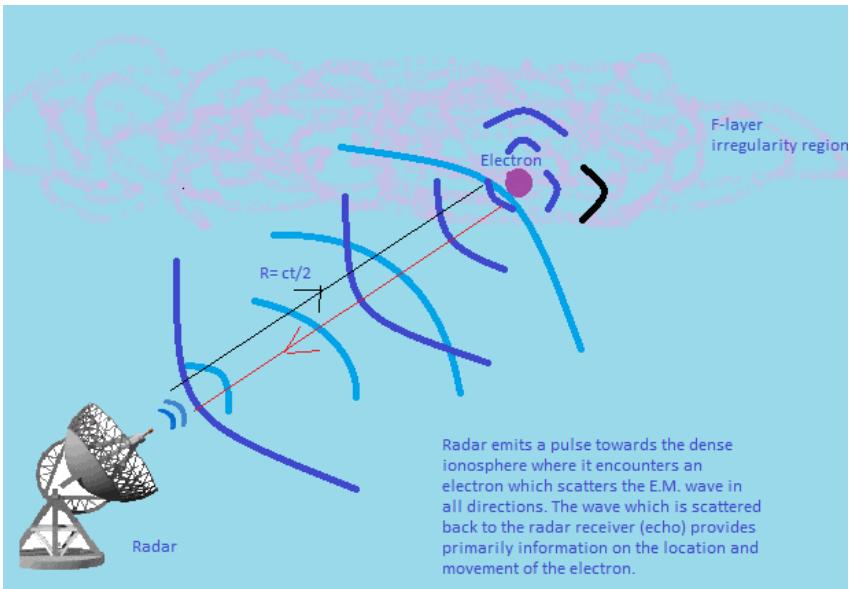

Figure 3.2-1: The simple concept of radar. The range is the wavespeed c, times the delaytime t/2.

3.2.1 Coherent Scatter Radars and SuperDARN

Coherent scatter radars utilize frequencies in the HF-band (3-30MHz) to study irregularities in the F-region. In order to do so, the rays are bent by refraction (due to the increasing refraction index) to see amplitude structures aligned with the magnetic field. In other words, the rays are bent in order to become perpendicular to the magnetic field lines. This is an advantage for studying the F-region, because the radar range is extended due to the refraction [St-Maurice, 2012; Baker, 2011]. Figure 3.2-2 illustrates the principle of refraction to perpendicularity with B-field lines for the CSR. CSRs can only see field aligned structures and fails to see thermal fluctuations in the plasma. Nevertheless CSRs sees the unstable structures, such as the gradient drift instability and the Farley-Buneman instability [St-Maurice, 2012].

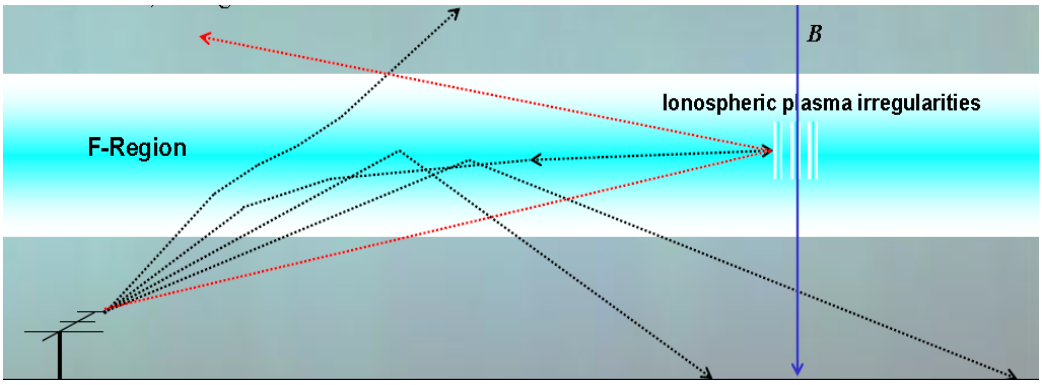

Figure 3.2-2: The possible ray paths from the HF-radar. As the ray travels through dense F-region, the rays are bent due to larger refraction index. When perpendicular to the magnetic field, the ray encounters the field aligned irregularities. Adapted from: Baker [2011].

3.2.1.1 Super Dual Auroral Radar Network (SuperDARN)

The SuperDARN is an international project with 11 collaborating countries based on a "scientist-to scientist" interaction level, where the PI agreements specifies the general principles of management. The original network of radars in high latitudes was extended to form the SuperDARN above 60° MLAT from 1995. From 2005 also mid-latitude radars were included in the network [http://center.stelab.nagoya-u.ac.jp/hokkaido/site1/intro_e.html, 2011; Baker, 2011; Greenwald et al., 1995]. The concept of the forerunner, DARN, and SuperDARN is the pairing of radars to overlap the same field of view [Chisham et al., 2007]. Today the SuperDARN consists of 32 radar arrays distributed around the world with the aim to conduct research on the upper atmosphere and ionosphere. The distribution and f.o.v. for all the operative radars are shown in Figure 3.2-3.

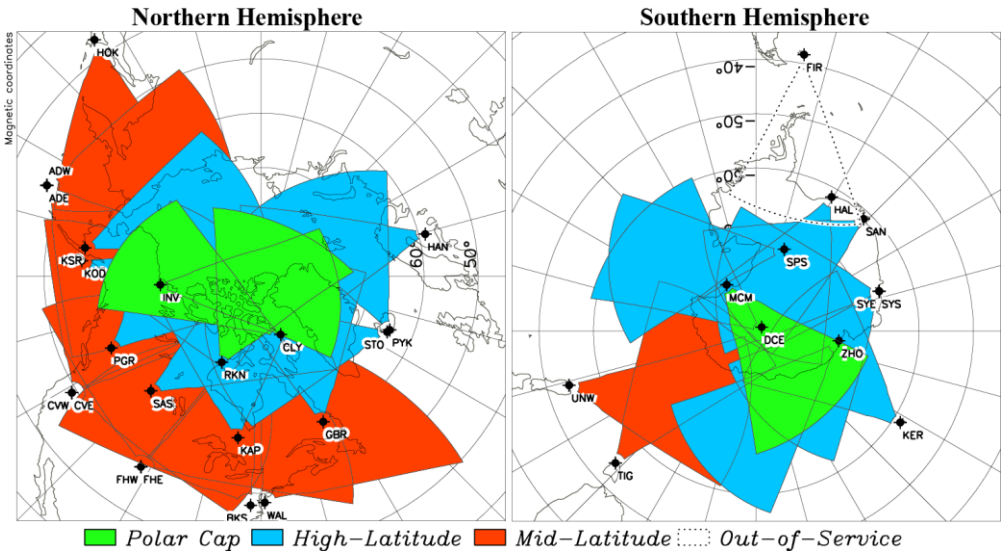

Figure 3.2-3: The field of view for all the SuperDARN radars. Image from: *http://vt.superdarn.org/tiki-index.php?page=Radar+Overview, 2014*

All radars have the same basic design, based on the original HF-radar from 1983, in Goose Bay, Canada [Chisham et al.,2007]. They operate within 9-18 MHz with approximately 10kW peak power. Electronically phased array steering enables the radars to look into at least16 beam directions. The paired radars look in the same f.o.v. and allows for simultaneous measure of range and Doppler velocities which are used to make plasma convection maps [Greenwald et al.,1995; Baker, 2011; Chisham et al., 2007; Ruohoniemi et al., 2012]. Figure 3.2-4 shows the original Goose Bay antenna array.

Figure 3.2-4: The Goose Bay HF-radar antenna arrays. This radar's characteristics served as a prototype for the SuperDARN radars. *Image from: http://vt.superdarn.org/tiki-index.php, 20014.*

SuperDARN has a wide range of utilities in the research of the ionosphere and upper atmosphere and has proven to be a valuable tool to study the dynamical processes [Baker, 2011; Chisham et al., 2007].

In this thesis I have used the convection maps for the northern hemisphere as quick looks in order to get an overview of the convection cells, enhanced flow regions and polar cap potential. The maps were downloaded from the Wallops Island Radar Facility run by the JHU/APL, before their data acquisition site was closed in September 2013. Three models were used to construct the maps in this thesis, see Figure 3.2-5. The RG96-model (Fig. 3.2-5a) is based on the statistical model developed by

Ruohoniemi and Greenwald in 1996 based on data from the Goose Bay HF-radar [Ruohoniemi and Greenwald, 1996]. The second model is the APL-model which was developed by Ruohoniemi and Baker [1998], (Fig.3.2-5b). The third model is the CS10 statistical model developed by Cousins and Sheperd, (Fig.3.2-5c). This is an improved model which uses OMNI data which are based on multi-space craft measurements of IMF (including tilt) and account for the time delay to the sub-solar point [Cousins and Sheperd, 2010]. As we can see from the figure, the convection cell pattern and polar cap potential differ slightly from each model. The enhanced flow regions are quite similar, however.

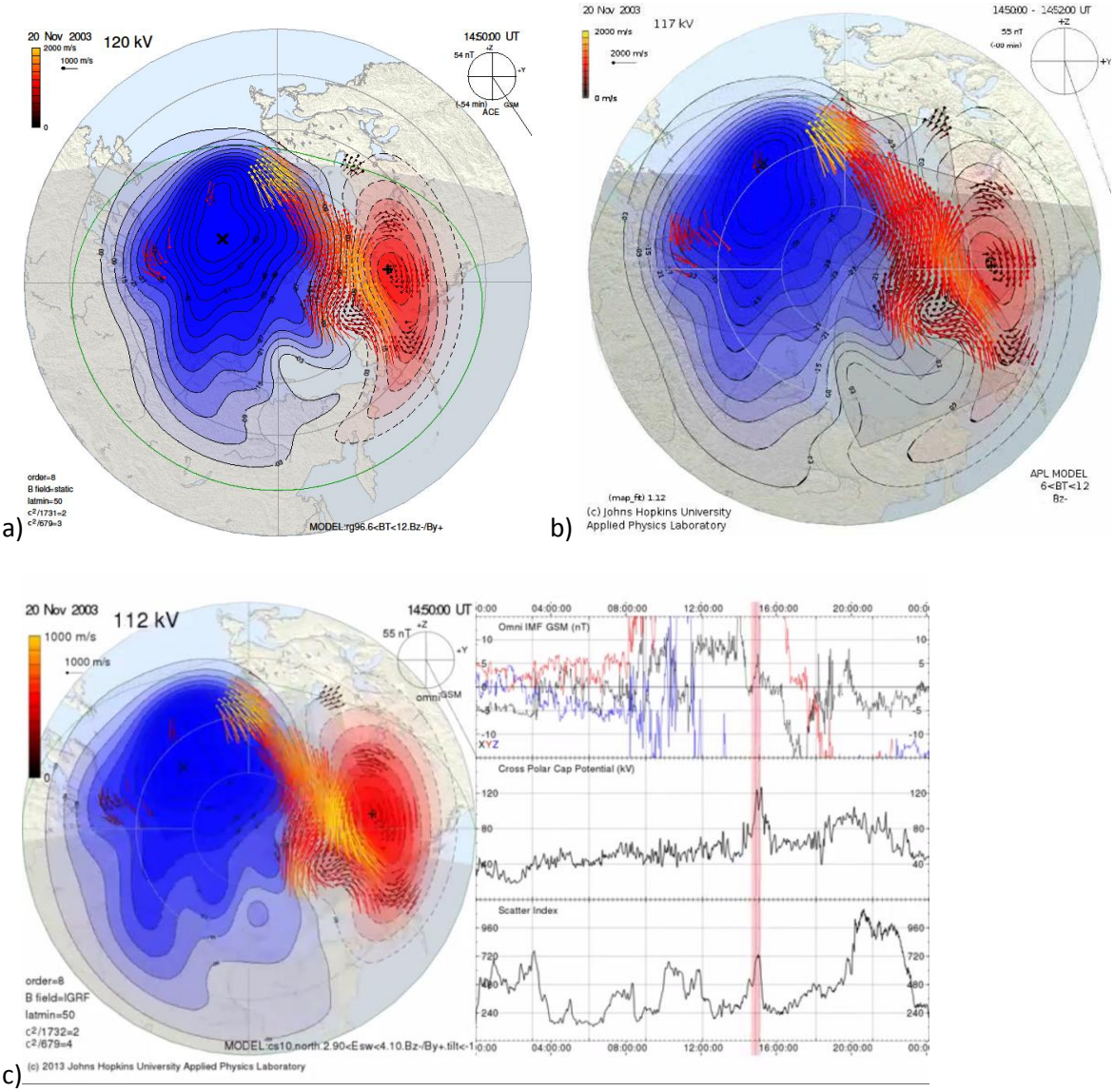

Figure 3.2-5: SuperDARN convection maps derived from three models in the same time. a) RG96-model from Rohoniemi and Greenwald. b) APL-model developed by Ruohoniemi and Baker. c) A screenshot from a convection movie shows the output of the CS10-model, developed by Cousins and Sheperd. All models are based on the ExB convection measured by the HF-radars making up the SuperDARN network. Some differences in the polar cap potential and cellpattern occur for all three models. All images from: superdarn.jhuapl.edu, 2013.

3.2.2 Incoherent Scatter Radars

ISRs are operating at higher frequencies than CSRs; in the VHF and UHF band (30-300MHz and 300-3000 MHz, respectively). This enables them to see thermal structures in all directions, not only perpendicular to the ray as for CSRs, Figure 3.2-6. ISRs provide information of the plasma densities, temperatures and particle movements in the ionosphere. The higher operation frequencies enable the radar pulse to travel to high altitudes, because they do not suffer that much from attenuation (recall section 2.4.1).

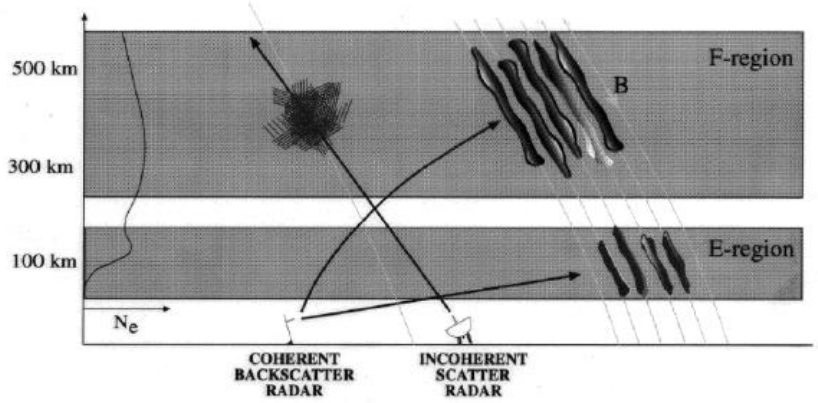

Figure 3.2-6: CS- radars can look at field aligned structures in the ionosphere when the ray path is refracted to hit perpendicularity. IS- radars can look see structures aligned in all directions. Adapted from: St-Maurice, 2012

As long as the plasma is stable (electron drift velocities are below140 kms^{-1}), the electron spectra can be derived with a linear recipe [St-Maurice, 2012]. The transmitted radio waves undergo Thomson-scattering on encounter with free electrons in the ionospheric plasma. A high density volume can contain 10^6 electrons/cm^{-3}, all of them in random thermal motion, thus causing the backscattered frequency to become Doppler shifted and consequently smeared out into a spectrum. Only a small fraction of the transmitted power is scattered back to the receiver antenna, but if the conditions are stable, these frequency spectra provide useful information on the plasma dynamics. The echoes are processed with Fourier transform into a characteristic spectrum as shown in Figure 3.2-7 [Gordon, 1958; Strømme, 2011]. The thermal motions disperse the electrons however; they are shielded by ions, and these shielding layers have scale sizes of the Debye length. The thermal motion generates ion acoustic waves and Langmuir waves in the plasma. The ions follow a Maxwellian distribution and the velocity of the ion acoustic waves, are affected by the velocities of the ions. Some ions are slower, while others are faster than the wave, and contribute to add, or feed energy off the wave. This phenomenon is often referred to as Landau-damping. The Doppler shift in the frequency makes two spectral lines on either side of the transmitted frequency. As these merge together the spectrum is broadened and the characteristic hump in the spectrum due to the Landau-damping occurs. The peaks become sharper as the electron temperature increases, and reduce the damping effect. Langmuir waves (electrons) are not damped, thus it is the ions that dictate the shape of the spectrum [Beynon and Williams, 1978]. Figure 3.2-7 a) illustrates this concept. From the top: ion acoustic dispersion relation, the velocity distributions of ions and electrons in the middle, and bottom shows the merged spectral lines. As we can see; the higher electron temperature is, the weaker damping of the ion-acoustic wave. A simple interpretation of the spectrum provides the temperature of ions and electrons, the Doppler shift in frequency is a measure of the mean ion velocity, whilst the area under the curve gives the density, see Figure 3.2-7 b), [e.g. Strømme, 2011].

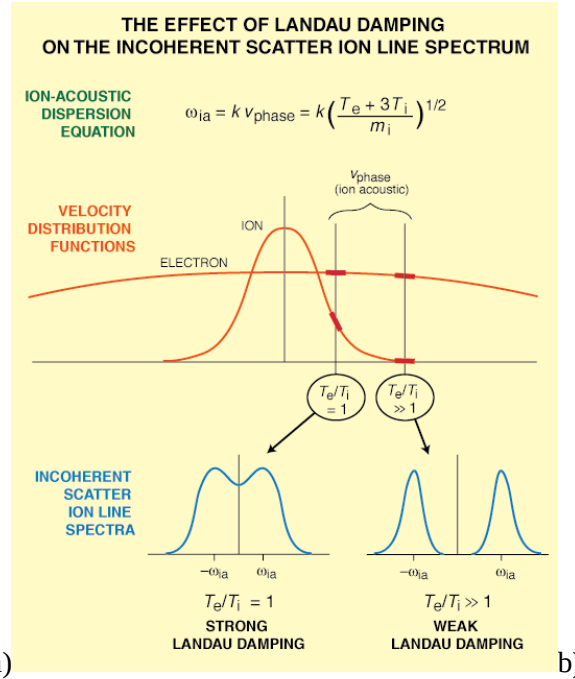

a)

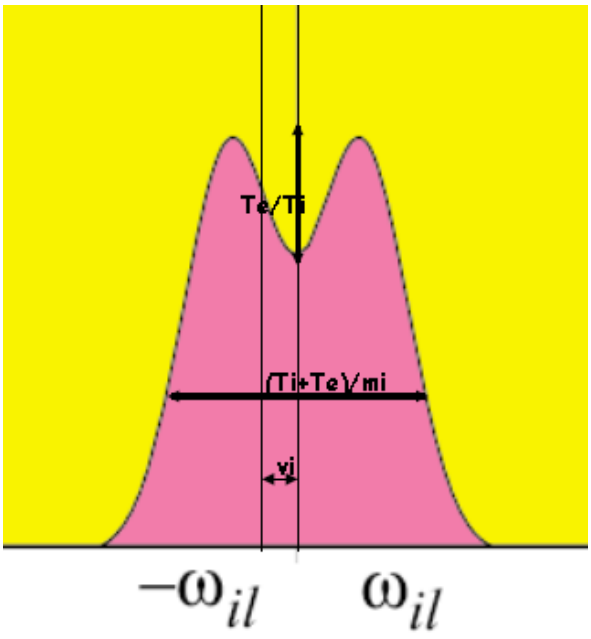

b)

Figure 3.2-7: a) The illustration of the origin of the characteristic IS-spectra with two examples of Landau-damping. b) The spectrum reveals key-parameters of the plasma; the area under the graph (pink) is proportional to the density, the Doppler shift from center frequency gives the ion velocity, v_i. The width of the spectrum is the ion temperature $(T_i+T_e)/m_i$, where $T_{i,e}$ are the ion and electron temperatures respectively and m_i is the ion mass. The height of the "wings" is the electron temperature (T_e/T_i). Both figures are adapted from: Strømme, A. [2011].

3.2.2.1 Millstone Hill

The Millstone Hill incoherent scatter radar is a part of the Massachusetts Institute of Technology (MIT) Haystack Observatory Atmospheric Sciences Group. It is located in Westford Massachusetts at 42.6°N, 288,5°E (53.4 Λ). This location is ideal for observing density enhancements in the sub-auroral region [e.g. Foster et al., 2002]. The ISR consists of two UHF-transmitters with independent operation output of 2.5MW, and frequency range 440.0-440.4 MHz. There are two associated antennas; a fixed 68m dish zenith antenna with a 0.6° beam width and a 46m steerable MISA antenna with a 1.2° beamwidth. Data are acquired and processed with the Millstone Incoherent Data Acquisition System (MIDAS) and available from the Madrigal database (http://madrigal.haystack.mit.edu/madrigal/). Figure 3.2-8a) shows the two ISR antennas. The MISA antenna in the back, and the zenith antenna in front.
[http://www.haystack.mit.edu/atm/mho/instruments/isr/index.html, 2014].
Foster et al. [2005] used data from the Millstone Hill radar to track the TOI through the dayside cusp on November 20, 2003. In addition they used 2D-TEC maps constructed from a network of GPS-receivers after the technique developed by Coster et al. [1992, 2003].

a)  b) 

c) 

Figure 3.2-8: a) The two ISR-antennas at Millstone Hill, the zenith antenna in front and the steerable MISA- antenna in the back (photo: *http://www.haystack.edu/atm/mho/index.html*). b) The Sondrestrom ISR-antenna accompanied by the LIDAR (photo: *isr.sri.com*). c) The UHF-antenna of the EISCAT Tromsø ISR (photo: Thomas Ulich, *http://blog.eiscat3d.org/2012/04*)

3.2.2.2 SRI International , Sondrestrom Research Facility

The Sondrestrom incoherent scatter radar is located in Søndre Strømfjord in Greenland. Just 100 km above the Arctic Circle at ~67°N, 309°E ,(74Λ). The radar is operated by SRI International in Menlo Park, California and in cooperation with the Danish Meteorological Institute. The radar operates in the L-band with frequency range 1290-1290.6 MHz, and 3.5 MW peak power output. The 32m steerable antenna dish has a 0.5° beamwidth and above 30° elevation. Data from SRI Sondrestrom are available from the Madrigal database (http://isr.sri.com/madrigal/) or the homepage (http://isr.sri.com/) [McCready and Heinselman, 2013; http://isr.sri.com/about.html , 2014]. A picture of the radar facility is shown in Figure 3.2-8b).

I have used summary plots from Sondrestrom radar as visualization of the high density patch, and the plasma parameters. They were downloaded from the SRI-homepage.

3.2.2.3 EISCAT Tromsø

European Incoherent Scatter Scientific Association (EISCAT) operates three of the ten ISR-facilities in the world, and they are all located in the northern part of Scandinavia (above the Arctic Circle). The EISCAT Tromsø UHF-radar is a tri-static radar located in Ramfjordmoen at 69.35°N, 19.14°E, (66 Λ) with one antenna here. The other two antennas are located in Kiruna, Sweden (67.52°N, 20.26°E) and Sodankylä, Finland (67.22°N, 26.38°E). The UHF-radar operates at an approximate frequency of 931MHz and maximum power output is more than 2.0 MW. The antenna in Tromsø is a fully steerable 32m antenna dish [https://www.eiscat.se/about/whatiseiscat_new, 2014]. A picture of this antenna is shown in Figure 3.2-8 c).

The radar data from Tromsø used in this thesis has been processed with the GUISDAP-software (Grand Unified Incoherent Scatter Design and Analysis Package) [Lehtinen and Huuskonen, 1996]. This program combines several analysis methods of IS-raw data to provide a visual display of the parameters to simplify the interpretation. Raw-material processed and analyzed with GUISDAP, is issued on the EISCAT-page (https://www.eiscat.se/rtg/rtg.cgi) including real time data. Archived data are available from the EISCAT Madrigal database (https://www.eiscat.se/madrigal/).

Figure 3.2-9 shows a summary plot from October 29, 2003.

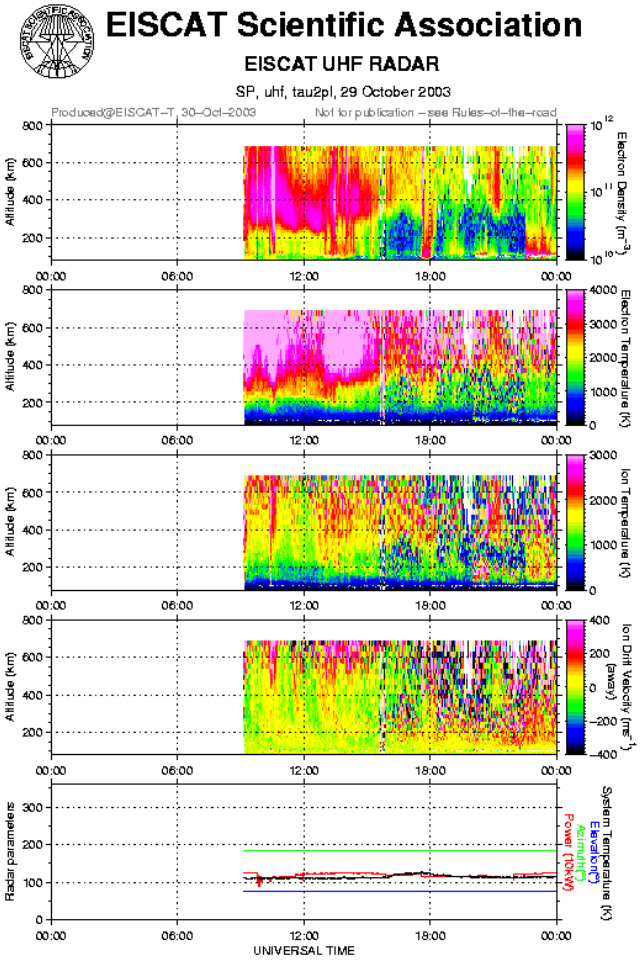

Figure 3.2-9: A summary plot of the key parameters from the EISCAT-Tromsø, UHF-ISR. Electron density and temperature in the two top panels followed by ion temperature and ion drift velocities. Pink drift velocities correspond to strong ion upflow. Credit: EISCAT *(https://www.eiscat.se/madrigal/)*

3.2.3 Ionosondes

Ionosondes are like small radars that sweep the HF-range (1-20MHz). The reflected signals from the ionosphere are binned and used to create maps of the bottomside ionospheric layers. The virtual height of the ionospheric layers and frequency Doppler shifts can be used to determine the location and movement of plasma irregularities [Leyser, 2011; Weber et al., 1984]. During quiet conditions the ionospheric layers are characterized by smooth curves (traces) at different virtual heights [Davis, 1996]. When there are irregularities present in the F-layer, a phenomenon called "spread F" occurs. In short; several traces of the reflected signal are present and the F-trace becomes smeared out or spread [Davis,1996; Buchau et al., 1983; Reinisch, B., private communication, 2014]. The ionograms I have used in this thesis are created from measurements from a digisonde. Both Sondrestrom and Tromsø used the Digital™ Portable Sounder DPS-4, developed by University of Massachusetts Lowell Center for Atmospheric Research (UMLCAR). This is a vertical incidence sounder which consists of a portable sounder and a magnetic loop antenna, with 100-500 W output power and frequency range from 1.0-45MHz [http://www.digisonde.com/instrument-description.html,2014]. Figure 3.2-10 shows the DPS and the loop antenna and, Figure 3.2-11 shows a real time ionogram from Tromsø. Archived data can be downloaded from GIRO Lowell DIDbase internet site (http://umlcar.uml.edu/DIDBase/). Real time data from Tromsø is operated by QinetiQ, Radio Science and Propagation Group in Malverne,UK.

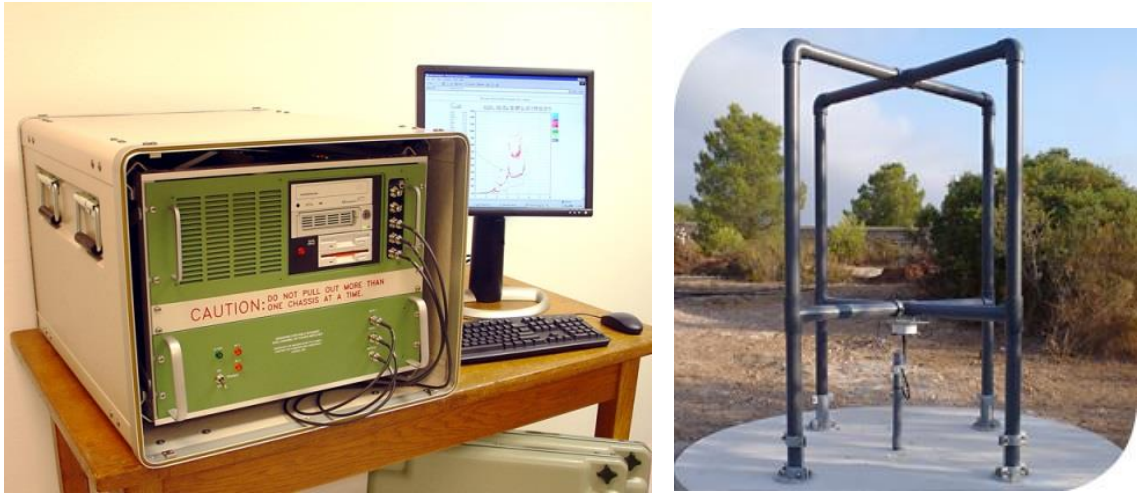

Figure 3.2-10: The Digital Portable Sounder to the left and antenna to the right. Picture from: *http://umlcar.uml.edu/DPS.htm; http://www.digisonde.com/instrument-description.html*

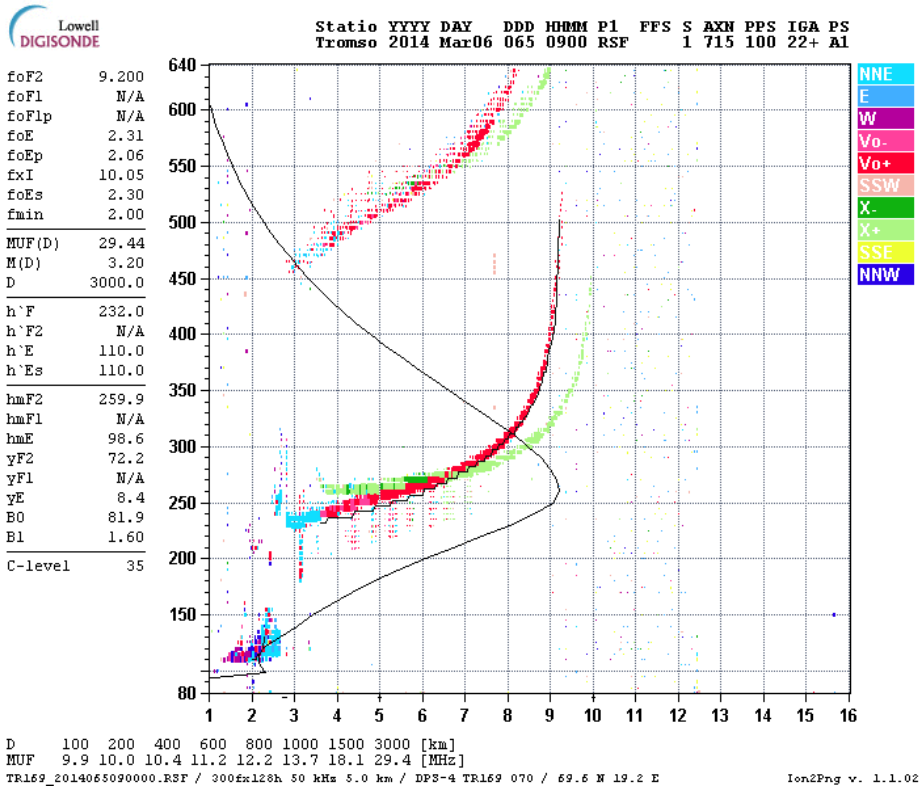

Figure 3.2-11: A real time ionogram from Tromsø, March 05, 2014. A sporadic E layer is visible in the lower left corner, a fine F-layer with separate ordinary and extraordinary modes. The left pane lists the derived parameters of the ionospheric layers. The right pane is a directogram; the directions of the movement are color coded. Cold colors means movement towards north, bright colors means movement towards east. Green colors are extraordinary polarization mode of the wave, whereas red are the ordinary mode [http://umlcar.uml.edu/directograms.html, 2014]. Ionogram from: *http://www.tgo.uit.no/ionosonde/*, Credit: GIRO/QinetiQ, 2014.

3.3 Magnetometers and Electrojet Indices

It is common to use fluxgate magnetometers to measure variations in the geomagnetic field induced by ionospheric and magnetospheric currents. There are many types of fluxgate sensors, but the general principle is as follows: A core rod of ferrite (or other susceptible material), is affected by an external field which induces a magnetic flux in the core. Since the core has a high susceptibility, it becomes magnetized by the external field. However; if the core becomes saturated, no more flux will build up. Thus the core is being saturated/de-saturated by an alternating current within a driving coil. A secondary pick up coil detects the variation in flux, and a signal proportional to this variation is induced. As the core de-saturates, magnetic flux is removed from the core, and by Lenz Law, the system will oppose the change by inducing a positive current in the pick-up coil, and vice versa. Tri-axial fluxgate magnetometers have three sensors in all three perpendicular directions to measure all vector components of the magnetic field variations [Primdahl, 1979; www.uio.no/studier/emner/matnat/fys /Fys/3610/h08/undervisningsmateriale / compendium/magnetometer, 2008]. Figure 3.3-1 shows a simple illustration of the Residence Times Difference (RTD) fluxgate design.

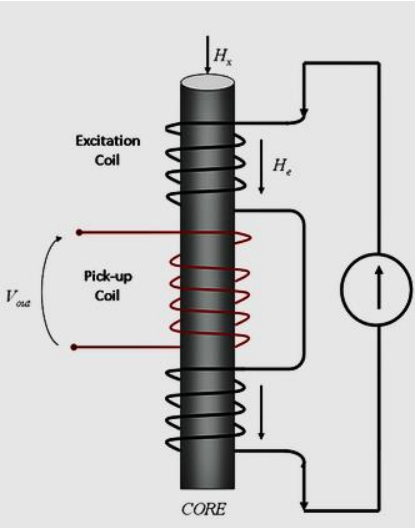

Figure 3.3-1: A schematic sketch of an RTD-fluxgate sensor. The external field and the induced core field point in the same direction, the driver coil (here called excitation coil) contributes to alter the flux in the core, whereas the pick-up coil produces a signal in response to the changes in the flux. Figure adapted from*: www.measurement.dees.unict.it/rtd_ fluxgate.html*, 2014.

3.3.1 International Monitor for Auroral Geomagnetic Effects (IMAGE)

The IMAGE magnetometer network consists of 31 stations arranged from Tartu in Estonia in the South to Ny Ålesund in Svalbard, Norway in the north. IMAGE was founded in 1990/91 and the original EISCAT Magnetometer Cross stations were implemented in the new chain. The original contributors were research institutions from Finland and Germany, and over the years more contributors from Russia, Poland, Estonia, Sweden and Norway have joined the network. Today there are a total of 10 institutes within these countries who operate and maintain these magnetometer stations. Also; the Sub-Auroral Magnetometer Network (SAMNET) in the UK incorporate their magnetometers in the IMAGE chain. Figure 3.3-2 shows the locations of the stations as of present day, and Table 3.3-1 lists the coordinates of the stations I have included in magnetograms. Near real time magnetograms have been available online since 2012 on the IMAGE homepage as well as some of the collaborating research institutes. [http://www.space.fmi.fi/image/, 2014].

STATION	GEOLAT (°N)	GEOLONG (°E)
Ny Ålesund, Norway (NAL)	78.92	11.95
Bear Island , Norway (BJN)	74.50	19.20
Sørøya, Norway (SOR)	70.54	22.22
Andenes, Norway (AND)	69.30	16.03
Kiruna, Sweden (KIR)	67.84	20.42
Rørvik, Norway (RVK)	64.94	10.98
Dombås, Norway (DOB)	62.07	9.11
Tartu, Estonia (TAR)	58.26	26.46

Table 3.3-1: Locations of the IMAGE chain stations used in magnetograms listed from north to south. Notice Kiruna and Tartu are east of the easternmost Norwegian boundary.

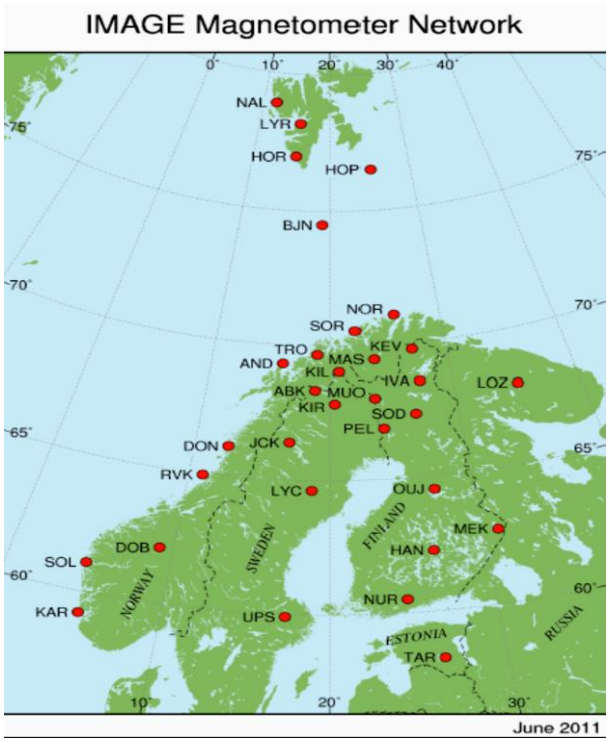

Figure 3.3-2: The stations connected to the IMAGE-network. Figure from: *http://space.fmi.fi/image/beta/?page=maps*, 2014.

3.3.2 Electrojets

During geomagnetic disturbances the electrojets in the auroral zone cause deviations in the H-component of the geomagnetic field. Thus magnetometers can be used to determine the location and amplitude of the auroral electrojets. The eastward electrojet (EEJ) is associated with a positive bay in the x-component, thus magnetometer stations located in the dusk MLT will record a positive disturbance in the magnetogram. Stations located in the dawn sector hence record a negative bay produced by the westward electrojet (WEJ) [McPherron in Kivelson and Russell, 1995]. Magnetograms can be used to derive electrojet indices. In this thesis I have used the local electrojet indices from the IMAGE BEAR project, derived with the so-called characteristic point method. The measurements are based on a meridional chain of 11 magnetometer stations from Nurmijärvi in Southern Finland to Ny Ålesund in Svalbard. The electrojets are approximately corresponding to the most negative or positive excursions in the x-component. The maxima and minima are roughly corresponding to the center of the electrojet currents. Thus the AU-index are the positive excursions associated with the EEJ, and the AL-index are the negative excursions associated with the WEJ. Typical amplitudes of the AL-index are from -200nT to -2000nT [www.space.fmi.fi/image/bear, 2004]. Figure 3.3-3 shows the chain of selected stations for the electrojet and the extension in kilometers. The image on the right in Figure 3.3-3 shows how the electrojets are located in the x-component magnetogram and z-component magnetogram respectively.

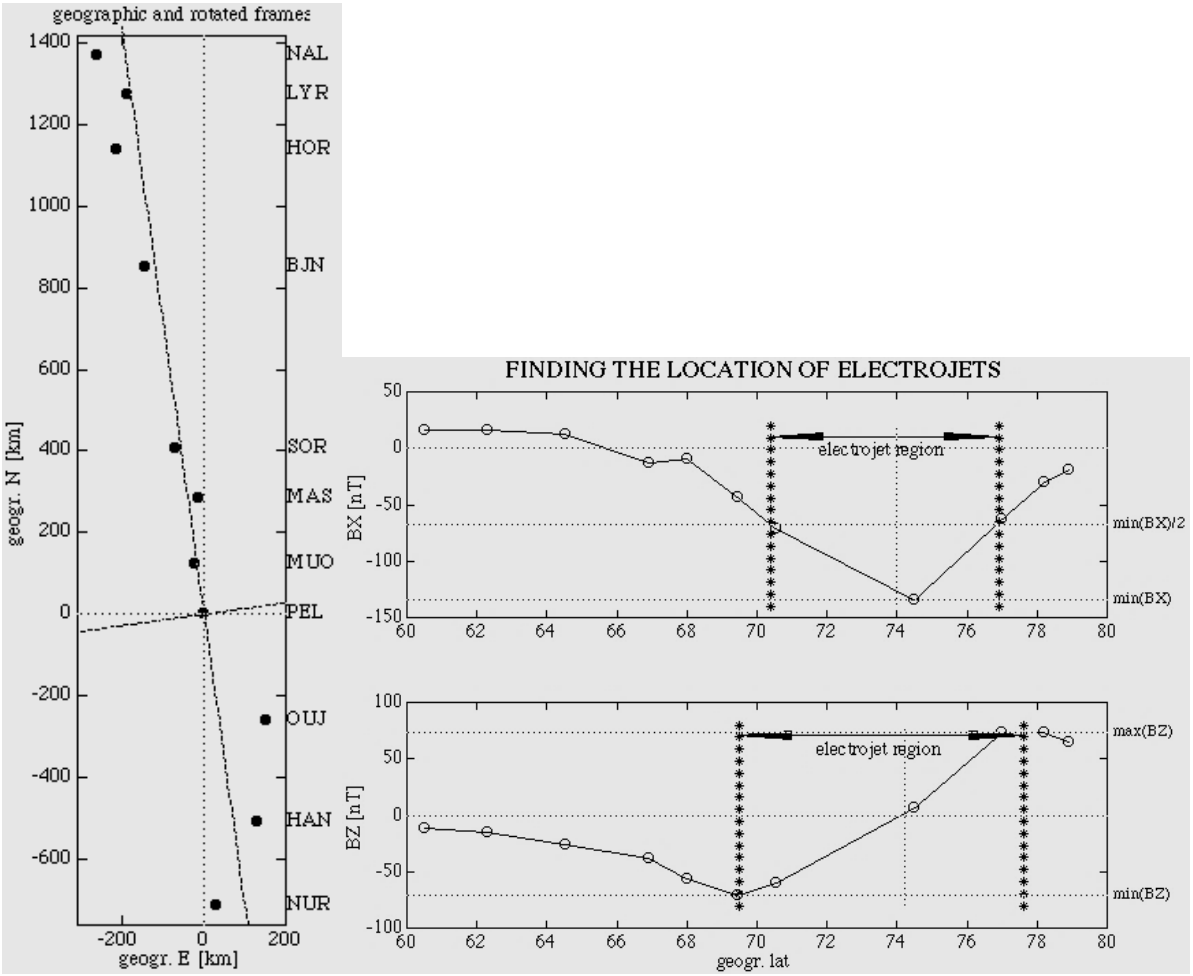

Figure 3.3-3: Left: the extent of the IMAGE chain used for deriving the local AU and AL indices. Right: How the locations of the electrojets were extracted from the magnetometer data. Credit: IMAGE BEAR, 2004. (*http://www.space.fmi.fi/image/bear/bear_ej.html*)

The AU/AL indices are especially useful to study the phases of substorms. The onset of a storm is recognized by a positive spike in the x-component magetogram, thus relating to a sudden increase in the AU-index. The ongoing increase in the AU-index corresponds to the storm growth phase where magnetic flux is transported from the dayside merging site across the polar cap. During the growth phase, AL-index only reveals a slow decline. At the onset of the expansion phase, the AL-index drops sharply indicating tail reconnection and storm time enhancement of the WEJ. The AL-index slowly begin to climb from its minimum along with the AU-index during the recovery phase [McPherron in Kivelson and Russell, 1995]. Figure 3.3-4 illustrates how such a substorm development may look like in terms of the AU/AL-indices.

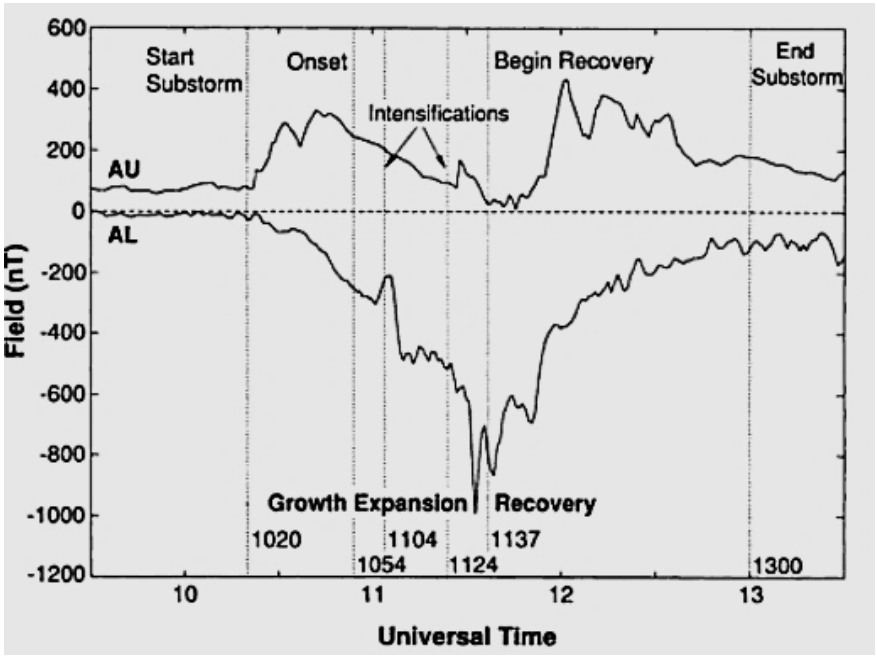

Figure 3.3-4: The phases of a substorm in terms of the AU and AL electrojet indices. Figure adapted from: McPherron in Kivelson and Russell [1995], p. 428.

3.3.3 All Sky Camera (DASC)

Actual images of the aurora are useful to study the dynamics of geomagnetic disturbances with an auroral display. All Sky cameras are equipped with a fish eye lens to ensure a ~180° view of the overhead night sky. Some cameras also have filters for studying the specific wavelengths. In 2003, the Swedish IRF (Institute for Space Research) operated the Digital All Sky Camera (DASC) in Kiruna (67.5°N, 24.4°E). This was an automatic Fuji FinePix S2Pro digital camera equipped with a Nikon Nikkor 8mm fish eye lens. The camera had an effective resolution of 6.17 megapixels and a so called Super CCD of ~6.50 megapixels [www.fujifilmusa.com/shared/bin/S2_Brochure.pdf] . The camera was automatic, controlled by a computer and the images were downloaded to a second computer for processing and upload on the homepage (http://www.irf.se/allsky/). The images were available within one or two days [Brändström,www.irf.se/allsky/dasc, 2004]. In this thesis I have used the 1min resolution images. Figure 3.3-5 illustrates the directions in the field of view. Notice that the images in section 4.3.1.are tilted -90° from this illustration image.

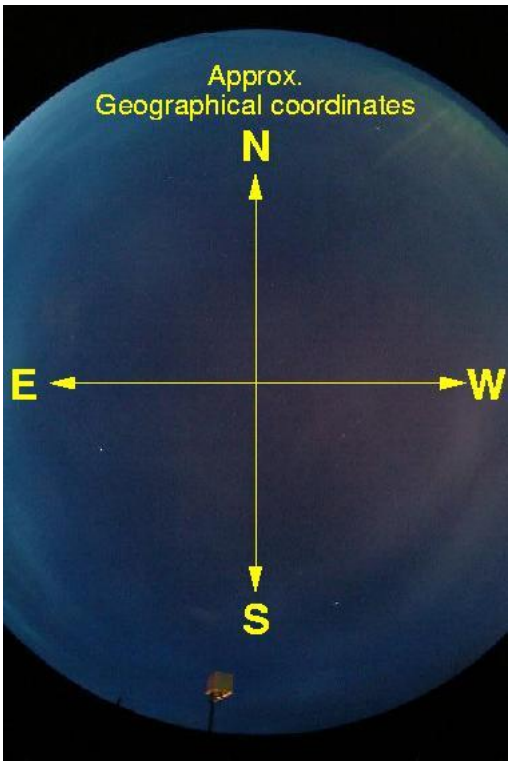

Figure 3.3-5: The view directions of the Kiruna DASC. Credit: Brändström, U., 2004. (*www.irf.se/allsky)*

3.4 GPS receiver Trimble MS750

The NMA used the same Real Time Kinematic/ On-The-Fly[2] (RTK/OTF) dual frequency receivers in all the reference stations studied in this thesis. This receiver provides real time data with centimeter accuracy based on RTK, and real time sub-meter positioning based on L1 C/A code phase solutions. The simple principle of RTK-positioning is the use of one reference receiver and one or more rovers (mobile receivers). In this case the reference receiver is stationary on bedrock (recall section 2.5.4). All satellite data collected from satellites in view is broadcasted to the rovers in the area, which compare it with the data they have collected. The rovers use this information to estimate their own position relative to the reference station. A typical measurement and position solution rate is 1Hz for both receivers. To achieve centimeter level accuracy, the receivers use the carrier phase signals to determine position. The phase ambiguity must be resolved for both the reference receiver and the rover, or initialized if the satellite signal is interrupted. The time required for initialization depend on satellite geometry, base line length, multipath and atmospheric errors. The initialization is automatic in the MS750 (OTF) [Trimble Navigation Limited, 2000]. In the following section, a brief description of the important features of the MS750 RTK-receiver for tracking and initialization is given.

3.4.1 Trimble Positioning modes

There are four different modes available for different requirements of accuracy. To achieve the highest possible accuracy, the most common mode is the Synchronized RTK (hereafter referred to as S-mode). This has an update rate of 1Hz and requires a high bandwidth data-link , because the rover must await reference updates before it can carry out the base line vector computing (latency of 0.5-2s). Thus another mode; the Fast Update Synchronized RTK (FUS-mode), is recommended for applications

[2] On The Fly refers to automatic initialization of phase ambiguity regardless of the movement of the receiver.

which demands fast positioning. The latency in this mode is the same as for S-mode (1Hz), but the update rates can be 5 or 10Hz. Fast synchronization requires fast output, therefore the bandwidth and datalink must be high. To reduce the latency in positioning solution, Low Latency RTK (LL-mode) is used. The latency is about 20ms and the update rate is about 20Hz, but the accuracy is sacrificed for the increase in timeliness. LL-mode is highly dependent on accuracy in the phase measurements from the reference station. Although the receiver can predict and project forthcoming measurements for a few epochs based on the previous data from the reference receiver with approximately the same latency, this mode strongly rely on phase data from the reference receiver. Increased latency in data link causes phase projection errors of increasing number of cycles, resulting in error in positioning. If there are fewer satellites in view (PDOP, multipath or disturbed atmosphere/ionosphere), the positioning errors increase. Thus the data link and the carrier phase initialization must be sufficient. The last mode; Moving Baseline RTK refers to applications where both the reference receiver and the rover are moving relative to one another [Trimble Navigation Limited, 2000]. Since the reference receivers are stationary, this mode will not be treated.

3.4.2 Phase Initialization Requirements

Every time the satellite signals are interrupted (or the receiver turned on), the phase ambiguity needs to be resolved. What is of crucial importance here is that, the rover and the reference receiver must track at least ***5*** common satellites in order for automatic initialization of phase ambiguity. In addition are L1 and L2 carrier measurements and precise code range measurements to the satellites, also required for automatically phase initialization. In case only 4 common satellites are in view, the ambiguity initialization is not required if, and only if, these satellites have been tracked continuously prior to the cycle slip. The MS750 counts the number of continuous epochs (of 1s) between initializations, and it is capable of generating a float solution with reduced accuracy (meter level) during the ambiguity initialization process. This process usually takes less than one minute, and the solution mode automatically switch back to centimeter level accuracy when fixed. Poor initialization may result in positioning errors of 1-3m. The receivers are capable of detecting and solving such erroneous initialization, but it may take long (minutes) before the error is detected if there are few common satellites in view. A low PDOP (<4.0) is favorable, although the elevation mask (cut-off) may deselect some of the satellite in view due to low elevation. The default cut off is 13°, but is changeable. Multipath errors are often in order of 1-5cm, which is not acceptable for high precision applications. The maximum separation between reference station and rovers should be less than 10 km for optimal initialization performance [Trimble Navigation Limited, 2000].Table 3.4-1 summarizes the key features described above.

RTK mode	Update rate (Hz)	Latency (s)	Data link required (baud)	Horizontal accuracy	Vertical accuracy
S-mode	1.0	0.50-2.5	2400	1 cm + 1ppm	2cm + 2ppm
FUS-mode	5.0 or 10	0.50-2.5	9600	1cm+2ppm	2cm+2ppm
LL-mode	20 (max)	0.02	2400	2cm+2ppm	3cm+2ppm

Table 3.4-1: The key features of the MS750 RTK-modes. Note that accuracy in centimeters in the receiver corresponds to accuracy in ppm in the baseline vector.

3.5 On the MATLAB Computations and Plots

In this section I give a brief outline on the how calculations were performed in MATLAB.

3.5.1 Solar wind data from ACE

ACE-data was downloaded from the ACE Science Center at www.srl.caltech.edu/ACE. Solar wind ion parameters from the SWEPAM instrument with 64s time resolution and magnetometer data from ACEMAG of 1s resolution was selected.
The space craft was situated approximately in (240, 27, -9.5)R_E on the actual day.

For both datasets the missing data was set to NaN and replaced by the closest mean values. Plots of solar wind velocity (x-component), and ion density were generated as a function of time. Similarly the total IMFB-field and separate components were plotted. Also, average ion density and solar wind velocity was calculated, in addition to time delay of propagation between ACE and the magnetopause.

3.5.1.1 Calculating Propagation Delay

In order to calculate the time it takes for the solar wind to travel from ACE to the Earth's magnetopause, ion velocity and density is required. The average distance from Earth's center to L1 is approximately $1.5 \cdot 10^6$ km or ~$235.5R_E$. The approximate stand-off distance can be calculated from eq. (2.50) in section 2.3.2) In order to use this approximation we assume that the magnetosphere pressure balances the solar wind pressure at the subsolar point and that the standoff distance vary inversely with the sixth root of the solar wind dynamic pressure. Further we assume that the solar wind-discontinuity (shock) follows the 1-D Rankine-Hugoniot[3] relations (MHD) and moves within a normal incidence frame. Thus it is customary to align the axis normal of the discontinuity parallel with the Sun-Earth line and the direction of the solar wind propagation (assuming the solar wind moves linear and parallel to the S-E line) [e.g. Paschmann and Daly, 1998]. Figure 3.5-1 illustrates the geometry of the solar wind within a NIF. Here the subscript 'u' corresponds to 'upstream', and we see that the upstream flow V_u, and the shock normal $\hat{n}$ are aligned in the same plane and both perpendicular to the electric field E_u and the magnetic field B_u.

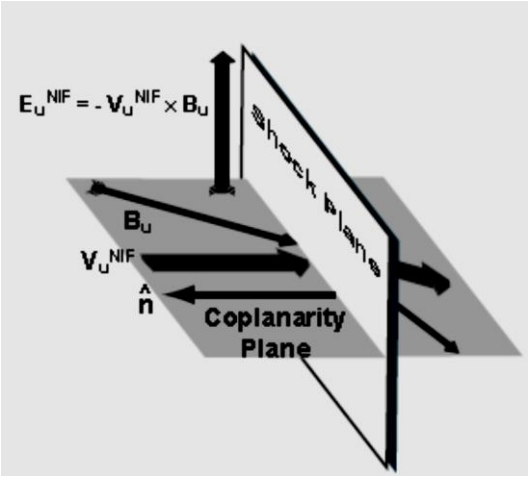

Figure 3.5-1: The geometry of normal incidence frame for a solar wind discontinuity.

[3] Relations are not treated. In short they describe six plasma parameters in which uniquely determine the downstream conditions of a shock in terms of the upstream conditions [Burgess in Kivelson and Russell, 1995].

Based on the proton density parameters from SWEPAM, the calculated mean solar wind density was: n =12.313 cm^{-3} and the average solar wind computed from the x-component was $u_{sw} = -555.27\ kms^{-1}$.
Eq. (2.50) yields:

$$R_{mp} = 107.4(nu_{sw}{}^2)^{-\frac{1}{6}} = 107.4(12.313 \cdot (-555.27)^2)^{-\frac{1}{6}} = \underline{\underline{8.589R_E}}$$

Thus the average distance from Earth to the magnetopause was ~8.6R_E. This means that the mean distance from ACE to the magnetopause must be:

$$R_{A-E} = 235.5 - 8.589 = 226.9 \approx \underline{\underline{227\text{RE}}}.$$

The propagation time from ACE to the magnetopause is thus:

$$t_{delay} = \frac{R_{A-E}}{|u_{sw}|} = \frac{226.9 \cdot 6371\ km}{557.27\ kms^{-1}} = 2594s = \underline{\underline{43.2\ min}}.$$

Some differences in this calculation and in the MATLAB code in appendix are due to rounding, nevertheless; the final propagation delay time is the same.

3.5.2 GPS-satellite data

The GPS-data used are converted from RINEX-files to a simpler text format for simpler MATLAB processing. There is one file for each station containing satellite PRN-number, delay meter on L_1, ionospheric pierce points (IPPs) at 350 km altitude and time. The time resolution is 30s for all sets. To plot satellite visibility and elevation plots for each station, the simplified text-file were loaded in to MATLAB and data arranged in arrays. All satellites were put into a loop which skipped to next satellite if some of the PRNs were missing. This enabled visualization of the missing satellite signals in both types of plots. All TEC-, scintillation- and - ROTI maps from NMA were made by Knut Stanley Jacobsen with the RTIM-program with the same datasets. In section 4.4 the IPPs of the satellites were included in the RTIM-maps for a better visualization of where the satellites were in relation to the enhanced density regions. Coordinates of the o/c boundary were also implemented to visualize the auroral oval. These data were downloaded from the OVATION site (*http://sd-www.jhuapl.edu/Aurora/ovation/datasets.html)* and plotted in the RTIM-maps.

3.5.3 Other Plots

Some other calculations and plots are also done in MATLAB and included in the appendix. These are the plotting of the hourly Dst-index, the calculation of the distance from Millstone Hill to Tromsø, and the cross correlation plots in sections: 4.1.2, 5.2.2 and 5.2.5.

4 Data presentation

4.1 Introduction

The storms of October and November 2003 have been thoroughly studied by several authors. This thesis concerns only the superstorm event of November 20, 2003 when the Norwegian Mapping Authority (NMA) suffered from severe loss of satellite reception during the main phase of the event. I will start with the source of the problems at the Sun and then present some of the results authors have found before I present the data from NMA.

4.1.1 The Sun and solar wind

The active regions that were responsible for the severe Halloween storms in October, returned in November. The active region AR484 re-appeared at the solar limb as AR501 November 13. Figure 4.1-1 shows a series of photos of the solar disk and the active regions taken at different wavelengths around the time of interest on November 18.

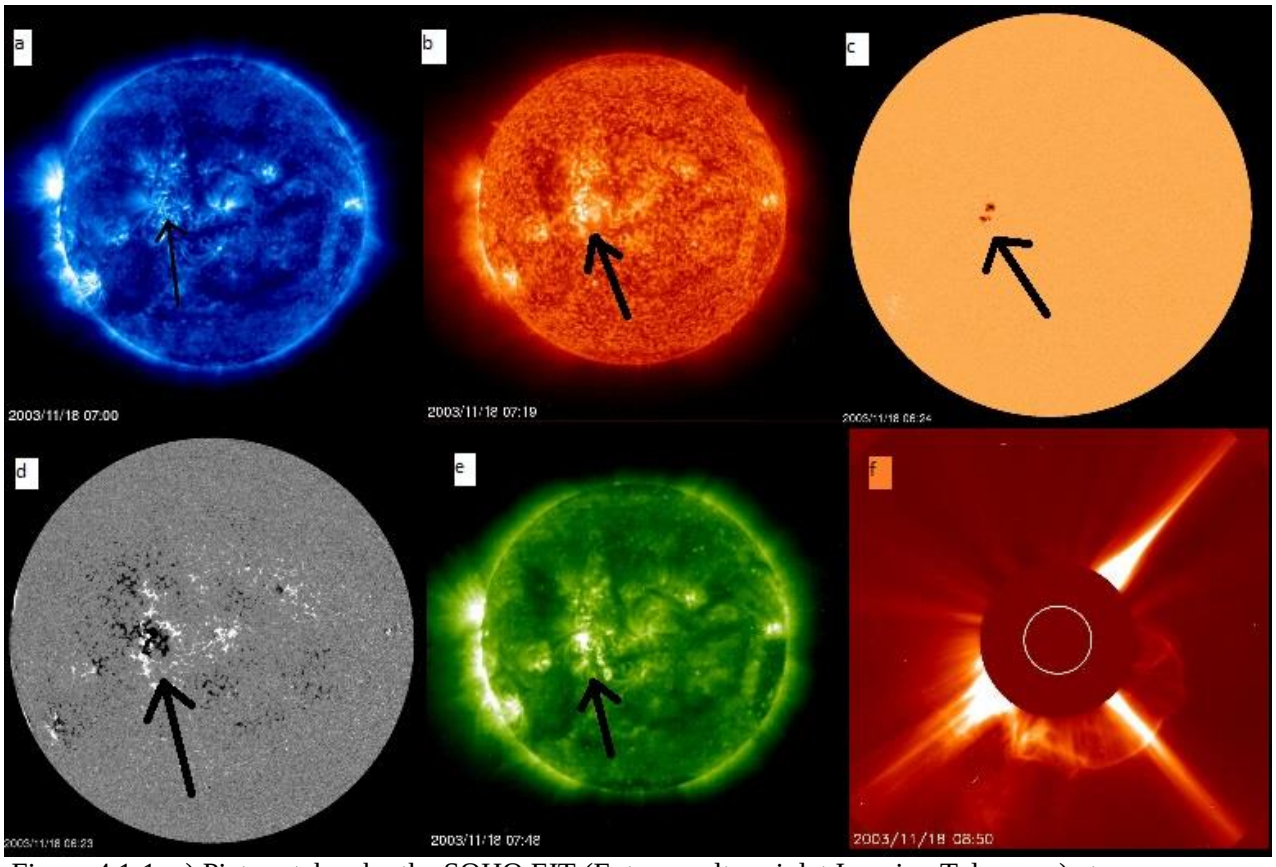

Figure 4.1-1: a) Picture taken by the SOHO EIT (Extreme ultra violet Imaging Telescope) at a wave length of 171Å. The arrow indicates the AR501. b) Picture taken at 304Å c) Picture of the solar disk taken by the SOHO MDI (Michelson Doppler Imager). The active region is associated with a sunspot. d) SOHO MDI real time magnetogram of the solar disk. The white areas refer to positive magnetic polarity, whereas the black; negative polarity. e) Picture taken by SOHO EIT at 195Å. f) The eruption of the CME from AR501 at 08:50 UT. Picture taken by: SOHO LASCO (Large Angle and Spectrometric Coronagraph). Credit: SOHO/NASA/ESA (*http://sohodata.nascom.nasa.gov/cgi-bin/data_query)*

Gopalswamy et al. [2005a] investigated the possible sources of the event on November 20 and found that AR501 was in the proper position for being a candidate on November 18. During the days it was visible in the disk, it had produced several flares, and on November 18, two M-flare events took place in the morning (UT). It was the second flare, and associated CME, at 08:50 UT that became responsible for the super storm on November 20. Figure 4.1-2a) shows the filament inside the CME developing from AR501. The white line indicates the outer boundary of the filament, with the filament itself shown as the dark U-shaped region in the apex. Figure 4.1-2b) and 4.1-2c) reveal the superposed contours of the LOS magnetic field where it clearly illustrates that the legs of the filaments are anchored in opposite magnetic polarities on each side of the neutral line [Gopalswamy et al., 2005a].

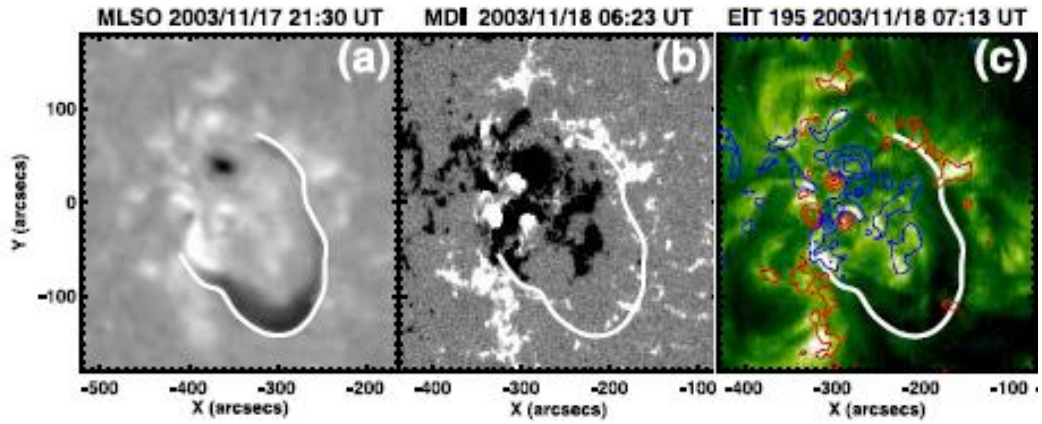

Figure 4.1-2) a) The dark filament with white outlining in a H-alpha picture taken by the Mauna Loa Solar Observatory. b) A SOHO/MDI magnetogram revealing the opposite polarities of the magnetic field within the active region. c) SOHO/EIT picture with superposed magnetic contours complement the findings in the magnetogram in b). Notice the two legs are anchored in opposite magnetic polarity regions. All figures are adapted from: Gopalswamy et al. [2005a]

The whole CME erupted in the M-flare at 08:50 UT, however the MC originated from the CME was believed to emerge from the flux rope that enclosed the filament, rather than the filament itself. Data reveals that it was only the 08:50 UT eruption that was a plausible candidate for the storm event by having the right direction and speed towards the Earth [Gopalswamy et al. 2005a; Grechnev et al. 2005]. The MC had an East-South-West (ESW) chirality, consistent with the results of Huttunen et al.[2005] described in section 2.1.5. The MC also had an extremely strong axial B-field component of ~ -56nT with a steep inclination of 73.4º, nearly perpendicular to the geomagnetic field. Such steep southwards inclinations of the axial field in MCs are associated with geomagnetic storms, whereas northwards inclinations are not [Gopalswamy et al.2005a]. Alex et al. [2006] associated another flare event at 07:23UT with the superstorm, however they do not argue why this particular associated CME was a plausible candidate. Also Srivastava [2005] studied solar images from LASCO and EIT, and found evidence of several flares within the time period from ~07:30 UT- 09:00 UT. All were associated with the AR 501. Some important parameters of the CME from his article are summarized in Table 4.1-1 [Srivastava, 2005].

The velocity of the CME near the Sun was approximately 1660 kms^{-1}. The associated MC was heavily decelerated during propagation (~5.2 ms^{-2}, nearly following the linear relation between acceleration and CME-speed near the Sun described by Gopalswamy et al.[2001]). Near the Earth (1AU) the MC

had a measured velocity of 738 kms^{-1} in the leading edge. Due to expansion of the MC, the trailing edge had a measured velocity of 532 kms^{-1}, giving an average cloud speed of about 600 kms^{-1} [Gopalswamy et al., 2005a].

Active region	AR 10 501
Location	S02E18
Area	$3.7 \cdot 10^7 A_\odot$
Number of sunspots	25
Area per sunspot	$1.5 \cdot 10^7 A_\odot$
Field strength	2600-3000 G
Flare Class	M3.9
Halo	Full
Initial Speed	1660 kms^{-1}
Magnetic energy	$3.5 \cdot 10^{32}\ ergs$
Shock speed	730 kms^{-1}
Ram pressure at L_1	$1.7 \cdot 10^{-7}\ dynes\ cm^{-2}$
B_Z, B_T	-55 , 60 nT
V_{Bz}	35.75 mV/m
$T_{Bz\ (duration)}$	13 hr
$V_{BZ}T_{Bz\ (interplanetary\text{-}magnetospheric\ coupling\ parameter)}$	464.75 (mV/m) hr

Table 4.1-1: The most important parameters classifying the solar source of the superstorm event of November 20, 2003. The source region is relatively small, but the interplanetary-magnetospheric coupling parameter is high. The initial speed of the CME contributes to a high ram pressure and consequently strong geomagnetic activity [Srivastava, 2005].

On November 20, 2003 ACE was located at (240.4, 26.8, -9.5) R_E in GSE-coordinates[4]. Figure 4.1-3 shows the MATLAB-plots of the solar wind parameters at measured by ACE SWEPAM and MAG. The red and green lines indicate interesting features. In the first plot, Figure 4.1-3a), we notice a sharp and sudden increase in the velocity around 07:30 UT, which is consistent with the results Gopalswamy et al. [2005a] found. They argued that this was the arrival of the upstream shock that hit ACE at 07:28UT and that the MC itself did not arrive at ACE before about 10:00UT. The peak velocity occurs at approximately 08:30UT and is just below 750kms^{-1}. The next peak is at the arrival time of the MC around 10:00UT. After that, the velocity slowly declines during the passage of the cloud. Figure 4.1-3b) shows various peaks in the solar wind proton density throughout the event. The mean density calculated from this dataset in MATLAB, was 12.3cm^{-3}.

[4] GSE-coordinates are Geocentric Solar Elliptic coordinates with x-axis pointing from Earth towards the Sun, y-axis in the ecliptic plane pointing towards dusk, and z-axis pointing towards ecliptic north pole [Hapgood, 1992].

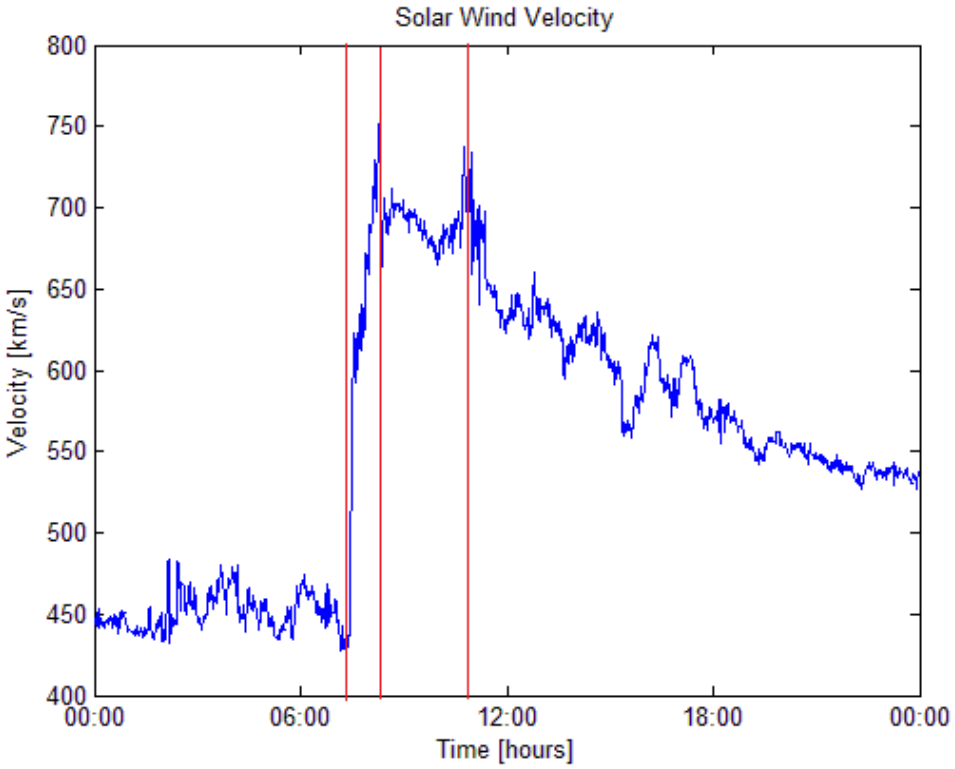
Solar Wind Velocity
Velocity [km/s]
800
750
700
650
600
550
500
450
400
00:00
06:00
12:00
18:00
00:00
Time [hours]

a)

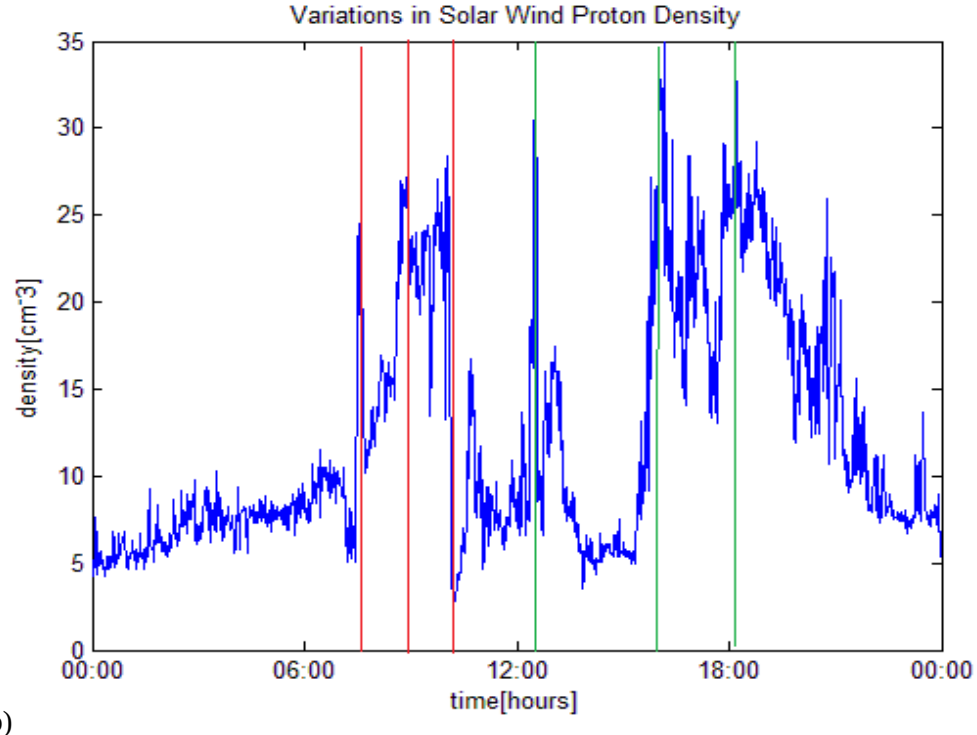
Variations in Solar Wind Proton Density
density[cm^3]
35
30
25
20
15
10
5
0
00:00
06:00
12:00
18:00
00:00
time[hours]

b)

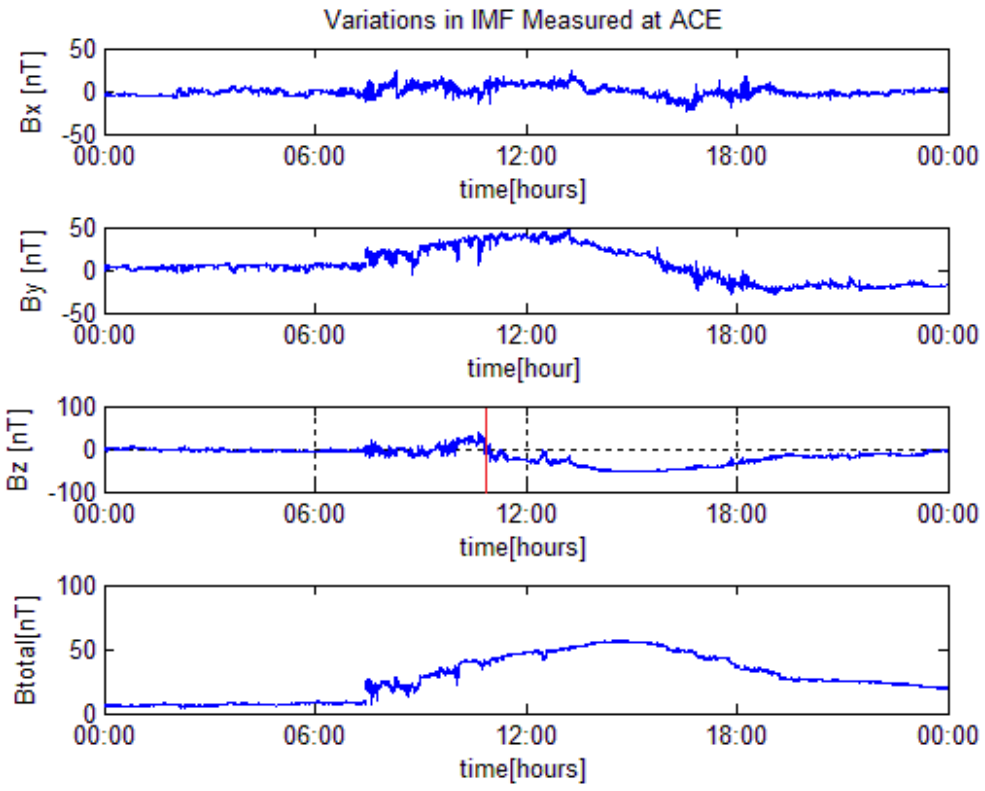

c)

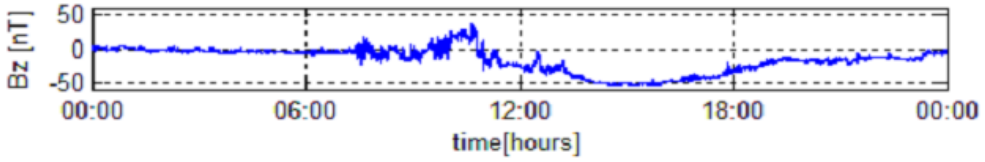

d)

Figure 4.1-3: a) The solar wind velocity measured during the day on November 20, 2003. b) The proton density variations.Red and green lines correspond to interesting incidents. c) variations in the IMF-components. The red line indicates the arrival of the MC. d) A close up of the Bz-component of the IMF.

Figure 4.1-3c) shows the variations in the different IMF-components. The By-component is slightly positive at first, but turns negative about 17:30UT. The Bz-component turns negative as the MC arrives and remains negative during the whole passage of the cloud and recovery phase, duration of more than 12 hours. Figure 4.1-3 d) shows the Bz-component which is negative during the whole passage of the magnetic cloud. The minimum value is about -50nT, which is fairly close to the result of Gopalswamy et al. [2005a]. The delay time between ACE and the magnetopause was estimated to be about 43 minutes for my computations (See section 3.5.1).

4.1.2 The Geomagnetic Behavior

A storm sudden commencement (SSC) was reported at 08:03UT the actual day by e.g. Becker-Guedes et al. [2007] and Alex et al. [2006]. The time of incident matches well with the arrival of the up-stream shock monitored at ACE 07:28UT, given a delay time of ~ 35 minutes. Alex et al. [2006] associates the arrival of shock at 07:40UT, but they have used an ACE-location at ~240R_E as basis for their calculations.

Considering Figure 4.1-3d), there are two small peaks in the Bz-component around 12:00 UT. Mishin et al. [2007] studied substorm-events during the time interval from 00:00-14:00UT during the same day. Their goal was to present energetic parameters of the ionosphere and magnetosphere to compare substorms and driven events, and consider the processes of current disruptions driving them. They found that, when the Bz-component turned northward at 10:30UT, the solar wind dynamic pressure dropped, but the AE-index revealed no substorm indications. They explained this as a so-called null event described by Lyons et al. [2005]. In short; a null event means that the sudden turn in the IMF-Bz-component leads to a decrease in the solar wind and plasma sheet E-field. At the same time, the magnetic field in the plasma sheet also decrease due to the drop in solar wind dynamic pressure. The ratio of E and B therefore remains unchanged and the plasma sheet sustains its equilibrium state [Mishin et al. 2007; Lyons et al. 2005]. This is why there are no peaks in the AE-index, but rather a slow decrease. However; there are indications of disturbance in the magnetograms on Earth. Also the pointing flux ε' and the disturbance powers released in the ionosphere (Q_i) and ring current (Q_{DR}), were calculated, and there was a decrease in the pointing flux as well before 11:12UT. After that it gradually increased along with Q_{DR} deposited in the ring current. They argued that the lacking increase in Q_i stem from saturation of the ionospheric electric fields and currents between 11:12 and 12:10UT, and therefore a redistribution of the energy input to the ring current. This can be explained in terms of a replacement of the large scale current disruption in the tail (NENL), with smaller scale current disruptions (CD) without reconnection taking place in the tail. This and the partially lack of substorm indication, led to the conclusion that the magnetospheric responses in the time interval from 10:30-12:10UT was a predominant driven mode disturbance with two null events [Mishin et al. 2007]. Figure 4.1-4 illustrates what Mishin et al. [2007] found during their investigation.

The Dst-index reached a minimum of -472nT about 20:00UT during the Nov. 20 event, which gave it the status of being the largest geomagnetic storm of the solar cycle 23 [Gopalswamy et al. 2005; Ebihara et al. 2005]. The ring current and the magnetosphere-ionosphere coupling were investigated by Ebihara et al. [2005]. They found a correlation between the two density peaks in the solar wind proton density graph at ~16:00UT and ~18:00UT in Figure 4.1-3b), and two peaks in plasma sheet density measured by the LANL satellites located in the night sector at ~18:00 UT and ~20:00 UT respectively (not shown). Two of the four LANL satellites were located on each side of the magnetic midnight, and registered the two peaks almost simultaneously, indicating that the plasma sheet density increased nearly at the same time in a region from 21:00-02:00 MLT. Despite the apparent correlation, the correlation coefficient was only 0.31, which most likely is due to a more complex ion transport mechanism than expected by the looks of the data. Anyway, the increased particle density must have contributed to an enhancement of the ring current.

They also found that the Earthward shift of the inner edge of the plasma sheet was as deep as L=1.5 at the end of the main phase of the storm (19:00UT), before it retreated during the recovery phase. The plasma sheet particle density also decayed rapidly and gave rise to interchange instabilities because of a difference in density between the inner and outer edge of the plasma sheet. This instability in turn lead to a complicated distribution of multiple field aligned current (FAC) sheets because of changes in the plasma pressure distribution within the plasma sheet. These FAC-sheets may also have contributed to the observed fluctuations in the cross polar cap potential. The DMSP F13-satellite measured a

potential drop of 200kV during over flight from dawn to dusk [Ebihara et al. 2005].
Figure 4.1-5a) shows the Dst-index with hourly values plotted from data from WDC Kyoto. Since hourly values give a poor time resolution, the ASY-H index provides a more accurate estimate of the disturbances in the H-component of the geomagnetic field. Figure 4.1-5b) shows a five minute resolution plot, where the minimum value reaches ~ -470nT , which is consistent with the results found by e.g. Gopalswamy et al. [2005a].

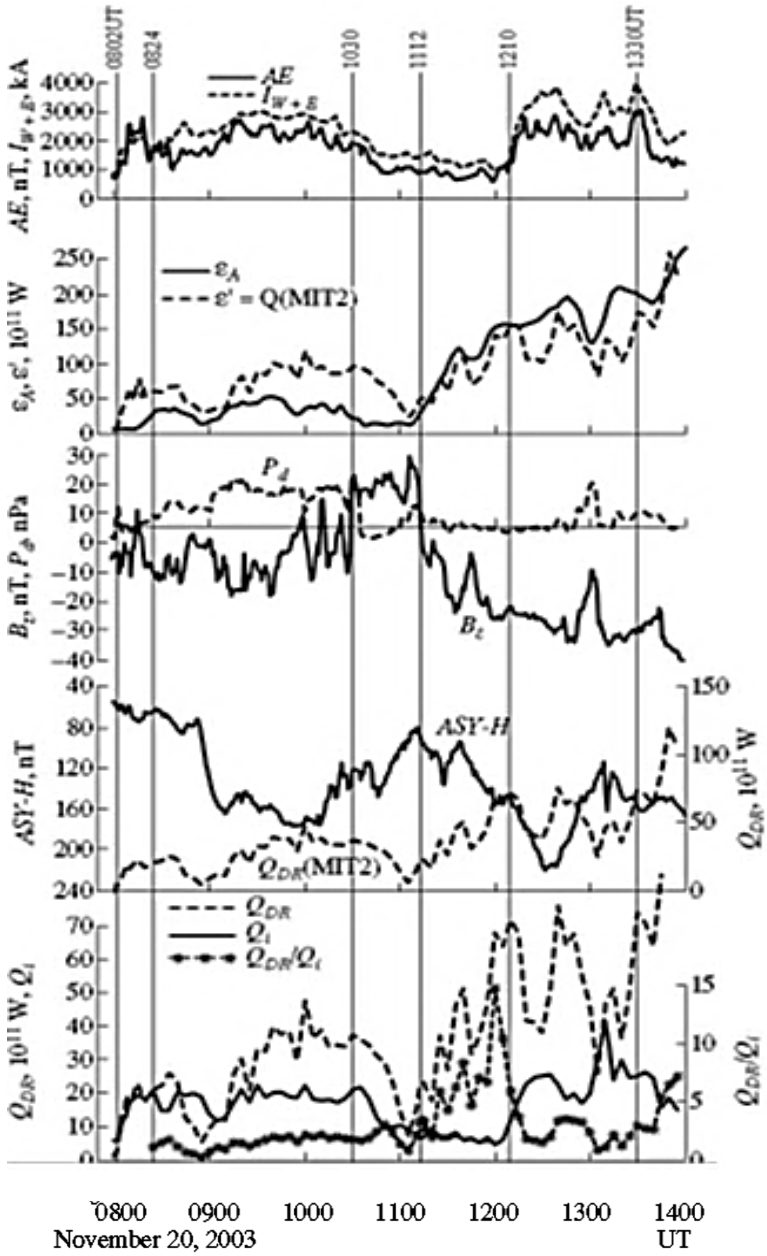

Figure 4.1-4: The panels shows the different parameters investigated by Mishin et al.[2007]. From the top; the AE-index and total electro jet currents, the Poynting flux (two models), the solar wind dynamic pressure and IMF Bz-component, the asymmetric disturbance in H-component (ASY-H) and ring current disturbance power, and the disturbance powers of ionosphere and ring current along with their ratio. One can notice the simultaneous increase in Q_{DR} and Poynting flux in contrast to decrease in IMF Bz, AE-index and solar wind dynamic pressure. Adapted from: Mishin et al. [2007].

a)

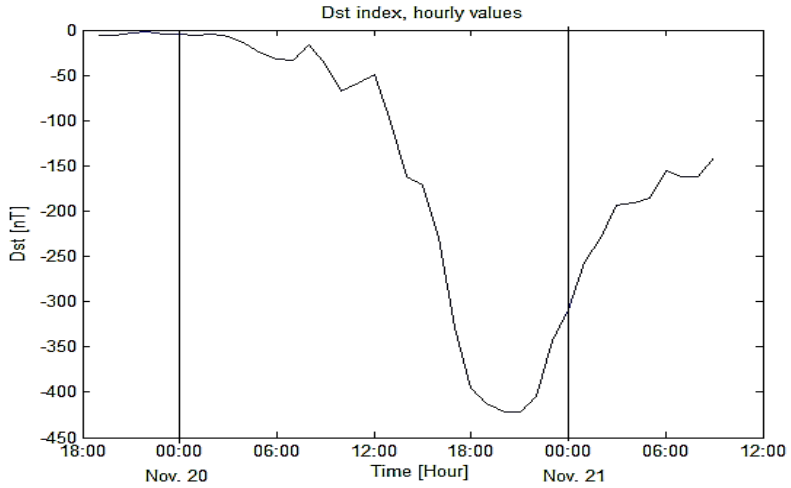

b)

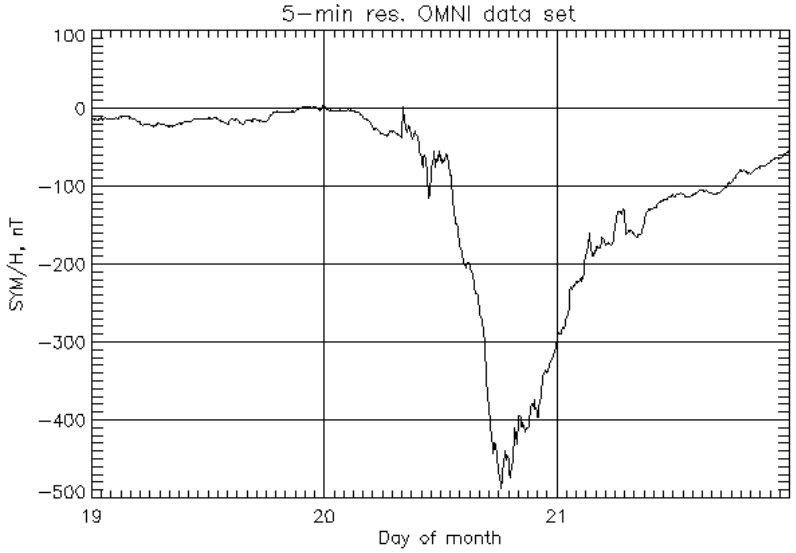

Figure 4.1-5: a) The plotted hourly values of the Dst-index reveals a minimum value of -422nT at 20:00UT. (Data was downloaded from*: http://wdc.kugi.kyoto-u.ac.jp/dstae/* and plotted with MATLAB). b) The SYM-H plot from OMNI reveals a minimum in vicinity of -470 nT at 20:00UT Credit: GSFC/SPDF OMNIWeb, (*http://omniweb.gsfc.nasa.gov*).

In addition to the Dst- and SYM-H indices, the auroral electro jet index (AE) reflects the magnetic disturbance in the auroral zone. As mentioned in section 2.4.4. the AU index refers to the eastward electrojet and AL to the westward. Due to the rotation of the Earth, Norwegian main land is situated underneath the MLT evening and midnight sector of the auroral oval during nighttime. During disturbed conditions the westward electrojet is enhanced due to the contribution from the storm time current system in the tail [Prölss,2004]. Tomita et al. [2011] found that, during disturbed times, the AU ranged from about 15:00-20:00 MLT and the AL form 00:00-06:00 MLT. Gjerloev et al.[2003] discovered that the electrojets overlap in MLT approximately two hours (20:30-22:15 MLT). During this particular superstorm, the estimates from the electrojet boundary plots calculated from the IMAGE-magnetometers reveals that the overlap occurs between 12:00 and 14:00 UT (see Figure 4.1-6).

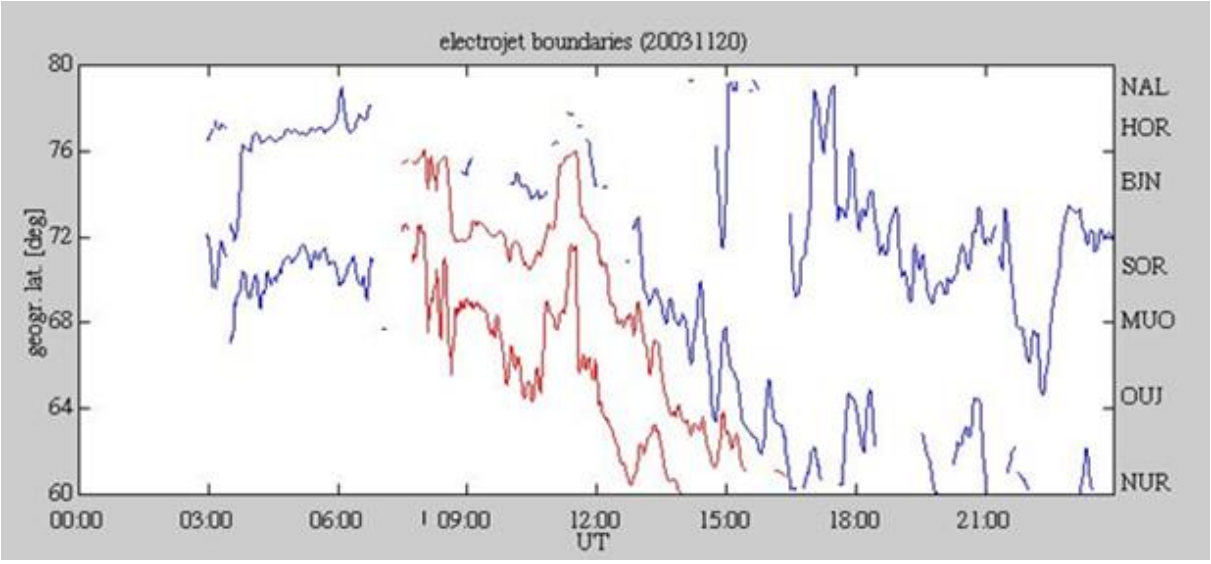

Figure 4.1-6: The calculated electro jet boundaries for selected magnetometer stations along the IMAGE chain. The red line is the eastward electro jet associated with positive disturbance in the H-component, whereas the blue line indicates the westward electro jet. Graph taken from: IMAGE at: *http://space.fmi.fi/image/beta/?page=il_index*

Alex et al. [2006] investigated the energy input in the magnetosphere during the Halloween storms and the November 20 superstorm. The solar wind energy that enters the magnetosphere is represented by the energy flux parameter ε, that was introduced by Perrault and Akasofu in 1978. The ε-parameter depends on the magnitudes of the solar wind velocity and the IMF, and is related to the Poynting flux. During the November 20, storm, the ε increased to a magnitude of $2.8 \cdot 10^{13}$ W at 15:40 UT, and slowly decreased throughout the rest of the day [Alex et al. 2006]. Table 4.2-1 illustrates the energy dissipation and consumption Alex et al. [2006] found in their study.

Average energy dissipated	Ring current injected power	Auroral precipitation energy consumption	Joule heating energy consumption
$3.3 \cdot 10^{12}\ W$	$1.1 \cdot 10^{12} W$	$5.5 \cdot 10^{11}\ W$	$1.6 \cdot 10^{12} W$

Table 4.1-2: The magnetospheric energy input during the superstorm November 20.
Adapted from Alex et al. [2006]

4.1.3 The ionospheric behavior

During the main phase of the storm, the K_p –index reached maximum (K_p = 9) as the Dst-index continued dropping. At 16:00 UT, Ebihara et al. [2005] reported that the polar cap boundary reached as low as ~60º MLAT, almost coinciding with the Heppner-Maynard boundary [Imber et al. 2013], and the DMSP F-13 satellite measured at cross polar cap potential (CPCP) drop of 200 kV (dawn-dusk). The expansion of the ionospheric flow boundary was investigated with DMSP-satellites by Pokhotelov et al.[2008] in the same interval of time. They found that the equatorward ExB-convective flow boundary extended as low as ~35º MLAT, as shown in Figure 4.1-7. However; they cautioned that it could be the auroral polarization streamers (SAPS) that occupied these zones, as described by Foster et al. [2005].

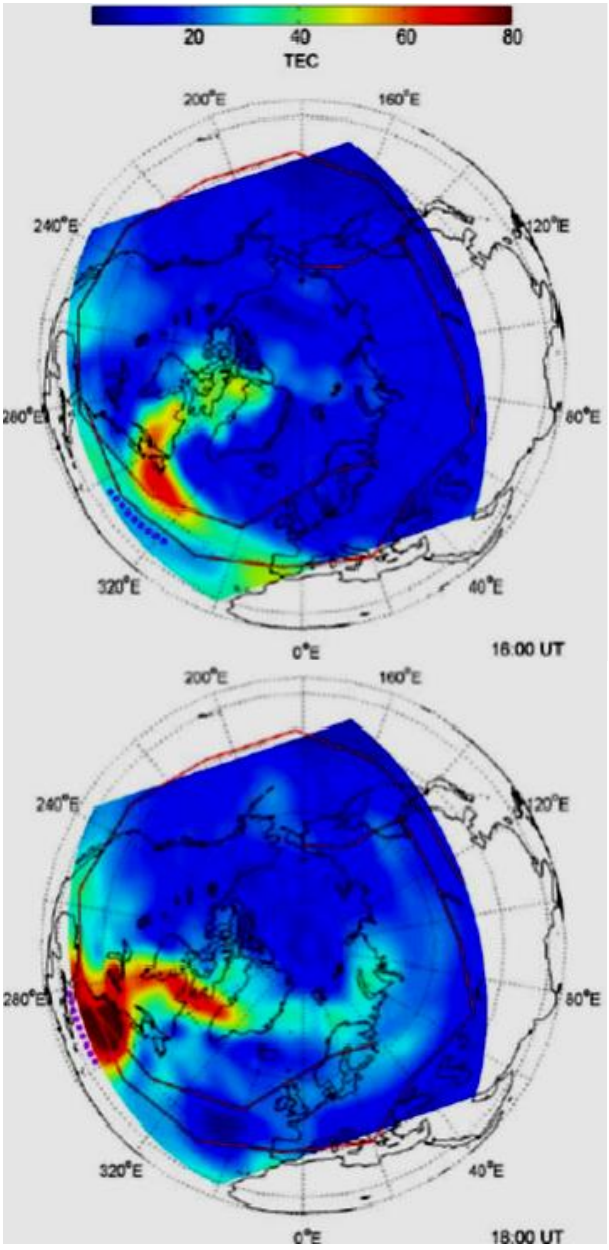

Figure 4.1-7: Top: The flow boundaries at 16:00 UT indicated with red lines on top of a TEC-map. The dotted line in the lower left corner is the longitudinal extent of the TEC anomaly over the American sector. Bottom: The same as above at 18:00 UT. This image reveals the poleward drift of the TEC –enhancement. Both figures adapted from: Pokhotelov et al. [2008].

There were also reports of plasma density peak uplifts in mid-latitudes at 16:00UT. The mechanisms behind it have been investigated by several authors. Jin et al.[2008] studied TEC over South-Korea and suggested that a strong eastward electric field caused the upraise of the h_mF2 –peak. Whereas Crowley et al. [2006], who studied the $[O]/[N_2]$ ratio over Europe and North Africa, argued that the electric fields had no impact on the uplifts. They meant that neutral winds due to heating at higher latitudes played a role in rearranging the plasma distribution, by pushing it upwards. The neutral wind explanation is supported by e.g. Bruinsma et al. [2006] and Yin et al. [2006].

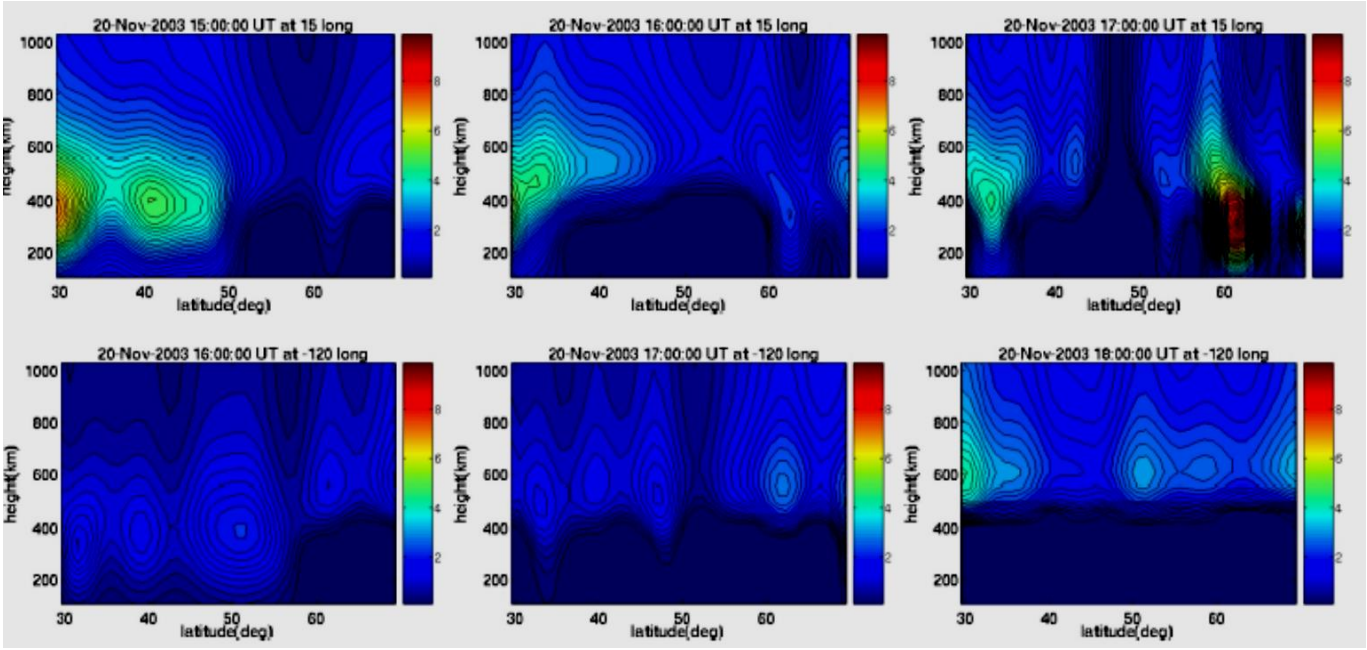

Figure 4.1-8: Upper panel illustrates the electron density (10^{11} m^{-3}) by constructed by the MIDAS-algorithm over Europe (15ºE). Notice how the peak elevation propagates from high to low latitudes from 15:00 UT (left) to 17:00 UT (right). Bottom panel shows the same development for the US sector at 120ºW. Figures adapted from: Yin et al. [2006].

Yin et al. [2006] reported that the uplift followed both longitudinal and latitudinal time delay. The uplift first occurred over Europe and moved westwards to the American sectors. During this event, the uplift first occurred at higher latitudes and then propagated to lower latitudes. Figure 4.1-8 shows that the uplift first occurred at high latitudes at 16:00 UT and then at lower latitudes about an hour later. In USA the uplifts were accompanied with TEC- elevation, while in Europe; TEC- depletion and depressed h_mF2 –peak heights. They considered this as an effect of lack of photo ionization in Europe in the evening sector, whilst USA was located in the day sector.
Yizengaw et al. [2006] also reported depressed F2 peak heights during this event. Ionosonde stations in Rome and Athens recorded that the h_mF2 was as low as ~220 km in the cusp region/ magnetic noon, and ~350 km over Europe. In the same study, comparisons between ground measurements of GPS TEC and density measurements from the CHAMP satellite found a discrepancy; whereas ground measurements found elevated TEC values, the satellite found no evidence of enhanced densities (see Figure 4.1-9. This was probably because the satellite flew at an altitude of ~400 km, well above the peak density altitude. Also Bruinsma et al.[2006] used the CHAMP satellite along with the GRACE satellite to investigate density anomalies that occur during geomagnetic disturbances. These are large scale gravity waves that propagate from high latitudes to low latitudes with periods of 1-3 h, and velocities of 0.5 – 1 kms^{-1}. Typical scale sizes are from 1000-10 000km and these waves are present

both in day and night. Medium scale wave structures occupy the high to medium latitudes, while small scale structures at medium to low latitudes. Becker –Guedes et al. [2007] suggested that these density anomalies could explain the spatial variations in the f_0F2 plasma frequency seen in the Brazilian sector during this event.

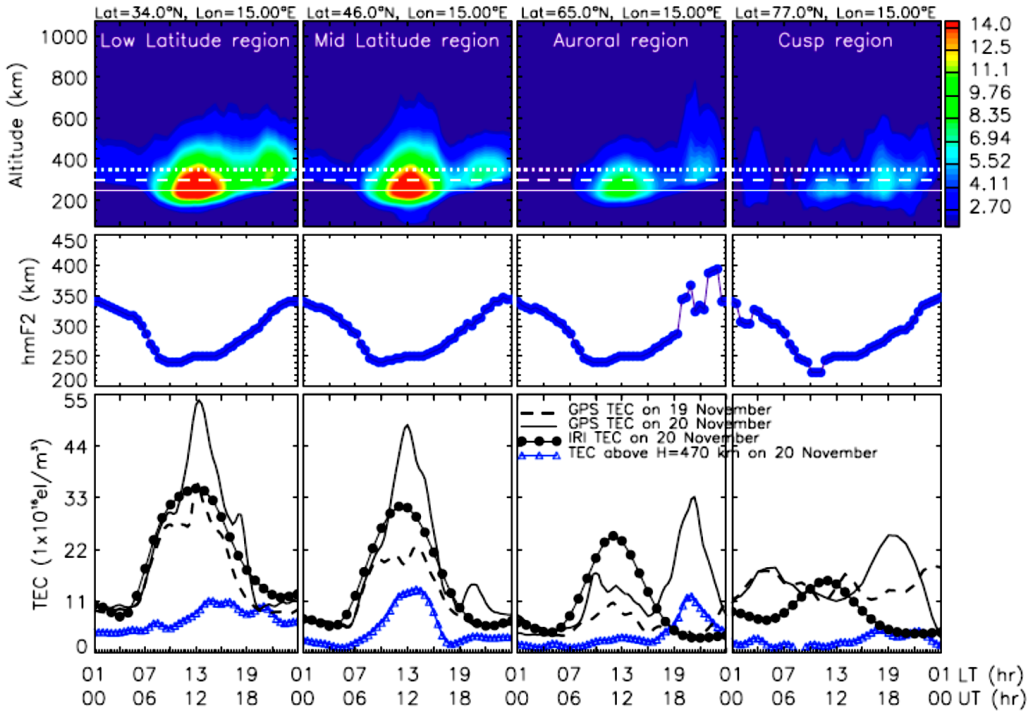

Figure 4.1-9: The unusual low observed peak densities and peak height. Figure adapted from Yizengaw et al.[2006].

What is of main interest here, are the plasma irregularities that caused the severe scintillation and satellite lock at high latitudes.

Foster et al. [2005] investigated the passage of the TOI with high latitude incoherent scatter radars at Millstone Hill, Sondrestrom and EISCAT,Tromsø, and compared the observations with the convection pattern obtained from SuperDARN and DMSP and combined GPS TEC maps. They observed a storm enhanced density (SED) plume emerge from low latitudes over the American sector with densities exceeding 100 TECU. The continuous stream of plasma extended into a polar tongue of ionization (TOI) with a cross-plume width of more than 800 km. During the TOI's passage through the cusp, across the polar cap and into the nightside, all three radars reported approximately the same characteristics of the TOI. The density peak altitude was between 400 and 500 km with peak densities $\sim 1 - 1.5 \cdot 10^{12}$ m^{-3}, which was ten times greater than the background plasma density. At altitudes from 150-1000 km, the TEC was ~55 TECU in the polar cap patch. The electron and ion temperature were characteristically low about 2000-2500 K, suggesting that the plasma was not due to particle precipitation, but rather from the storm time erosion of the plasma boundary layer which characterizes the SED [Foster et al. 2005 and references therein]. Figure 4.1-10 illustrates the convection of the TOI across the polar cap at the three different locations.

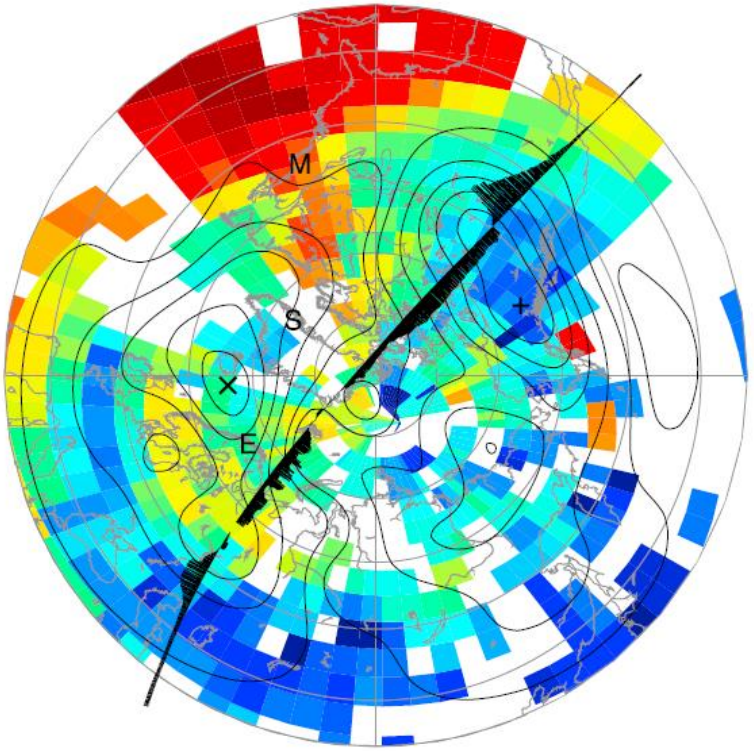

a)

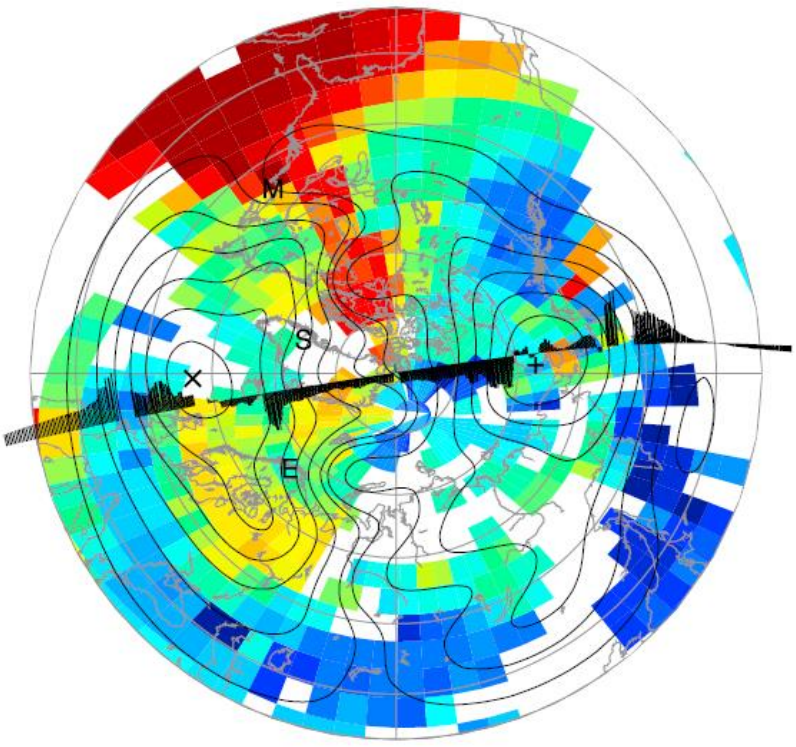

b)

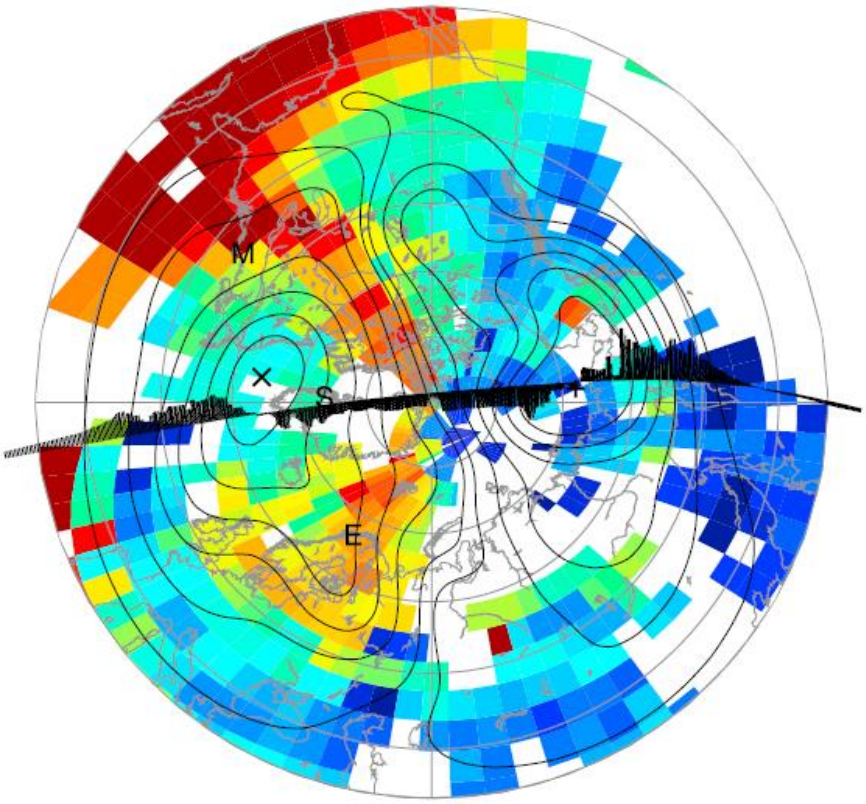

c)

Figure 4.1-10: a) At 17:30 UT the SED plume was above the Millstone Hill radar (M) and the TOI were extending through the cusp region. b) At 18:20 UT the TOI has convected into polar latitudes and is in view from Sondrestrom. c) The final scenario is the exit of the TOI/patch close to midnight sector viewed by EISCAT in Tromsø at 19:45 UT. This was 15 minutes before Dst reached minimum level. Notice the enhanced TEC at low latitudes in dusk region, which are the SAPS, and the enhanced TEC over Norway/Fennoscandia associated with the sunward auroral convection flow. The DMSP F13 measured the drift across the polar cap indicated with the black velocity vectors. All figures are adapted from: Foster et al. [2005].

De Franceschi et al. [2008] investigated the scintillation associated with the event. They used a GPS Ionospheric Scintillation and TEC monitor (GISTM) – chain covering latitudes from 53º-79º and combined GPS data with the MIDAS tomography. All data were acquired from the satellites in view over the GISTM-stations during a time interval from 19:00-19:30 UT. They observed severe amplitude and phase scintillation associated with steep TEC-gradients at the edges of the TOI/patch as illustrated in Figure 4.1-11.

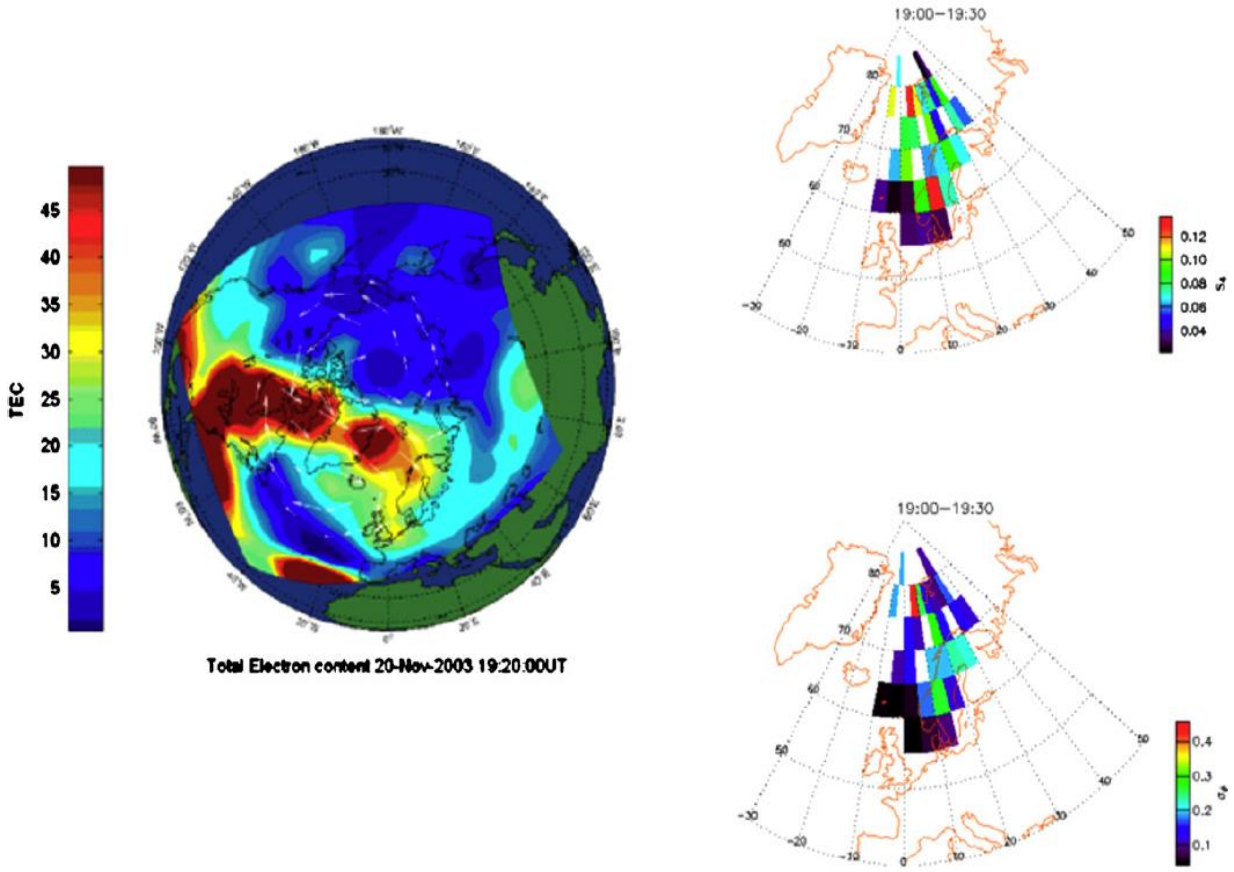

a)

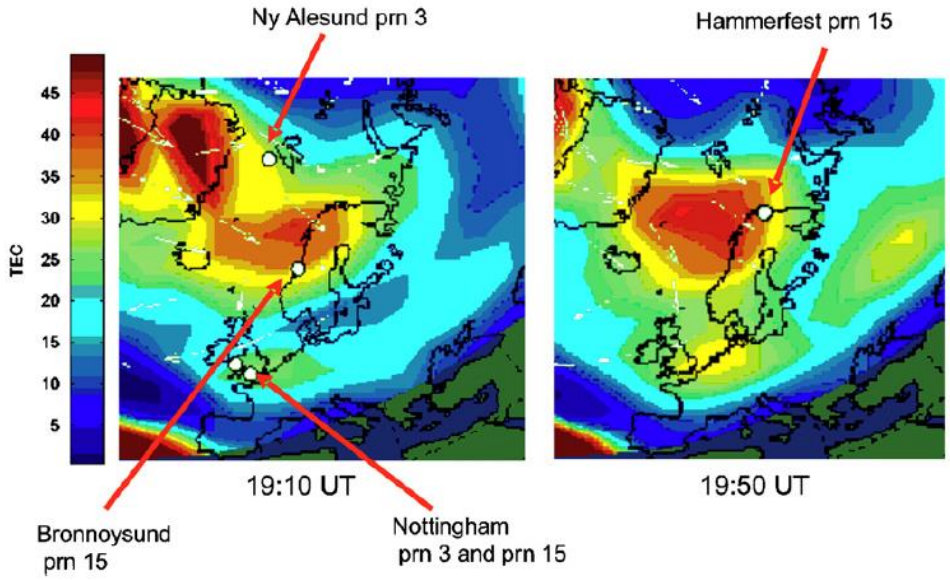

b)

Figure 4.1-11 :Left: VTEC-map of the northern hemisphere constructed from MIDAS algorithm. Notice the TOI extending from lower latitudes across the polar cap. The patch is about to exit in the midnight sector as described by Foster et al. [2005]. Right: S_4 (top) and σ_φ scintillation indices from the ionospheric projection of the GISTM-chain during 19:00-19:30UT. b) Enhanced TEC over Norway associated with the TOI/patch. The arrows are pointing towards stations recording the σ_φ – maxima for selected satellites. All figures are from: De Franceschi et al. [2008].

4.2 The SATREF data

During the storm, the NMA experienced that their SATREF GNSS stations suffered from severe loss of signals from approximately 14:00UT. Figure 4.4-1 is a plot showing the SATREF Ionospheric Model (SIM) versus the Global Ionospheric Model (GIM) illustrates delay on the L_1 frequency recorded at Hønefoss (60ºN, 10º E). The SIM data are based on signals received16 grid points with 30 seconds interval from 02:00-14:00 UT [Jensen, personal conversation in 2009]. The SIM model is more sensitive to variations in the ionosphere because it there is no smoothing or filtering applied [Jensen et al. 2008]. Therefore this plot illustrates quite well the loss of signal during the main phase of the event.

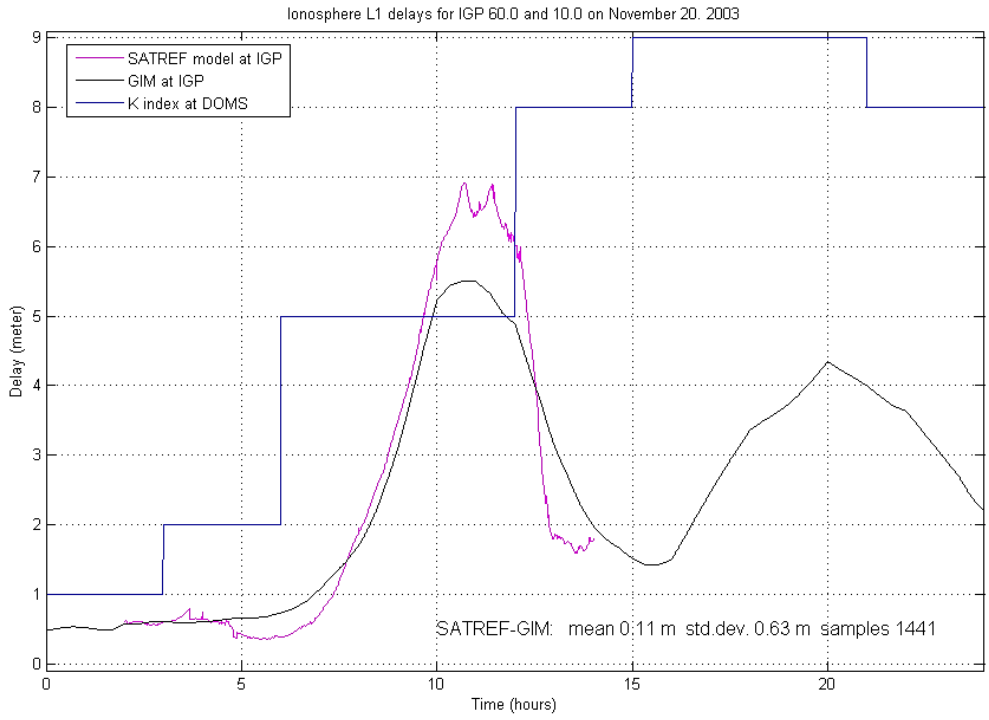

Figure 4.2-1: The SIM vs GIM plot with the increasing K_p-index registered at Dombås in the background. Credit: Jensen, A., Kartverket 2009

Data from five GNSS stations in the southern part of Norway are used to illustrate the loss of satellite signals throughout the afternoon and night, see Figure 4.2-2. The time resolution of the data is 30s and since the GPS satellites have a 12 h period and at least five satellites are required to be in view for RTK service [Trimble Navigation Limited, 2000], it becomes obvious that this led to problems in deliverance of positioning service during the event when so many time intervals were affected. Arranged from North to South, one can see that the occurrence of the problems starts around 14:00 UT for all stations and escalating from 16:00 UT. The colored bars consist of all the points in time when the receiver records the satellite time and position. Thus good reception provides continuous bars, and all blank spaces in the color bar represent a loss of satellite lock for that instant of time. Signal loss begins a little earlier at Dagali than the other stations, and Bergen is most severe affected of all stations. All stations suffer most loss of satellite lock around 20:00 UT.

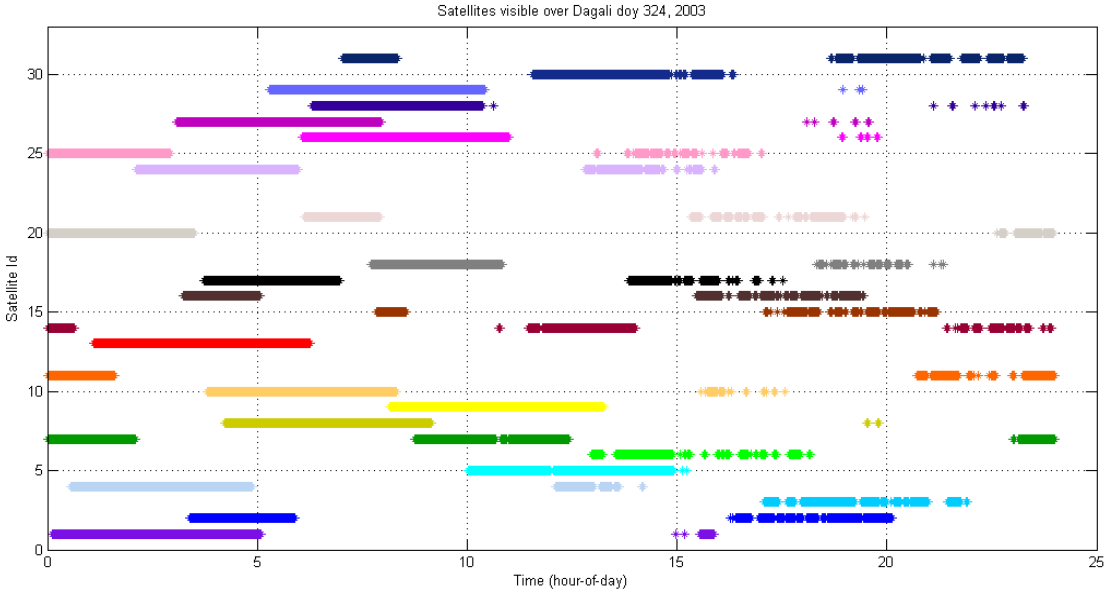
Satellites visible over Dagali doy 324, 2003
Satellite Id
Time (hour-of-day)
0
5
10
15
20
25
30

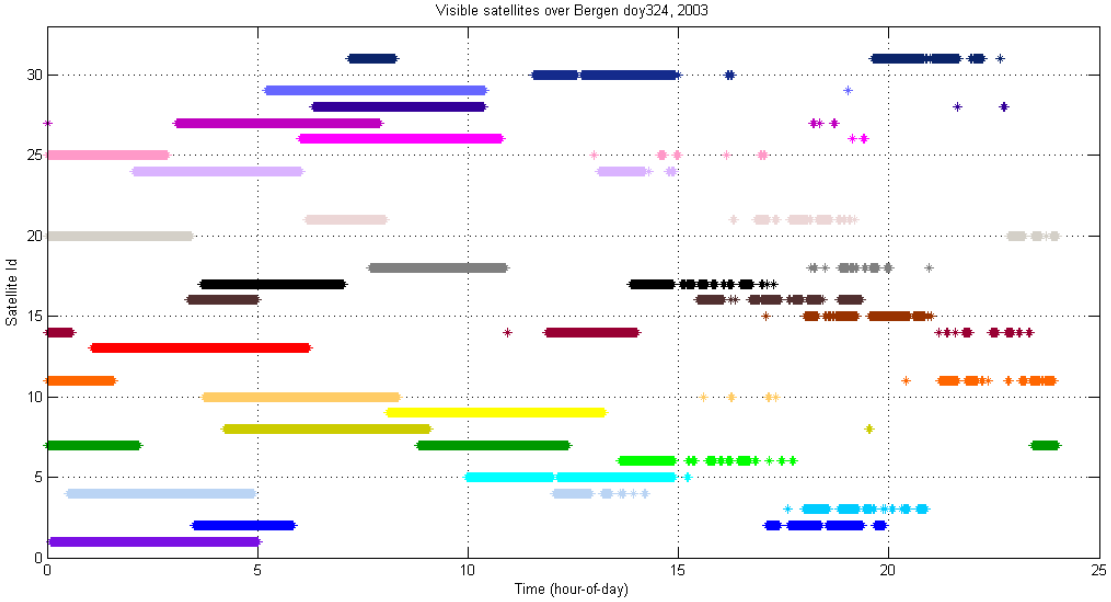
Visible satellites over Bergen doy324, 2003
Satellite Id
Time (hour-of-day)
0
5
10
15
20
25
30

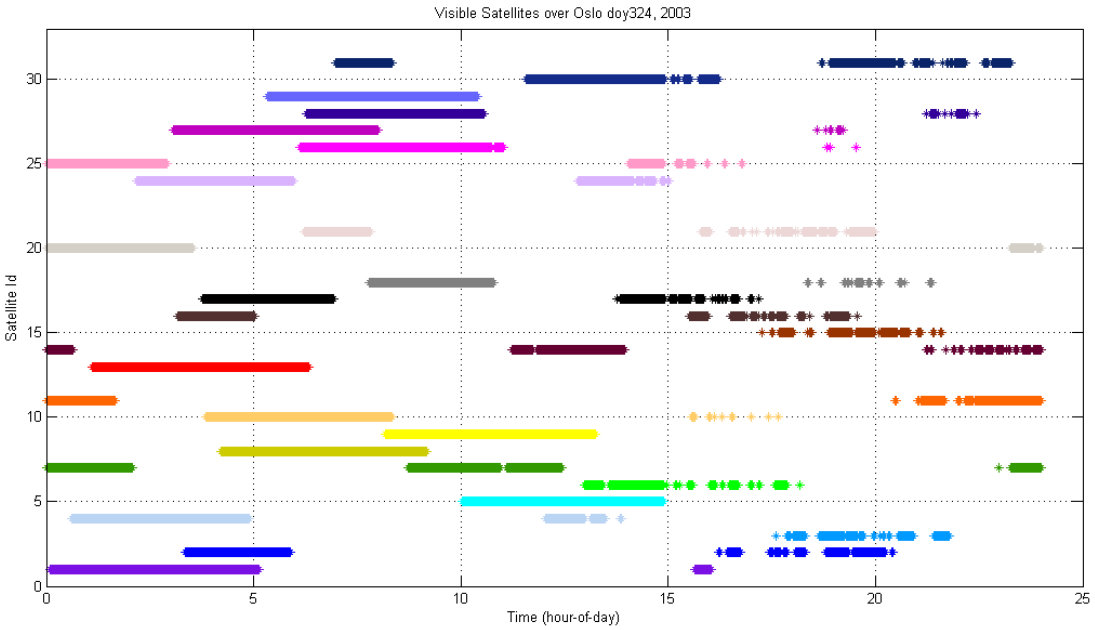
Visible Satellites over Oslo doy324, 2003
Satellite Id
Time (hour-of-day)
0
5
10
15
20
25
30

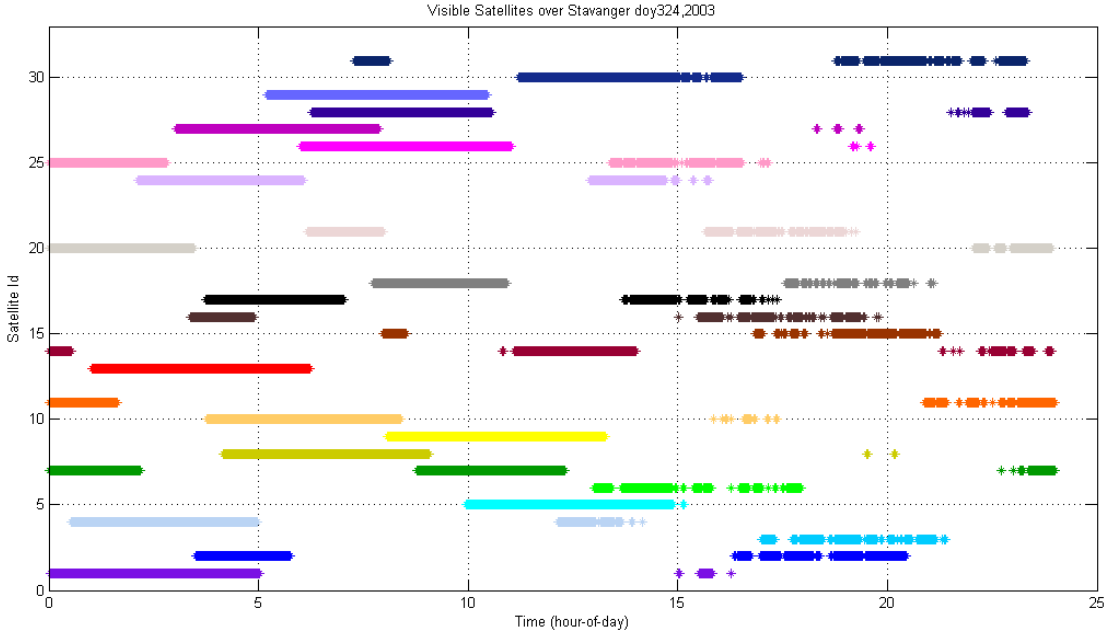
Visible Satellites over Stavanger doy324,2003
Satellite Id
Time (hour-of-day)
0
5
10
15
20
25
30

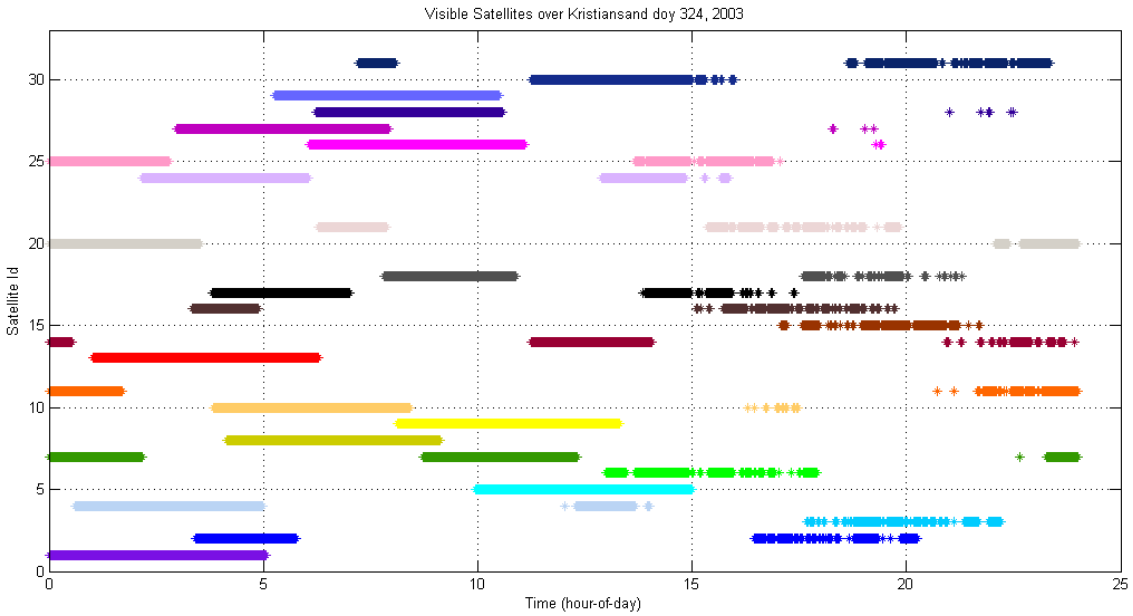

Figure 4.2-2: Plot of Satellite ID vs time. These are the 27 satellites in view over the five different SATREF GNSS stations. From top: Dagali (60.4ºN, 8.5ºE), Bergen (60.2ºN, 5.1ºE), Oslo (59.7ºN, 10.4ºE), Stavanger (59ºN, 5.5ºE) and Kristiansand (58º N, 7.9ºE).Every satellite (PRN 1-32) have their own color code and should ideally be solid bars. Blank spaces in the color bars represent loss of signal. As we can see; stations are suffering from poor reception from the afternoon as the number of blank spaces increase for all the satellites, and simultaneous loss of signals for five or more satellites indicates failed positioning.

The outage intervals vary from each station. The southernmost receivers are less affected because the satellite tracks are more overhead for these stations. Although enough satellites are present in e.g. Stavanger and Kristiansand plots in Figure 4.2-2, the signals are fluctuating so much that there are periods with coinciding blank spaces (loss of lock) with duration up to several minutes. Thus the overall RTK-service was too unstable throughout the whole afternoon and evening for all stations. This is reflected very well in the SATREF GIM-plot in Figure 4.2-1.

Since Bergen was the most affected and second northernmost of the five stations, the IPPs at 350 km for all satellites are plotted vs time illustrating the satellite elevation for this station in Figure 4.2-3. Apart from PRN 1 and 13 (which are too low on the horizon) all satellites are in view from Bergen at least in the morning, but the reception becomes poorer in the evening. As expected; the northernmost satellites are more affected than the satellites with IPPs below ~60°N latitude; however this is also the case for satellite IPPs below ~55°N latitude.

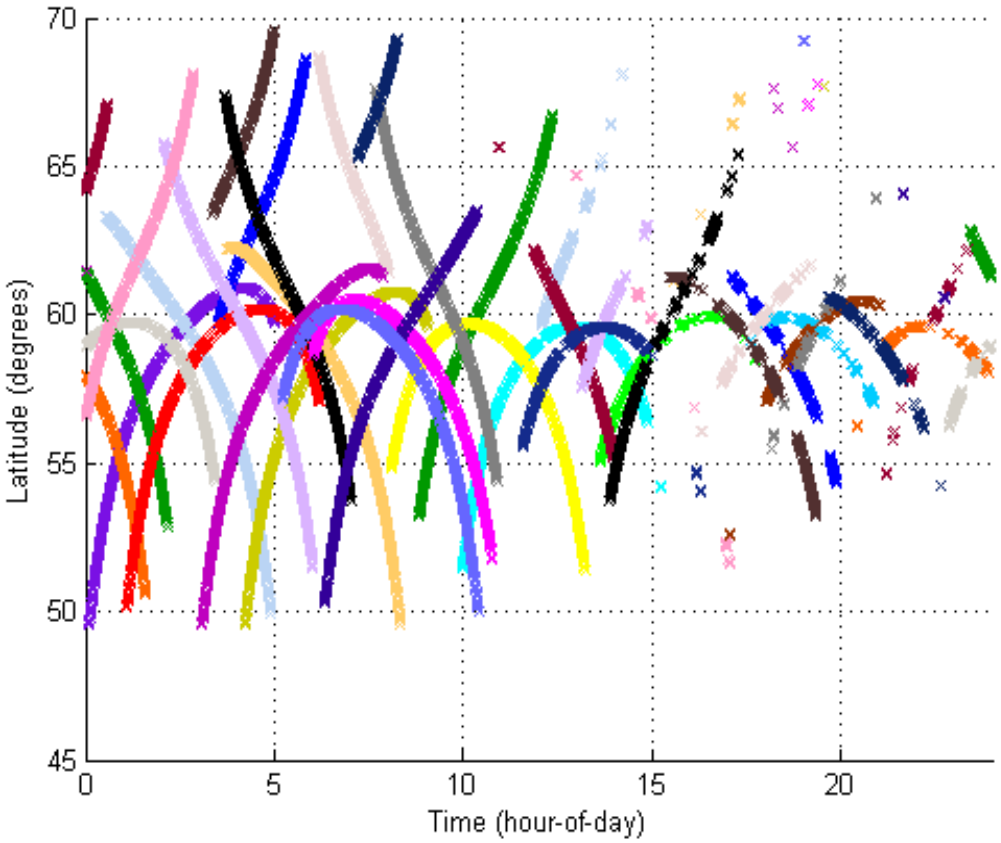

Figure 4.2-3: The elevation plot for Bergen receiver station. The color codes are the same as before, PRN 1 and 13 are not in view. As we can see the northernmost IPP tracks at 350 km altitude are strong and continuous in the morning, but are weak or missing in the evening. Satellites with IPPs above ~60° latitude are most affected in the evening. Also satellites with IPPs below ~55° latitude are affected.

Two afternoon/evening plots for Bergen station are showed in Figure 4.2-4. In figure 4.2-4a) we see that the criterion of five or more satellites in view, is compromised from approximately 15:00UT. Apart from small sporadic time intervals of a few minutes, there are generally too few satellites in view to maintain an RTK service for the rest of the day. Compared with figure 4.2-4b), the strongest signals originate from the satellites with IPPs in zenith above the receiver. Thus the weakest signals originate from the satellites with the most oblique ray path through the ionosphere, as would be expected.

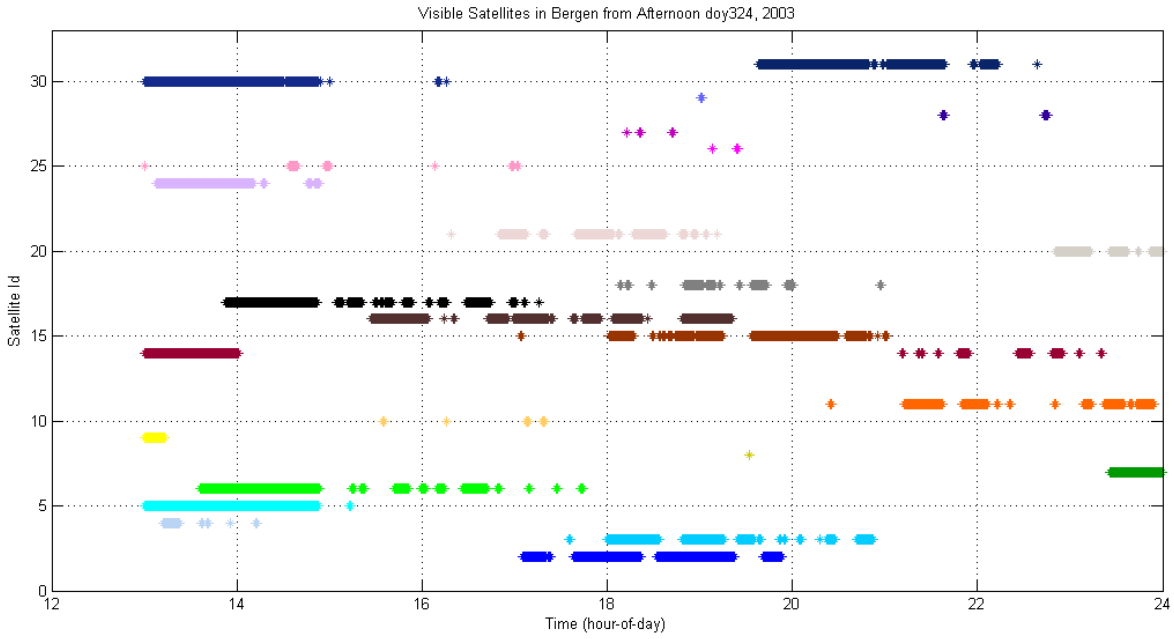

a)

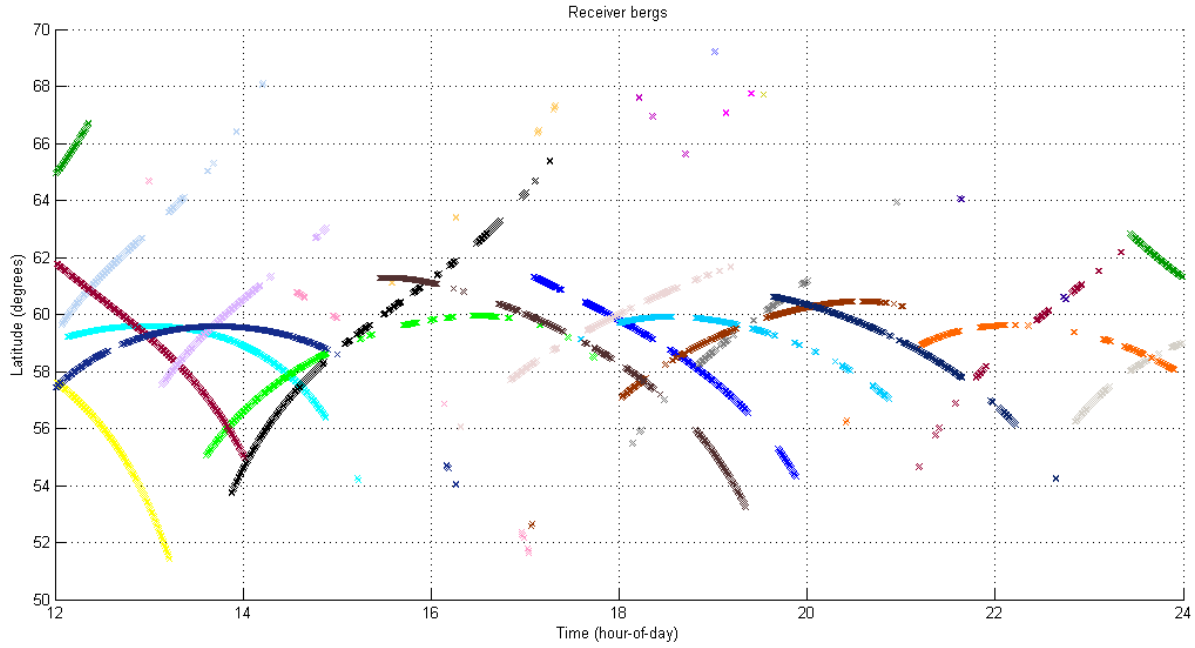

b)

Figure 4.2-4: a) Plot of visible satellites from Bergen receiver station. Simultaneous loss of lock on several satellites from ~15:00UT are visualized as blank spaces in the color bars. b) Elevation plot from the same interval of time. The signals from the satellites with IPPs approximately above the station are less affected. These are e.g. PRN 2, 3,15, 16 and 17.

The NMA Real-Time Ionosphere Monitor (RTIM) program was used in order to make the following plots from the event. The first figure series (Figure 4.2-5), is the mean ROTI observed with a two hour interval at the ground stations from 13:55-23:55 UT during the event. In the data (not shown) the ROTI on ground revealed fluctuations throughout the night and early morning with increasing values for the northern stations from ~08:00 UT. In southern parts, the ground ROTI showed variations throughout the whole day as the large values persisted in the northern part. The most severe ROTI measurements in the southern stations were recorded in the afternoon (15:00UT) and evening, but slightly lighter before midnight.

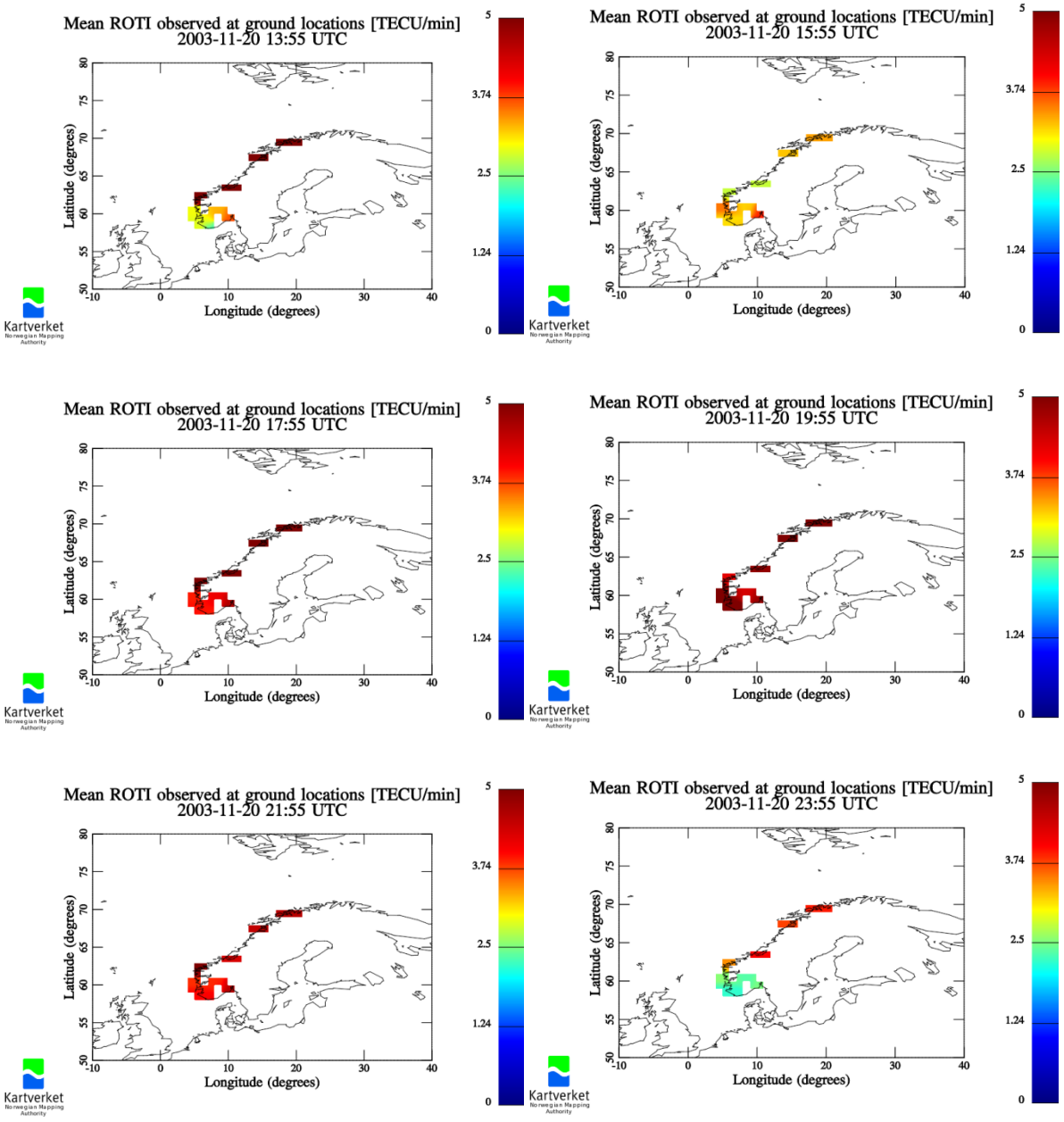

Figure 4.2-5: Mean ROTI as observed by the receiver stations in the SATREF network. Here, also stations at higher latitudes are included. The disturbances are most severe in the evening hours all over the country. Credit: Jacobsen, K.S., Kartverket, 2013.

The ROTI in Figure 4.2-6 is the ionospheric ROTI at the altitude of the IPP (350km for this dataset). Recalling section 2.5.2, the ROTI is a measure of the small scale irregularities which cause phase scintillation. When ROTI exceeds a value of 5 TECU/min, the disturbance is very severe (strong phase scintillation) [Pi et al. 1997; Kartverket, sesolstorm.kartverket.no].

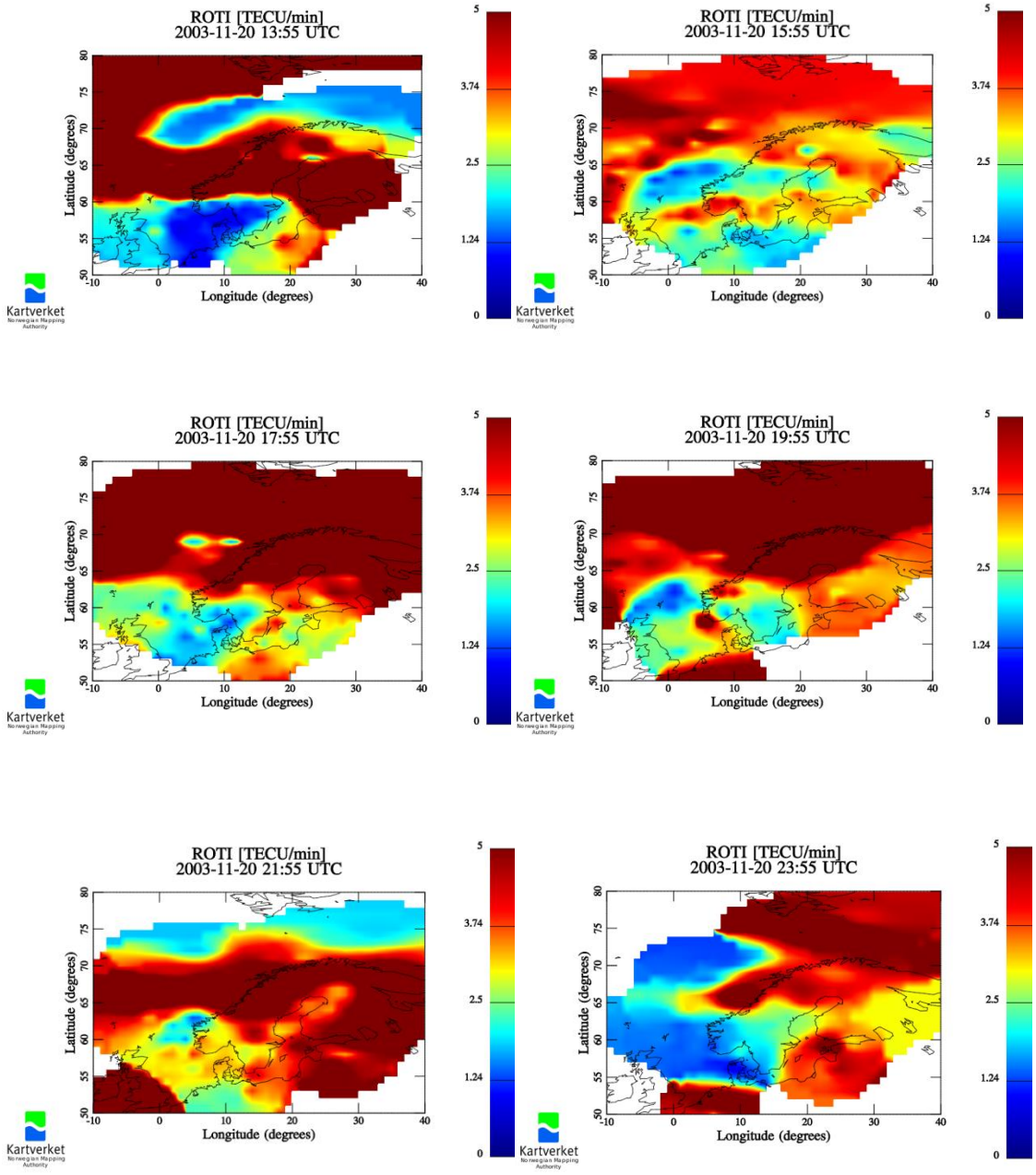

Figure 4.2-6: The ROTI seen from the altitude of the ionospheric pierce points (350 km). Same time series as in fig. (4.2-5).Credit: Jacobsen, K.S., Kartverket 2013.

The highest values of ROTI were seen outside Norway mainland, but covering Svalbard in the night and early morning. From ~10:00UT the ROTI increased over the northern stations and a zonal band of enhanced ROTI values emerged across Mid-Norway from ~14:00UT. After about an hour, the band had extended further south covering the whole mainland. The enhancements started withdrawing from the southern parts around ~19:00UT, but with large fluctuations. Just before midnight the southern stations were clear. As we can see for both series of plots, the ROTI is more severe for the stations at higher latitudes than for the five stations in this study, but also these are affected in the evening. The

differences between the ground ROTI and the ionospheric ROTI are due to the fact that the satellites seen from one point on the ground are not directly overhead, but distributed throughout the sky. Ionospheric ROTI shows where the disturbances are present in the ionosphere [Jacobsen, K.S., private communication, 2013].

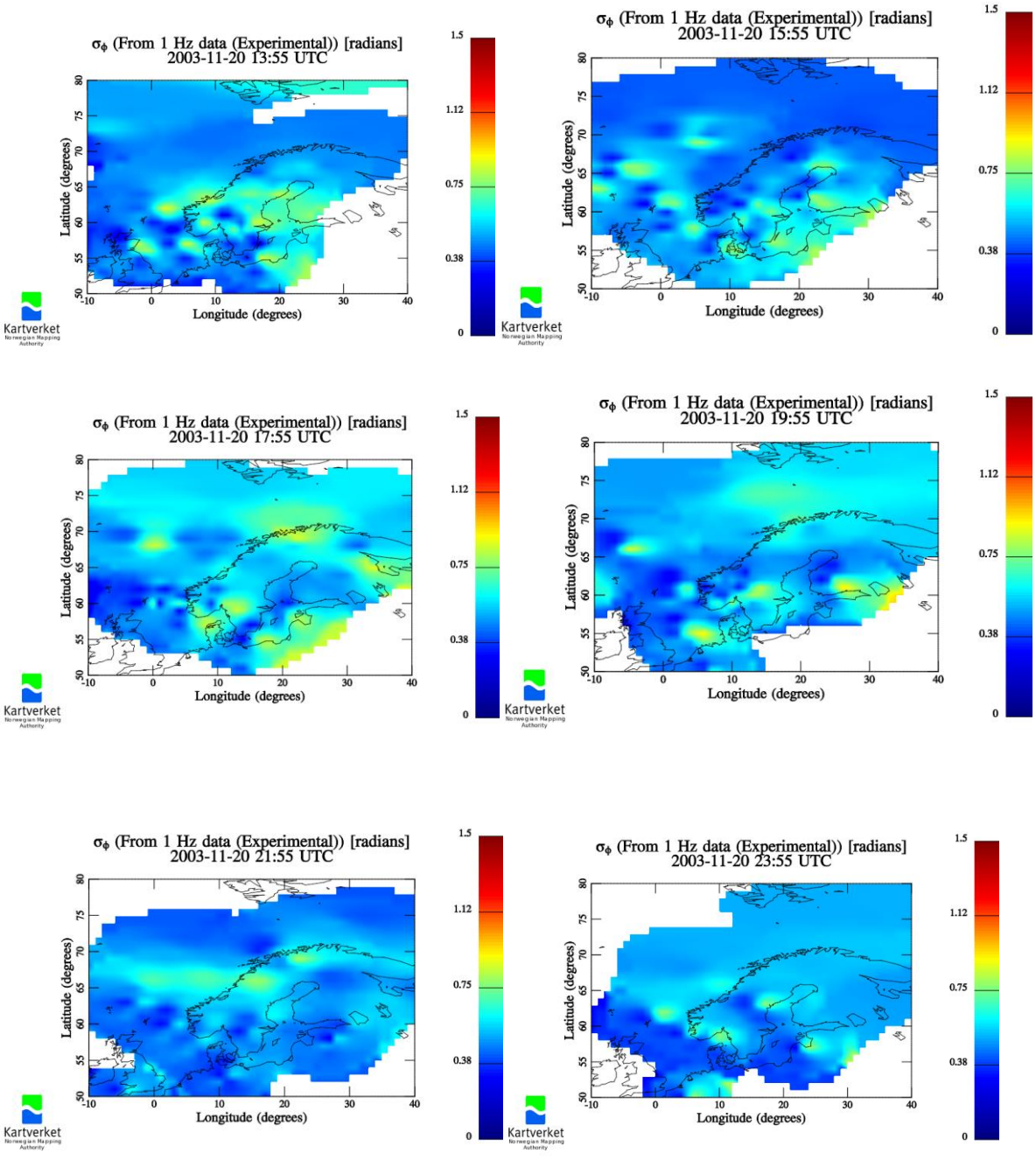

Figure 4.2-7: The experimental phase scintillation constructed from the original data through the RTIM. (Same times as in the ROTI-plots). Credit: Jacobsen, K.S. , Kartverket 2013

The phase scintillation plots in Figure 4.2-7 reveal that there is moderate scintillation throughout the whole day, with enhancements in the afternoon and evening. The strongest scintillation recorded exceeds 0.8 radians, which on the other hand is quite strong. (Recall section 2.5.3.1). It is worth mentioning that these plots are sampled at a 1.0 Hz frequency which is not recommendable, and thus may contain noise and errors [Jacobsen, K.S., private communication, 2014] .

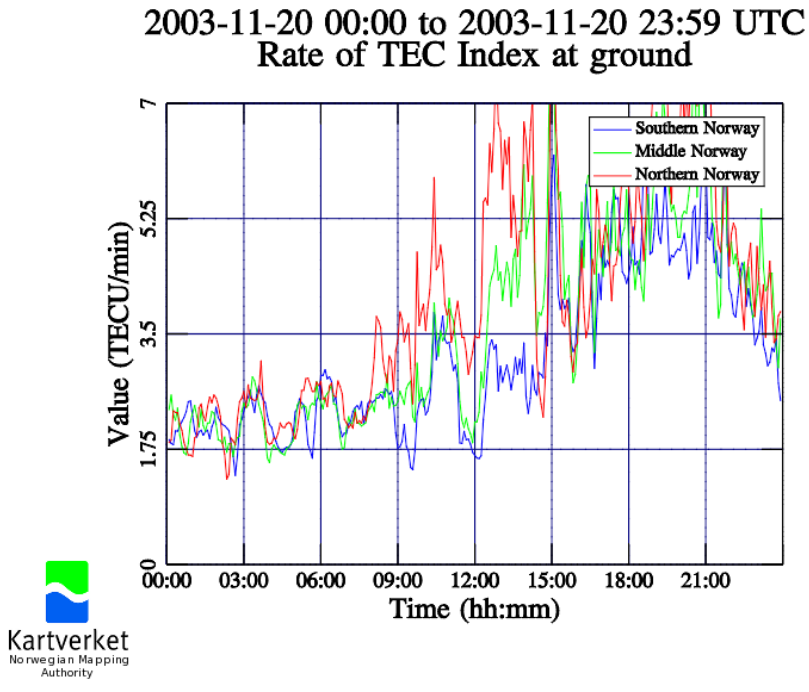

a)

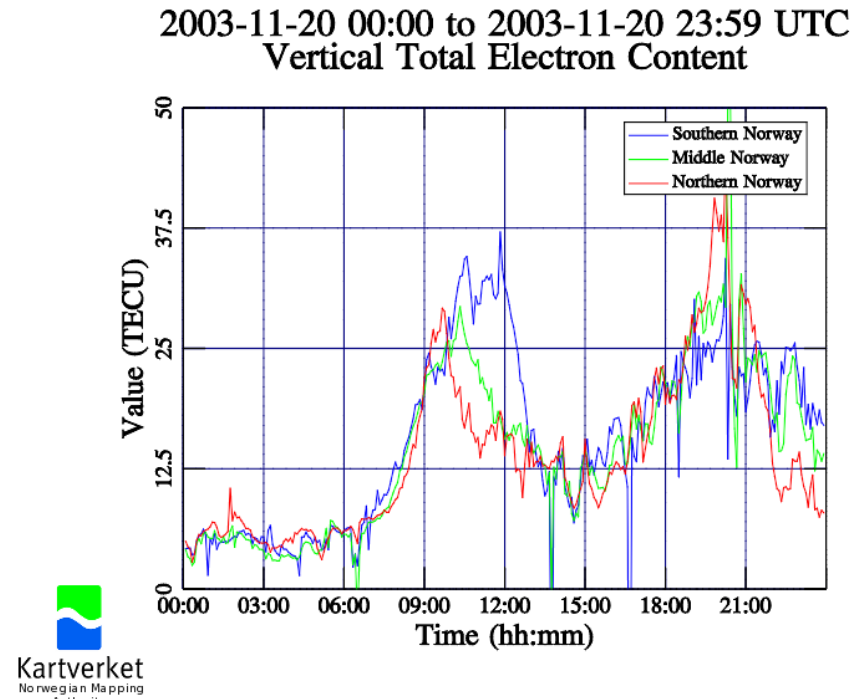

b)

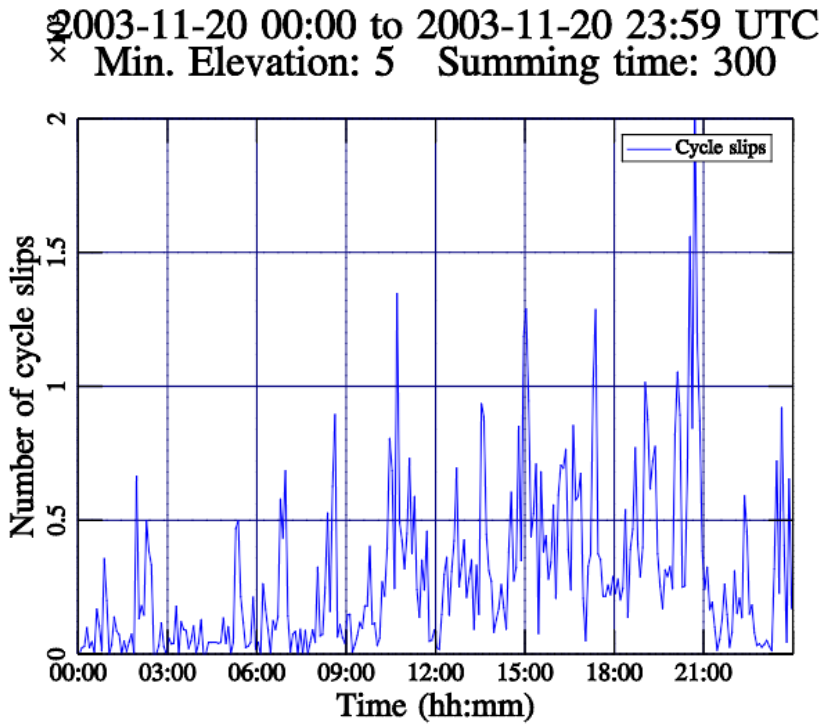

Kartverket
Norwegian Mapping Authority

c)

Figure 4.2-8: a) The ROTI at ground shown as a time series. The different colors refers to different regions. b) The VTEC shown as a time series for the whole event. Notice how the peaks propagate from north to south with time. c) The number of cycle slips detected throughout the day. All figures have coinciding peaks with variations in density and solar wind. Credit: Jacobsen, K.S. , Kartverket 2013

In Figure 4.2-8a) the ground ROTI is shown as a time series. Stations are divided into northern, mid and southern regions. The red line represents the ROTI registered by receivers in Northern Norway and it clearly peaks around 14:00UT and 20:00UT. From 15:15UT all three regions peaks simultaneously before they sharply drop and slowly increase to a new peak value around. 20:00UT. The VTEC in Figure 4.2-8b) reveals an opposite behavior, whereas the VTEC peaks for the southern stations before midday and steeply declines to a value of ~12 TECU. The northern stations register the peak enhancements in VTEC a little after 09:00UT followed by the stations in the mid region shortly after. This behavior suggests that the VTEC enhancement propagates from north to south. All three regions fluctuate around ~12 TECU before they start to climb towards a new peak around 20:30 UT where Mid-Norway reaches the highest value of 50 TECU. Such high VTEC values in the evening are unusual, thus it must be due to plasma patches from the dayside [Jacobsen, K.S., private communication,2014].
Figure 4.2-8c) illustrates the number of cycle slips throughout the event. Although this plot is meant for monitoring the RTIM performance, and thus may contain some false positive values [Jacobsen, K.S. private communication, 2014], the pattern mostly correlates well with the other data presented.

4.3 Observation and Investigation

In this section I will look deeper into some of the data presented in the former sections. I will also include some other data for additional support and closer investigation of the cause of scintillation. I will look at different times and events of interest in order to describe the dynamics throughout the day

4.3.1 Electrojets and Aurora

The satcom outage did not develop until after 14:00UT on November 20, 2003. Nevertheless; it was sudden and unexpected when it finally happened. In order to try to understand what led to this outage, we need to investigate the storm dynamics prior to the outage. Due to the long duration of the outage, we also need to understand why the problems persisted throughout the day. Here follows a brief study of the geomagnetic development at interesting times during the event.

The induced Hall currents and enhanced electrojets cause the perturbations in the geomagnetic field measured by magnetometers. Recall from section 3.3.2 that the positive bay in the x-component of the magnetogram corresponds to the Eastward electrojet (EEJ). This current flow in the dusk auroral oval and its strength is derived in the AU-index.
Figure 4.3-1 a) is a magnetogram of the x-component derived from selected stations along the IMAGE magnetometer chain. Incidents of interest are marked by the colored lines at certain UTs. The corresponding local AU/AL index from IMAGE is also marked identically in Figure 4.3-1b). This figure will form the basis of the discussion of the development of the geomagnetic activity.
The onset caused by the upstream shock at 08:03UT is marked with the red line. It is a positive spike in the x-component as expected when dayside merging initiates.
The orange line, a little prior to 10:30UT marks the reversal of the IMF Bz-component from negative to positive. We can see in both the magnetogram and the AU-index that there is an increase in the Eastward electrojet (EEJ) with a peak of ~700nT at 10:30UT. Normally this indicates the growth phase of the substorm when reconnection takes place on the dayside [McPherron in Kivelson and Russell, 1995]. In Figure 4.3-4 in next section, the OVATION plot from 10:30UT shows a contracted polar cap which is characteristic for northward IMF Bz [Milan et al. 2003 in Moen et al., 2004].
The light green line at about 11:30UT indicates the reversal of the IMF Bz back to southwards orientation. This marks the arrival of the MC, and the onset of a new growth phase. In the interval between the two green lines in the plot of the local AU/AE index, there are fluctuations in the electrojets which are caused by intensifications of the magnetic activity. Negative excursions in the AL index correspond to an increase in WEJ caused by tail reconnection. Hence positive excursions in the AU index indicate dayside reconnection [McPherron in Kivelson and Russell, 1995]. These fluctuations could imply unbalanced reconnection (see section 2.4.2). Such transient reconnection events are shown to play a role in patch formation (recall section 2.4.3.1). Thus the ongoing storm along with storm enhanced densities, as described by e.g. Foster et al. [2002], could produce patches in the dayside.

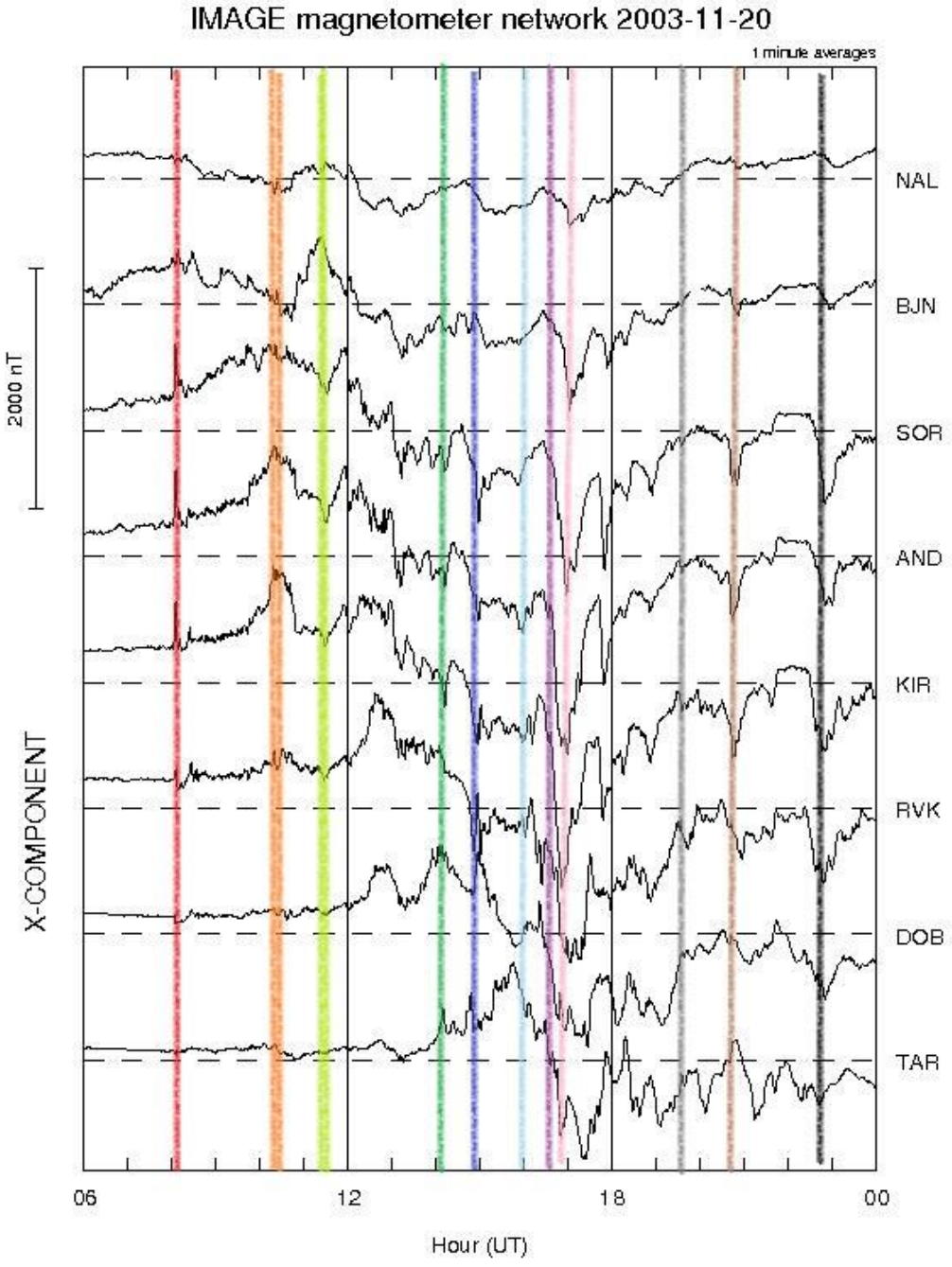
IMAGE magnetometer network 2003-11-20
1 minute averages
NAL
BJN
SOR
AND
KIR
RVK
DOB
TAR
2000 nT
X-COMPONENT
06
12
18
00
Hour (UT)

a)

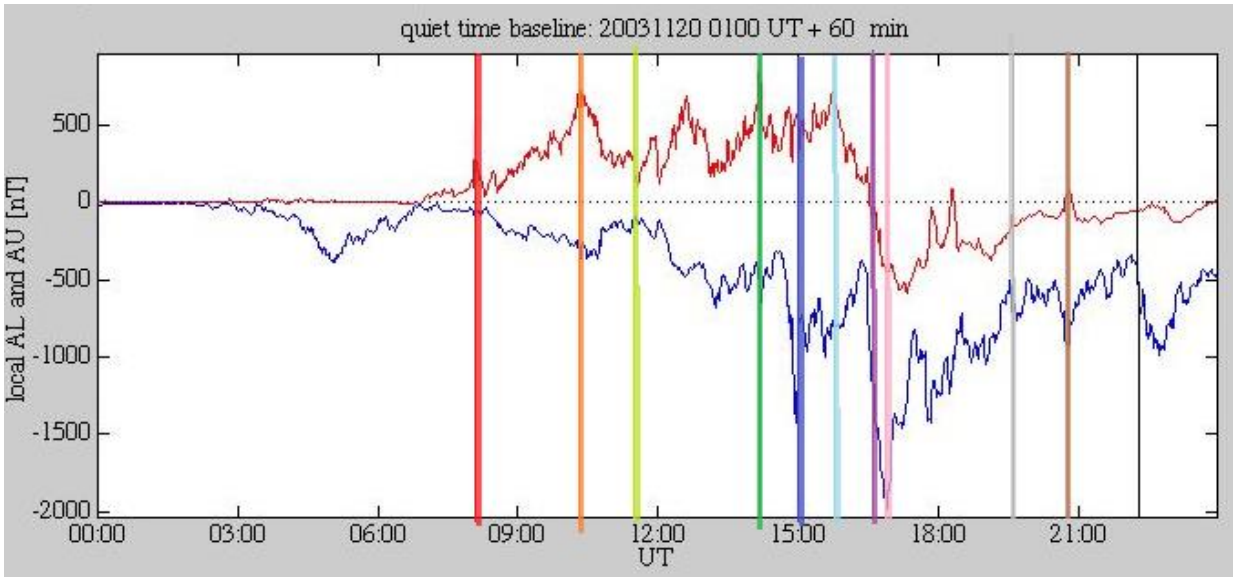

b)

Figure 4.3-1: a) Magnetogram of the x-component. The colored lines mark interesting features in the development of the storm. b) The local AL and AU index with the same color markings as the magnetogram in a). Credit: IMAGE, *http://space.fmi.fi/image/beta/?page=il_index*

The dark green line at ~14:00UT in marks the approximate time for the NMA's first abrupt loss of satellite communication. There is only a small dip in the x-component in the magnetogram, and the AU-index has a local maximum of ~1000nT. The electrojets have migrated equatorwards and they overlap, see Figure 4.1-6 in section 4.1.2. Norway is situated under the 16-17 MLT auroral oval at this moment. A look at the OVATION plot from 14:00UT in the next section, reveals that there is strong precipitation in the night sector, but from the All-Sky data from Kiruna, there is no visible auroral display at this moment, see Figure 4.3-2

The blue line in Figure 4.3-1b), prior to 15:00UT, indicates the onset of a massive expansion phase. The local K-index is 9 (see e.g. plot in Figure 4.2-1) and the steep negative excursion in the AL that follows reaches a minimum of ~1400nT. This implies a strong westward current which is compatible with the intensification of WEJ from the storm time current wedge (section 2.4.4). The visual display of this current is captured by the All-Sky camera in Kiruna in Figure 4.3-2 and corresponds to the so-called westward travelling surge as the aurora moves rapidly westwards across the sky. This figure series illustrates one session of tail reconnection during the expansion phase at approximately 15:00UT. The fluctuating intensity correlates well with the fluctuations in the AL-index and thus the WEJ.

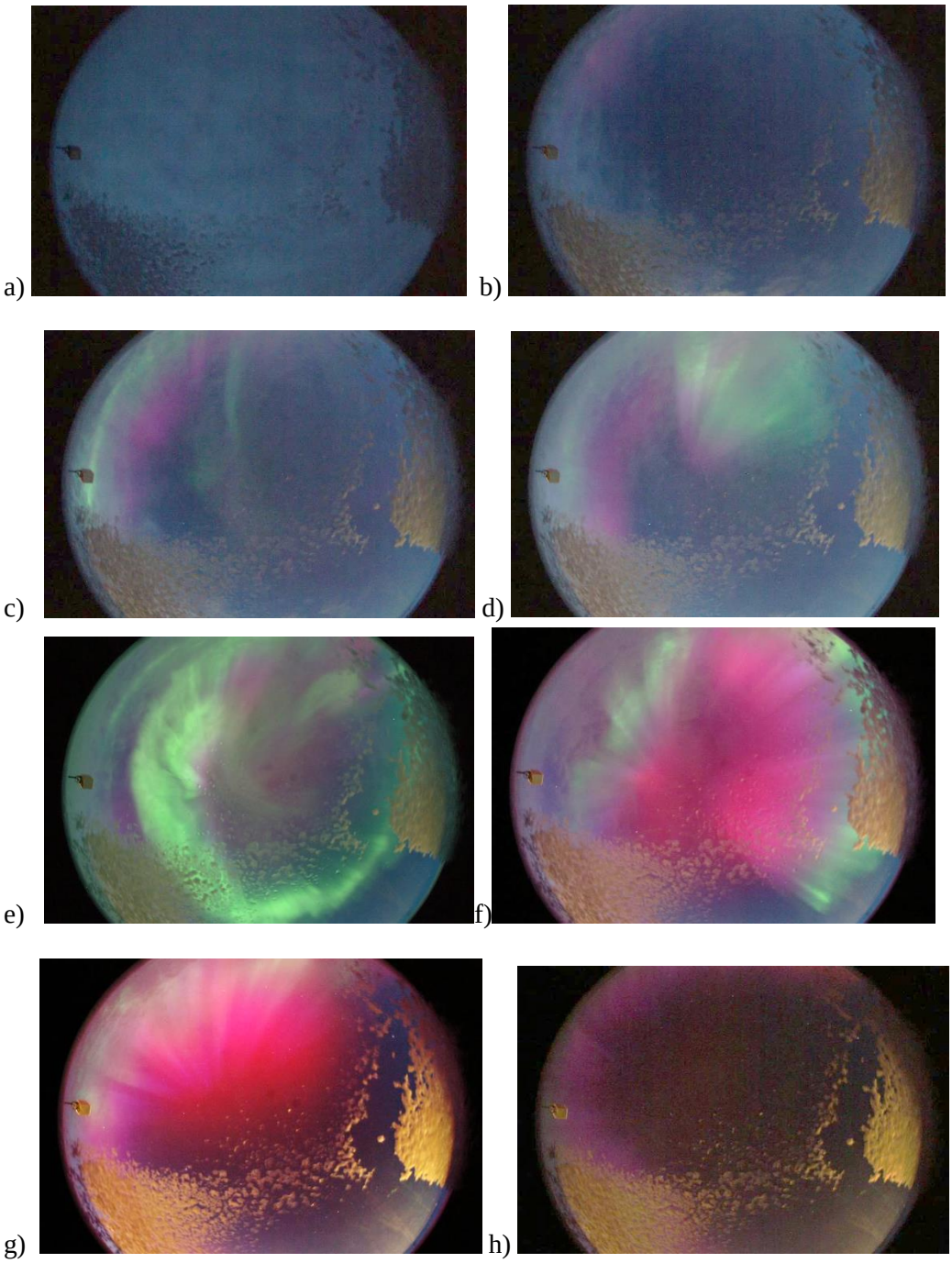

Figure 4.3-2: a) All-sky camera image at 14:00UT. There are no signs of auroral activity. B) at 14:48UT, the first magenta colored glimpse of the aurora can be seen in the eastern sky. C) 14:51UT, the aurora travels across the sky towards west.d) A beautiful corona is about to burst into view above the camera site at 14: 53. E)-f) from 14:57 to 15:02, the bright aurora is above the station. G) The aurora withdraws to the eastern horizon about 15:15UT and is merely visible in h) at 15:26UT before a new expansion begins about 15:35 UT (not shown). Credit: U. Brändstöm, IRF

At 16:00, the AU-index begins to decline from about 700nT to zero in 30 minutes. This is indicated with the turquoise and purple lines in Figure 4.3-1. According to Ebihara et al. [2005] the polar cap boundary reached as far as ~60º geographic latitude at 16:00UT, along with a peak in the solarwind density (see section 4.1.2). This equatorward shift of the dayside oval is confirmed by an OVATION-plot (not shown). The equatorward expansion along with the negative IMF Bz, implies magnetic fieldline merging at the dayside magnetopause. The results from Ebihara et al. [2005] revealed a peak in the plasmasheet density at about 18:00UT, which could be attributed the infusion of the solarwind at 16:00UT. The massive expansion phase with onset at 16:30UT sends the AL index to the minimum of -2000nT and the WEJ completely dominates over the EEJ. Norway is now situated in the evening sector of the auroral oval and is thus affected by this strong current.

At about 17:30UT, the pink line in Figure 4.3-1 marks that the IMF By-component changes from positive to negative, thus re-arranging the cellpattern in the polar cap. As we know from section 2.4.3, both patches and scintillation depend on the By-component of the IMF. First of all, recalling that patches are entrained within the convection, a change in this pattern will alter their destination and distribution. Secondly, the changes in the By-component itself may lead to patch production in terms of FCEs (see section 2.4.3.1). And third, the By-component is of importance as dictates the o/c-boundary position and consequently the inflow of high density plasma [Zhang et al. 2011]. The scintilliation occurrence also depend on certain configurations of the By-component. As Li et al. [2010] described; a positive By-component favors scintillation in the noon and pre-midnight sector, whereas a negative By-component favors scintillations in the late afternoon and post midnight sector. If this is valid, then it is somewhat the opposite of what we have observed here. The scintilliation effect began in the afternoon when the By-component was positive, and as the NMA- data shows, it continues throughout the evening when the By-component still is negative.

We know from Figure 4.1-10 from Foster et al. [2005] that the patch exited the polar cap at 19:45UT. In order for a patch to exit, it must pass the o/c-boundary which is only possible during tail reconnection e.g. [Zhang et al., 2013]. The grey line in Figure 4.3-1, marks the exit. Prior to 19:45UT, an increase in the current suggests a growth phase, and although it is followed only by a small negative excursion, this would be the time of exit. This is confirmed by the all-sky photo in Figure 4.3-3 where a sudden brightening occurs in within an interval of 15 minutes around 19:40UT.

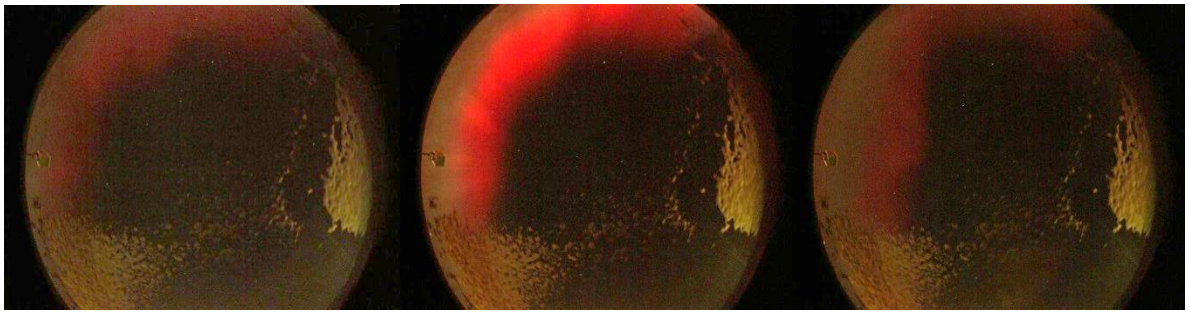

Figure 4.3-3: Images from Kiruna all-sky camera. From left: At 19:35 there is only a weak glow in the eastern sky. Middle: Five minutes later a bright red arc is visible in the northeastern sky. This is the signature of the exiting patch. Right: Ten minutes later it is only the dim aurora in the eastern horizon. Credit: U.Brändström, IRF.

According to the Dst-and SYM-H indices in section 4.1.2, the storm reached is most negative disturbance about 20:00UT with a Dst-value of -472nT. By this the recovery phase is initiated and the AL-index begins to increase. The brown (20:45) and black (22:40) lines in Figure 4.3-1 are examples of substorm expansions and tail reconnection during the recovery phase. When nightside reconnection occurs, patch material is likely to be pushed into the auroral oval and turned into blobs [Crowley et al. 2000; Zhang et al., 2013]. The o/c-boundary becomes adiaroic when tail reconnection is turned off, thus patchmaterial will be pushed equatorward with the expanding boundaries. Hence the patches becomes sub-auroral blobs [Zhang et al., 2013; Tsunoda, 1988], and recall section 2.4.3.

4.3.2 Auroral Oval and Reconnection

Selected OVATION maps were used as proxies for the location of the auroral oval, and were described in section 3.1.3. What is of main interest is to study the oval with respect to reconnection and location over Norway. Figure 4.3-4a) shows the auroral oval at 09:51UT. At this moment, the IMF Bz has been negative for almost two hours and reconnection in the dayside takes place. Norway is situated at noon MLT, and we can see that the auroral oval boundary is shifted equatorward due to dayside merging. (Recall section 2.3.3 for details on reconnection). In Figure 4.3-4 b) the IMF Bz is positive. At 10:30UT the polar cap area has now shrunk substantially, but the oval itself has broadened, which is a characteristic feature of a substorm-intensification [Lorentzen et al., 2004]. This could perhaps correspond to the small fluctuations in the AL-index in Figure 4.3-1b) (orange line).

The next OVATION plot in Figure 4.3-4c) is at 14:00UT. The whole auroral oval is expanded and increased precipitation is indicated by higher current densities. There was no aurora visible in Kiruna at this time, hence there was probably not visible aurora in Norway either. The size and shape of the oval indicates ongoing balanced reconnection with an equatorward displaced dayside and slightly poleward shifted nightside. There are small differences in the plots for the next two hours, therefore they are not shown here.

There were no available plots from the time interval from 16:00UT to 20:30UT from OVATION. The POES-plots from NOAA are not very reliable for these heavy storms either, because there are very few storms with Kp >7 recorded in order to make the statistical oval plot for larger geomagnetic storms such as this [Viereck, R., private communication, 2014]. Thus the next plots in the series are from the evening. In Figure 4.3-4 d) at 20:30UT, the plot reveals a broad oval with contracted polar cap with a poleward shifted nightside. This indicates tailreconnection which is consistent with the expansion phase in Figure 4.3-1b).

At 22:00UT in Figure 4.3-4 e) the polar cap is expanded again, and the dayside is shifted equatorwards due to dayside merging. In the last plot; at 22:40, the oval is again broadened and the polar cap is contracted. The nightside is shifted into the geographic polar cap, indicating a new intensification and tailreconnection.

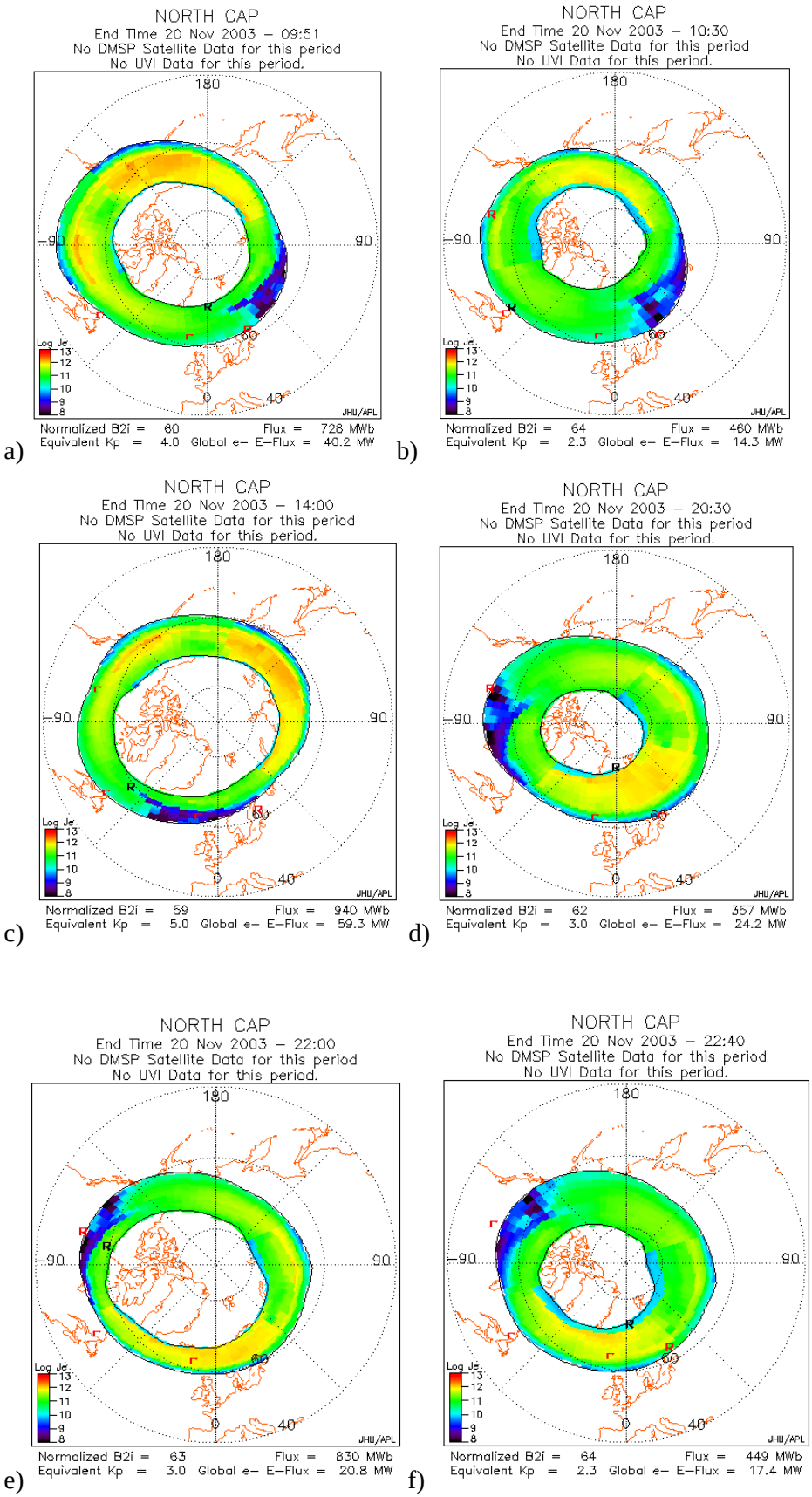

Figure 4.3-4: OVATION plots from different times of the day. Notice how the oval expand and contract with respect to the reconnection process. The oval covers Norway for most of the selected times. Credit: OVATION/JHU/APL

These six OVATION plots from different times of the day, reveals that the polar cap expands and contracts with the variations in the reconnection processes. Recalling section 2.4.3.1, we know that EUV-ionized plasma from the dayside and/or storm enhanced densities (SEDs) from the nightside, may enter the polar cap convection during growth phase when the o/c-boundary migrates equatorwards. If the reconnection process is steady, as in the Dungey- model, the high density plasma would form a continuous TOI. Transient reconnection on the other hand, would produce patches by segmenting the TOI [Lockwood and Carlson, 1992].

4.3.3 SuperDARN

HF-radar maps are not appropriate to discern whether the enhancements really are due to blobs or patches (Moen, J., private communication, 2013), however the HF-backscatter could stem from field aligned decameter irregularities either in the E-or-F-region or both. The flow vectors are line of sight Doppler velocities only [Chisham et al., 2007 and references therein].
The selected convection maps are screenshots from a convection movie from November 20, 2003. The model used is the cs10 based on OMNI data.

4.3.3.1 Onset and IMF Bz- reversal

The first plot in Figure 4.3-5a) depicts the situation at 08:16UT; about ten minutes after the first onset. Norway is situated in the MLT morning sector underneath the dusk cell. The By-component is positive and hence the dusk cell is elongated (see section 2.4.2). The increased flow in the cusp region could be attributed the magnetic reconnection at the dayside magnetopause. Some smaller flows are also seen in the midnight sector in each cell. The plot in figure b) is from the interval of northward IMF Bz, between the shock and the MC. At 10:48UT Norway is in the magnetic noon sector. The dusk cell has an irregular shape, but its enhanced flows in the dayside, follows the sunward convection. The dawn cell is located in the post- midnight sector and has flows in the conventional directions, however the size if the cell is very small. In addition; two lobe cells are located in the morning sector. A modest enhancement in the reverse flow in these cells, could imply reconnection [Chisham et al., 2004; Grocott et al., 2005]. Since the OVATION plot in Figure 4.3-4 reveals a contracted polar cap during positive IMF Bz, it could be due to the reconnection on lobe cells in both hemispheres as described by Chisham et al. [2004, and references therein]. It is also worth mentioning that reconnection in the tail has found place during northwards IMF Bz [Zhang et al., 2013]. Now; recalling what Mishin et al. [2007] stated in section 4.1.2: There were no indication of a substorm, but a so-called null event where the conventional tail current disruption was replaced by smaller current disruptions, and thus no reconnection.

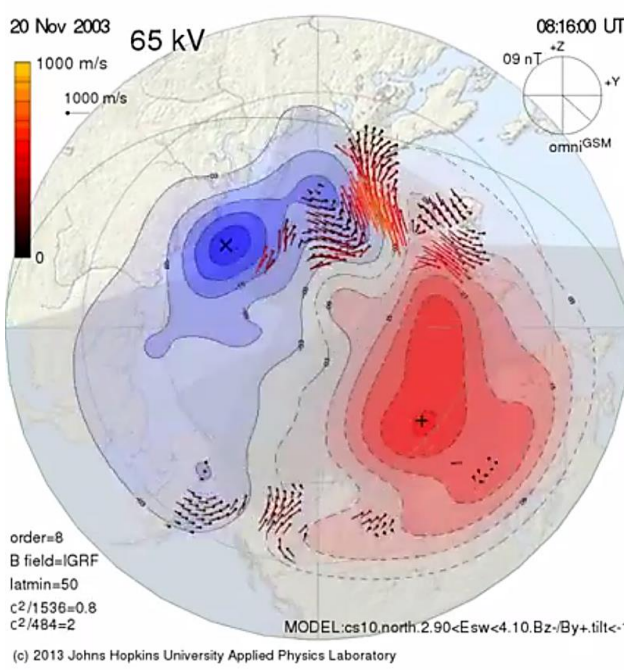

a)

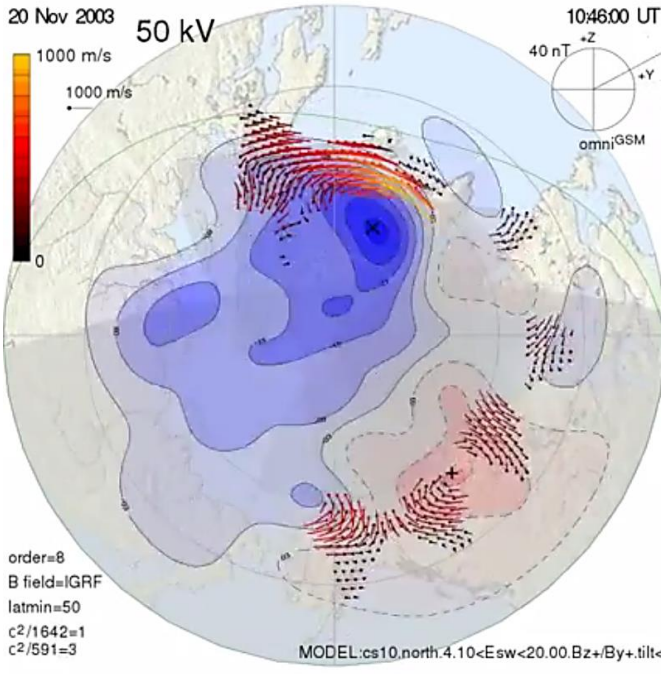

b)

Figure 4.3-5: a) Minutes after onset of storm. Increased flow in the dayside cusp region. b) During an interval of positive IMF Bz. Two lobe cells in the dawn sector, reveal hints of reverse flow. Norway is situated in magnetic noon. Increased return flow in the dusk cell in noon sector, could it be a TOI? Credit: SuperDARN/JHU/APL

4.3.3.2 Afternoon convection

When the MC arrived, the IMF Bz turned southwards, and stayed negative throughout the day. Thus the convection pattern in the polar cap was the conventional two-cell pattern. A positive By-component contributes to a shift of the cusp region towards pre-noon MLT. In Figure 4.3-6, a series of plots are shown from approximately 14:00UT. In Figure 4.3-6a) the SuperDARN snapshot from 13:56UT reveals a little flow enhancement in the returnflow over Northern Norway and an enhancement in the anti-sunward flow from the cusp which suggests ongoing reconnection on the dayside. In Figure 4.3-6b) high velocity flows are located in the anti-sunward flow of the polar cap. From the cell pattern it could seem as plasma are dragged into the polar cap via the cusp during growth phase of the substorm. The following series of plots in Figure 4.3-6 c-f) illustrates this. It is tempting to attribute this to a TOI, but there is no evidential data to support this (except from some increased TEC over Canada/ Greenland in MIT Global TEC maps, see Figure 5.2-4). Neither does the enhancement seem to exit in the nightside. On the other hand; the massive expansion phase which initiated at 14:49UT, could contribute to patch exit across the nightside o/c boundary. Small hints of flow are present in the return flow in both convection cells.

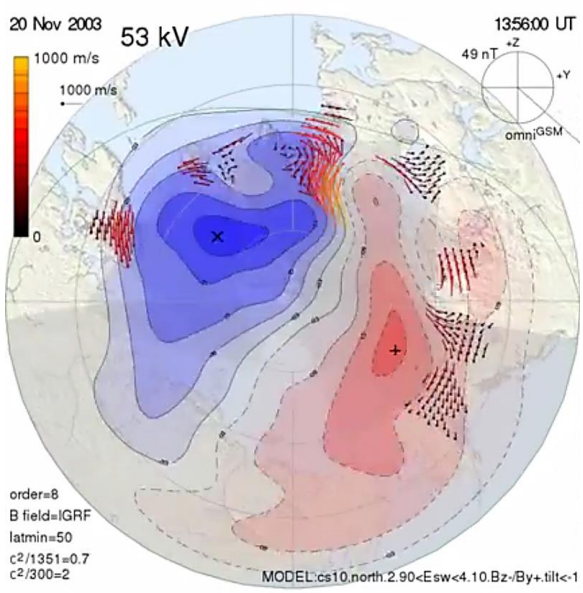

a)

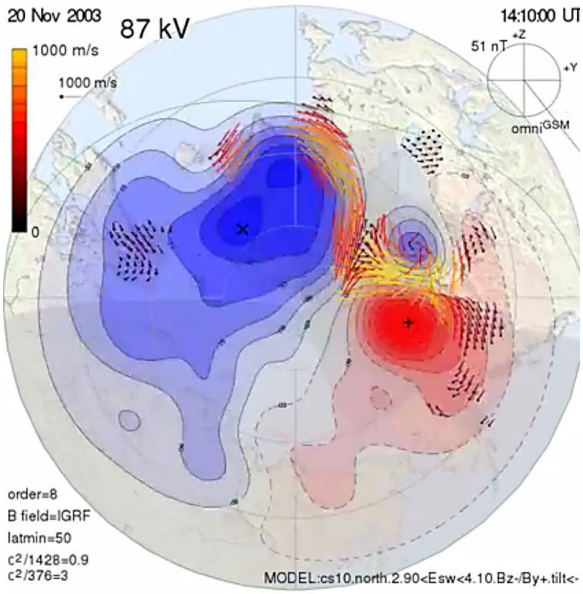

b)

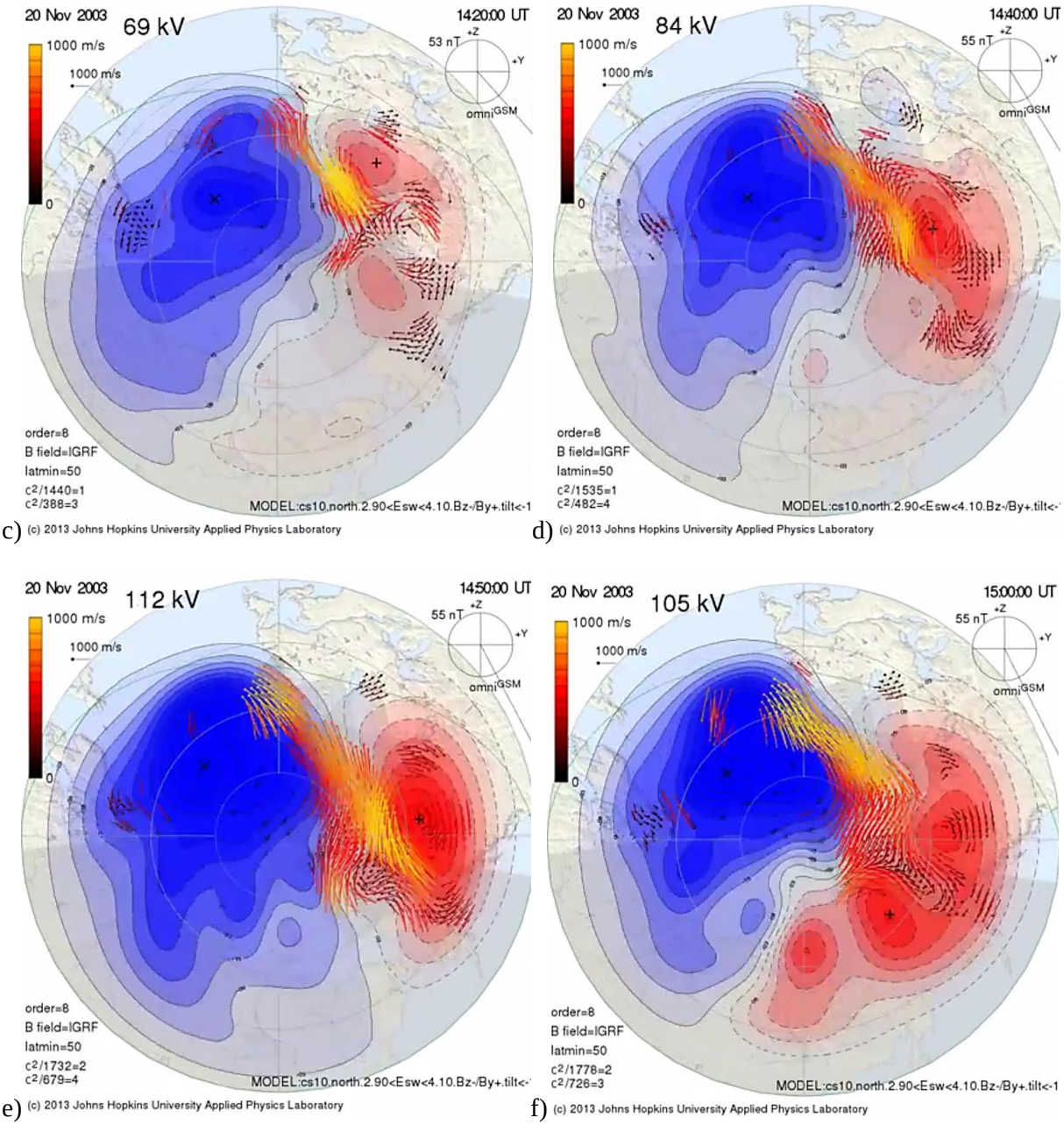

Figure 4.3-6 : A series of convection maps with increased flow in the anti-sunward convection in the polar cap. Plots c-f are interesting, since they might reveal the presence of a TOI or patch crossing the central polar cap. Credit: SuperDARN/JHU/APL

4.3.3.3 Reversal of By-component:

About 16:30 UT, the By -component began to decrease and remained zero for almost an hour before it finally became negative about 17:30UT.This can be seen as a flat interval in the By-component of the ACE By-plot around 16:00UT in Figure 4.1-3, or in SuperDARN convection maps (not shown). Two SuperDARN convection maps with 30 minutes interval reveals that there is more flow activity after the reversal of the By-component, see Figure 4.3-7.We know from Foster et al., [2005] that the TOI was entering the polar cap within this interval of time. It is tempting to think that the reversal of the By-component contributed to “suck” the high density plasma from the dayside into to the transpolar flow. Despite the lack of radar data earlier this day, the passage of the TOI is recorded and thoroughly

described in Foster et al. [2005] and DeFranceschi et al. [2008]. In their TEC-maps there is clearly a patch over Norway situated within the transpolar flow, according to the DMSP crosstrack plot. Another interesting feature is the enhanced flow in the nightside of the dusk cell. This could be due to reconnection, and perhaps even the exit of patch material from the increased polar cap convection we saw in Figure 4.3-6.

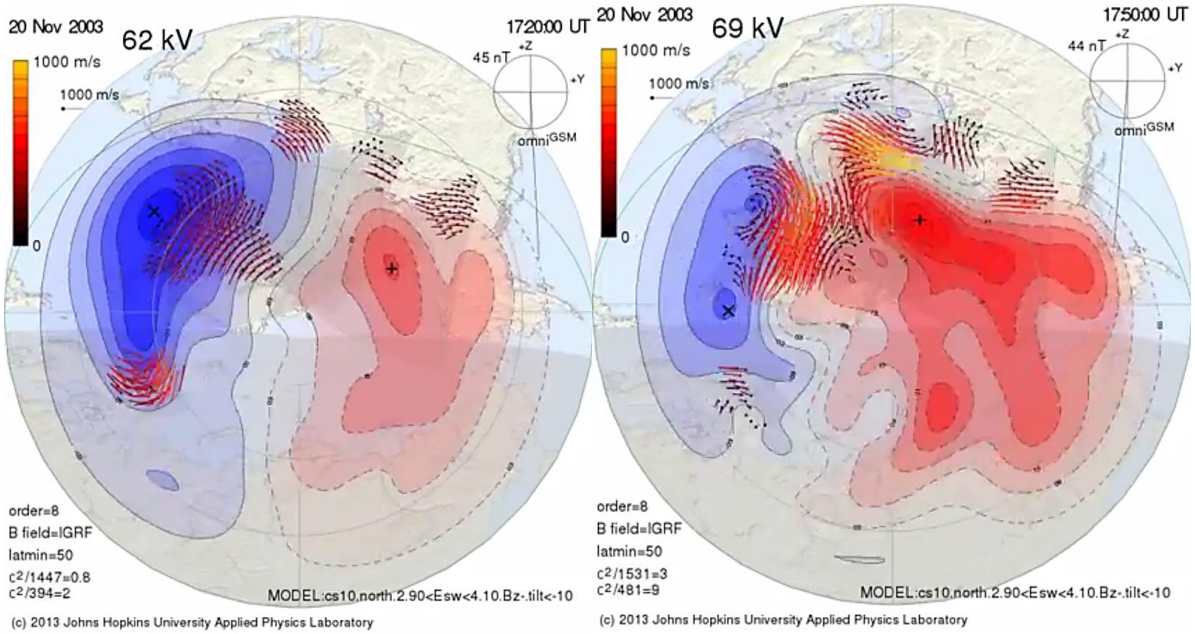

Figure 4.3-7 SuperDARN plots with a 30 min interval. The By-component goes from zero to negative about 17:30UT. The same time the TOI was captured by the Millstone Hill Radar. The latest plot reveals high velocity flows between the two cells in anti-sunwards direction. Credit: SuperDARN/JHU/APL

4.3.3.4 Possible patch exits?

In these evening plots (Figure 4.3-8) there are flow enhancements in the nighttime dusk cell over Norway. At 20:32UT a rather large region of enhanced flow occupies the anti-sunward flow in the dusk cell. What is a matter of fact, is that ever since late afternoon (~16:00UT) increased flows have resided in the flow reversal region of the dusk cell (seen in SuperDARN maps, not shown). This could of course be attributed to reconnection, but we also know from the AL-index that from about 15:00UT, that the reconnection process was highly tail dominated at certain times (expansion phases). Hence it is tempting to attribute some of these flows to polar cap patches awaiting exit through the o/c-boundary. For instance; we know from previous section, that there was a growth phase at 22:00UT, with no considerable tail reconnection. Thus the flow enhancement in the night sector could be attributed to patches or rest of the TOI. The tail reconnection initiated few minutes later as can be seen from the decline of ~500nT in the AL-index. At 20:30UT, the Kiruna all sky camera indeed captured a bright red arc in a burst of tail reconnection, similar to the brightening in Figure 4.3-3.

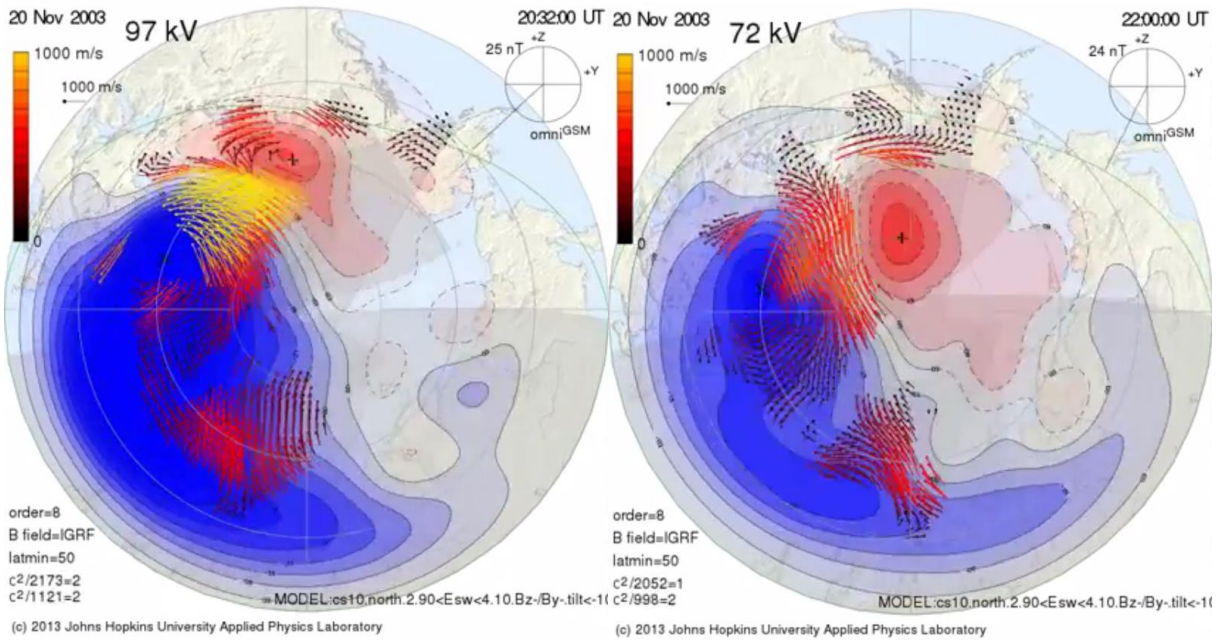

Figure 4.3-8: SuperDARN convection maps from the evening reveal increased flow region in night sector of the polar cap. To the left: during an interval of tail reconnection. Right: During an interval of dominated dayside merging. Credit:SuperDARN/JHU/APL

4.3.4 Ionograms and Incoherent Scatter Radar Data

Interpreting high latitude ionograms with auroral and patchy features is a complicated task [Reinisch,B., private communication 2014], and it is not the main goal of this presentation. Nevertheless there are certain characteristic features in the various ionograms during the event which stand out.

Starting with the quick-look ionogram from CADI, see Figure 4.3-9. This is taken from the former Rankin Inlet station located at 62.81°N, 267.89°E. We can see that there is a spread-F development after 02:00UT and a sporadic E-layer in the ionogram at 04:00UT (both blue). The signals are heavily attenuated by noise for the rest of the day. This is due to the fact that the CADI-system is using low power ionosondes to increase the temporal resolution, but in return they are very sensitive to absorption from underlying layers [Themens, D., private communication, 2014]

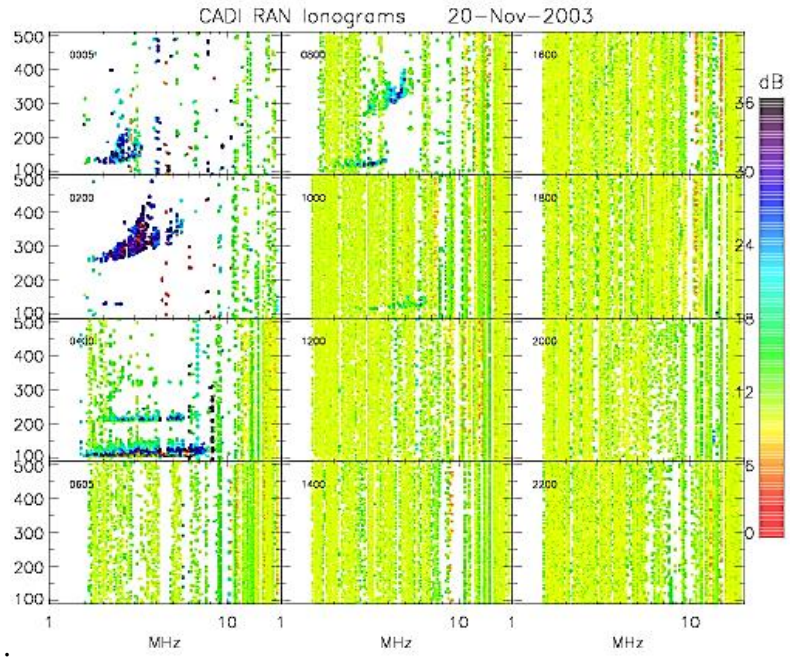

Figure 4.3-9: The ionogram from Rankin Inlet. The ionosondes used by the CADI-network are sensitive to absorption and therefore data throughout the day are missing. Credit: CADI/CHAIN

Other ionosonde stations operating in Greenland and Norway provide data with less noise. All of the following data in Figure 4.3-10 are from the GIRO Lowell Digital Ionogram Database, and the data were available in real-time at the different stations already back in 2003 [Reinisch, B., private communication, 2014]. Starting with the ionograms from Sondrestrom, Greenland located at 67.0ºN, 309.1ºE. The first ionogram-plot at 17:10UT reveals a quiet condition with an f_0F2-frequency of 4.00 MHz and an h_mF2 at 418.4 km. This is a moderate increase in the ionospheric density, which I suspect is due to the ongoing storm event. At 17:20UT, the frequency increase to 6.85MHz, and the F-traces are spreading out. The height is somewhat lower. In the next two ionograms from 17:50UT and 18:20UT the f_0F2 –frequencies are 9.90 MHz and 10.6 MHz respectively, indicating a high density plasma region above. This could be the signature of the passing TOI/patch overhead the station. In the last two ionograms, at 18:50 UT and 19:15UT, the f_0F2 -frequency drops from 9.40 MHz to 5.25MHz which implies that the patch has passed, and the plasma density is back to its prior level. The plot in Figure 4.1-10b) from Foster et al. [2005] is a snapshot at 18:20UT, the same time as the plasma frequency reached its maximum value. Clearly this is not a coincidence, and thus it is evident that the sequence of ionograms from Sondrestrom captures the passage of the TOI/patch.

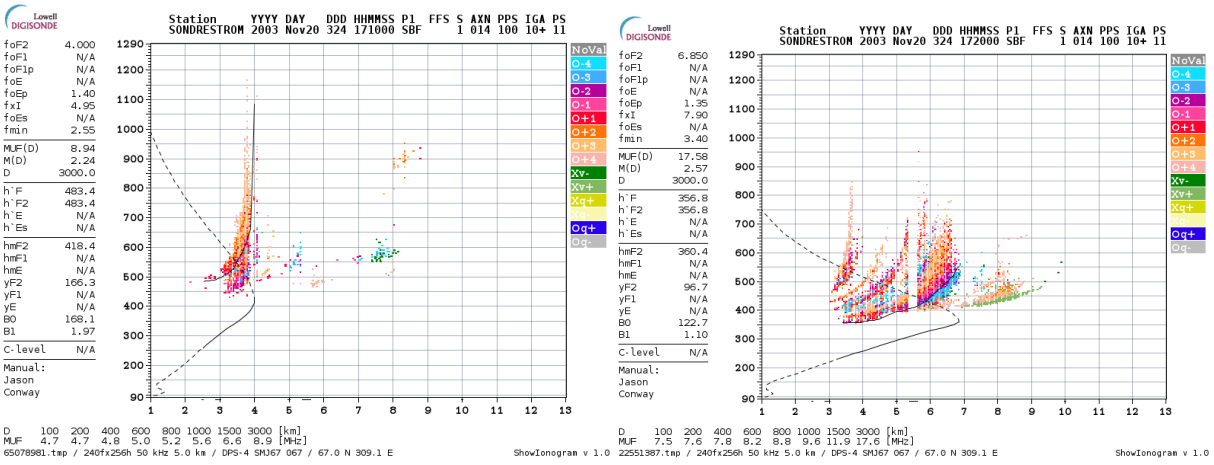

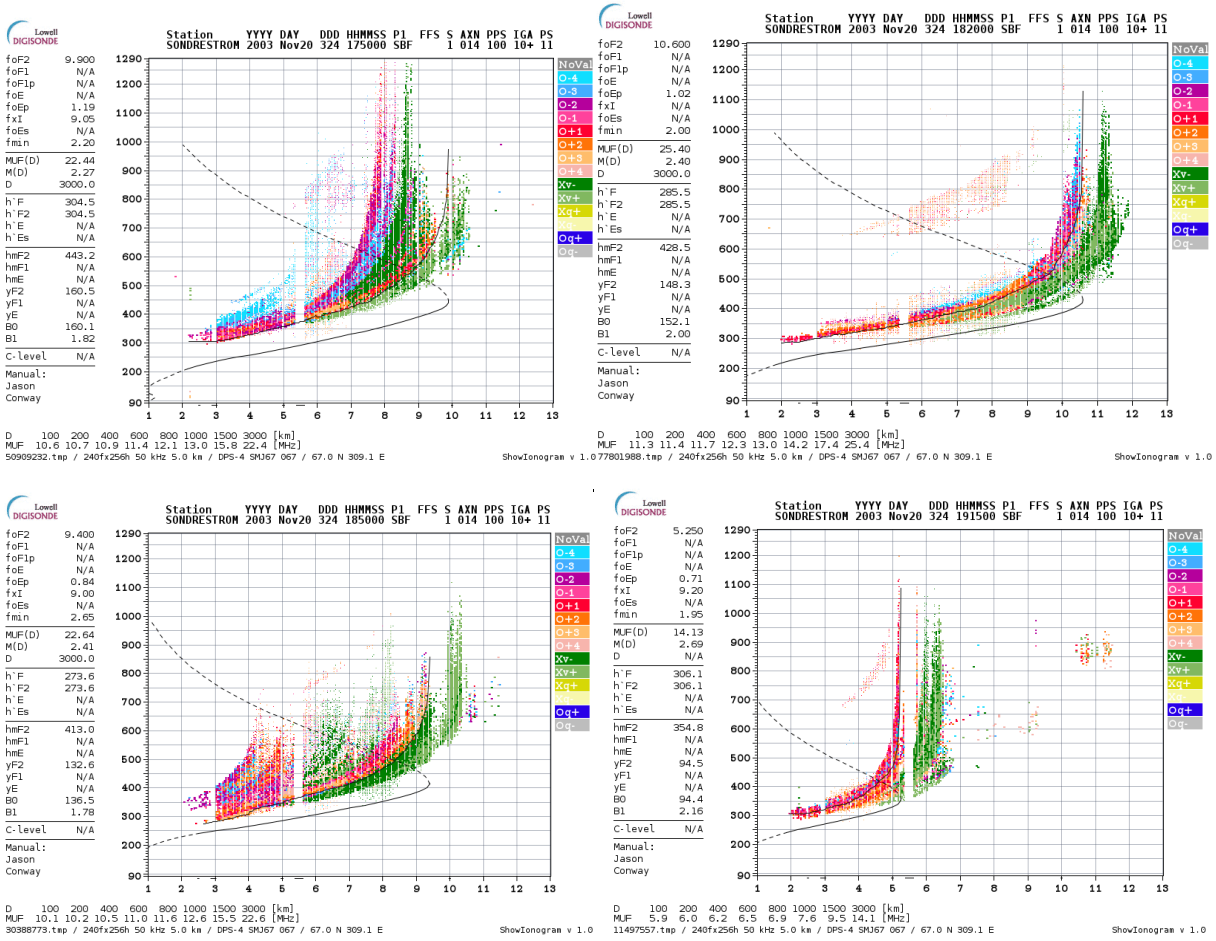

Figure 4.3-10:The time development of the F2 plasma frequency during the passage of the TOI/patch above Sondrestrom, Greenland. The first ionogram (top row, left) is taken before the TOI approaches the station. The maximum plasma frequency is 10.6MHz at 18:20UT. The F-trace is spread during the passage of the TOI and the maximum uplift is 428.5 km at 18:20UT. The last ionogram (bottom, right) shows the situation after the TOI/patch has passed Sondrestrom. Credit: GIRO Lowell DIDbase

The same is also evident for the Tromsø-ionograms The Tromsø station is located at 69.6ºN, 19.2ºE, and the data are also found in the GIRO Lowell DIDbase. Some of the F2-data were not available for all times, but the collage in Figure 4.3-11 reveals the passage of the TOI. As we can see from the ionogram at 18:16 UT, the background plasma frequency is quite low (3.625 MHz), however there is a slight spread F. One hour later, at 19:16UT, the spread F is stronger, but the f_0F2 is still low. The 19:46UT-ionogram corresponds to Figure 4.1-10c) from Foster et al. [2005], and there is a spread F, but low plasma peak frequency and plasma height. This is also the case for the next ionogram at 20:01UT, but by now the patch should have exited the polar cap and entered the return flow. At 20:16UT, the plasma frequency is 2.925MHz and in addition to a spread F, there is also an E-trace. At 21:01UT, the plasma frequency is a little higher, but the height is a little below 250 km. There were no Dynasonde data available from Tromsø on this day. The ionosonde data from the Swedish Institute of Space Physics (IRF) in Kiruna (located 67.84ºN, 20.41ºE), have no recorded data from after noon-time for this date, so there are no comparative data to the Tromsø-data unfortunately. The same is the case for Sodankylä Geophysical Observatory (67.22ºN, 26.38ºE). For the rest of the day, the measurements are absorbed by the lower layers of the ionosphere for these stations.

As we shall see in the next section, the increased ionospheric density caused trouble for the GPS-receivers from early afternoon.

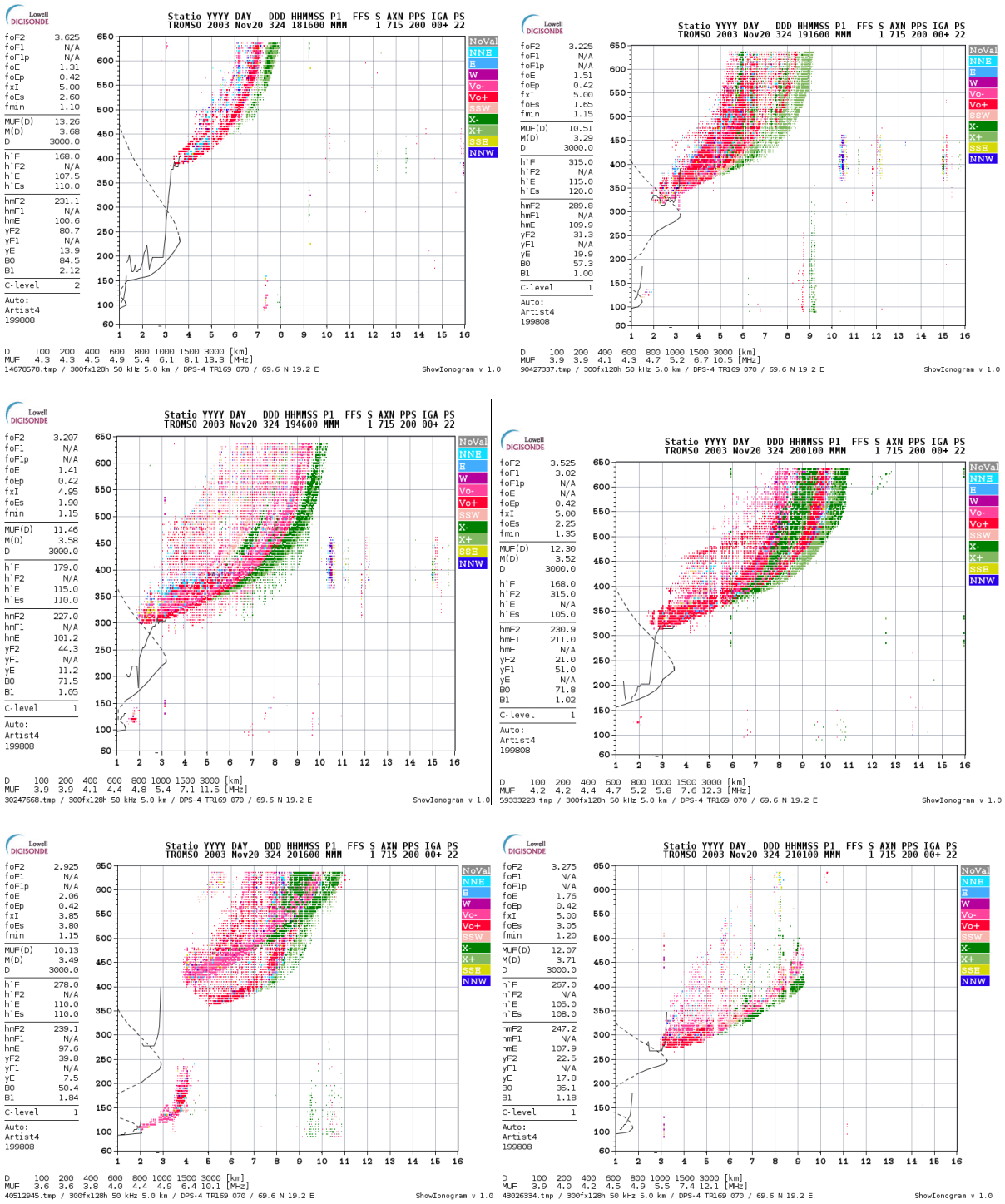

Figure 4.3-11: The time sequence of the passage of the TOI/patch above Tromsø. Throughout the whole time the plasma frequency and layer height remained low, but the spread in the F-trace reveals there are irregularities overhead. Credit: QinetiQ and GIRO Lowell DIDbase.

It is also possible to identify the TOI/patch from quick-look plots from the Sondrestrom ISR and the EISCAT-radar in Tromsø. The plots in Figure 4.3-12a-c) are representing electron temperature (T_e), the ion temperature (T_i) and the electron density (n_e) at 350 km altitude from the Sondrestrom ISR. The time interval chosen covers the passage of the TOI/patch. For the temperature plots, a well-defined region with enhanced temperature is present in the T_e-plot. Here, the electron temperature is within the range from 2900-3200 K, and this region stretches from ~70º-75º MLAT between ~18:00-20:30 UT. The ion-temperature is somewhat lower in the same region, apart from the two narrow longitudinal bands at ~18:50UT and 19:45UT. The overall background temperature is, however, higher in the T_i-plot. The final plot, Figure 4.3-12c), is the height profile of the electron density revealing a region extending from about 350 km to 700 km within the time interval from ~18:00 UT-19:00UT. The densest part of this region is at 400-550 km with electron densities between $7.0 \cdot 10^{11} - 1.3 \cdot 10^{12} \mathrm{m}^{-3}$.

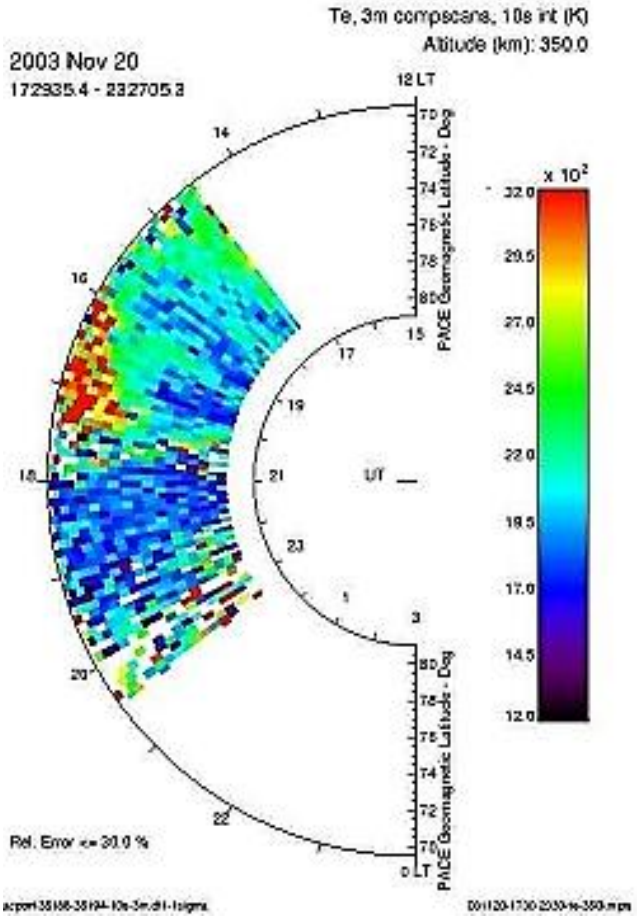

a)

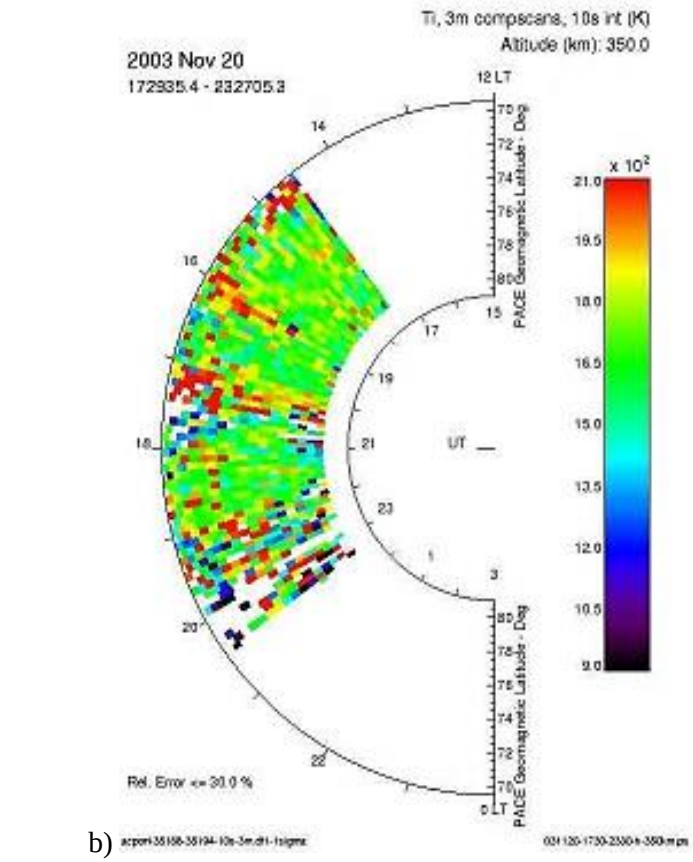

b) acport-35188-35194-10s-3m.dti-1sigma 031120-1730-2330-ti-350km.ps

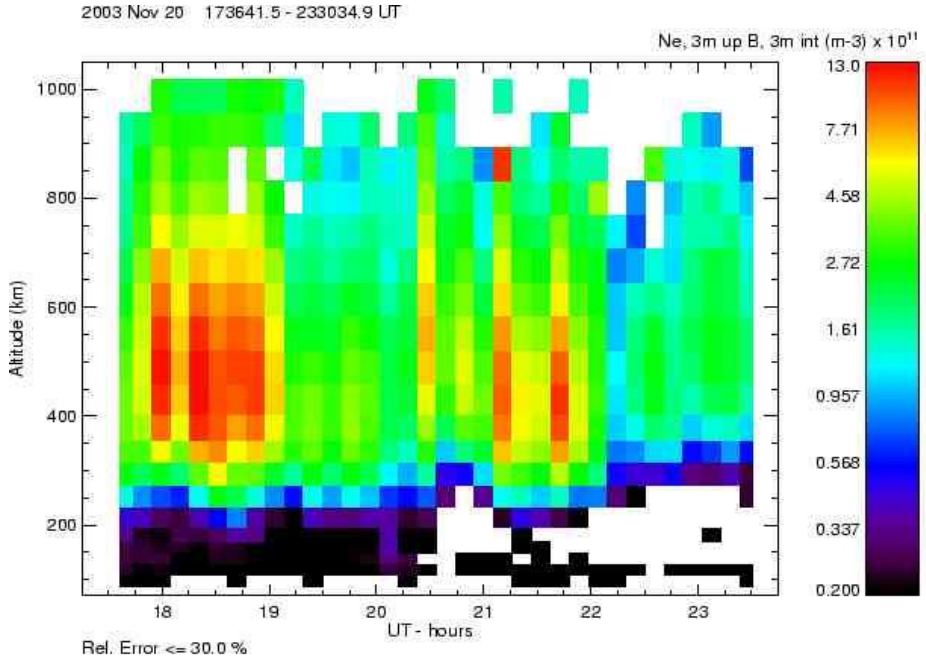

c) acport-35188-35194-10s-3m.dti-1sigma 031120-1730-2330-ne-upb-3m.ps

Figure 4.3-12: a) The electron temperature at 350km. The red region shows the TOI/patch entering the field of view at approximately 18:00UT at 70º MLAT and exits at 75º about one hour later b) The ion temperature is enhanced allover, but there are narrow regions with temperatures exceeding 2000K. c) The vertical electron density reveals regions with increased densities above 350 km. More patches are present later in the afternoon. Credit: SRI, Sondrestrom ISR

Figure 4.3-13 is from the UHF-radar in Tromsø during the time interval from 19:00UT- 24:00UT. The top plot is the electron density and we see a patch arrives at 19:00UT approximately. The light pink color represents the highest density corresponding to 10^{12} m^{-3}. The patch leaves the radar field of view at approximately 21:45UT. The lesser dense areas between the pink regions could be irregularities within the patch or gaps between isolated patches. The temperature profiles of the irregularities reveal that, apart from a red area in the T_e-map around 21:00UT, the electron-temperature is rather cool (2000K). The ion-temperature is slightly increased all over (2100K) and also in the same region around 21:00UT. The vertical ion drift velocity indicates ion upflow before 20:30 UT and ion downflow at 20:45UT. Ion upflow could be driven by frictional heating or plasma instabilities [Endo et al., 2000]. The low mean velocity is common within "radarheight," and studies suggest that the ions will have greater velocities with increasing altitude [Ogawa et al., 2009]. The downflow is probably caused by ions with energies which are too low to escape, and thus fall down because of gravity. The auroral precipitation will enhance downflow as well [Endo et al., 2000]. The location of the Tromsø radar, at 66º invariant latitude, can be within the polar cap when the auroral oval is expanded, but usually inside the auroral oval [Feldstein and Starkov, 1967 in Endo et al., 2000]. If this is the case, the Tromsø-data is consistent with the findings of Yaun et al. [2008] and Foster et al. [2005]. They found that in both cusp and nightside auroral sector there were upward velocities of respectively 350 and ~100 ms^{-1}, whereas over the polar cap the downward velocity was ~100 ms^{-1}. As the TOI entered the cusp, the F-region was elevated from 350km to ~500 km and an upward flux of O^+-ions of $3 \cdot 10^{14} m^{-2} s^{-1}$ was observed at 650 km [Foster et al. 2005].

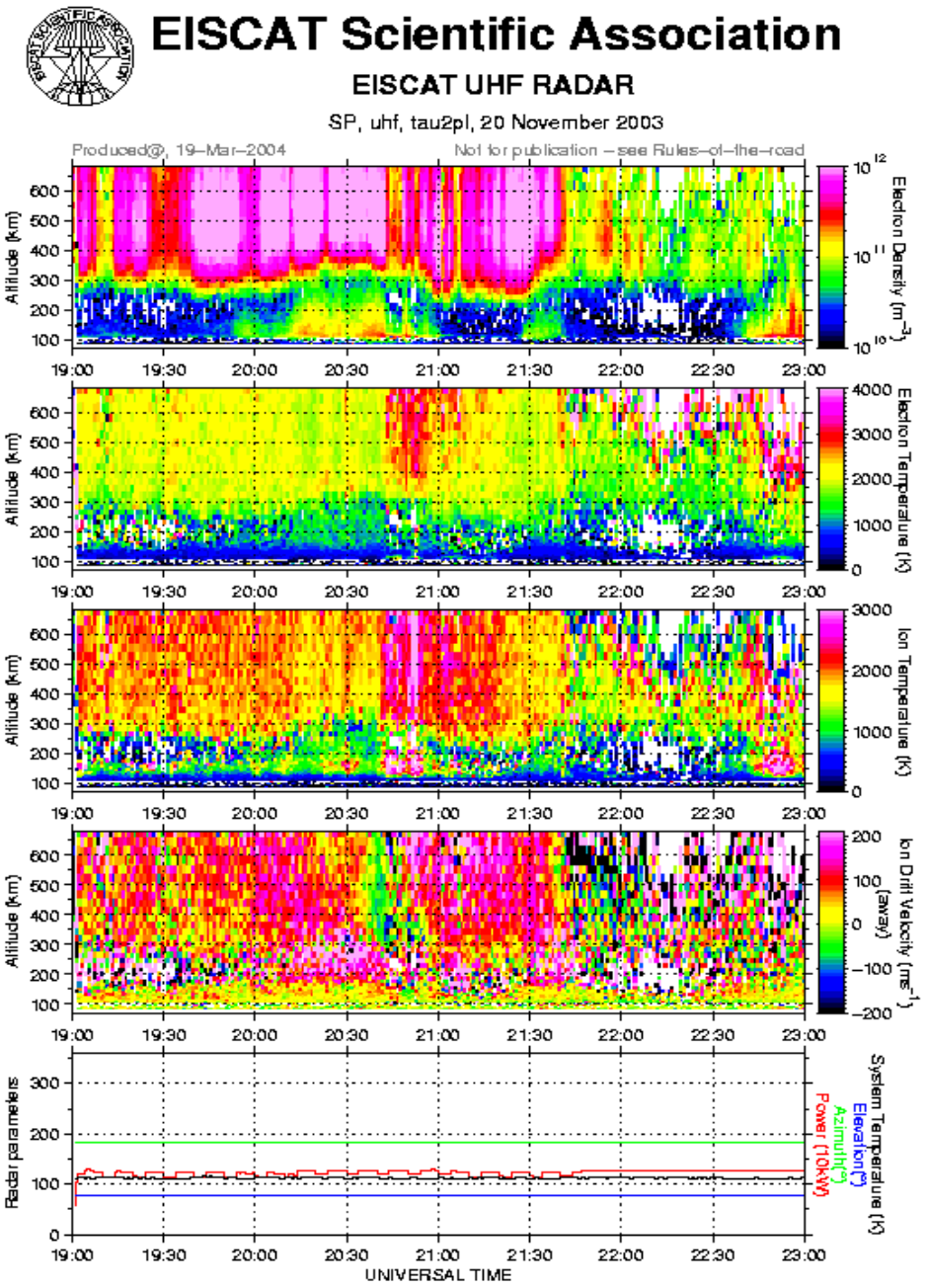

Figure 4.3-13: A quick-look plot from the UHF-radar at EISCAT Tromsø. The top panel shows the regions of enhanced electron densities. There could be separate patches or irregular density distribution within the patch corresponding to the regions with lower densities. The temperature panels reveal approximately the same temperature for both ions and electrons (~2000K). A region around 21:00UT is enhanced in both plots. Ion upflow is indicated by the red/pink region before 20:30 UT in the drift velocity panel. The green region at ~20:45 UT in the same panel indicates ion downflow. Credit: EISCAT Tromsø/Madrigal.

4.4 Combined TEC and Auroral Oval Maps

It is well known that phase scintillation can occur at the edges of the ionospheric troughs and in relation to SAPS at sub auroral latitudes [Siddle et al.,2004; Foster and Burke, 2002; Coster et al. 2006; Prikryl et al., 2013]. In the gradient map, the gradients are steepest at the boundaries of the density-regions. From section 2.4.3.2 we have learned that the gradient drift instability arise from **E**x**B**-drift perpendicular to a density gradient. This instability mechanism structures the plasma further and contribute to irregularites of smaller scales which contributes to scintilliation. The large scale gradients and the ROTI maps are constructed from the same dataset with the RTIM. Some precautions concerning the gradient maps must be made: First; the gradients have scale sizes of hundreds of kilometers, hence the smaller irregularity structures cannot be seen. Second; in the edges of the maps, there are empty regions where data are missing (e.g. corners). Often there are large effects on the boundaries between these empty regions and those regions with acceptable data. These are false effects, and must be disregarded [Jacobsen, K.S. private communication, 2014].

It is crucial for our understanding to visiualize where the satellite IPPs are in relation to high TEC regions and the auroral oval. For each receiver station, the satellite IPPs were plotted in the RTIM maps along with the coordinates of the auroral oval boundaries from OVATION. Some differences occurs from station to station due to their different view of the sky and the satellite cut off. The least and the most affected stations were selected. Bergen was the second northernmost and heaviest affected, Stavanger was the second southernmost and least affected. Both stations are situated on the western coast of the mainland. There are ROTI and spatial gradient maps for eight selected times of the day: 08:00UT, 11:00UT, 14:15UT, 15:00UT, 17:30UT, 19:00UT, 20:30UT and 22:30UT. The right column in the figures 4.4-1(Bergen) and 4.4-3 (Stavanger) shows the gradients in mm/km and the left column shows the ROTI-maps in TECU/min for the same time. Plots from 17:30UT and 19:00UT lack auroral oval due to missing OVATION data. In Figures 4.4-2 (Bergen) and 4.4-4 (Stavanger) the plots of visible satellites are shown with black lines to mark each of the times. Encircled PRN-bars illustrate how location affect the reception or tracking of satellites in e.g. due to cut-off angles, or oblique ray path. Also notice that there is a discrepancy between the satellitte PRNs in the maps and in the visible sattelite plot. This has probably to do with handover effect between satellites coming in or leaving the receivers view, or that the signals are too weak when they are outside of map/far away from station (cut off or multipath).

Beginning with Bergen, panel A in Figure 4.4-1 is from 08:00UT, and prior to onset. The auroral oval is only covering the northern parts of Norway (equatorward boundary ~74°), and there are no disturbances in the signals. Out of nine PRNs in the plot, there are seven received. PRN 3, 15 and 27 in the map are replaced by 9 and 10 in the plot in Figure 4.4-2. At 11:00 in panel B, the IMF Bz is northwards and the auroral oval lies across Mid-Norway. (Equatorward boundary ~60°). Although there is only a small region of enhanced ROTI here, the TEC-gradient are quite steep within the oval. There are four out of six satellites received, but PRN 14 have fading signal strength and its IPP is on the equatorward boundary of the auroral oval (green). PRN 28 have left the satellite view and PRN 11 are not received at all.

The next two panels C, and D, are from the time of the satcom outage onset. Up until 14:00UT there were no significant disturbances in the NMA satellite data. Of the eight PRNs present in the maps from 14:15UT, PRN 1 is located within the polar cap on the edge of a gradient, PRN 4 is inside the auroral oval and PRN 24 is on the equatorward boundary. The rest are located equatorwards of this boundary, however in the vicinity of TEC gradients. The ROTI map and indicates strong variation in TEC (5.0 TECU/min). This can be attributed to irregularities of a few kilometers in scale size (section 2.5.2).

At 15:00UT (panel D), PRN 4 is in the polar cap and PRN 1 is inside the oval along with PRN 24. From the plot in Figure 4.4-1 we can see that PRNs 4, 10, 24, 25 and 30 are severely affected due to

high ROTI values. The auroral oval covers Norway from ~61°N to ~69°N. In Figure 4.1-6 we can see the westward electro jet is protruding as far south as ~61° geographic latitude. These currents has a tendency to cause scintillation effects, as described by Jacobsen and Schäfer [2012].
For panels E and F, there were no OVATION data to plot the oval, however it is plausible to assume it is still covering the Norwegian northern and mid-parts. At 17:30UT there should be at least eight satellites present according to Figure 4.4-1E. All of these are affected by loss of lock and for severeal minutes there are less than three satellites in view simultaneously. More or less all the IPPs are situated within regions of high ROTI (3-5 TECU/min).
The situation is a little better at 19:00UT (panel F), but still all the satellites are affected. From the ROTI map we can see that IPPs equatorwards of Southern Norway are within a calmer region.
ROTI-and-gradient maps from 20:30UT and 22:30 are shown in panel G and H. The polar oval is slowly retreating poleward. Of six PRNs, four are received to a certain degree. The strongest PRNs are 31 and 15 which are at maximum elevation (Figure 4.2-3). The situation is not much better at 22:30UT. The PRN 9 which is located within the oval is not received at all. All IPPs are located within moderate to strong ROTI regions.
In Figure 4.4-3 the same maps are plotted for Stavanger receiver station. The maps are the same, but the IPPS and reception are different. The PRNS in panel C at 14:15UT in Stavanger are less affected than in Bergen. Of the eight PRNs there is only PRN 4 which is affected. This IPP is located inside the auroral oval where the ROTI is extremely high. At 15:00UT two of the satellites, PRN 4 and 13 are located inside the polar cap and are not received, PRN 1 is inside the oval and PRN 24 is on the equatorward boundary with poor signals. All satellites in view, apart from PRN 30 are suffering from fluctuating signals at this time. Panels E and F show that in comparison with Bergen, there are more satellites in view over Stavanger in the evening , and/or this receiver is more capable of maintaining lock on satellites. See e.g. PRN 15, 18 and 21 in Figure 4.4-4, which are more continuous for the Stavanger receiver, than for the Bergen receiver in Figure 4.4-2.This tendency is also marked by the circles in Figure 4.4-4 where for instance PRN 1, 8 and 28 actually are in view from Stavanger.

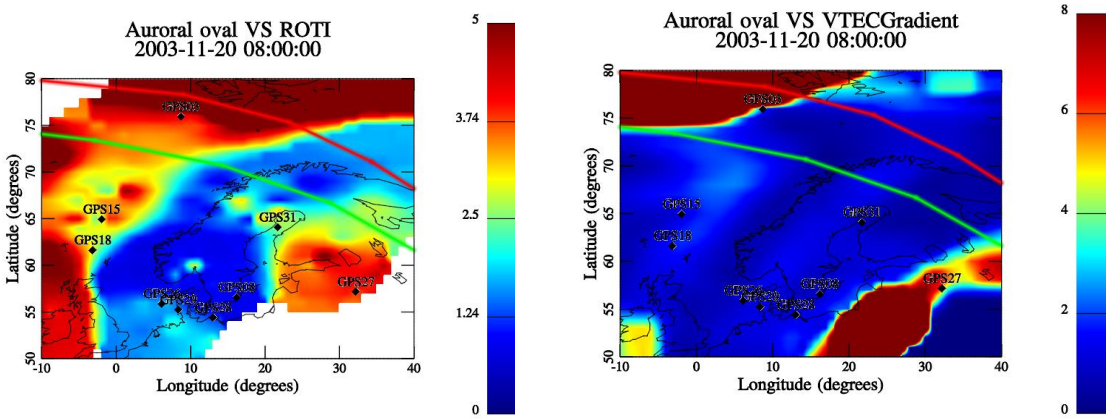

A:

B:

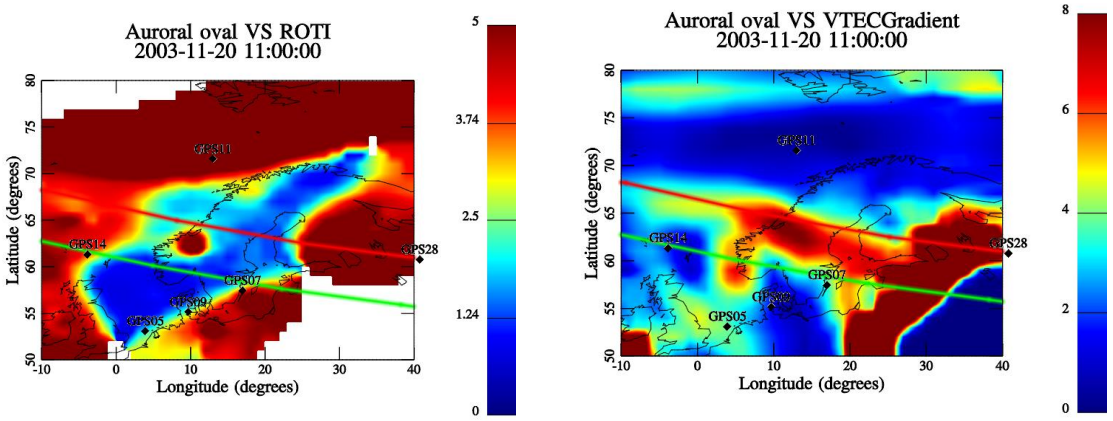
Auroral oval VS ROTI
2003-11-20 11:00:00
Auroral oval VS VTECGradient
2003-11-20 11:00:00
Latitude (degrees)
Longitude (degrees)
GPS11
GPS14
GPS28
GPS07
GPS05

C:

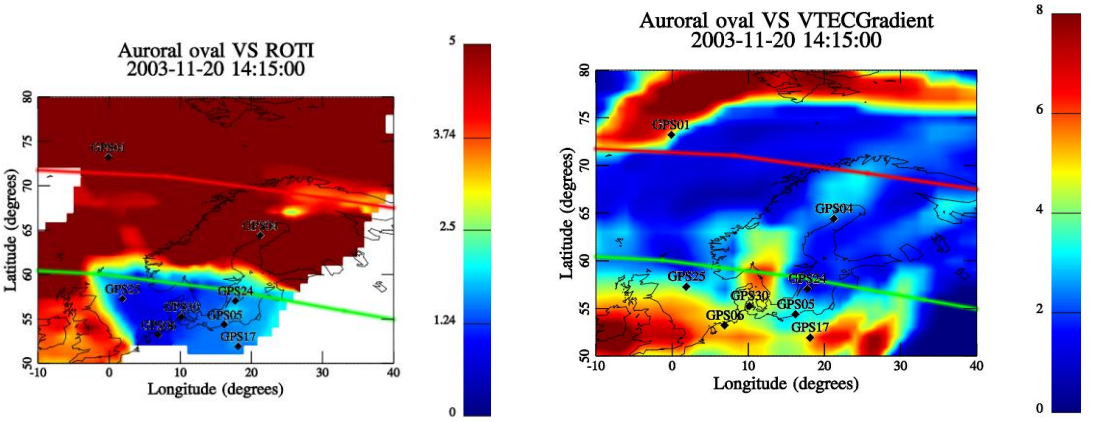
Auroral oval VS ROTI
2003-11-20 14:15:00
Auroral oval VS VTECGradient
2003-11-20 14:15:00
Latitude (degrees)
Longitude (degrees)
GPS01
GPS04
GPS25
GPS24
GPS30
GPS05
GPS06
GPS17

D:

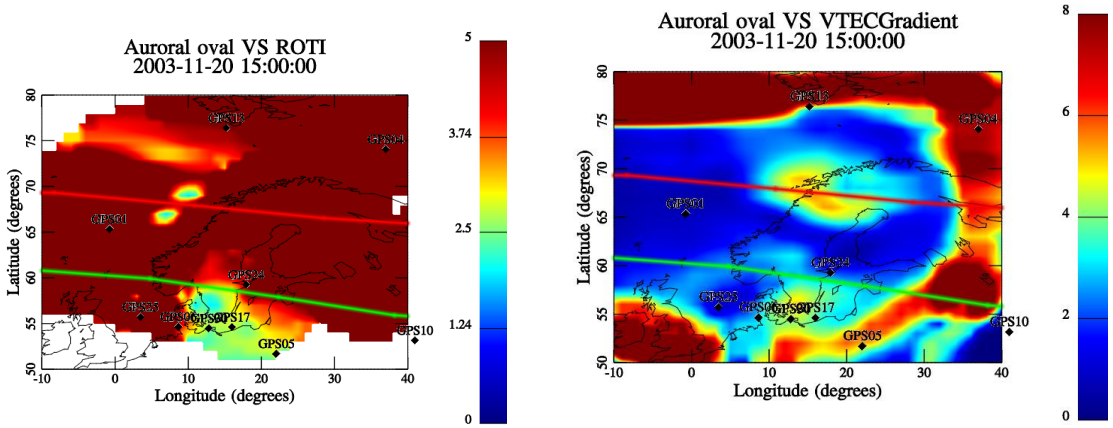
Auroral oval VS ROTI
2003-11-20 15:00:00
Auroral oval VS VTECGradient
2003-11-20 15:00:00
Latitude (degrees)
Longitude (degrees)
GPS13
GPS04
GPS01
GPS24
GPS10
GPS05
GPS17

E:

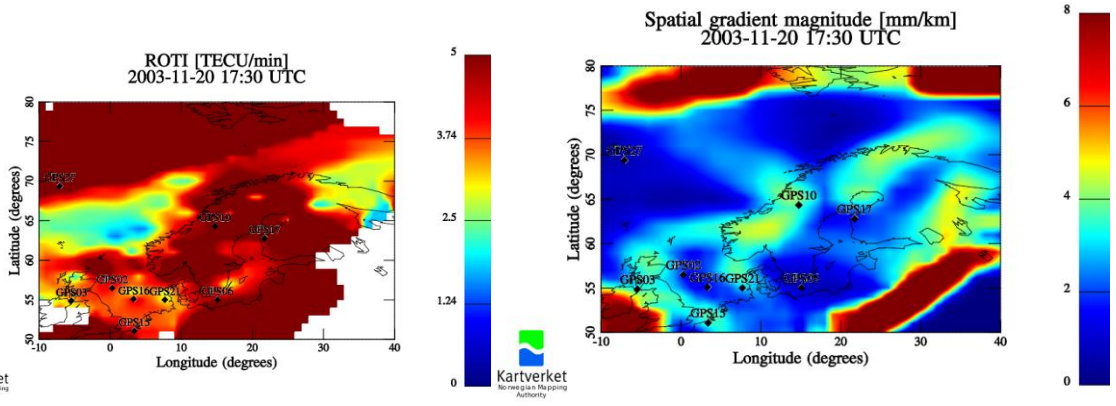
ROTI [TECU/min]
2003-11-20 17:30 UTC
Spatial gradient magnitude [mm/km]
2003-11-20 17:30 UTC
Latitude (degrees)
Longitude (degrees)
GPS27
GPS10
GPS17
GPS02
GPS03
GPS16GPS21
GPS06
GPS15
Kartverket
Norwegian Mapping Authority

F:

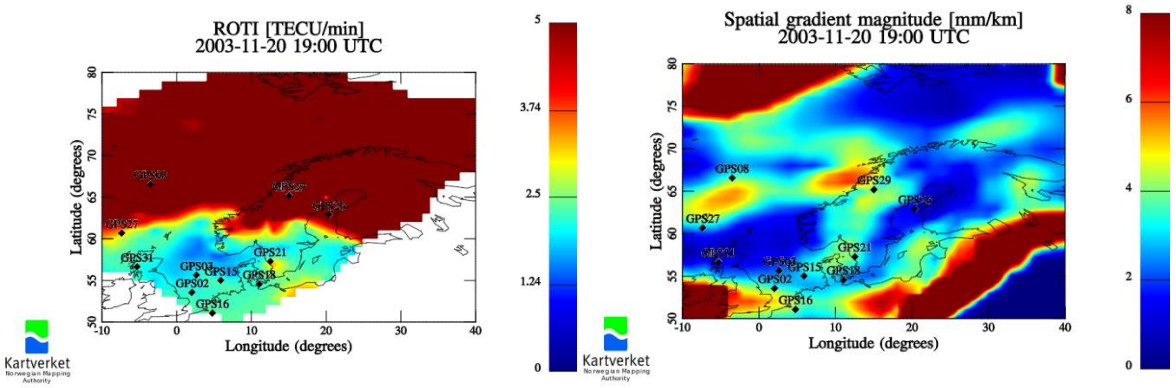

G:

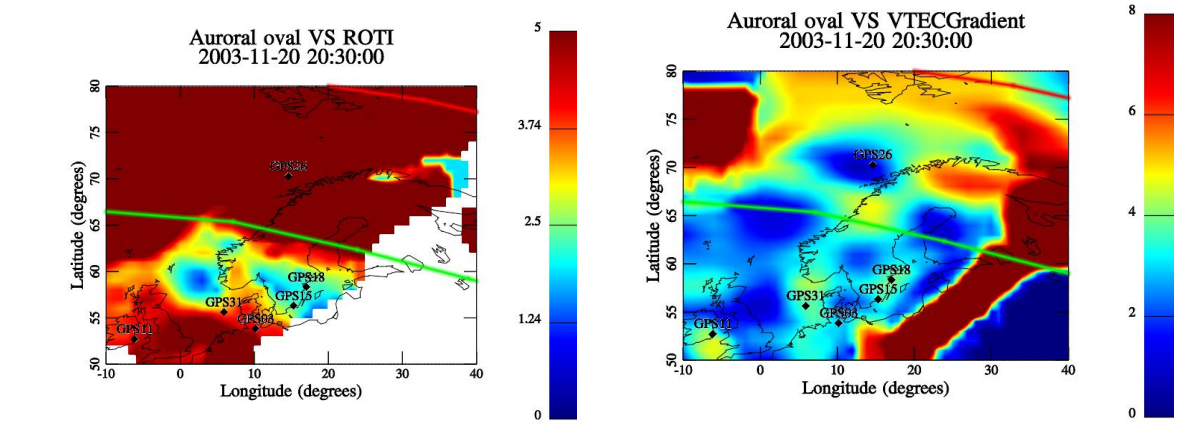

H:

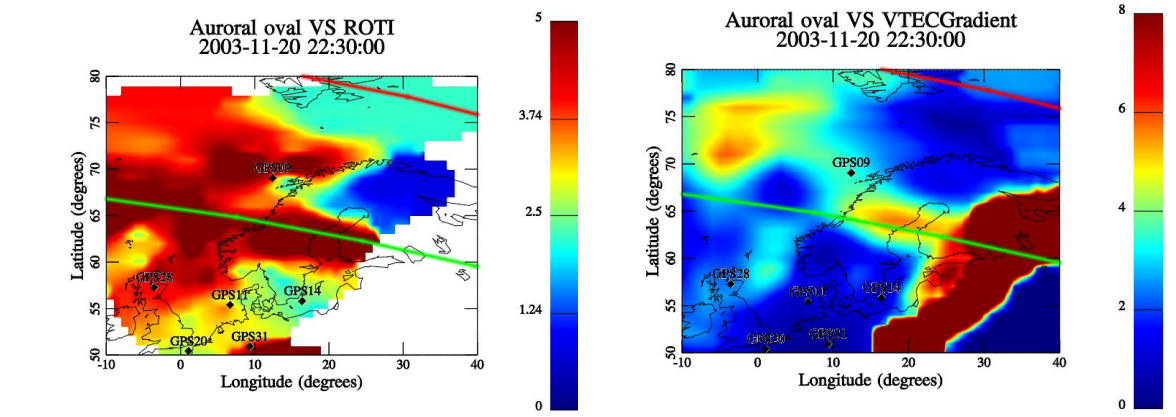

Figure 4.4-1: ROTI and gradient maps for Bergen receiver station. The equatorward (poleward) boundaries of the auroral oval are marked in green (red). The oval migrates equatorwards until the evening, then it slowly retreats. The location of the satellite IPPs are marked with PRN numbers. Satellites inside the oval or at the borders are affected by disturbances. Credit: Kartverket, Jacobsen,K.S., 2014.

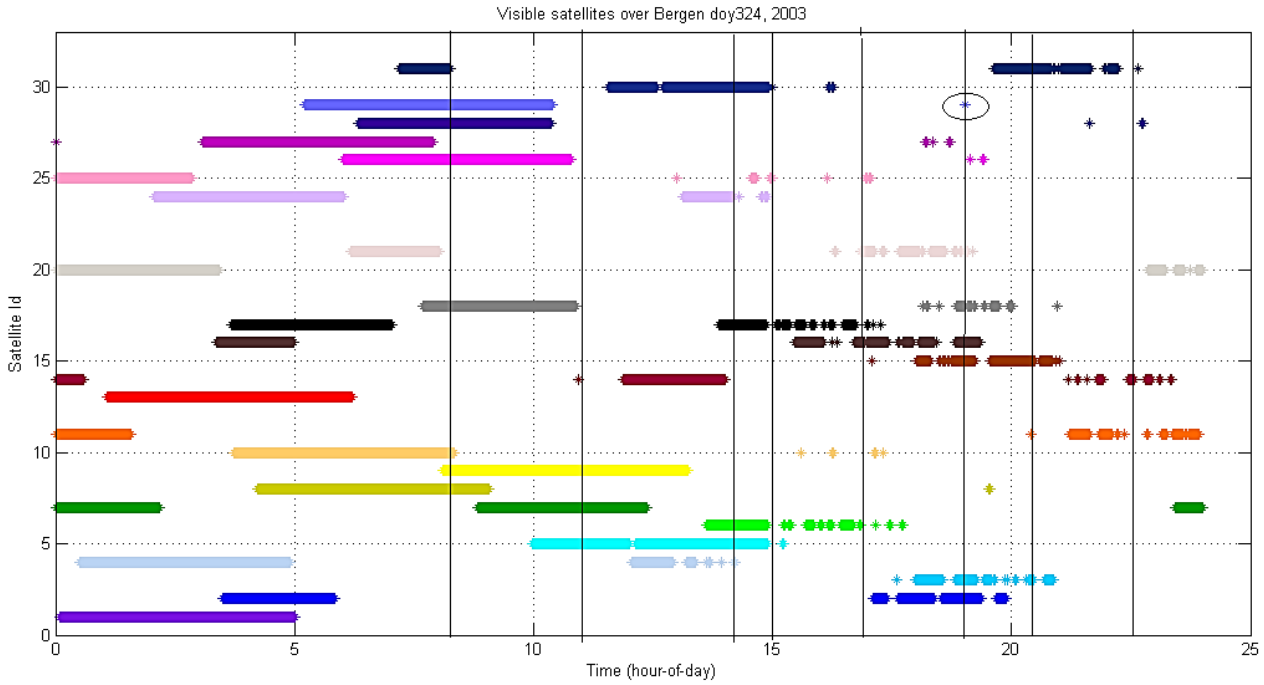

Figure 4.4-2: Plot over visible satellites over Bergen. Black vertical lines marks the selected times corresponding to the ROTI and gradient maps. Encircled PRN are not present in Stavanger plot.

A:

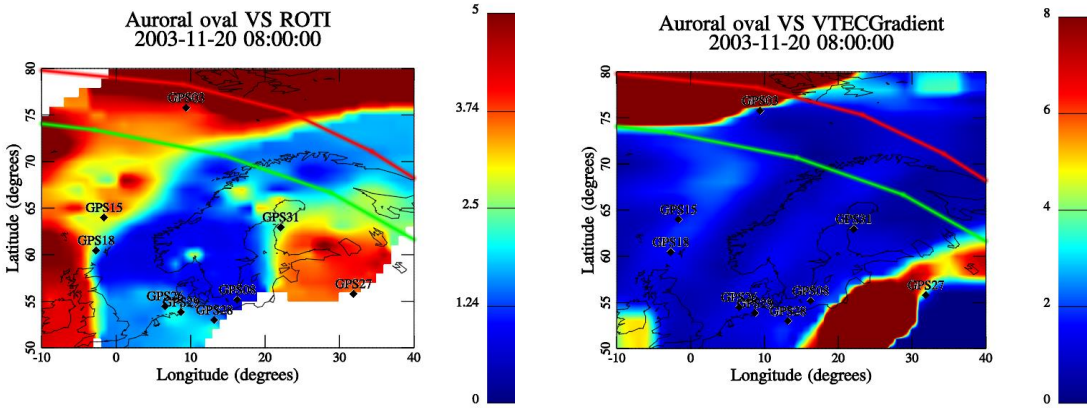

B:

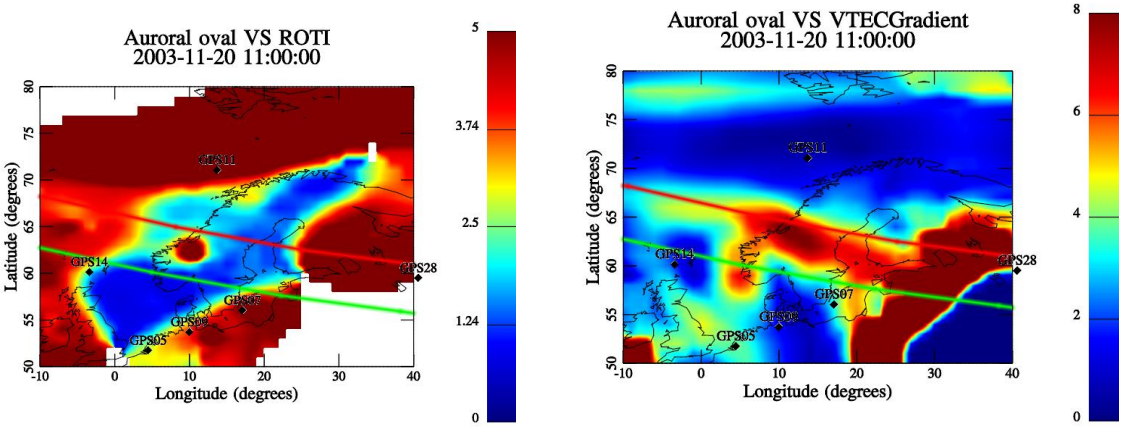

C:

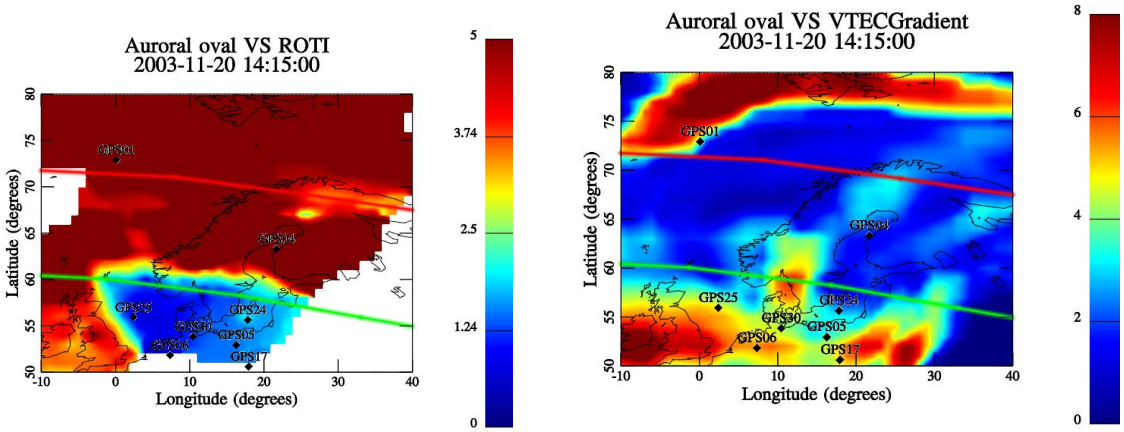
Auroral oval VS ROTI
2003-11-20 14:15:00
Auroral oval VS VTECGradient
2003-11-20 14:15:00
Latitude (degrees)
Longitude (degrees)

D:

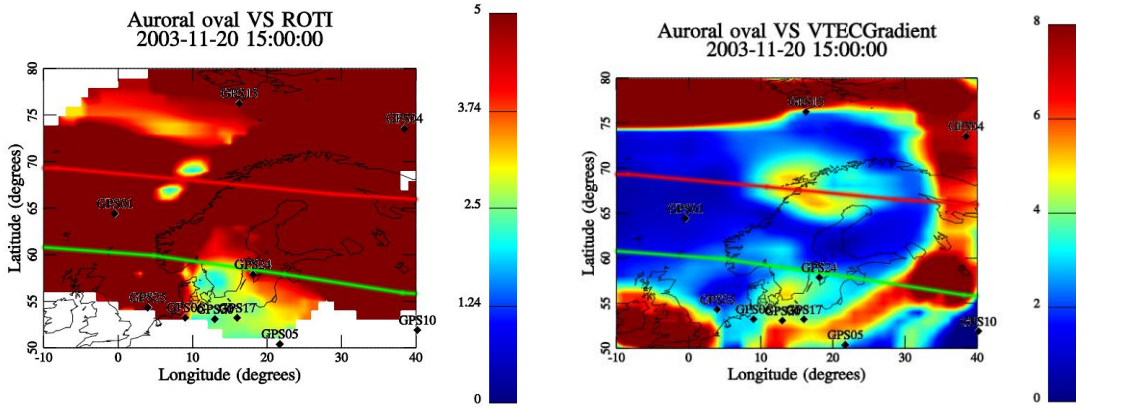
Auroral oval VS ROTI
2003-11-20 15:00:00
Auroral oval VS VTECGradient
2003-11-20 15:00:00
Latitude (degrees)
Longitude (degrees)

E:

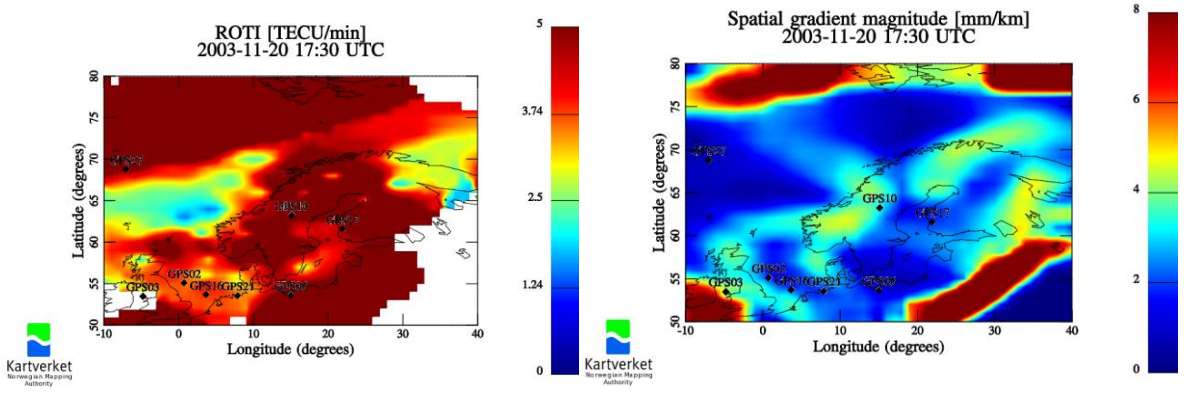
ROTI [TECU/min]
2003-11-20 17:30 UTC
Spatial gradient magnitude [mm/km]
2003-11-20 17:30 UTC
Kartverket
Latitude (degrees)
Longitude (degrees)

F:

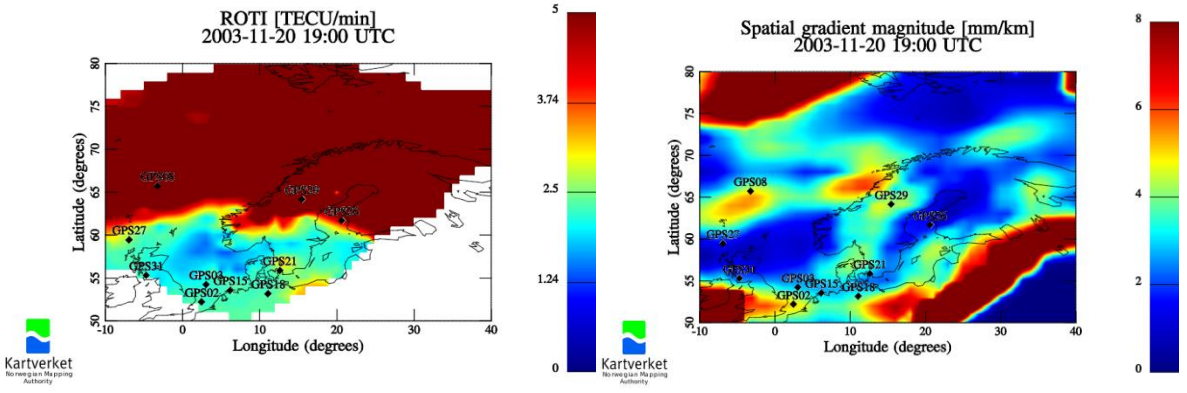
ROTI [TECU/min]
2003-11-20 19:00 UTC
Spatial gradient magnitude [mm/km]
2003-11-20 19:00 UTC
Kartverket
Latitude (degrees)
Longitude (degrees)

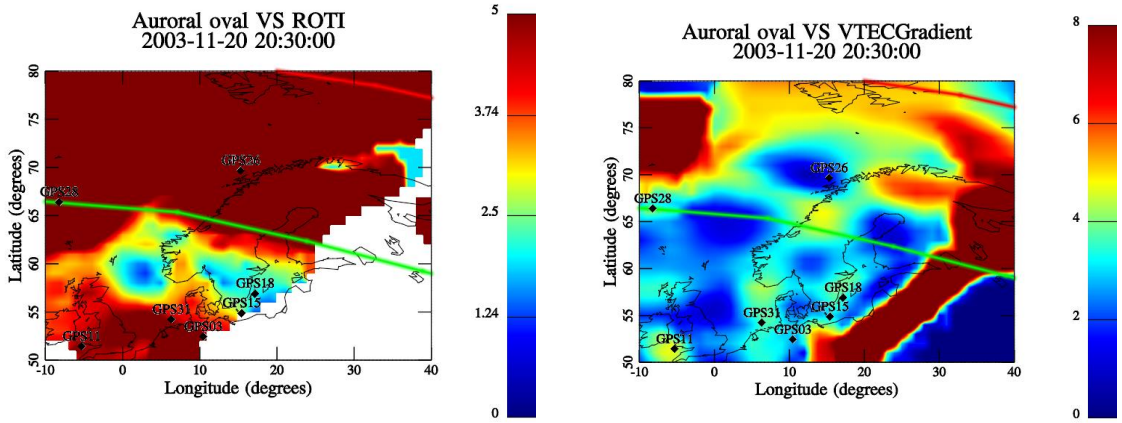

G:

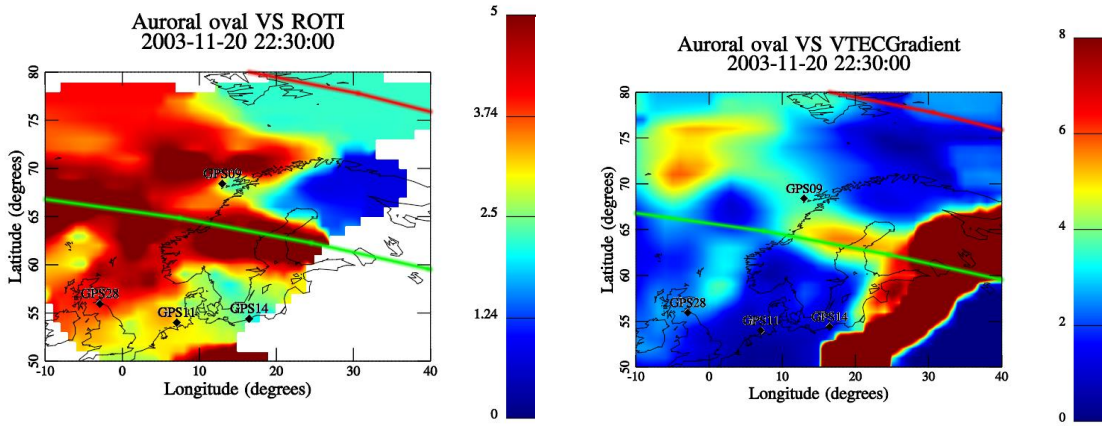

H:

Figure 4.4-3: ROTI and gradient maps for Stavanger receiver station. The maps are the same, but the satellite IPPs differ from Bergen in figure 4.4-1. Credit: Kartverket, Jacobsen, K.S., 2014.

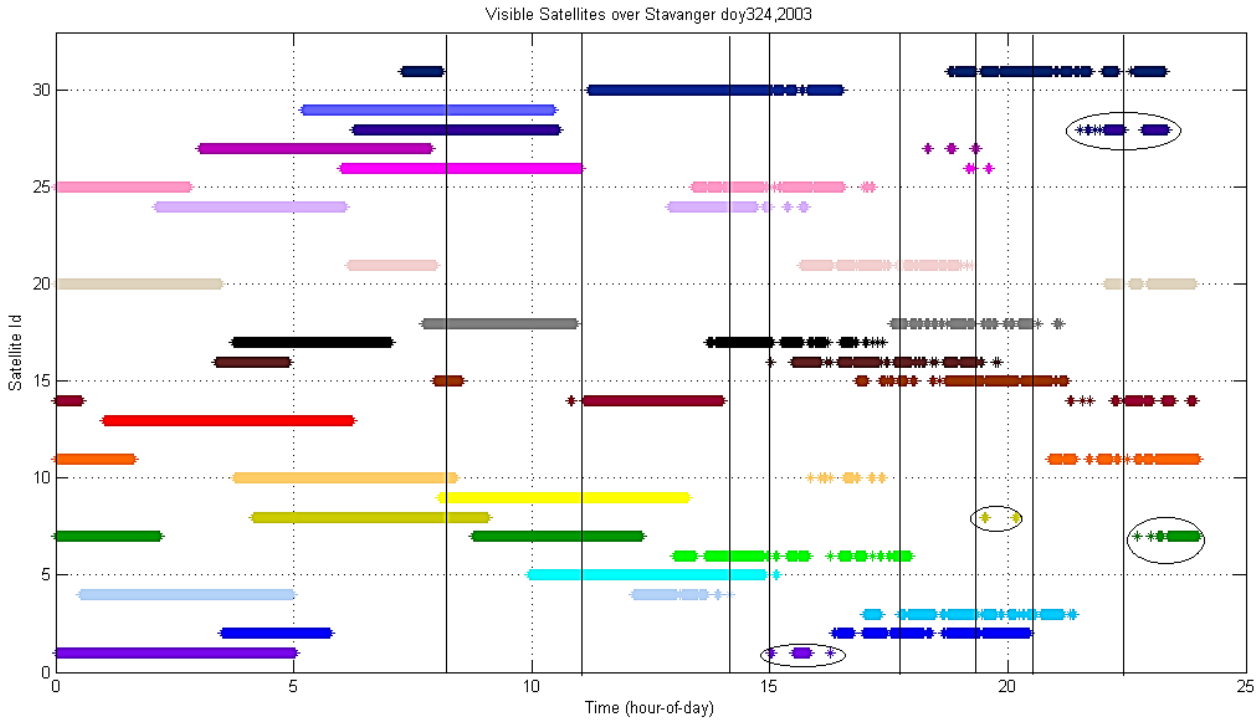

Figure 4.4-4: Plot of visible satellites over Stavanger. The selected times are marked by black vertical lines. The encircled PRNs illustrate differences in reception for Bergen and Stavanger.

5 Discussion and Conclusion

5.1 Forecasting

The data presented shows that the event November 20, 2003 was well monitored and recorded by different installations throughout the day. The question whether the NMA could have been notified at an early stage, depends on what caused the perturbations and consequently the loss of communication with the satellites. If the main cause was due to the geomagnetic activity, the NMA could have been notified of a severe storm approaching Earth two days in advance. If the plasma patches were of the main concern, the ISR network could have notified the NMA in the afternoon. However; in 2003 the NMA had no access to relevant space weather forecasts, and were caught off guard in what concerned their ability to provide a reliable positioning service and alert their clients.

5.1.1 Monitoring the sun and solar wind

Since the scientific community was expecting the return of the active regions responsible for the Halloween storms, the sun and solar activity was closely monitored. For instance, the SOHO-satellite provided near real-time quick looks and hotshots of the solar activity on their homepage (http://soho.nascom.nasa.gov/data/realtime-images.html) [Fleck, B. private communication, 2014]. Images taken by the LASCO coronagraph on board SOHO, could be used to model the velocity and propagation time of the CME/MC [Zhang et al., 2002; Gopalswamy et al. 2001]. The average time for a CME/MC to reach Earth was found to be 64 hours by Zhang et al. [2002]. However; fast transit events, such as the storm on October 29, 2003 or the August 1972 event, which arrived after 19 and 17 hours respectively, are likely to occur during solar maximum [e.g. Murtagh et al., 2004]. This means that the minimum notification time for CMEs/MCs must be less than 24 hours. In general the warning window should be as accurate as possible. Several models seek to get a good estimate of the arrival time at 1AU. Venkatakrishnan and Ravindra [2003] found a relationship between the magnetic energy stored within an active region and the initial velocity of a CME assuming all the energy is released:

$$log_{10}v = -12.4 + 0.481 log_{10}E \qquad (5.1)$$

where v is the initial velocity and E is the magnetic energy.

Zhang et al. [2002] used the following relation to estimate the transit time, *T*, from the initial velocity of the CME, *v* :

$$T = 96 - \frac{v}{21} \qquad (5.2)$$

Gopalswamy et al. [2001] used a modified model to estimate the arrival time assuming that the acceleration would cease at some distance d_1 from the Sun. The remaining distance from cessation to approximately 1 AU is denoted d_2:

$$t_{total} = \frac{-u + \sqrt{u^2 + 2ad_1}}{a} + \frac{d_2}{\sqrt{u^2 + 2ad_1}} \qquad (5.3)$$

where *u* is the CME-speed at 2 solar radii calculated from LASCO-images, *v* is the ICME-speed at 1AU calculated from WIND-data. The acceleration, *a*, is given by the linear expression:

$$a = 2.193 - 0.0054u \qquad (5.4)$$

For the November 20 event, the linear relation in eq.(5.4), gave a deceleration of -6.8 ms^{-2} compared to the actual deceleration of -5.2 ms^{-2} [Gopalswamy et al.,2005a].

Dryer et al. [2004] and his "Fearless Forecast" team at the Geophysical Institute (GI) at University of Fairbanks (gse.gi.alaska.edu) used four different models to estimate the 1AU arrival time on November 20, 2003. Two of the models gave a good estimate of the arrival time: The HAFv2-model (Hakamada-Akasofu-Fry, version 2) was a modified kinematic model which simulated the propagation time based on continuously updated data reports. The ISPM-model (Interplanetary Shock Propagation Model) used a 2D-simulation of the MHD-wave to predict the arrival of the shock. The first model predicted impact at 09:00UT, whereas the latter predicted the impact at 04:49UT. As we recall from section 4.1 the actual shock arrived at 07:28UT. Although the models performed satisfactory, they pointed out that none of them were perfect.

During the Halloween storms a month earlier, various space weather forecasting groups/bureaus issued their predictions either online, by mail or telephone. Oler [2004] did a survey on the notification time and preciseness of the warning windows selected forecasters issued to the Northeast Power Coordinating Council (NPCC). For instance, the Space Environment Center (www.sec.noaa.gov, now SWPC), issued their forecast to worldwide clients within a 24h window. The Solar Terrestrial Dispatch (STD) is the primary space weather forecast bureau for the NPCC, and they issued their forecast by mail and online (www.spacew.com) 12 hours before the storm on October 19, 2003. STD argues that they were the fastest notifier, while Dryer's "fearless forecast" only had a 9-12h error on their forecast making the HAFv2-model the most accurate in this survey.

Although there were uncertainties in the time windows, these groups/bureaus could have notified the NMA of the upcoming storm on November 20, 2003. The Ionospheric Prediction Service (IPS) in Australia (www.ips.gov.au/space_weather), the Solar Influences Data Center (SIDC) in Belgium (sidc.oma.be), the Geologic Survey of Canada (GSC, http://www.spaceweather.gc.ca/index-eng.php), along with the centers mentioned earlier, could all reach the public either by mail or website.

There are some challenges worth mentioning. First of all; the SOHO-data is not available on a 24 hour basis. When the ground station restores contact with the satellite, archived data is processed first in order to check for missed events. This leads to a delay in the real-time data up to several hours. The Hotshots are also processed (manually) in this way [lasco-www.nrl.navy.mil; Haugan, S.V. H., private communication, 2014]. Concerning prediction of geomagnetic storms from solar activity, there is more to be considered. For instance solar storms which does not originate from the front side of the solar disk, does not leave a signature in EIT-images [Zhang et al., 2002]. This means these could be difficult to forecast. Also, the active region responsible for the November 20 -superstorm was relatively small. This makes it difficult to estimate the relationship between the magnetic energy and initial speed of the ICME/MC, and thus the ram pressure at the magnetopause [Srivastava et al., 2005]. Therefore it is also difficult to predict the magnitude of the geomagnetic activity. Another issue is the inclination of the axial component and chirality of the MC. This is of importance concerning the magnitude of geomagnetic activity. Flux rope helicity in the MC changes direction with the solar cycle [Lepping et al., 2003]. Theoretically this could be useful in order to estimate the arrival and duration of the MCs, however: MCs with strong southwards Bz-components, such as this one, does not follow a solar cycle pattern [Mulligan et al.,2001 in Gopalswamy et al., 2005a]. Despite these challenges, improved models and automated CME detection services such as CACTus, ARTEMIS and SEEDS are now available online [Webb and Howard, 2012]. The STEREO satellites that were launched in 2006 are a valuable contribution to the forecasting of CMEs/MCs [SSC, stereo-ssc.nascom.nasa.gov,2014].

In addition to the SOHO-data, solar observatories such as the Big Bear Solar Observatory in California (www.bbso.njit.edu) or the Mauna Loa Solar Observatory (http://www2.hao.ucar.edu/mlso/mlso-home-page) could detect solar flares. Unfortunately activity reports/observation logs from these observatories were posted in the evening universal time (www.bbso.njit.edu; http://download.hao.ucar.edu/d5/mlso/log/event/mlso.daily_and_events.2003), whereas the CME responsible for the November 20 storm erupted in the morning, UT. This could have been too late if the ICME was a fast-transit-event.
Since a solar flare is recognized by an increase in the X-ray flux, (section 2.1.5), the solar X-rays are measured by the GOES satellites. In 2003, the GOES12 SXI could provide X-ray images along with X-ray flux measurements [www.osd.noaa.gov/GOES/, Brekke,P. and Haugan, S.V.H. private communication, 2014]. NOAA kept a constant automated watch on solar energetic particle (SEP) fluxes. For SOHO's behalf, automated text message alerts were sent when the levels became too high [Haugan, S.V.H., private communication, 2014]. As for solar wind data from ACE, NOAA issued these in real time from their homepage (www.swpc.noaa.gov/ace/ace_rtsw_data.html) [Bisecker, D., private communication, 2013]. As we know, solar wind data from ACE can be used to estimate the arrival time at the magnetopause and monitor variations in the IMF in less than one hour in advance.

5.1.2 Monitoring patches and electro jets

When the solar wind arrives at the magnetopause, the alerts change from "forecast" to "nowcast." Although the data were gathered in real time, not all services issued them online or to the public. Some of the following services were online and easy accessible in 2003.
Kyoto WDC collected real time magnetometer measurements to derive the AE-index, and quick look data were issued on webpage from 1996 [http://wdc.kugi.kyoto-u.ac.jp/wdc/Sec1.html]. The Aurora Watch administered by University of York issued free aurora alerts to registered users from 2000 [http://www.york.ac.uk/news-and-events/news/2000/aurorawatch/]. OVATION plots were also online in real time in 2003 [Newell et al., 2002]. Thus geomagnetic data were available for quick look purposes.
Most radars run on schedules, but the ISRIM (Incoherent Scatter Radar Ionospheric Model) was online in (http://www.openmadrigal.org/) from August 2003. The real time service was not online until May 2004. This model was meant as a complement when the radars were not running [Holt et al., 2002]. The SuperDARN HF-radars operated in near real time and automated generation of convection maps were posted on the former online operative site (http://super-darn.jhuapl.edu/) [Chisham et al., 2007]. Ionosonde data were available online from the Lowell DIDbase in 2003, and ionograms from Tromsø and Greenland have always been online in real time [Reinisch,B., private communication, 2014].
GNSS-data were available online from IGS (International GNSS Service), but with a one day delay. In addition the US National Geodetic Survey's CORS network (Continuous Operating Reference Station), and the Continental US receiver network, were available [Klobuchar, 1997]. NASA Jet Propulsion Laboratory in California provided crude TEC maps online on their homepage (http://iono.jpl.nasa.gov//latest_rti_global.html). So did also NOAA SPWC [Foster, J.C., private communication, 2014].
Concerning this particular event; the research community was awaiting the return of the active regions from the prior month. Hence the IS-radars at Millstone Hill, Sondrestrom and EISCAT Tromsø were running. The use of TEC maps was quite pre-liminary, however the research team from Millstone Hill and Lincoln Laboratory were the leading edge with their Millstone Hill GPS Real Time Ionosphere Mapping System (GRIMS) developed by Coster et al. [1992]. GRIMS was connected to over 120 GNSS receivers all over the American continent to construct TEC maps [e.g. Coster et al., 2003].

The bottom line is that although the radars were not running with the purpose of forecasting a TOI, the researchers at Millstone Hill were aware of the possible formation of one. The concept of the TOI was not very well established at this time [Foster, J.C., private communication, 2014], but Millstone Hill researchers had studied the storm enhanced density (SED) plumes, which convect into the polar cusp, for a decade [Foster, 1993]. With this information, the NMA could have been notified of the possibility of patches and eventual blobs trapped within the ionospheric convection pattern and auroral zone during evening and midnight hours. Concerning scintillation warnings, the Italian ISACCO[5] GISTM-receiver in Ny Ålesund [DeFranceschi et al., 2006] were transferring hourly updates to INGV in Rome. Thus scintillation data could have been accessed through the ESWUA[6]-project [Romano et al., 2008] for near real time monitoring of increased scintillation [DeFranceschi,G. private communication, 2014].

5.2 What Caused the Outage?

In order to settle the cause of the satcom outage, we need to look into the relation between the storm dynamics, increased TEC and scintillation.

5.2.1 Onset of Outage

The outage occurred almost simultaneously over the whole Southern part of Norway from approximately 14:00UT. According to Aquino et al. [2006], daytime disturbances are due to geomagnetic activity caused by ionospheric currents and the consequent expansion of the auroral oval due to reconnection processes. Hence we investigate these data further. The solar wind proton density in Figure 4.1-3 shows an increase of 30 cm^{-3} at ~12:30UT. With an approximate 40 min propagation time from ACE, this dense solar wind would reach the dayside magnetopause around 13:00UT. According to SuperDARN data from 13:04UT (not shown), the CPCP reached a maximum of 76kV indicating an increase in polar cap flux due to dayside reconnection. Simultaneously, we see a drop in the AL-index in Figure 4.3-1b), which indicates tail reconnection as well. Hence the reconnection could be steady state at this moment. Norway is situated in the afternoon MLT sector, and there is some enhanced flow in the return flow over Northern Norway, but as mentioned earlier it is uncertain what it implies. In Figure 4.4-1 at 14:15UT, we can see that the auroral oval indeed covers most of Norway except from the southernmost part, such as Kristiansand. This could explain why the GPS-signals were less affected in Kristiansand than the other stations before 15:00UT. The ROTI is increased along the equatorward boundary of the oval, with 1.5-3.0 TECU/min in Bergen at 14:15UT Figure 4.4-1. From Figure 4.1-6 we see that the EEJ and WEJ overlap in the manner described in section 2.4.4.1. Although there was no visible aurora in view for the Kiruna All Sky camera at this instant, the ongoing reconnection, the broad auroral oval and associated electrojets are the most likely cause of the perturbations. Up until 14:30UT, there has been a moderate feeding of flux (CPCP ~50kV). The onset of the expansion phase at 14:48UT was captured by the Kiruna camera in terms of a westward traveling surge in Figure 4.3-2. At 15:00UT we can see that the ROTI is extremely increased and the auroral oval has migrated even further equatorward. The CPCP reach a maximum of 126kV at 15:06UT according to SuperDARN data (not shown). It is left beyond doubt that the severe increase in auroral activity and associated currents contribute to the loss of signals in all receiver stations. In addition to the increased auroral activity at 15:00UT, SuperDARN plots in Figure 4.3-6 reveal enhanced flow activity in the polar cap, which implies that a TOI might be entrained within the anti-sunward convection.

[5] ISACCO-Ionospheric Scintillations Arctic Campaign Coordinated Observation
[6] ESWUA-Electronic Space WeatherUpper Atmosphere

5.2.2 Increased Solar Wind Density or Polar Cap Patch?

Around 15:30-16:00UT a new increase in the solar wind proton density occurs. Could it be responsible for the massive drop in the AL-index at 17:30UT?

The growth phase until ~16:00UT could be caused by the increased solar wind density increase. In the AL-index in Figure 4.3.1 we see an onset of tail reconnection about 17:30UT. At the same time the AU-index becomes negative implying that the WEJ completely dominates over EEJ. The AL-index drops to a minimum of -2000nT, but the CPCP remains moderate increased ~65kV. Recalling the Sym-H/Dst-index, we are now within the main phase of the magnetic storm. The ROTI-map from 17:30UT lacks the auroral oval, but it is reasonable to think it at least reach as far south as Mid-Norway. Western Norway and Southern part of Norway reveal ROTI values of about 3.6 TECU/min and 4.0TECU/min respectively. It would be reasonable to relate these values to the strong storm activity. However; another scenario may also add to it:
The SuperDARN plot from 17:24UT shows an enhancement in the flow reversal region over Norway. If it indeed was a TOI which traversed the polar cap in the figure series in Figure 4.3-6, this could very well be the exit of it. The average flow velocity in Figure 4.3-6 is 800-1000m/s. If we assume an average flow velocity of 900m/s and an approximate distance of 5500km (estimate based on calculated distance from Millstone Hill to Tromsø, see appendix), and straight forward path ,we get an average drift time of: $t = \frac{5500km}{0.900km} s = 1h, 40min.$ This is quite consistent with the observations. If the patch/TOI exited the polar cap at about 17:30UT it could contribute to the increased VTEC observed in Figure 4.2-8. Here we can see TEC values around 20-25TECU over the receiver stations, and an enhanced region over Svalbard. At 17:50UT another TEC-map reveals a region of strong TEC over Northern Norway, which could be attributed patch material. Considering the expansion and contraction of the polar cap due to reconnection processes throughout the day, it is very likely that patches have been formed in the dayside by mechanisms described in previous sections.
The AL-index begins to recover after 17:30UT, but the AU-index remains negative. As the Dst-index reaches about -470nT, the storm enters its recovery phase about 20:00UT. Prior to that; the TOI Foster et al. [2005] tracked, exited the polar cap at 19:45UT. By then it had spent ~2h traversing the polar cap. Calculation of drift time as above is highly risky, since patches rotate, stagnate or change trajectory during transpolar convection [e.g. Oksavik et al. 2010; Dahlgren et al., 2012]. Thus it holds for an estimate only, despite that 1.5-2h convection time is reasonable for high flow velocities.

Rest of the evening is affected by night side disturbances in the form of aurora. The auroral oval covers a large part of Norway with its equatorward boundary at ~66° latitude. It slowly retreats polewards as shown in Figure 4.4-1 panel G and H. In the SuperDARN plots there were flow enhancements in the anti solar flow over Norway. This could be attributed the TOI or patches from the dayside. The ionosonde data from Tromsø and Sondrestrom for the rest of the evening had poor quality, but the radar spectra from EISCAT Tromsø, reveals increased densitites in the evening F-region. From the radar started scanning around 19:00UT, the density spectrum show that a train of high density pathces traverse the beam until ~21:45UT. Thus it may seem as even though the storm recovered, the nightside reconnection allowed these patches to exit the polar cap.

As for the ionograms presented in section 4.3.4, it could be worth mentioning the low density in the Tromsø data. The ionograms from Sondrestrom revealed an increased plasma peak frequency of about 9.4 MHz and a peak height of 413km at 18:50 UT. Converted to number density, this corresponds to n= $1.1 \cdot 10^{12} m^{-3}$. This is consistent with high density patches that originate from solar EUV ionization [Carlson, 2012], thus this must be part of the TOI. The Tromsø ionograms reveal spread F, but low plasma peak frequencies and peak heights. The plasma peak frequency as the patch exits the

polar cap is 3.2 MHz corresponding to a number density of n= $1.3 \cdot 10^{11} m^{-3}$ and a peak height of 227km. This is a rather weak patch strength and could imply that it originated from somewhere else or was produced by auroral precipitation [Carlson, 2012]. However; the Eiscat data from Tromsø measured much higher densities at higher altitudes consistent with the patch data from Sondrestrom. Thus, the dicrepancy between the ionogram and radar data could be due to location of the ionosonde relative to the radar beam field of view. Besides, ionosondes measure the bottomside ionosphere, so it probably captured precipitation in the auroral oval instead of the TOI-material.

5.2.3 VTEC

In the VTEC time series plot in Figure 4.2-8a) we see that the VTEC increases from early morning and peaks around 10:00UT for Norhtern and Mid-Norway. The peak propagates southwards with time and the VTEC reaches a maximum of ~40TECU at noon. Since the VTEC increases simultaneously in the morning for all regions, it could be attributed the daytime ionization. Another explanation is the arrival of the MC. Hence the southward migration of the VTEC maximum could imply that either is the ionization strongest in Southern Norway, or an expanded auroral oval with associated irregularity zone [Aarons,1997] migrates equatorwards with the reconnection processes caused by the MC. According to Basu et al. [1983] TEC enhancements can be registered at onset of negative excursion of the H-component in magnetograms, and in association with increased phase and amplitude scintillation. The increased TEC in Southern Norway at noon and Mid-Norway registered at noon and 20:30UT respectively, are indeed coinciding with the onset of expansion phasis in the AL-index in Figure 4.3-1b). The increased VTEC of ~50TECU in Mid-Norway at approximately 20:30UT, is due to the patchmaterial from the TOI. It is unusual to record such high TEC values in the evening unless there are EUV-plasma patches that have drifted across the PC from the dayside involved [Jacobsen, K.S., private communication, 2014]. Apart from the peaks in the midday and evening, the VTEC decreases to ~10TECU in the afternoon. Thus the VTEC was actually quite low at the moment the satcom outage intiated, compared to before. Instead the ROTI was increased and it is reasonable to belive that the scintillation effects stem from smaller scale irregularities in the auroral oval and vicinity produced by soft precipitation gradients in the F-region [Basu et al., 1983], and eventual GDI .

5.2.4 TEC gradients, Instabilities and IPPs

Although the large scale gradient plots in section 4.4 have some unreliable features, they appear to reveal the fact that gradients are indeed situated along the edges of the auroral oval and enhanced TEC-regions, see e.g. Figure 4.4-1.
In the ROTI maps (section 4.2 and 4.4) we see that latitudes equatorward of Norway have increased ROTI (and TEC). This could be attributed to the irregularity oval as described by Aarons [1997] which is far more extended than the auroral oval itself. We also know that SAPS flow sunward in the dusk sector along the mid latitude trough during geomagnetic activity e.g.[Foster and Burke, 2002]. On the edges of the trough we find steep TEC gradients which are suitable to house irregularities due to instability growth [Fremouw et al., 1978 in Rino et al., 1978].
Recalling section 2.4.3.2 the two most important instability procesess in the high latitude F-region ionosphere were the Kelvin Helmholtz instability (KHI) and the gradient drift instability (GDI). Whereas the first process is associated with differing flow velocities in the plasma convection, the second is associated with differing densities along the plasma flow. We know that instabilities occur where there is abrupt separation between high and low density plasma, such as in the trailing edge of a patch or along the wall of a trough or precipitation boundary. The GDI can grow within order of tens of seconds along such steep TEC gradients in the right conditions (see section 2.4.3.2). In the E-region, and especially within the auroral oval, the irregularities are current driven. There are different instability mehcanisms which produce the irregularities. Larger scale irrgularities are associated with

Ex**B**-drift with a density gradient parallel to the magnetic field [Keskinen and Ossakow, 1983]. An E-region variant of the GDI is the current convective instability where a field aligned current (auroral precipitation) flows parallel to the magnetic field de-stabilizing the **E**x**B**-drift [Ossakov and Chaturvedi,1979]. Smaller scale irregularities are attributed the Farley-Buneman instability (aka two stream instability). This instability is associated with the auroral electrojets where the magnetized electrons follow the Hall drift perpendicular to the **E**-field, pervading the Pedersen drift of the ions (parallel with the **E**-field) and hence de-stabilize the plasma [Farley,1963; Schiffler,1996]. Thus it is plausible that the smaller scale irregularities observed in the ROTI maps stem from GDI instabilities along TEC gradients on the edges of region with higher TEC in the F-region, and from Farley Buneman instabilities associoated with the currents in the E-region. It is worth mentioning that irregularities associated with the auroral precipitiation can extend to altitudes above the E-layer [Skone et al., 2008], and similarily; irregularities can extend from the F-layer to the layers below (E and D) [Prikryl et al., 2013].

The satellite IPPs were plotted in the maps in Figure 4.4-1 and Figure 4.4-3 in section 4.4. They showed a clear correspondence between poor signal reception and IPPs situated on the auroral boundaries or with high or low elevation as viewed from the receiver (see Figure 4.2-3). All satellites located either in near vicinity of the equatorward auroral oval boundary, inside the actual auroral oval, or within the expanded polar cap, were the most affected at all times. This implies that radio signals within these regions were prone to scintillation effects visualized by the high ROTI. Inside the auroral oval and in the polar cap, the ROTI were as high as 5 TECU/min, whereas for the equatorward boundary the ROTI were ~2TECU/min. Most of the IPPs were actually equatorwards of Norway and the equatorward boundary of the auroral oval, placing them in a region with TEC gradients likely associated with the trough walls. The SAPS are associated with weak phase scintillation [Prikryl et al., 2013] and are collocated with the troughs close to the equatorward boundary of the auroral oval. As most satellite IPPs are located in this region, it is likely that this also contribute to cycle slips. The irregularity oval extends latitudinally beyond the auroral oval during disturbed conditions. Hence increased ROTI in these regions could also be attributed this expanded region, or the turbulent energies infused by the storm disturbance [Aarons, 1997].

5.2.5 Cycle Slips and Scintillation

In the high latitudes and auroral zone, phase scintillation and combined phase and amplitude scintillation are significantly higher than amplitude scintillations [e.g. Aquino et al. 2006]. Thus ROTI maps which correspond to smaller scale irregularities causing phase scintillations, provide a good estimate of scintillation occurrence. Prikryl et al. [2011, 2013] found that phase scintillation and consequent cycle slips were related to enhanced auroral activity.

The phase scintillation plots in section 4.2 were sampled at a much lower rate than recommended, however they do reveal a relation with the increased ROTI and number of cycle slips. The cycle slip plot in Figure 4.2-8c reveals several peaks, and despite a fluctuating number of peaks, they increase in amplitude and number throughout the day. For instance a peak around 08:30UT of ~900 cycle slips and a moderate increase in σ_φ of ~0.4-0.5 radians (please recall section 2.5.3.1 for scintillation values), is most likely related to the IMF Bz reversal at shock arrival. The reversal to northward IMF Bz could be attributed a peak of 1400 cycle slips and an increased value of σ_φ at ~0.8radians around 10:45UT. Interestingly there is a minimum of cycle slips at noon, when in fact the VTEC has a peak of almost 40TECU in Southern Norway. The phase fluctuations are σ_φ ~0.4-0.5 radians as in the morning. The number of cycle slips increase throughout the afternoon as expected from the SATREF data in section 4.2 and 4.4, and the phase scintillations increase accordingly. At 16:00UT, however;

another minimum of cycle slips and phase scintillation occurs. This seems a bit odd when comparing it to a ROTI map from 16:00UT (Figure 5.2-1). At this moment there are several satellite IPPs in the ROTI map, but as seen in the visible satellite plot from Bergen (see Figure 4.4-2), only PRN 6 and 16 are received. As for the Stavanger receiver PRNs 10, 16,17 21,25 and 30 are received, see Figure 4.4-4. Hence the low number of cycle slips could correlate well with Stavanger data, but not with Bergen data. A GIVE plot (Grid Ionospheric Vertical Error) in Figure 5.2- 2 reveals a moderate increase (20 TECU/min). A high GIVE indicates few gridpoints, or IPPs [e.g. Sunda et al., 2013], but the moderate GIVE from this plot suggests that there are a certain amount of registered gridpoints after all. Assuming that the Bergen receiver was operating satisfactory with e.g. no thermal noise or errors, there should be no difference in receiver performances between Bergen and Stavanger (both Trimble MS750). Thus we can rule out technical issues. An explanation to the dicrepancy could be the assumption of the IPP height and use of the SLM, which does not take the 3D-TEC distribution into consideration see eg. [Smith et al., 2008]. Another plausible explanation to this, must be due to averaging in the cycle slip calculation.

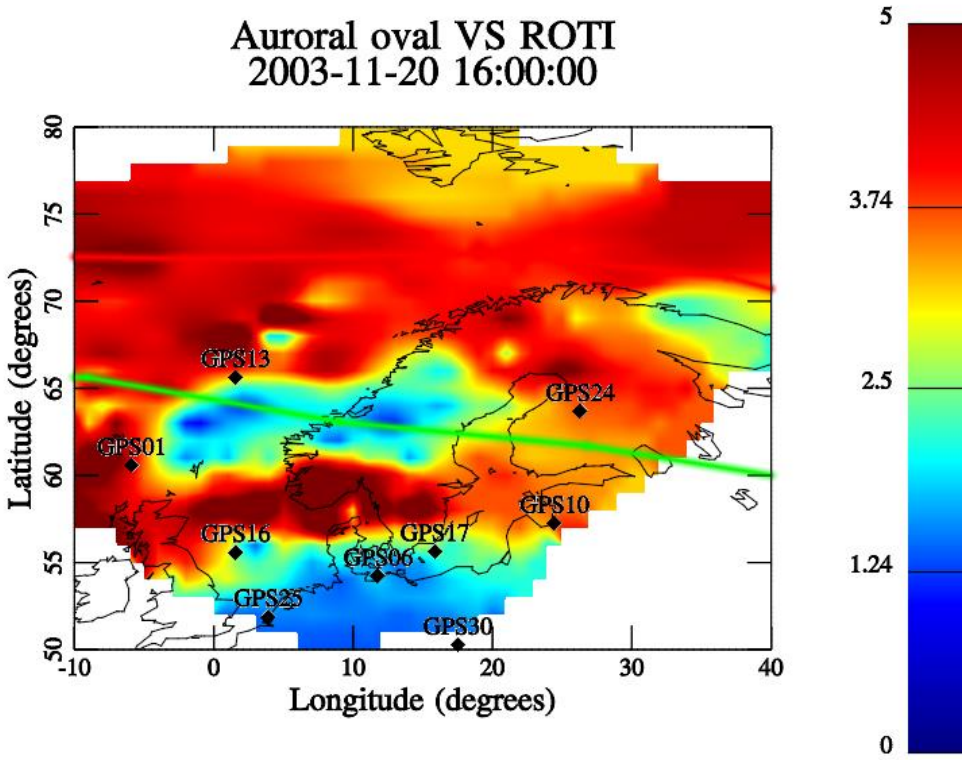

Figure 5.2-1: At 16:00UT there is a discrepancy between the low number of cycle slips recorded and the actual low number of received satellite signals. This plot from Bergen shows that the satellite IPPs are located in high ROTI regions, thus explaining the cause poor reception.
Credit: Jacobsen, K.S., Kartverket , 2014

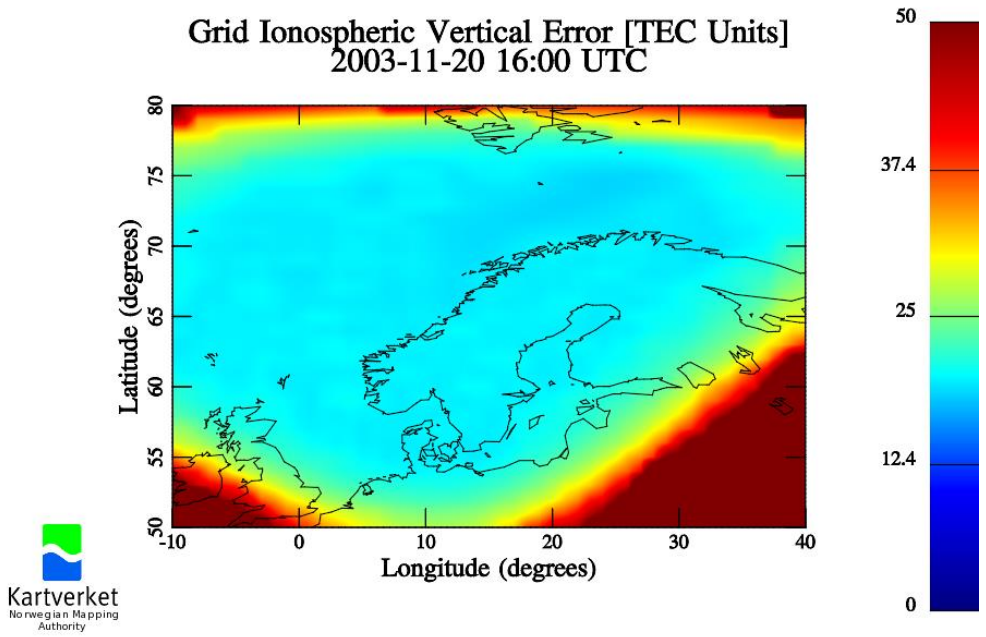

Figure 5.2-2: GIVE- map reveals only moderate error increase, indicating that there must be satisfactory amount of gridpoints, and hence IPPs available. Credit: Jacobsen,K.S., Kartverket, 2014.

Recalling section 2.4.3.1. on the fate of patches, the patches exiting in the midnight sector crosses the o/c-boundary and becomes entrained in the convection of closed field lines. Thus they join the return flow in the nightside auroral oval as so-called blobs. In the nightside oval, auroral precipitation may enhance the electron density [Burns and Hargreaves, 1996; MacDougall and Jayachandran, 2007]. Consequently will the blobs and auroral precipitation further increase the possibility of irregularity growth and scintillation in the evening and night sector. Although there are no solid evidence of blobs in the return flow (all visible enhancements in flow or TEC seems to be located in the anti-sunward flow in data presented here), the TOI/patches in the evening seen in the EISCAT Tromsø spectrogram (Figure 4.3-13) , and the tail reconnection seen in the AL-index, implies that this high density material must exit the polar cap and become entrained in the sunward return flow at some point. At 17:30UT and 20:30UT there are peaks in the cycle slip plot of 1300 and 2000 cycle slips respectively, with corresponding σ_φ values of 0.75-0.8 radians. These maxima could be attributed high density patchmaterial from TOIs, and for the latter it is certain, due to simultaneous increase in VTEC as commented earlier.

A list of the corresponding magnitudes and events discussed so far are summarized in Table 5.2-1. As we can see there are some weak correlations between onset of the expansion phase and the number of cycle slips in the evening, however there are no correlation in VTEC versus onset of expansion for these time, as Basu et al. [1983] reported. Neither are there any correlation between VTEC and number of cycle slips (see Figure 5.2-3b) with a correlation coefficient of r = 0.063. This indicates that there is not necessarily the TEC, but rather the fluctuations in TEC, such as ROTI, which is related to cycle slips through scintillation. In Figure 5.2-3a) we can see that there is a positive correlation between the number of cycle slips and phase scintillations. The correlation coefficient of r = 0.77 clearly suggest that the number of cycle slips increase with increasing phase scintillation. The correlation between mean ROTI and phase scintillation is r = 0.63,(Figure 5.2-3 c). This may seem low, but from the plot we see that moderate to strong phase scintillation is associated with increasing levels of ROTI.

One should be cautioned however; these calculations were just made on a minor excerpt of the data set and there could be larger deviations (or perhaps correlations) with all data included. Nevertheless; as a summary of the interesting times investigated, it still provides a good estimate.

Time (UT) (approximate)	Expansion onset in AL-index (nT)	Mean VTEC (TECU)	Mean ROTI (TECU/min)	Cycle slips	Phase scintillation (radians)	Other comments
08:30		12.5	3.0	900	0.4 – 0.5	Growth phase
10:45	no	25	4.0	1400	0.8	Peak in VTEC in south, decline in north
12:00	-200	40	2.0	<50	0.4-0.5	VTEC peak only in south
14:00	-200	15	4.5	900	0.6-0.8	Sporadic localized high sigma phi
15:00	-1000	15	7.0	1300	0.6	Onset at 14:48
16:00	no	20	3.0	250	0.35-0.4	
17:30	-1500	22	5.5	1300	0.7-0.8	
20:30	-400	45	7.0	1600-2000	0.75	50TECU in Mid-Norway, 40TECU in north
22:00	-600	25	5.0	350	0.6	

Table 5.2-1: Overview of parameters from selected times of day. The same data are plotted below.

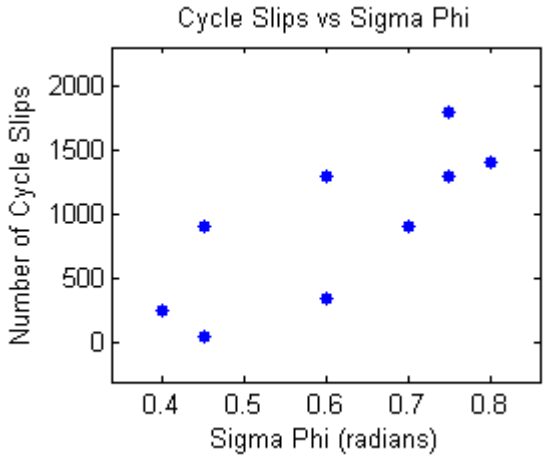

a)

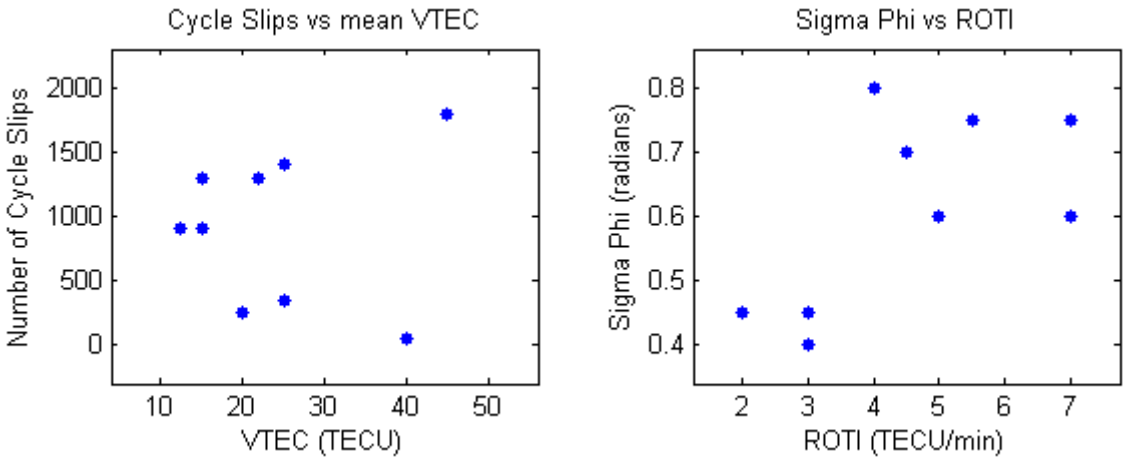

b) c)

Figure 5.2-3: a) There is a positive correlation between cycle slips and phase scintillation for the selected times of day. b) there is seemingly no correlation between cycle slips and VTEC. c) A positive correlation between ROTI and phase scintillation as expected.

Other aspects which have not been treated here, are in e.g. the possible role of unbalanced reconnection and expanding/contracting polar cap with respect to the formation of patches. Neither the contribution of the SAPS feeding TOI formation throughout a whole day of geomagnetic activity. We also know that TOIs form over the European sector (see section 2.4.3), hence it could be likely that the same scenario as reported by Foster et al. [2005] in the American sector, also occurs earlier in the day over Europe. Figure 5.2-4 shows how the enhanced TEC varied on a global scale in daytime. Although the TEC values are modest, we can see that there are slight enhancements in the polar regions where the plasma enters the dayside cusp. The ongoing reconnection processes ensure to transport this plasma into the polar cap where they can become segmented into polar cap patches. Last, but not least, the contributions from the thermosphere have not been considered. Neither the morphology of the aurora nor the details of the MI-coupling have been studied; hence there are still many options to sort out in order to get the full picture. Still this overview have given some insight to the main contributors to the satcom outage; the ionospheric currents and the polar cap patches.

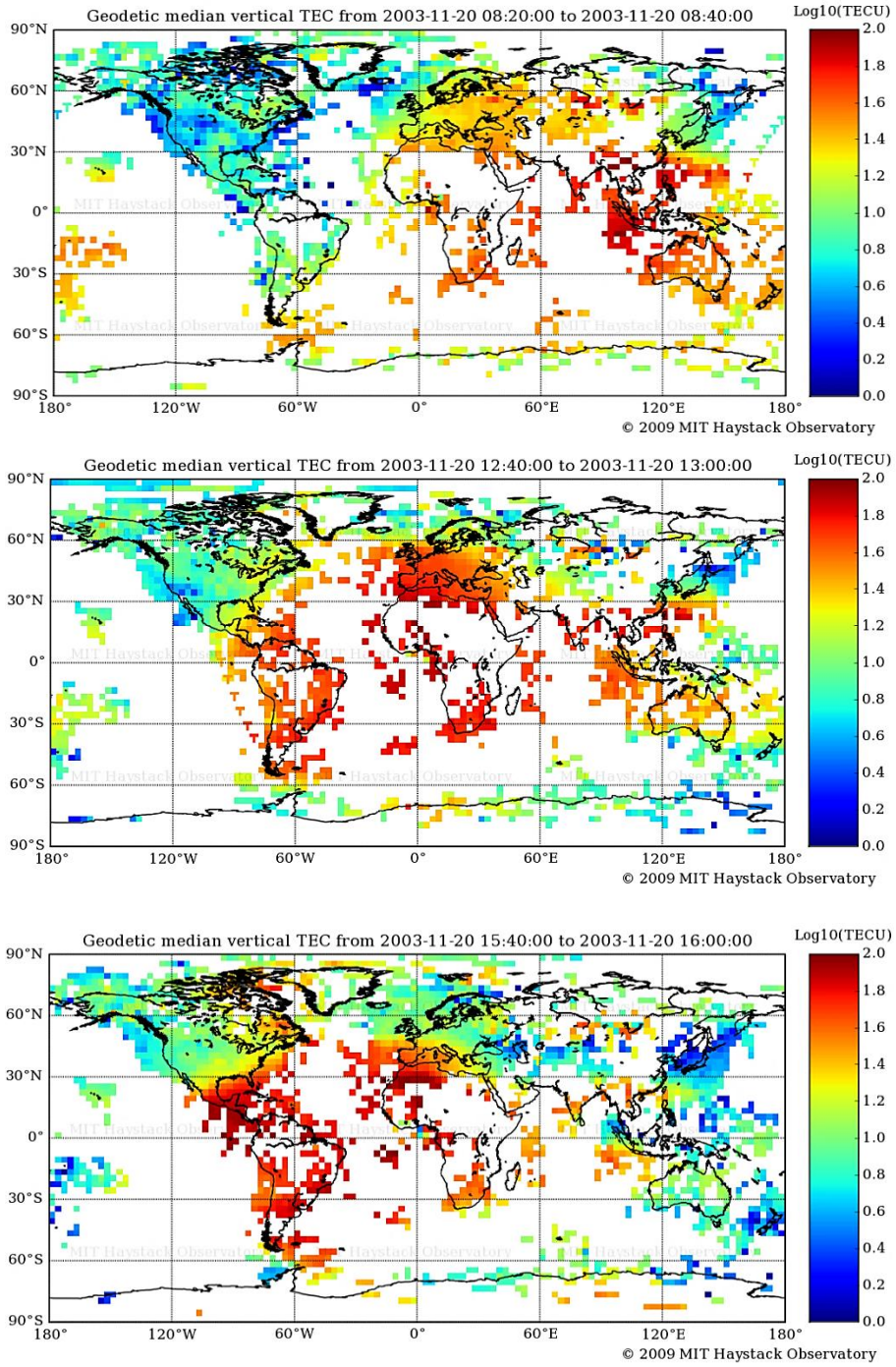

Figure 5.2-4: A picture series of global median VTEC in the daytime. VTEC is increased in noon sector MLT. From the 15:40 plot, enhancements are visible above the Canadian and Greenland artic sector which can imply the formation of the TOI. CREDIT: MIT-madrigal/Haystack Observatory, Coster, A. 2009.

5.3 Conclusion

The investigation of the possible causes of the satcom outage which occurred during this event may seem meaningless today as our understanding concerning these scenarios has increased during the last decade. However; this can be viewed as a statement of the necessity of being able to forecast such events.

The outage occurred approximately at14:00UT and was most likely caused by the increased geomagnetic activity due to the passage of the MC. The ongoing activity led to expansions and contractions of the polar cap with subsequent latitudinal migration of the auroral oval, and enhanced currents in the lower ionosphere. Instability mechanisms contributed to a structuring of the storm enhanced ionospheric densities producing radio wave scintillations. The increased ROTI associated with the auroral oval and currents, and the density gradients on the oval boundaries implied smaller scale irregularities which are known to house phase and amplitude scintillations. There was a positive correlation between the number of cycle slips which caused loss of lock, and increased phase scintillations. The most affected satellites were located in close vicinity of the equatorward auroral oval boundary (trough wall), inside the auroral oval, or within the expanded polar cap. These regions were characterized by increased ROTI which could be attributed to particle precipitation and density gradients.

When the Norwegian mainland was situated in the MLT evening/night sector, increased VTEC was registered in correspondence with the exit of solar EUV ionized patch material of densities ~ $10^{12}m^{-3}$. As these patches exit the polar cap and join the return flow they contribute positively to the auroral activity and associated currents. Thus this super storm event contributed to the following;

1. An extended period of southwards IMF Bz with associated auroral precipitation in expanded auroral regions.
2. Sunwards transport of dense plasma due to a storm time polarization E-field (SAPS) and contribution to build up of dense plasma in dayside ionosphere.
3. The transport of high density solar EUV ionized plasma into and across the polar cap due to reconnection and convection processes with a duration of ~12 hours.
4. Instability-and- irregularity growth due to increased ionospheric densities and flows.
5. Scintillations caused by small scale irregularities associated with ionospheric currents and plasma patches.
6. Satcom outage due to prolonged scintillation effects and consequent loss of satellite lock.

In retrospective the NMA could have been notified of the approaching geomagnetic disturbance in advance. The scientific research communities were aware of the flare and the MC, and the NOAA SWPC issued real time alerts on their website. The relation between geomagnetic disturbances and radio wave scintillation had also been known for decades. Hence; the storm could have been forecasted, and the probable consequences could have been foreseen to a certain extent with a proper warning. With that said, the *actual* extent of the problems caused by the disturbance would have been difficult to foresee without real-time monitoring of the storm dynamics. Today we have developed/improved techniques to aid us with gaining a better overview of the temporal development and motion of the auroral oval and patches, despite that not all the processes are fully understood (e.g. irregularity and instability mechanisms).
It is evident that on the behalf of the Norwegian mainland, it is the evening and night sector which is exposed to these disturbances. Whereas the daytime disturbances in Southern parts of Norway are related to IMF and auroral activity, the nighttime disturbances are additionally attributed the contribution of the solar EUV high density plasma. The IMF and solar wind parameters can be

monitored with approximately one hour delay from e.g. ACE, patches from the dayside are expected to transit the polar cap within a couple of hours (assuming steady convection). All this must be seen within a bigger picture. This case was taken out of context, thus what was already present in the ionosphere or what happened on a global scale was not taken into account.

5.4 Status Quo and Beyond:

A lot has happened in space weather research and forecasting since 2003. During the last years the NMA has established contact with NOAA SWPC for space weather updates (from 2012), they have developed a real time ionosphere monitor (RTIM) based on TEC from all the SATREF receivers and they have installed a network of twelve Septentrio PolaRxS 100 Hz scintillation receivers strategically placed from north to south in Norway and to Iceland in the west. They have also made their own webpage for this RTIM service (http://sesolstorm.kartverket.no/) [Hanssen, 2013].
With real time surveillance of the ionosphere above the Norwegian region, they are much better prepared for geomagnetic disturbances today than 10 years ago.
Still their concern is the smaller scale irregularities associated with the auroral oval and ionospheric currents. Thus it is useful to monitor the location of the auroral oval and precipitation fluxes. Traditionally the auroral oval has been modeled by the OVATION now casting service (http://sd-www.jhuapl.edu/Aurora/ovation_live), or from Jan. 2014: (http://www.swpc.noaa.gov/ovation), or the NOAA POES auroral oval (http://swpc.noaa.gov/pmap.index.html). Recently Sigernes et al., [2011a,b] have developed an online now cast and forecast auroral oval model; the SvalTrackII (kho.unis.no). This is based on two oval models (Starkov and Zhang and Paxton) and uses the Kp-index as input for calculation of the auroral oval location. SvalTrackII can provide 1 hour forecast of the oval location. Another real time service is the AFFECTS auroral tracker provided by the Tromsø Geophysical Observatory (fox.phys.uit.no/AFFECTS). This model uses real time magnetometer measurements to locate the auroral electrojets. Hence; with the assumption that the electrojets are collocated with the auroral oval, the oval boundaries are calculated and updated every minute with the magnetograms [Gullikstad Johnsen, 2013]. Although these services can give an approximate location of the auroral boundaries and electrojets, the instability mechanisms which produce the irregularities are poorly understood. Hence it is difficult to deduce the chances of, and the extent of irregularity growth.
Several authors have described methods to track and monitor TOIs and patches. Techniques based on TEC-maps, radars and supplementing instruments have proved to be useful. In e.g. tomographic TEC-maps with additional instruments such as the Multi Instrument Data Analysis System (MIDAS) has been developed by the INVERT group at the University of Bath [Spencer and Mitchell, 2007]. They provide real time 3D- TEC maps in real time on the webpage (http://www.bath.ac.uk/elec-eng/invert/iono/rti_3d.html). Tracking of patches have been done by e.g. Bust and Crowley [2007] using a combined TEC and convection pattern to provide a 3D- plasma distribution. This technique is known as the Ionospheric Data Assimilation 3 Dimensional (IDA3D). Also radars have been used to track the motion of patches. Oksavik et al. [2010] used injection of test particles to track patch trajectories back and forth in time. This study revealed valuable new insight on the motion of patches within the polar cap. Mid-latitude SuperDARN radars in combination with TEC maps over America have been used to study SAPS [Clausen et al., 2012]. The Virginia Tech SuperDARN web page provides similar TEC maps in combination with SuperDARN data in so called four plots [Thomas, 2013]. The TEC-maps are constructed from the World Wide GPS Receiver Network by Millstone Hill (PI: Coster, A.). The data are available either at the VT-SuperDARN site (http://vt.superdarn.org/tiki-index.php?page=DaViT+TEC+Four+Plot) or from the Millstone Hill Madrigal database (http://madrigal.haystack.mit.edu/cgi-bin/madrigal/gSimpleUIAccessData.py). The data lags with a

couple of days, but this proves that the technology is there, and that these plots can reveal valuable information on both SAPS and increased TEC in the American sector.
With respect to the higher latitudes; ionosonde and GPS networks in the American/Canadian arctic sector would provide a good overview of TOI formation and convection into the polar cap. In order to forecast patches exiting the polar cap in the Norwegian MLT night sector, we need to know when they are formed or enter the polar cap. The Canadian High Arctic Ionospheric Network (CHAIN) is a network of groundbased instruments with objective to study and monitor TOIs, patches and associated scintillation. The ionosonde (CADI) and GPS receivers are located in a latitudinal extent from 53.35°N to 79.99°N, thus some stations are located within the polar cap. Several of the CHAIN stations provide near real time data. Hourly RINEX files are downloadable for registered users on (ftp://chain.physics.unb.ca/). Ionograms and scintillation maps are available in near real time online on the webpage [Jayachandran et al., 2009]. Scintillation forecasting models have been proposed over the years; e.g. Fremouw and Secan [1984], Béniguel [2002], Aquino et al. [2009] and Prikryl et al. [2012].
NMA's interest in the forecast of patches and blobs concerns the smaller scale irregularities and associated scintillations. This calls for an analysis method of the irregularity growth within the patch. Since patches do not move in a straight manner, but twist and turn the irregularities inside the patch both change their internal position and hence change the conditions for different instability mechanisms. The growth rates of such instabilities are so fast that the time resolution of the analysis must be of short time scales. Luckily; irregularities are possible to measure with scintillation receivers or by ROTI in real time, but difficult to forecast due to the rapid instability growth rates. Hence the forecast timeline is very short. To be on the safe side, one should assume that patches will house an amount of irregularities causing scintillation. If, on the other hand, a patch reveals severe scintillation or ROTI early or upon entering the polar cap it would seem very unlikely that the patch will not cause scintillation when exiting the polar cap. Thus scintillation must be now-casted along with the location of the auroral oval, whereas polar cap patches can be forecasted by real time monitoring of the formation and motion of the patches in the dayside cusp region.

To meet the requirements of good space weather forecasts, it is desirable to further develop and expand existing research infrastructure. This involves an increase in number of receiver stations, along with the further collaboration between the German[7] and the French [8]space centers in developing and running RTIM and the RTIS (real time ionospheric scintillation monitor) for ionospheric surveillance and modeling. It also involves an extended use of the current, and implementations of new, instruments including ionosondes, riometers and all sky cameras, and close international cooperation. An important contribution would include membership in the SuperDARN network by installing a HF-radar facility in the south-western part of Norway. This would contribute to expand the coverage of the northern regions by overlapping the field of view of the STARE radars [Barth, 2012].
An ESFRI[9] priority project is the construction of a new EISCAT facility. The EISCAT 3D is, as of writing, still in the preparatory phase, but will be operational from 2018 with the proper funding. EISCAT 3D will be a phased array incoherent scatter radar, which enables large scale volumetric measurements with high resolution. For further reading, please see (https://www.eiscat3d.se/science). Meanwhile, as the development of better techniques and instruments proceeds, one has to consider the existing space weather forecasting services and research facility data, as a platform for an overview of the ionsopheric phenomena, and cross calibration of existing models.

[7] DLR –Deutsche Zentrum für Luft und Raumfahrt (German Aerospace Center)
[8]CNES – Centre National d'Etude Spatiales

[9] European Strategy Forum on Research Infrastructures

6 Literature

6.1 Articles

Aarons, J., (1982)
Global Morphology of Ionospheric Scintillations,
Proceedings of the IEEE, Vol.70, No.4,pp 360-378

Aarons,J. (1997)
Global Positioning System Phase Fluctuations at Auroral Latitudes
Journal Of Geophysical Research, Vol. 102, No. A8, Pages 17,219-17,231,1997

Akasofu , S-I. (1963)
The Dynamical Morphology of the Aurora Polaris
Journal of Geophysical Research Letters, Vol.68, No,6

Akasofu,S-I. (1976)
RecentProgressinStudies of DMSP Auroral Photographs
Space Science Review 19, 169, 1976

Alex,S., Mukherjee,S. and Lakhina, G.S. (2006)
Geomagnetic signatures during the intense geomagnetic storms of 29 October and 20 November 2003
J. Atmospheric and Solar-Terrestrial Physics, 68, (2006) 769-780, doi:10.1016/j.jastp.206.01.003

Alfonsi,L., Kavanagh,A.J.,Amata,E., Cilliers,P., Correia,E., Feeman,M., Kaurisitie,K., Liu,R.,
Luntama., J.P., Mitchell,C.N. and Zherebtsov,G.A. (2008)
Probing the High Latitude Ionosphere from Gorund-based Observations: The State of Current
Knowledge and Capabilites during IPY (2007-2009)
Journal of Atmospheric and Solar Terrestrial Physics, 70(2008),2293-2308

Alfonsi,L., Spogli,L., de Franceschi,G., Romano,V., Aquino,M., Dodson,A. and Mitchell,C.N. (2011)
Bipolar Climatology of GPS ionospheric scintillation at solar minimum,
Rad. Sci. (46), RS0D05, doi:10.1029/2010RS004571,2011

Alfonsi,L. Spogli,L., Tong,J.R., DeFranceschi,G., Romano,V., Bourdillon,A.,
Le Huy,M. and Mitchell,C.N.(2011a)
GPS Scintillation and TEC Gradients at Equatorial Latitudes in April 2006.
Advances in Space Research 47(2011)1750-1757, doi:10.1016/j.asr.2010.04.020

AndersonD.N., Buchau,J. and Heelis,R.A. (1988)
Origin of Density Enhancements in the Winter Polar Cap Ionosphere
Radio Science, Vol 23, No.4, pp 513-519

Aquino,M., Rodrigues,F.S., Souter,J., Moore,T., Dodson,Al and Waugh,S. (2006)
Ionospheric Scintillation and Impact on GNSS Users in Northern Europe: Results of a 3 Year Study
Space Communications 20 (2005/2006) 17-29 IOS Press

Aquino,M., Monico,J.F.G.,Dodson,A.H.,Marques,H.,DeFranceschi,G.,Alfonsi,L.,Romano,V.
and Andreaotti,M. (2009)
Improving the GNSS Positioning Stochastic Model in the Presence of Ionospheric Scintillation
J. Geod: 83:953-966, Doi:10.1007/s00190-009-0313-6

Baker,J.B.H. (2011)
The Super Dual Auroral Radar Network (SuperDARN)
RBSP SWG, May 24th 2011 http://vt.superdarn.org/tiki-index.php?page=sd_tutorial

Barth, V.L. (2012)
Romvær-infrastruktur i Norge- eksisterende og ønsket infrastruktur
NRS-rapport 2012/2

Basu,S.,MacKenzie,E.,Basu,S.,Carlson,H.C.,Hardy,D.A.,Rich,F.J. and Livingston,R.C. (1983)
Coordinated Measurements of Low-energy ElectronPrecipitation and Scintillations/TEC
in the Auroral Oval
Radio Science, Vol.18, No.6,pp 1151-1165,1983

Basu,S., Basu,S., Mackenzie, E., Coley, W.R., Sharber,J.R. and Hoegy,W.R. (1990)
Plasma Structuring by the Gradient Drift Instability at High Latitudes and Comparison With Veloscity
Shear Driven Processes,
J. Geophys. Res. 95, A6, 89JA03081

Beach, T. L. (2006),
Perils of the GPS phase scintillation index (sf),
Radio Sci., 41, RS5S31,doi:10.1029/2005RS003356.

Becker-Geudes,F., Sahai,Y., Faundes,P.R., Espinoza,E.S.,Pillat,V.G., Lima, W.L.C., Basu,S.,Otsuka,Y., Shiokawa,K.,Mackenzie,E.M.,Pi,X., Bittencourt,J.A. (2007) Ionospheric response in the Brazilian sector during the super geomagnetic storm,
Ann.Geophys.,25,863.873,2007

Bekkeng,T.A. (2009),
"Prototype Development of a Multi-Needle Langmuir Probe System,"
Master Thesis, University of Oslo, Department of Physics, May 25, 2009

Béniguel,Y. (2002)
Global Ionospheric Propagation Model for Scintillations of Transmitted Signals
Radio Science Vol.37, No.3, pp 4.1-4.3,2002

Béniguel ,Y., V. Romano, L. Alfonsi, M. Aquino, A. Bourdillon, P. Cannon, G. De Franceschi, S. Dubey, B. Forte, V. Gherm, N. Jakowski, M. Materassi, T. Noack, M. Pozoga, N. Rogers, P. Spalla, H.J. Strangeways, M. Warrington, A. Wernik, V. Wilken and N. Zernov (2009)
Ionospheric Scintillation Monitoring and Modeling
Annals Of Geophysics, Vol. 52, N. 3/4, June/August 2009

Beynon,W.J.G. and Williams,P.J.S. (1978)
Incoherent Scatter of Radio Waves From the Ionosphere
Rep. Prog. Phys., Vol. 41, 1978

Bothmer, V. and Schwenn, R. (1998)
The structure and origin of magnetic clouds in the solar wind.
Ann. Geophys., 16, 1, 24, 1998

Bowline,M.D., Sojka,J.J. and Schunck,R.W. (1996)
Relationship of Theoretical Patch Climatology to Polar Cap Patch Obersvations,
Radio Sci, 31(3), 635-644, doi:10.1029/96RS00236

Brändström,U. (2004)
The First Digital All-sky Camera in Kiruna
www.irf.se/allsky/dasc

Brekke,A. and Moen,J. (1993)
Review Paper: Observations of High Latitude Ionospheric Conductances
Journal of Atmospheric and Terrestrial Physics Vol.55, No. 11/12, pp 1493-1512,1993

Brueckner,G.E., Howard,R.E., Koomen,M.J., Korendyke,C.M., Michels,D.J., Moses,J.D., Socker,D.G., Dere,K.P, Lamy,P.L., Llebaria,A., Bout,M.V., Schwenn,R.,Simnett,G.M., Bedford,D.K. and Eyler,C.J. (1995)
The Large Angle Spectroscopic Coronagraph. LASCO-Visible Light and Spectroscopy.
Solar Physics Vol 162, pp 357-402,1995

Bruinsma, S., J. M. Forbes, R. S. Nerem, and X. Zhang (2006),
Thermosphere density response to the 20–21 November2003 solar and geomagnetic storm from CHAMP and GRACE accelerometer data,
J. Geophys. Res., 111, A06303,doi:10.1029/2005JA011284.

Brunini,C., Camilion,E. and Azpilicueta,F. (2011)
Simulation study of the influence of the ionospheric layer height in the thin layer ionospheric model
J.Geod.(2011) 85:637-645, doi:10.1007/s00190-011-0470-2

Buchau ,J., Reinisch,B.W., Weber,E.J. and Moore,J.G. (1983)
Structure and Dynamics of the Winter Polar Cap F Region
Radio Science, Vol.18, No.6, pp995-1010, 1983

Buchau ,J., Weber,E.J., Anderson,D.N., Carlson, H.C. Jr., Moore, J.G., Reinisch, B.W. and Livingston, R.C. (1985)
Ionospheric Structures in the Polar Cap: Their Origin and Relation to 250MHz-Scintillation,
Radio Science, Vol. 20, No.3, pp 325-338.

Burke, W. J., L. C. Gentile, and C. Y. Huang (2007),
Penetration electric fields driving main phase Dst,
J. Geophys. Res.,112, A07208, doi:10.1029/2006JA012137

Burlaga,L.F. and Lepping,R.P. (1990)
Global Configuration of A Magnetic Cloud
Physics of Magnetic Flux: Geophysical Monograph Series, Vol.58, 1990

Burns,C.J. and Hargreaves, J.K. (1996)
The Occurrence and Properties of Large-scale Electron-density Structures in the Auroral F-region
Journal of Atmospheric and Terrestrial Physics, Vol. 58, No. 1-4, pp. 21%232, 1996

Burrel,A.G., Bonito,N.A. and Carrano,C.S. (2008)
Total electron content processing from GPS observations to facilitate ionospheric modeling
GPS Solut. (2009) 13:83-95, doi:10.1007/s10291-008-0102-3
Bust, G. S., and G. Crowley (2007),
Tracking of polar cap ionospheric patches using data assimilation,
J. *Geophys. Res., 112, A05307, doi:10.1029/2005JA011597.*
Carlson, H.C.Jr, (1990)
Dynamics of the Quiet Polar Cap
J. Geomag. Geoeletr. 42,667-710,1990
Carlson,H.C.Jr, (1994)
The Dark Polar Ionosphere:Progress and Future Challenges
Radio Science Vol.29, No1, pp 157-165,1994
Carlson, H. C., J. Moen, K. Oksavik,C. P. Nielsen, I. W. McCrea, T. R. Pedersen, and P. Gallop (2006),
Direct observations of injection events of subauroral plasma intothe polar cap,
Geophys. Res. Lett., 33, L05103, doi:10.1029/2005GL025230.
Carlson,H.C. Oksvik,K. and Moen,J. (2008)
On a New Process for Cusp Irregularity Production
Ann. Geophys, 26,2871-2885,2008.
Carlson, H. C. (2012),
Sharpening our thinking about polar cap ionospheric patch morphology, research,
and mitigation techniques,
Radio Sci., 47, RS0L21, doi:10.1029/2011RS004946.
Carrano, C.S.and Grove,K.M. (2007)
TEC Gradients and Fluctuations at Low latitudes Measured with High Data Rate GPS Receivers,
Proceedings of the 63rd Annual Meeting of The Institute of Navigation, Cambridge, MA, April 2007
https://www2.bc.edu/charles-carrano/
Carrano, C.S. (2008)
GPS-SCINDA: A Real-Time GPS Data Acquisition And Ionospheric Analysis System For SCINDA (Draft)
AFRL-VS-TR-2007-0000 Air Force Research Laboratory MA 01731-3010
Chisham,G.,Freeman,M.P.,Coleman,I.J., Pinnock,M., Hairston,M.R., Lester,M. and Sofko,G. (2004)
Measuring The Dayside Reconnection Rate During An Interval Of Due
Northward Interplanetary Magnetic Field
Annales Geophysicae (2004) 22: 4243–4258 SRef-ID: 1432-0576/ag/2004-22-4243
Chisham,G., Lester,M., Milan,S.E., Freeman,M.P., Bristow,W.A., Grocott,A., McWilliams,K.A.,
Ruohoniemi,J.M., Yeoman, T.K., Dyson,P.L., Greenwald,, RA., Kikuchi,T., Pinnock,M., Rash,J.P.S.,
Sato,N., Sofko,G.J., Villain,J.-P. and Walker, A.D.M. (2007)
A Decade of Super Dual Aouroral Radar Network (SuperDARN): Scientific Achievements, New Technique and Future Directions.
Surv Geophys (2007) 28:33–109 DOI 10.1007/s10712-007-9017-8
Chiu,M.C.,Von Mehlum,U.I., Willey,C.E., Betenbaugh,T.M., Maynard,J.J.,Krein,J.A., Conde,R.F.,Gray, W.T.,
Hunt,j.W.Jr., Mosher,L.E., McCullough,M.G., Panneton,P.E., Staiger,J.P. and Rodberg,E.H. (1998)
ACE Spacecraft
Space Science Reviews Vol 86,pp 257-284
Cho, K.-S., Y.-J. Moon, M. Dryer, C. D. Fry, Y.-D. Park, and K.-S. Kim,
A statistical comparison of interplanetary shock and CME propagation models,
J. Geophys. Res., 108(A12), 1445, doi:10.1029/2003JA010029, 2003.
Clausen, L. B. N., Baker,J.B.H., Ruohoniemi,J.M., Greenwald,R.A., Thomas,
Cousins, E. D. P., and S. G. Shepherd (2010),
A dynamical model of high-latitude convection derived from SuperDARN plasma drift measurements,
J. Geophys. Res., 115, A12329, doi:10.1029/2010JA016017.
Cowley,S.W.H. and Lockwood,M. (1992)
Excitation and Decay of Solar Wind Driven Flows in the Magnetosphere-Ionosphere System
Ann. Geophys. 10,103-115(1992)
Cowley, S.W.H. (2000)
Magnetophere-Ionosphere Interactions: A Tutorial Overview
Magnetic Current Systems, Geophysical Monograph 118, American Geophysical Union
Coster,A.J., Gaposchkin,E.M. and Thornton,L.E. (1992)
Real-Time Ionospheric Monitoring Using the GPS,
Massachusetts Institute of Technology, Lincoln Laboratory, Technical Report 954

Coster,A.J.,Foster, J.C. and Erickson,P. (2003)
Monitoring the Ionosphere With GPS
GPS World, May 2003, pp42-49
Coster, A.; Colerico, M.; Foster, J.C.; Ruohoniemi, J.M. (2006)
Observations of the Tongue of Ionization with GPS TEC and SuperDARN.
In *Characterising the Ionosphere* (pp. 7-1 – 7-14). Meeting Proceedings RTO-MP-IST-056, Paper 7.
Neuilly-sur-Seine, *France: RTO.Available from: http://www.rto.nato.int/abstracts.asp*.
Crane, R.K. (1977)
Ionospheric Scintillation
Proceedings Of The IEEE, February 1977, pp 180-199
Crooker,N.U. (1992)
Reverse Convection
Journal Of Geophysical Research, Vol. 97, No. A12, Pages 19,363-19,372,1992
Crowley,G., Ridley,A.J., Deist,D., Wings,S., Knipp,D.J., Emery,B.A., Foster,J.C., Heelis,R.,
Hairston,M. and Reinisch,B.W. (2000)
Transformation of High Latitude Ionospheric F-region Patches into Blob during the March 21, 1990 Storm,
Journal of Geophys. Research Vol 105,No.A3,pp5215-5230
Crowley, G.,Hackert,C.L.,Meier,R.R.,Strickland,D.J.,Paxton,L.J.,Pi,X.,Manucci,A.,Christensen,A.B.,
Morrison,D.,Bust,G.S.,Roble,R.G.,Curtis,N. and Wene,G.(2006),
Global thermosphere-ionosphere response to onset of 20 November 2003 magnetic storm,
J. Geophys. Res., 111, A10S18, doi:10.1029/2005JA011518.
Curtis,S.A.,Hoegy,W.R., Brace,L.H., Maynard,N.C. and Sugiura,M. (1982)
DE-2 Cusp Observations: Role of Plasma Instabilities in Topside Ionospheric Heating and Density Fluctutations,
Geophysical Research Letters Vol. 9, No.9,pp997-1000
Dahlgren,H., Perry,G.W., Semeter,J.L., St.-Maurice,J.-P., Hosokawa,K., Nicolls, M.J., Greffen,M.,
Shiokawa,K. and Heinselman,C. (2012)
Space-time variability of polar cap patches: Direct evidence for internal plasma structuring,
J. Geophys. Res. 117, A09312, doi:10.1029/2012JA017961,2012
Dandekar,B.S. and Bullet,T.W. (1999)
Morphologyof Polar Cap Patch Activity
Radio Science, Vol. 34, No.5, pp 1187-1205,1999
David,L. (1999)
Saving SOHO
Aerospace America May, 1999, http://soho.nascom.nasa.gov/operations/Recovery/aerospace.pdf
Davis,C. (1996)
Interpreting an Ionogram
http://www.ukssdc.ac.uk/ionosondes/ionogram_interpretation.html
DeFranceschi,G. ,Alfonsi,L. and Romano,V. (2006)
ISACCO: An Italian Project to Monitor the High Latitudes Ionosphere by Means of GPS Receivers
GPS Solutions, DOI 10.1007/s10291-006-0036-6
DeFranceschi,G.,Alfonsi,L.,Romanov,V., Aquino,M., Dodson,A., Mitchell,C.N., Spencer,P.
and Wernik, A.W. (2008),
Dynamics of High-Latitudes Patches and Associated Small Scale Irregularities During the October and November 2003 Storms
Journal of Atmospheric and Solar Terrestrial Physics Vol.70 (2008), 879-888
Delaboudinière,J-P.,ArtznerG.E.,Brunaud,J.,abriel,A.H.,Hochedez,J.F.,Millier,F.,Song,X.Y.,Au,B.,
Dere,K.P.,Howard,R.A.,Kreplin,R.,Michels,D.J.,Moses,J.D.,Defise,J.M.,Jamar,C.,Rochus,P.,
Chauvuneau,J.P.,Marioge,J.P.,Catura,R.C.,Lemen;J.R.,Shing,L.,Stern,R.A.,Gurman,J.B..Neupert,W.M.,
Maucherat,A.,Clette,F., Cugnon,P.and Van Dessel,E.L. (1995)
EIT:Extreme Ultraviolet Imaging Telescope For the SOHO Mission
http://umbra.nascom.nasa.gov/eit/images/instrument_paper.pdf
Dryer, M., Z. Smith, C. D. Fry, W. Sun, C. S. Deehr, and S.-I. Akasofu (2004),
Real-time shock arrival predictions during the ‘‘Halloween 2003 epoch,’’
Space Weather, 2, S09001, doi:10.1029/2004SW000087.
Dyrud,L.,Jovancevic,A., Brown,A., Wilson,D. and Ganguly, S. (2007)
Ionospheric Measurements with GPS
Center for Remote Sensing Inc, http://www.cfrsi.com/pdf/NewREceiverBrochure_GPSWorl_final.pdf

Feldstein, Y.J. and Starkov, G.V. (1967)
Dynamics of Auroral Belt and Polar Geomagnetic Disturbances
Planet Space Sci. Vol 15, pp 209-229
Feldstein,Y.I., Prigancova,A.,Vorobjev,V.G., Cumnock,J.A., Strkov,G.V., Yagodkina,O.I. and Blomberg,L.G. (2007)
High Latitude Electrojets, Auroral Luminosity and Auroral Particle Precipitation,
Physics of Auroral Phenomena, Proc.xxx Annual Seminar, Apatity,pp 55-59.2007
Ebihara,Y., Fok,M.-C., Sazykin,S., Thomsen,M.F., Hairston,M.R., Evans,D.S., Rich,F.J. and Ejiri,M. (2005)
Ring current and the Magnetosphere-Ionosphere coupling during the superstorm of 20 November 2003
J.Geophys.Res.,110,A09S22, doi: 10.1029/2004JA010924
Endo,M., Fuji,R., Ogawa,Y.,Buchert,S.C., Nozawa,S., Watanabe,S. and Yoshida,N. (2000)
Ion Up-Flow And Down-Flow At The Topside Ionosphere Observedby The EISCAT VHF Radar
Ann. Geophysicae 18, 170-181 (2000)
Elphinstone,R.D.,Murphree, J.S., Hearn,D.J., Heikkila,W.,Henderson,M.G., Cogger,L.L. and Sandahl,I. (1993)
The Auroral Distribution and its Mapping According to Substorm Phase
Journal of Atmospheric andTerrestrial Physics Vol.55, No. 14,pp1741-1762,1993
Farley,D.T.Jr. (1963)
A Plasma Instability Resulting in Field-Aligned Irregularities in the Ionosphere
Journal of Geophys. Res. Vol. 68, No.22,1963
Foster, J.C (1984)
Ionospheric Signatures of Magnetospheric Convection
Journal of Geophysical Research, Vol 89, No. A2, pp 855-865
Foster,J.C. and Doupnik,J.R. (1984)
Plasma Convection in the Vicinity of the Dayside Cleft
Journal of Geophysical Research Vol 89, No.A10, pp 9107-9113
Foster,J.C. (1993)
Storm Time Plasma Transport at Middle and High Latitudes
Journal of Geophysical Research, Vol 98 No. A2, pp 1675-168
Foster,J.C. and Burke, W.J. (2002)
SAPS: A New Categorization for Sub-auroral Electric Fields
EOS, Vol 83,No.36 pp 393-394
Foster,J.C., Erickson,P.J., Coster,A.J., Goldstein,J. and Rich,E.J. (2002)
Ionospheric signatures of plasmaspheric tails
Geophysical Research Letters, vol. 29, no. 13, 1623, 10.1029/2002gl015067, 2002
Foster, J. C., and H. B. Vo, (2002)
Average characteristics and activity dependence of the subauroral polarization stream,
J. *Geophys. Res., 107(A12), 1475, doi:10.1029/2002JA009409, 2002*.
Foster,J.C.,Coster,A.J.,Erickson,P.J., Holt,J.M., Lind, F.D., Rideout,W., McCready,M.,van Eyken,A., Barnes, R.J., Greenwald, R.A., Rich, F.J.,(2005)
Multiradar observations of the polar tongue of ionization,
J. Geophys. Res,110, A09S31, doi:10.1029/2004JA010928.
Fremouw,E.J., Leadabrand,R.L., Livingston,R.C., Cousins, M.D., Rino, C.L., Fair,B.C. and Long, R.A. (1978)
Early Results from the DNA Wideband Satellite Experiment - Complex Signal Scintillation
Radio Science Vol.113,No.1, pp 167-187,1978
Fremouw,E.J. and Secan,J.A. (1984)
Modeling and Scientific Application and Scintillation Results
Radio Science Vol.19, No3, pp 687-694
Friis-Christensen,E., McHenry,M.A., Clauer,C.R. and Vennerstrøm,S. (1988)
Ionospheric Traveling Convection Vortices Observed Near the Polar Cleft: ATriggered Response to Sudden Changes in the Solar Wind.
Geophys. Res. Letters Vol.15,No.3,pp253-256
Garaud, Pascale, Prof. D. O. Gough and Prof. N. O. Weiss (2001)
PhD-thesis on "The dynamics of the solar tachocline", (Institute of Astronomy, Cambridge) and (Department of Applied Mathematics and Theoretical Physics, Cambridge)
http://users.soe.ucsc.edu/~pgaraud/Work/garaud_condom.pdf
Garrard,T.L., Davis,A.J.,Hammond,J.S., and Sears,S.R.
The ACE Science Center
Science Reviews, Volume 86, Nos. 1-4, 1998

Gjerloev, J. W., R. A. Hoffman, E. Tanskanen, M. Friel, L. A. Frank, and J. B. Sigwarth (2003)
Auroral electrojet configurationduring substorm growth phase,
Geophys. Res. Lett., 30(18), 1927, doi:10.1029/2003GL017851, 2003

Gopaslwamy,N., Lara,A., Yashiro,S., Kaiser, M.L. and Howard, R.A. (2001)
Predicting the 1AU arrival times of coronal mass ejections
J. Geophys. Res., 106,29,207

Gopalswamy,N., Barbieri,L., Cliver,E.W., Lu,G., Plunkett, S.P., Skoug,R.M.(2005)
Introduction to violent Sun-Earth connection events of October-November 2003,
J.Geophys. Res,110, A09S00, doi:10,1029/2005JA011268

Gopalswamy, N., Yashiro,S., Michalek,G., Xie,H., Lepping,R.P.and Howard, R.A. (2005a)
Solar source of the largest geomagnetic storm of solar cycle 23
Geophys. Res. Lett., 32, L12S09, doi:10.1029/2004GL021639

Gordon,W.E. (1958)
Incoherent Scattering of Radiowaves by Free Electrons with Applications to Space Exploration by Radar
Proceedings of IRE, 1958,pp 1824-129

Grechnev,V.V., Chertok,I.M., Slemzin,V.A.,Kuzin,S.V., Ignat'ev,A.P., Perstov,A.A.,Zhitnik,I.A., Delaboudinière, J.-P. and Auchere,F. (2005)
CORONAS-F/SPIRIT EUV observations of October-November 2003 solar eruptive events in combination with SOHO/EIT data
J. Geophys. Res.,110, A09S07, doi:10.1029/2004JA010931

Greenwald,R.A:, Baker,K.B., Dudeney,J.R., Pinnock,M., Jones,T.B., Thomas.C., Villain,J-P., Cerisier,J-C., Senior,C., Hanuise,C.,Hunsucker,R.D.,Sofko,G., Koehler,J.,Nielsen,E., Pemmlinen,R., Alker,A.D.M., Sato,N. and Yamagishi,H. (1995)
DARN/SuperDARN- A Global Review of the Dynamics of High-latitude Convection
Space Science Review Vol 71, pp 761.796,1995

Grocott,A., Yeoman,T.C., Milan,S.E. and Cowley, S.W.H. (2005)
Interhemispheric Observations of the Ionospheric Signature of Tail Reconnection During IMF-Northward Non-substorm Intervals
Annales Geophysicae, 23, 1763–1770, 2005 SRef-ID: 1432-0576/ag/2005-23-1763

Gullikstad Johnsen,M. (2013)
Real Time Determination and Monitoring of Aurorla Electrojet Boundaries
J. Space Weather Space Clim. 3 (2013) A28 DOI: 10.1051/swsc/2013050

Gussenhoven,M.S. (1989)
Polar Rain and the Question of Direct Particle Access
Nato ASI Series Vol.278, pp 43-60, 1989

Hanssen,R.I. (2013)
Varsling av Ionosfæriske forstyrrelser
Kartverket, Geodesidivisjonen, SATREF Brukerkonferanse 5.Desember 2013

Hapgood,M.A. (1992)
Space Physics Coordinate Transformations : A User Guide
Planet. Space Sci.. Vol. 40, No. 5. pp. 71 l-717, 1992

Henderson,M.G.; Kepko,L.,Spence,H.E., Connors,M.,Sigwarth,J.B.,Frank,L.A., Singer,H.J. and Yumoto,K. (2002),
The Evolution of North-South Aligned Auroral Forms into Auroral Torch Structures: The Generation of Omega Bands and Ps6 Pulsations via Flow Bursts
http://lib-www.lanl.gov/cgi-bin/getfile?00796918.pdf

Henderson, M. G., E. F. Donovan, J. C. Foster, I. R. Mann, T. J. Immel, S. B. Mende, and J. B. Sigwarth (2010),
Start to-end global imaging of a sunward propagating, SAPS-associated giant undulation event,
J. Geophys. Res., 115, A04210, doi:10.1029/2009JA014106.

Holt,J.M., Zhang,S-R. and Buonsanto,M.J. (2002)
Regional and Local Ionospheric Models Based on Millstone Hill Incoherent Scatter Radar Data
Geophysical Research Letters, Vol.29,No.8, doi:10.1029/2002GL014678,2002

Hood, A.W. and Hughes, D.W, (2011)
Solar magnetic fields
Physics of the Earth and Planetary Interiors 187(2011)78-91, doi:10.1016-7jpepi/2011.04.010

Hosokawa, K., K. Shiokawa,Y. Otsuka, A. Nakajima, T. Ogawa, and J. D. Kelly (2006),
Estimating drift velocity of polar cap patches with all-sky airglowimager at Resolute Bay, Canada,
Geophys. Res. Lett., 33, L15111, doi:10.1029/2006GL026916.

Hosokawa, K., T. Tsugawa, K. Shiokawa, Y. Otsuka, N. Nishitani, T. Ogawa, and M. R. Hairston (2010),
Dynamic temporal evolution of polar cap tongue of ionization during magnetic storm,
J. Geophys. Res., 115, A12333, doi:10.1029/2010JA015848.

Humphreys ,T.E., Psiaki,M.L. and Kintner,P.M. (2010)
Modeling the Effects of Ionospheric Scintillation on GPS Carrier Phase Tracking
Aerospace and Electronic Systems, IEEE Transactions Vol. 40, No.4, pp 1624-1637

Huttunen, K.E.J., Schwenn, R., Bothmer, V. and Koskinen, H.E.J. (2005)
Properties and geoeffectiveness of magnetic clouds in the rising, maximum and early declining phases of solar cycle 23
Annales Geophysicae (2005) 23:625-641, SRef-ID: 1432-0576/ag/2005-23-625

Imber,S.M., Milan,S.E. and Lester,M.
Solar Cycle Variations in Polar Cap Area Measured by the SuperDARN Radars (2013)
J. Geophys. Res, doi: 10.1002/jgra.50509

Jacobsen, K.S. and Schäfer,S. (2012)
Observed Effects of a Geomagnetic Storm on an RTK Positioning Network at High Latitudes
J. Space Weather Space Clim. 2 (2012) A13DOI: 10.1051/swsc/2012013

Jayachandran, P. T.,R. B. Langley, J. W. MacDougall, S. C. Mushini, D. Pokhotelov, A. M. Hamza,
I. R. Mann, D. K. Milling, Z. C. Kale, R. Chadwick, T. Kelly, D. W. Danskin, and C. S. Carrano (2009),
Canadian High Arctic Ionospheric Network (CHAIN),
Radio Sci., 44, RS0A03, doi:10.1029/2008RS004046

Jensen,A.,Ovstedal.O. and Grinde,G. (2007)
Development of a Regional Model for Norway
ION GNSS 20th International Technical Meeting
for the Satellite Division, 25-28 September2007, Fort Worth

Jensen,A.,Grinde,G. and Hanssen,R.I. (2008)
Systen for Performance Monitoring with Respect to Ionospheric Actvity at High Latitudes
Proceeding of ENC, 2008,Toulouse

Jin,S., Luo,O.F. and Park,P. (2008)
GPS Observations of the Ionospheric F2-layer Behavior During the 20th November 2003
Geomagnetic Storm over South Korea
J Geod (2008) 82:883–892 DOI 10.1007/s00190-008-0217-x

Kamei,T.,Sugiura,M. and Arak,T. (1992)
Auroral Electrojet (AE) Indices
http://wdc.kugi.kyoto-u.ac.jp/aedir/ae2/onAEindex.html

Kamide,Y. (1982)
The Relationship Between Field Aligned Currents and the Auroral Electrojets: A review
Space Science Reviews Vol31 (1982),pp 127-243

Karslioğlu,M.O. and Duraz,M. (2012)
Regional Spatio-temporal modeling of the ionospheric Vertical Total Electron Content (VTEC) using Multivariate Adaptive Regression B-Splines (BMARS)
J. of Geodesy and Geoinformation (1), 2, May 2012

Kelley,J.D. and Vickrey,J.F. (1984)
F-Region Ionospheric Structure Associated with Anti Sunward Flow Near the Dayside Polar Cusp
Geophysical Research Letters, Vol. 1 , No. 9, Pp9 07-910,1984

Kersley,L. and Chandra,H. (1988)
Scintillation at High Latitudes During Winter Magnetic Storms
Journal of Atmospheric and Terrestrial Physics Vol. 50, No.6,pp 565-575, 1988

Keskinen,M.J. and Ossakow,S.L. (1983)
Theories of High Latitude Ionospheric Irregularities: A Review
Radio Science Vol.18,No.6, pp 1077-1091,1983

Keskinen,M.J., Mitchell,H.G:, Fedder,J.A., Satyanaryana,P.,Zalesak,S.I.and Huba,J.D. (1988)
Nonlinear Evolution of the Kelvin Helmholtz Instability in the High Latitude Ionosphere
Journal of Geophysical Research Vol. 93,No.A1, pp137-152,1988

Kintner, P.M. and Seyler,C.E (1985)
The Status of Observations and Theory of High Latitude Ionospheric and Magnetospheric Plasma Turbulence,
Space Science Reviews 41 (1985) 91-129. 0038-6308/85.15 D. Reidel Publishing Company

Kintner,P.M.,Kil,H.,Bach,T.L and DePaula,E.R. (2001)
Fading Time Scales with GPS Signals and Potential Consequences
Radio Science Vol.36, No.4,pp 731-743
Kintner,P.M. and Ledvina,B.M. (2005)
The Ionosphere, Radio Navigation and Global Navigation Satellite Systems
Advances in Space Research 35 (2005) 788-811
Kintner,P.M., Ledvina,B.M. and de Paula,E.R. (2007)
GPS and ionospheric scintillations
Space Weather (5), S09003, doi:10.1029/2006SW000260,2007
KintnerP.M., Humphreys,T.E. and Hinks, J.C. (2009)
GNSS and Ionospheric Scintillation- How to Survive the Next Solar Maximum
Inside GNSS, July/August 2009, pp.22-30
Klobuchar,J.A. (1997)
Real Time Ionospheric Science: The New Reality
RadioS cienceV, olume 32, Number5 , Pages1 943-1952,1997
Knudsen,W.C. (1974)
Magnetospheric Convection and the High-latitude F2 Ionosphere
Journal of Geophys. Res. Vol.79,No.7,1974
Lehtinen, M.S. and Huuskonen, A. (1996)
General Incoherent Scatter Analysis and GUISDAP
Journal of Atmospheric and Terrestrial Physics, Vol. 58, No. 1~4, pp. 435~452, 1996
Lehtoranta,V.K. (1997)
Collection of Geomagnetic Indices and Like
http://www.sci.fi/~fmbb/astro/indices.htm
Lepping, R.P., Berdichevsky, D.B., and Wu, C-C. (2003)
Sun-Earth electrodynamics: The solar wind connection
Recent Res. Devel.Astrophys., 1(2003):139-171 ISBN: 81-271-004-8
Leyser,T. (2011)
Ionosondes
www.irf.se, 2011
Li,G., Ning,B., Ren,Z. and Hu,L. (2010)
Statistics of GPS Ionospheric Scintillation and Irregularities over Polar Regions at Solar Minimum
GPS Solut (2010) 14:331-341
Lockwood,M. and Carlson, H.C. Jr (1992)
Production of Polae Cap Electron Density Patches by Transient Magnetopause Reconnection
Geophysical Research Letteres, Vol.19, No.17,pp 1731-1734
Lorentzen, D. A., N. Shumilov, and J. Moen (2004),
Drifting airglow patches in relation to tail reconnection,
Geophys. Res. Lett., 31, L02806,doi:10.1029/2003GL017785
Lorentzen, D. A., J. Moen, K. Oksavik, F. Sigernes, Y. Saito, and M. G. Johnsen (2010),
In situ measurement of a newly created polar cap patch,
J. Geophys. Res., 115, A12323, doi:10.1029/2010JA015710.
Low, B.C., (2001)
Coronal mass ejections, magnetic flux ropes, and solar magnetism
Journal of Geophysical Research, 106, A11, 2000JA 004015
Lyons, L. R., D.-Y. Lee, C.-P. Wang, and S. B. Mende (2005),
Global auroral responses to abrupt solar wind changes: Dynamic pressure, substorm, and null events,
J. Geophys. Res., 110, A08208, doi:10.1029/2005JA011089.
MacDougall, J., and P. T. Jayachandran (2007),
Polar patches: Auroral zone precipitation effects,
J. Geophys. Res., 112, A05312, doi:10.1029/2006JA011930.
Mackay, Duncan H. (2012)
The Sun's global magnetic field
Phil. Trans. R. Soc. A(2012) 370, 3151-3168 doi: 10.1098/rsta.2011.0536
Manucci,A.J., Iijima,B.,Sparks,L.,Pi,X.,Wilson,B. and Linqwister,U. (1999)
Assessment of Global TEC Mapping using a Three-Dimensional Elctron Density Model
J. of Atmospheric and Solar-Terrestrial Physics, Vol.61, No.16, pp1227-1236
McCready,M.A. and Heinselman,C.J. (2013)
The Chatanika and Sondrestrom Radars – A Brief History
Hist. Geo Space Sci., 4, 1–6, 2013 www.hist-geo-space-sci.net/4/1/2013/ doi:10.5194/hgss-4-1 2013

McComas,D.J, Bame,S.J., Parker,P.,Feldman,W.C., Phillips,J.L.,Riley,P. and Griffee,J.W. (1998)
Solar Wind Proton Alha Monitor (SWEPAM) for the Advanced Composition Explorer
Space Science Reviews Vol 86,pp563-612,2998

Meggs, R.W.; Mitchell, C.N.; Smith, A.M. (2006)
An Investigation into the Relationship between Ionospheric Scintillation and Loss of Lock in GNSS Receivers.
In Characterising the Ionosphere (pp. 5-1 – 5-10). Meeting Proceedings RTO-MP-IST-056, Paper 5. Neuilly-sur-Seine, France: RTO. Available from: http://www.rto.nato.int/abstracts.asp.

McIlwain,C.E.(1961)
Coordinates for Mapping the Distribution of Magnetically Trapped Particles
Journal of Geophysical Research Vol.66, No.11

Middleton, H. R., S. E. Pryse, L. Kersley, G. S. Bust, E. J. Fremouw, J. A. Secan, and W. F. Denig (2005),
Evidence for the tongue of ionization under northward interplanetary magnetic field conditions,
J. Geophys. Res., 110, A07301,doi:10.1029/2004JA010800

Milan, S.E., Hutchinson,J., Boakes,P.D. and Hubert,B. (2009)
Influences of the Auroral Oval,
Ann. Geophys.27,2913-2924,2009

Mishin,V.M., Foerster,M., Saifudinova,T.I., Bazarhapov,A.D., Karavaev,Yu.A.,Sapronova,L.A. and Solovyev,S.I. (2007)
Spontaneous Substorms and Ordered Type of Magnetospheric Disturbances during the Superstorm of November 20,2003
Geomagnetism and Aeronomy, 2007,47,4,429,441, doi:10.1134/S0016793207040032

Mitchell, C.N., Spencer, P.S.J.(2003)
A three-dimensional time-dependentalgorithm or ionospheric imaging using GPS.
Ann. Geophys. 46 (4),687–696, 2003.

Moen,J. Carlson,H.C.,Milan, S.E., Shumilov,N., Lybekk,B., Sandholt, P.E. and Lester,M. (2001)
On the Collocation between Dayside Auroral Activity and Coherent HF-Radar Backscatter
Ann. Geophys. 18,1532-1549(2001)

Moen,J., Lockwood,M., Oksavik,K., Carlson,H.C., Denig,W.F., Van Eyken,A.P. and McCrea, I.W. (2004)
The Dynamics and Relationships of Precipitation, Temperature and Convection Boundaries in the Dayside Auroral Ionosphere.
Ann.Geophys. (2004)SRef:1432-057/ag/2004-22-1973

Moen,J., Carlson,H.C., Oksavik,K., Nielsen,C.P., Pryse,S.E., Middleton, H.R., McCrea,I.W. and Gallop,P. (2006)
EISCAT observations of plasma patches at sub-auroral cusop latitudes,
Ann. Geophys., 24,2363-2374,2006

Moen, J., Gulbrandsen,N., Lorentzen,D.A. and Carlson,H.C. (2007)
On the MLT Distribution of F Region Polar Cap Patches at Night.
Geophysical Research Letters Vol 34, L14113,doi:10.1029/2007/GL029632

Moen, J., Qiu,X.C., Carlson,H.C., Fujii,R. and McCrea, I.W. (2008)
On the Diurnal Variabilityin F2-region Plasma Density Above the EISCAT Svalbard Radar.
Ann. Geophys., 26, 2427–2433, 2008

Moen, J., K. Oksavik, T. Abe,M. Lester, Y. Saito, T. A. Bekkeng, and K. S. Jacobsen (2012),
First in-situ measurements of HF radar echoing targets,
Geophys. Res. Lett., 39, L07104, doi:10.1029/2012GL051407.

Moen,J., Oksavik,K., Alfonsi,L., Daabakk,Y., Romano,V. and Spogli, L. (2013)
Space Weather Challenges of the Polar Cap Ionosphere
J. Space Weather Space Clim. 3 (2013) A02 DOI: 10.1051/swsc/2013025

Murtagh, B. et al. (2004)
Intens Space Weather Storms October 19 to November 07, 2003
Service Assessment, U.S. Department of Commerce, NOAA, April 2004

Mushini,S.C., Jayachandran,P.T., Langley,R.B., MacDougall, J.W. and Pokhotelov,D. (2012)
Improved Amplitude-and-Phase Scintillation Indices Derived from Wavelet Detrended High Latitude GPS Data
GPS Solut (2012) 16:363–373 DOI 10.1007/s10291-011-0238-4

Newell,P.T., Wing,S.,Meng,C-I. and Sigillito,V. (1991)
The Auroral Oval Position, Structure and Intensity of Precipitation From 1984 Onward: An Automated Online Database
Journal of Geophysical Research Vol.96,No.A4,pp5877-5882,1991

Newell,P.T., Sotirelis,T., Ruohoniemi,J.M., Carbary,J.F., Liou,K., Skura,J.P., Meng,C-I., Deehr,C., Wilkinson,D. and Rich,F.J. (2002)
OVATION: Oval, Varioation, Assessment,Tracking, Intensity and Online Nowcasting
Ann. Geophys. (2002) 20: 1039-1047

Newell, P. T., T. Sotirelis, and S. Wing (2009),
Diffuse, monoenergetic, and broadband aurora: The global precipitation budget,
J. Geophys. Res., 114, A09207, doi:10.1029/2009JA014326.

Niu,F., Morton,Y.,Wang, J. and Pelgrum,W. (2012)
GPS Carrier Phase Detrending Methods and Performances for Ionosphere Scintillation Studies
International Technical Meeting (ITM) of The Institute of Navigation, Newport Beach, CA, January 30 - February 1, 2012

Norwegian Space Center (2013)
Vurdering av sårbarhet ved bruk av globale satellitt-navigasjonssystemer i kritisk infrastruktus
NRS-rapport,2013/3

Ogawa, Y., S. C. Buchert, R. Fujii, S. Nozawa, and A. P. van Eyken (2009),
Characteristics of ion upflow and downflowobserved with the European Incoherent Scatter Svalbard radar,
J. Geophys. Res., 114, A05305, doi:10.1029/2008JA013817

Oksavik, K., J. M. Ruohoniemi, R. A. Greenwald, J. B. H. Baker, J. Moen, H. C. Carlson, T. K. Yeoman, aM. Lester (2006),
Observations of isolated polar cap patches by the European Incoherent Scatter (EISCAT) Svalbard and Super Dual Auroral Radar Network (SuperDARN) Finland radars,
J. Geophys. Res., 111, A05310, doi:10.1029/2005JA011400.

Oksavik,K., Barh,V.L., Moen,J. and Lester,M. (2010)
On the entry and transit of high-density plasma across the polar cap,
J. Geophys. Res. 115, A12308, doi: 10.1029/2010JA015817,2010

Oksavik, K., J. I. Moen, E. H. Rekaa, H. C. Carlson, and M. Lester (2011),
Reversed flow events in the cusp ionosphere detected by SuperDARN HF radars,
J. Geophys. Res., 116, A12303, doi:10.1029/2011JA016788

Oksavik, K., J. Moen, M. Lester, T. A. Bekkeng, and J. K. Bekkeng (2012),
In situ measurements of plasma irregularity growth in the cusp ionosphere,
J. Geophys. Res., 117, A11301, doi:10.1029/2012JA017835.

Oler, C. (2004),
Prediction performance of space weather forecast centers following the extreme events of October and November 2003,
Space Weather, 2, S08001, doi:10.1029/2004SW000076.

Ossakow,S.L. and Chaturvedi,P.K. (1979)
Current Convective Instability in the Diffuse Aurora
Geophysical Research Letters Vol.6,No.4, 1979

Pandey, B. P. and Lakshina, G.S. (2001)
Driven reconnection and bursty bulk flows
Annales Geophysicae (2001) 19: 681–686

Perrault,P. and Akasofu,S-I. (1978)
A study of geomagnetic storms
Geophys. J. R. astr. SOC. (1978) 54,547-573

Pfaff, Robert E. Jr (2012)
The Near Earth Plasma Environment
Space Sci Rev (2012)168:23-112, doi: 10.1007/s11214-012-9872-6

Pi,X., Manucci, A.J., Lindqwister,U.J. and Ho, C.M. (1997)
Monitoring of Global Ionospheric Irregularities Using the Worldwide GPS Network
Geohys. Res. Letters, Vol. 24,No. 18,pp2283-2286,1997

Pokhotelov, D., C. N. Mitchell, P. S. J. Spencer, M. R. Hairston, and R. A. Heelis (2008),
Ionospheric storm time dynamics as seen by GPS tomography and in situ spacecraft observations,
J. Geophys. Res., 113, A00A16, doi:10.1029/2008JA013109.

Prikryl,P., Jayachandran,P.T., Mushini,S.C., Pokhotelov,D., MacDougall,J.W., Donovan,E., Spancswick,E.and St-Maurice,J-P. (2010)
GPS TEC, Scintillation and Cycle Slips Observed at High-Latitudes During Solar Minimum
Ann. Geophys.28,1307-1316,2010, doi:10.5194/angeo-28-1307-2010

Prikryl,P., Jayachandran,P.T., Mushini,S.C. and Chadwick,R. (2011)
Climatology of GPS Phase Scintillation and HF-radar Backscatter for the High Latitude Ionosphere under Solar Minimum Conditions
Ann. Geophys., 29, 377–392, 2011 doi:10.5194/angeo-29-377-2011

Prikryl, P., P. T. Jayachandran, S. C. Mushini, and I. G. Richardson (2012),
Toward the probabilistic forecasting of high-latitude GPS phase scintillation,
Space Weather, 10, S08005, doi:10.1029/2012SW000800.

Prikryl,P.,Ghoddousi-Fard,R., Kundur,B.S.R., Thomas,E.G., Coster,A.J., Jayachndran,P.T., Spanswick,E. and Danskin,D.W. (2013)
GPS Phase Scintillation And Proxy Index At High Latitudes During A Moderate Geomagnetic Storm
Ann. Geophys., 31, 805–816, 2013 doi:10.5194/angeo-31-805-2013

Primdahl,F. (1979)
The Fluxgate Magnetometer
J. Phys. E: Sci. Instrum., Vol. ***12,*** *1979.*

Provan,G., Lester,M., Mende,S.B. and Milan,S.E. (2004)
Statistical Study of High-latitude Plasma Flow During Magnetospheric Substorms
Ann. Geophys. Vol.22, pp 3607-3624,2004

Pryse,S.E., Kersley,L. and Walker, I.K. (1996)
Blobs and Irregularities in the Auroral Ionosphere
Journal of Atmospheric and Terrestrial Physics Vol. 58, No. 1-4, pp 205-215, 1996

Pryse,S.E., Wood,A.G., Middleton,H.R., McCrea,I.W. and Lester,M. (2006)
Reconfiguration of Polar Cap Plasma in Magnetic Midnight Sector
Ann.Geophys.,24,2201-2208,2006

Reinisch, B. W. ,X. Huang, I. A. Galkin, V. Paznukhov, A. Kozlov, P. Nsumei, G. Khmyrov(2005)
Recent advances in real time analysis of ionograms and ionospheric drift measurements with digisondes
IES Proceedings 2005

Reinisch, B.W. and Galkin, I.A. (2011)
Global Ionospheric Radio Observatory (GIRO)
Earth, Planets, Space 63,pp377-381,2011

Rino,C.L.,Linvingston,R.C. and Matthews,S.J. (1978)
Evidence For Sheet-like Auroral Ionospheric Irregularities
Geophysical Research Letters Vol. 5,No. 12, 1978

Rinne, Y., J. Moen, K. Oksavik, and H. C. Carlson (2007),
Reversed flow events in the winter cusp ionosphere observed by the European Incoherent Scatter (EISCAT) Svalbard radar,
J. Geophys. Res., 112, A10313, doi:10.1029/2007JA012366.

Rodger,S.E., Pinnock,M., Dudeney,J.R., Baker, K.B. and Greenwald,R.A. (1994)
A New Mechansim for Polar Patch Formation
Journal of Geophysical Research, Vol.99, No. A4, pp 6425-6436

Romano,V.,Pau,S.,Pezzopane,M.,Zuccheretti,E.,Zolesi,B.,DeFranceschi,G. and Locatelli,S. (2008)
The Electronic Space Weather Upper Atmosphere (eSWua) Project at INGV:
Advancements and State of the Art.
Ann. Geophys. 26, 345-351,2008

Rostoker,G., Armstrong,J.C. and Zmuda,A.J. (1975)
Field Aligned Current Flow Associated with Intrusion of the Substorm Intensified Westward Electrojet into the Evening Sector
J. Geophys. Res. Vol. 80, No.25, 1975

Rourke G.F. (1965)
Investigation of Q-Indices in the Antrctic
Geomagnetism and Aeronomy: Studies in the Ionosphere,
Geomagnetism and Atmospheric Radio Noise, Antarctic Research Series Vol. 4,pp 159-172

Rowlett, R (2003)
Solar Flare Intensity in How Many? A Dictionary of Units of Measurement
University of North-Carolina (2005)
http://www.unc.edu/~rowlett/units/scales/solar_flares.htm

Ruohoniemi,J.M. and Greewald,R.A.(1996)
Statistical patterns of high-latitude convectiono btainedf rom Goose Bay HF radar observations
Journal Of Geophysical Research,Vol. 101,NO. A10, Pages2 1,743-21,763 October 1, 1996
Ruohoniemi,J.M. and Baker,K.B. (1998)
Large-Scale Imaging Of High-Latitude Convection W Ith Super Dual
Auroral Radar Network HF Radar Observations
Journal Of Geophysical Research, Vol. 103, No. A9, Pages 20,797-20,811september 1, 1998
Ruohoniemi, J.M., Baker,J.B.H.,Frissel,N.,deLarquier,S. and Thomas,E.G. (2012)
Remote Sensing of the Ionosphere and Earth's Surface with HF Radar
OGIS April 13th , 2012 http://vt.superdarn.org/tiki-index.php?page=sd_tutorial
Russel, C.T. , (2000)
The Polar Cusps
http://www-ssc.igpp.ucla.edu/personnel/russell/papers/polarcusp/
Sandholt,P.E., Moen,J.,Rudland,A., Opsvik,D.,Denig,W.F. and Hansen,T. (1993)
Auroral EventSequences at the Dayside Polar Cap Boundary for Positive and
Negative Interplanetary Magnetic Field By
Journal of Geophysical Research Vol.90,No.A5,pp7737-7755
Scherrer,P.H., Bogart,R.S., Bush,R.I., Hoeksema,J.T., Kosovichev,A.G., Schou,J.,
Rosenberg,W., Springer,L., Tarbell,T.D., Title,A., Wolfson,C.J.,
Zayer,I. and the MDI Engineering Team (1995)
The Solar Oscillations Investigation - Michelson Doppler Imager
Solar Physics, Volume 162, Issue 1-2, pp. 129-188
Schiffler, A. (1996)
MSc Thesis on SuperDARN Measurements of Double-Peaked Velocity Spectra, University of
Sasktchewan, *www.ferzkopf.net/personal/Thesis*
Schunk,R.W., Scherliess,L. and Sojka,J.J. (2003)
Recent Approaches to Modeling Ionospheric Weather
Adv. Space Res. (31), 4, doi:10.1016/s0273-1177(02)00791-3
Sergeev,V.A.,Liou,K.,Newell,P.Y.,Ohtani,S-I.,Hairston,M.R.and Rich,F. (2004)
Auroral Streamers: Characteristics of Associated Precipitation, Convection and Field-Algined Currents
Ann.Geophys. Vol22, pp 537-548
Siddle, D. R., A. J. Stocker, and E. M. Warrington (2004),
Time of flight and direction of arrival of HF radio signalsreceived over a path along the midlatitude
trough: Observations,
Radio Sci., 39, RS4008, doi:10.1029/2004RS003049.
Sigernes,F., Dyrland,M., Brekke,P.,Gjengedahl, E.K., Chernouss,S., Lorentzen, D.A.,
Oksavik, K. and Deehr,C.S. (2011a)
Real Time Aurora Oval Forecasting-SvalTrackII
Sección Especial 37th AMASON/Special Section,37th, Amason Aurora
Sigernes,F., Dyrland,M., Brekke,P.,Chernouss,S., Lorentzen,D.A., Oksavik,K.., and Deehr,C.S. (2011b)
Two Methods to Forecast Auroral Displays
J.Space Weather Space Clim. 1 (2011) A03
Siscoe, G. L., W. Lotko, *and* B. U. Sonnerup *(*1991*)*,
A high-latitude, low-latitude boundary layer model of the convection current system,
J. Geophys. Res., *96*(*A3*), *3487–3495*, doi:*10.1029/90JA02362*.
Shagimuratov,I., Kranowski,A., Efishov,I. Zakharenova, I. and Terpenitsyna,N. (2009)
Occurrence of Phase Scintillation in Northern and Southern Hemisphere
Proceedings, 20th Int. Zurich Symposium on EMC, Zurich 2009
Sheperd.E.G. ,S.G.,Talaat,E.R.,Bristow,W.A.,Zheng,Y.,Coster,A.J.and Sazykin,S. (2012),
Large-scale observations of a subauroral polarization stream by midlatitude SuperDARN radars:
Instantaneous longitudinal velocity variations,
J. Geophys. Res., 117, A05306, doi:10.1029/2011JA017232.
Skone,S., Knudsen, K. and De Jong, M. (2001)
Limitations in GPS Reciever Tracking Performance Under Ionospheric Scintillation Conditions
Phys. Chem. Earth (A), Vol. *26, No. 6-8,* pp. *613-621, 2001*
Skone,S., Lachapelle,G., Yo,D., Yu,W. and Watson,R. (2005)
Investigating the Impact on Ionospheric Scintillation Using a GPS Software Receiver.
Presented at the ION GNSS 2005 Conference, Long Beach, CA, September 13 – 16

Skone,S.,Man,F.,Ghafoori,F and Tiwari,R. (2008)
Investigation of Scintillation Charcteristics for High Latitude Phenomena
Ion GNSS 2008, Session D5, Savannah, GA 16-19 September, 2008
Smith,M. (1994)
Transient Dayside Reconnection and its Effects on the Ionosphere
NATO ASI Series, Vol.425, Kluwer Academic Publishers, 1994
Smith,C.W.,L'Heureux,J., Ness,F., Acuña,M.H., Burlaga,L.F. and Scheifele,J. (1998)
The ACE Magnetic Fields Experiment
Space Science Reviews **86:** 613–632, 1998.
Smith,D.A.,Araju-Padere,E.A.,Minter,C. and Fuller-Rowell,T. (2008)
Acomprehensive Evaluation Of The Errors Inherent In The Use Of A
Two-Dimensional Shell For Modeling The Ionosphere
Radio Science, Vol.43, RS6008,doi:10.1029/2007RS003769,2008
Sotirelis,T., Newell, P.T. and Meng,C-I. (1998)
Shape of the open-closedb oundary of the polar cap as determined from observations of precipitating particlesby up to four DMSP satellites
Journal Of Geophysical Research, Vol. 103, No. A1, Pages 399-406,1998
Sotirelis,T. and Newell,P.T. (2000)
Boundary-Oriented Electron Precipitation Model
Journal Of Geophysical Research, Vol. 105, No. A8, Pages 18,655-18,67,2000
Southwood, D.G. (1987)
The Ionospheric Signature of Flux Transfer Events
Journal of Geophysical Research Vol.92, pp 3207-3213,1987
Spencer, P. S. J. and Mitchell, C. N. (2007)
Imaging of fast moving electron-density structures in the polar cap.
Annals of Geophysics, 50 (3). pp. 427-434. ISSN 1593-5213
Spogli,L., Alfonsi,L.,DeFranceschi,G., Romano,V., Aquino,M.H.O. and Dodson,A. (2009)
Climatology of GPS Ionospheric Scintillations over High and Mid-latitude European Regions
Ann. Geophys, 27,3429-3437,2009
Srivastava,N. (2005)
Predicting the Occurrence of Superstorms
Ann. Geophys., 23,2989-2995,2005
STD-SAT, Statens kartverk, Geodesidivisjonen (2009)
Satellittbasert Posisjonsbestemmelse
Standard Versjon 2.1, 2009
Steele,D.P. and Cogger, L.L. (1996)
Polar patches and the "tongue of ionization",
Radio Sci, 31,(3), 96RS00369
Stern,D.P. (2001)
The Plasma Sheet
http://www-spof.gsfc.nasa.cov/Education/wtail.html
St. Maurice,J-P, (2012)
Incoherent vs Coherent Scatter Radars (ISR's vs CSR's)
http://vt.superdarn.org/tiki-index.php?page=sd_tutorial
Stone, E.C.,Frandsen,A.M.,Mewaldt,R.A.,Christian,E.R.,Margolies,D.,Ormes,J.F. and Snow,F. (1998)
The Advanced Composition Explorer
Kluwer Academic Press, Netherlands,1998
Strømme,A., (2006)
Ionospheric and Magnetospheric Studies with Incoherent Scatter Radars
EISCAT School, Qingdau China, 31 October 2006
Strømme,A. (2011)
The Short Introduction to Incoherent Scatter (IS) Theory
International Scatter Radar Workshop, Kangerlussaq, Greenland 2011
Sugiura,M. and Kamei,T. (1986)
On the Dst Index
WDC-A World Data Center-A for Solar-Terrestrial Physics,
http://wdc.kugi.kyoto-u.ac.jp/dstdir/dst2/onDstindex.html

Sunda,S.,Vyas,B.M.,Satish,S.V.,Khekale,P.V. and Parikh,K.S. (2013)
Improvement of Positioning Accuracy with GAGAN and the Impact of Scintillation on GNSS
Positioning, 2013, 4, 282-288 Published Online November 2013 (http://www.scirp.org/journal/pos) http://dx.doi.org/10.4236/pos.2013.44028

Tiwari,R.,Bhattarchaya,S.,Purohit,P.K. and Gwal,A.K. (2009)
Effect of TEC Variation on GPS Precise Point at Low Latitude
The Open Atmospheric Science Journal, 2009,Vol.3, pp. 1-12

Thomas, E.G. (2013)
Interactive GPS/TEC Plotting-Four Plot: A Quick Guide
http://vt.superdarn.org/tiki-index.php?page=DaViT+TEC+Four+Plot

Tomita,S.,Nosé,M., Iyemori,T., Toh,H., Takeda,M., Matzka,J., Bjørnsson,G., Saemundsson,T, Janzhura,A., Trochichev,O. and Schwarz,G. (2011)
Magnetic Local Time Dependence of Geomagnetic Disturvbances Contributing to the AU and AL Indices
Ann.Geophys.,29,673-678,2011

Trimble Navigation Limited (2000)
MS-series Operation Manual, Part Number 408680-00
Trimble Navigation Limited Surveying and Mapping Division,USA

Trishchenko,A.P., and Garand,L. (2012)
Continuos Coverage of the Arctic: Two-Satellite Highly Elliptical Orbit (HEO) System is Better Than A Dozen of LEO Polar Orbiters
NOAA Satellite Science Week, Kansas City, MO, April 30-May 4, 2012

Tsunoda,R.T. (1988)
High Latitude F-Region Irregularities, A Review and Synthesis
Technical Report, SRI Project 1700

Valladares,C.E., Decker,D.T., Sheehan,R. and Anderson, D.N. (1996)
Modelling the Formation of Polar Cap Patches Using Large Plasma Flows
Radio Science, Vol.31,No.3, pp 573-593,1996

Valladares, C.E., Decker,D.T., Sheehan,R., Anderson,D.N., Bullett,T. and Reinisch,B.W. (1998a)
Formation of Polar Cap Patches Associated with North-to-South Transitions of the Interplanetary Magnetic Field
Journal of Geophys. Research, Vol.103,No.A7,pp14657-14670

Valladares,C.E.,Sheehan,R.,Carlson,H.C.Jr. and Bullett,T. (1998b)
Simultaneous observations of polar cap patches and Sun-aligned arcs during transitions of the IMF
Radio Science, Volume 33, Number 6, Pages 1829-1845,1998

Valladares,C.E.,Acaydé,D.,Rodriguez,J.V.,Ruohoniemi,J.M. and Van Eyken,A.P. (1999)
Observations of plasma density structures in association with the passage of traveling convection vortices and the occurrenceof large plasma jets
Ann. Geophysicae 17, 1020-1039 (1999)

Valladares. C. B., J. Moen, P.E. Sandholt, W. F. Denig, and O. Troshichev, (2002)
Simultaneous observations of dayside aurora from Heiss Island and Ny Alesund,
Geophys. Res. Lett., 29(24), 2202, doi:10.1029/2002GL01600l',2002

Vecchio, A., Laurenza, M., Meduri, D., CarboneV. And Stroini,M. (2012)
The dynamics of the Solar Magnetic Field, polarity reversals, Butterfly Diagram and Quasi- Biennieal Oscillations.
The Astrophysical Journal 749:27 (10pp), 2012 April 10, doi:10.1088/0004-637x/749/1/27

Venkatakrishnan, P. and Ravindra, B. (2003)
Relationship between CME speeds and magnetic energy of active regions,
Geophys. Res.Lett., 30, 2181, doi:10.1029/2003GL018100.

Walker,I.K., Moen,J.,Kersley.L. and Lorentzen,D.A. 1999
On The Possible Role Of Cusp/Cleft Precipitation In The Formation Of Polar-Cap Patches
Ann. Geophysicae 17, 1298-1305 (1999)

Wang,H.,Lühr,H.,Ridley,A.,Ritter,P. and Yu,Y. (2008)
Stromtime Dynamics of Auroral Electrojets: CHAMP Observation and the Space Weather Modeling Framework Comparison
Ann. Geophys.,26,555-570,208

Wanliss, J. A., and K. M. Showalter (2006),
High-resolution global storm index:Dstversus SYM-H,
J. Geophys. Res.,111,A02202, doi:10.1029/2005JA011034.

Webb,D.F. and Howard,T.A. (2012)
Coronal Mass Ejections: Observations
Living Rev. Solar Phys., 9, (2012), 3 http://www.livingreviews.org/lrsp-2012-3
Weber,E.J., Buchau,J.,Moore,J.G.,Sharber,J.R.,Livingston,R.C.,Winningham,J.D. and Reinisch,B.W. (1984)
F-layer Ionization Patches in the Polar Cap
Journal of Geophysical Research, Vol.89, No.A3, pp1683-1694,1984
Weber,E.J., Klobuchar,J.A., Buchau,J.,Carlson,H.C.Jr, Livingston,R.C., De la Beajardiere,O., McCready,M., Moore,J.G. and BishopG.J. (1986)
Polar Cap Flayer Patches: Structure and Dynamics
Journal of Geophysical Research Vol.91, No.A11, pp12121—12129,1986
Weimer,D.R. (1995)
Models of High-latitude Electric Potentials Derived with a Least Error Fit of Spherical Harmonic Coeffisients
Journal of Geophysical Research Vol.100, No.A10, pp 19595-19607,1995
Wernik,A.W., Secan,J.A., and Fremouw,E.J. (2003)
Ionospheric Irregularities and Scintillation
Adv. Space Res. Vol.31,No.4, pp971-981
Weydahl,D.J. (2009)
Satellittsystmer-og-baner
Satellitt-fjernmåling med avanserte radarinstrumenter
UNIK 4510 Lectures, FFI,2009
Willis,D.M. (1971)
Structure of the Magnetopause
Rev. of Geophysics and Space Physics, Vol.9, No.4,1971
Wolf,R.A., Spiro,R.W:, Sazykin,S. and Toffoletto, F.R. (2007)
How the Earth's Inner Magnetosphere Works: An Evolving Picture
Journal of Atmospheric and Solar Terrestrial Physics,69(2007), 288-302
Xu,W.Y. (2009)
Variations Of The Auroral Electrojet Belt During Substorms
Chinese Journal Of Geophysics Vol.52, No.2, 2009, Pp: 301-310
Yuan, Z.-G., X.-H. Deng, and J.-F. Wang (2008),
DMSP/GPS observations of intense ion upflow in the midnight polarionosphere associated with the SED plume during a supergeomagnetic storm,
Geophys. Res. Lett., 35, L19110,doi:10.1029/2008GL035462.
Yeates, A.R., Mackay, D.H., van Ballegooijen, A. A. and Conastable, J.A. (2010)
A non-potential model for the Sun's open flux
http://arxiv.org/abs/1006.4011v1
Yeh,K.C. and Liu, C-H, (1982)
Radio Wave Scintillations in the Ionosphere
Proceedings of the IEEE,Vol.70, No.4
Yin.P, Mitchell,C.N., Spencer,P.S.J. and Foster, J.C. (2004)
Ionosphere Electron concentration imaging using GPS over the USA during the storm of July 2000
Geophys. Res. Letters, (31), L12806, doi:10.1029/2004GL019899,2004
Yin, P., C. Mitchell, and G. Bust (2006),
Observations of the F region height redistribution in the storm-time ionosphere over Europe and the USA using GPS imaging,
Geophys. Res. Lett.,33, L18803, doi:10.1029/2006GL027125
Yizengaw, E., M. B. Moldwin, A. Komjathy, and A. J. Mannucci (2006),
Unusual topside ionospheric density response to the November 2003 superstorm
J. Geophys. Res., 111, A02308, doi:10.1029/2005JA011433.
Yizengaw, E.,M. B. Moldwin, and D. A. Galvan (2006b),
Ionospheric signatures of a plasmaspheric plume over Europe,
Geophys. Res. Lett., 33, L17103, doi:10.1029/2006GL026597.
Zhang,J., Dere,K.P., Howard,R.A. and Bothmer,V. (2002)
Identification of Solar Sources of Major Geomagnetic Storms Between 1996-2000
The Astrophysical Journal, 582:520-533, 2003
Zhang,Y., Wu,F., Kubo,N. and Yasuda,A. (2003)
Paper on: TEC Measurement by Single Dual-frequency GPS Receiver
www.denshi.e.kaiyodai.ac.jp/kubo/TEC.pdf

Zhang, J.-C., M. W. Liemohn, J. U. Kozyra, M. F. Thomsen, H. A. Elliott, and J. M. Weygand (2006),
A statistical comparison of solar wind sources of moderate and intense geomagnetic storms
at solar minimum and maximum,
J. Geophys. Res., 111, A01104, doi:10.1029/2005JA011065.
Zhang, Q.-H., Zhang,B-C., Liu,R-Y., Dunlop,M.W., Lockwood,M., Moen,J., Yang,R-Y.,
Hu,H-Q., Hu,Z-J., Liu,S-L., McCrea,I.W. and Lester,M. (2011),
On the importance of interplanetary magnetic field |By| on polar cap patch formation,
J. Geophys. Res., 116, A05308, doi:10.1029/2010JA016287
Zhang, Q-H., Zhang,B-C., Lockwood,M., Hu,H-Q., Moen,J., Ruohoniemi, J.M., Thomas,E.G., Zhang,S-R.,
Yang,H-G., Liu, R-Y., McWilliams,K.A. and Baker, J.B.H. (2013)
Direct Observations of the Evolution of Polar Cap Ionization Patches,
Science, Vol 339, 1597, DOI: 10.1126/science.1231487www.sciencemag.org
Zwickl,R.D., Doggett,K.A., Sahm,S., Barrett,W.P., Grubb,R.N., Detman,T.R.,
Raban,V.J., Smith,C.W., Riley,P.,Gold,R.E., Mewaldt,R.A. and Maruyama,T. (1998)
The NOAA Real Time Solar Wind (RTSW) System Using ACE Data
Space Science Reviews Vol 86, pp 633-648, 1998

6.2 Books

Cannon,P.S. and Bradley,P.A. in in Barclay, L . Ed. (2003)
Propagation of Radio waves 2.edition
Ionospheric propagation
The Institution of Electrical Engineers (IEE), London, UK
Cravens,T.E. (1997)
Planetary Ionospheres and Magnetospheres
ISBN 9780080432977
Advances in Space Research S Vol.20,No.2,1997
Bittencourt, J.A. (2004)
Fundamentals of Plasma Physics
http://www.springer.com/978-0-387-20975-3
Bothmer,V. and Daglis,I.A. (2007)
Space Weather – Physics and Effects
Praxis Publishing Ltd. Chichester, UK
Dunham,D.W. and Farquhar,R.W. in Gomez, Lo and Masdemont (2003)
Libration Points Orbits and Applications
Proceedings of the Conference
ISBN 981-238-363-8
World Scientific Publishing Co.Pte.Ltd
Freedman, Roger A. and KauffmannIII, William J. (2001)
Universe 6.edition
W.H. Freeman and Company, New York
Goodman J.M. (2005)
Space Weather and Telecommunication
The Kluwer International Series in Engineering and Computer Science
ISBN-0-387-23671—6
Springer Science+Busines Media, Inc.
Hofmann-Wellenhof, B., Lichtenegger,H. and Wasle,E. (2008)
GNSS-Global Navigation Satellite Systems, GPSGLAONASS, Galilieo, and more
Springer-Verlag Wien, Austria
Howard, John (2002)
Introduction to Plasma Physics
Australian National University, http://people.physics.anu.edu.au/~jnh112/AIIM/c17/.
Hutchinson, Ian H. (2001)
Introduction to Plasma Physics
Massachusetts Institute of Technology, Cambridge Massachusettes , USA
http://silas.psfc.mit.edu/introplasma/index.html

Kamide,Y. and Chian,A.C-L. (Eds) (2007)
Handbook of the Solar Terrestrial Environment
ISBN 973-3-540-40314-6, doi: 10.1007/b104478
Springer-Verlag Berlin Heidelberg New York
Kivelson, Margaret G. and Russel, Christopher T. (1995)
Introduction to Space Physics,
Cambridge University Press, UK
Levanon, N. (1988)
Radar Principles
ISBN0—471-8588-1
Wiley InterScience, John Wiley & Sons Inc, Canada
Nordian Aviation Training systems (2005)
Radio Navigation 2. Edition,
ISBN: 82-8107-052-81,ib
Nordian AS, Sandefjord
Paschmann, G., & Daly, P. W. (Eds.). (1998)
Analysis Methods for Multi-Spacecraft Data.
Noordwijk, Netherlands: ESA Publ. Div
Prölss, Gerd W,(2004)
Physics of the Earth's Space Environment An Introduction.
Springer Verlag Berlin Heidielberg
Moisan, M. and Pelletier, J. (2012)
Introduction to High- Frequency Discharges
htttp://www.springer.com/978-94-007-4557-5
Paschmann,G. in Jacobs, J.A. Ed. (1991)
Geomagnetism Ch.4: The Earth's Magnetopause
Academic Press, University of Michigan, US
Rishbeth,H. in Barclay, L . Ed. (2003)
Propagation of Radio waves 2.edition
Basic physics of the ionosphere
The Institution of Electrical Engineers (IEE), London, UK
Sandholt, P. E., Carlson, H.C. and Egeland, A. (2002)
Dayside and Polar Cap Aurora
Kluwer Academic Publishers, Netherlands
Saunders, Simon R. and Aragon-Zavala, Alejandro (2007)
Antennas and Propagation for Wireless Communication Systems 2.edition,
John Wiley and Sons Ltd, UK
Seeber,G. (2003)
Satellite Geodesy: Foundations,Methods and Applications 2nd Edition
ISBN-3-11-017549-5
GMBH&CO KG,10785 Berlin, Germany
Xu, Guachang (2007)
GPS-Theory, Algorithms and Applications 2.edition,
Springer-Verlag Berlin Heidelberg, New York
.Zarka, P. in Gargaud, M., Amils, R., Quintanilla, J.C., Henderson, J. C., Irvine, W.M., Pinti, D. L. and Viso, M. (2011)
Encyclopedia of Astrobiology
ISBN 978-3-642-11274-4
Springer-Verlag Berlin Heidelberg

6.3 Internet resources

GNSS:	http://glonass-iac.ru/en/index.php
	http://www.gsa.europa.eu/
	http://www.gps.gov/
	http://www.egnos-portal.eu/
	http://www.trimble.com/gps_tutorial/
Sun and Solar Wind :	
SOHO:	http://soho.nascom.nasa.gov/data/realtime-images.html
	http://sohowww.nascom.nasa.gov/about/about.html
	soi.stanford.edu
	http://lasco-www.nrl.navy.mil/
	http://umbra.nascom.nasa.gov/eit/
	http://sohodata.nascom.nasa.gov
ACE:	http://www.swpc.noaa.gov/ace/
	www.srl.caltech.edu/ACE
	http://www.ssg.sr.unh.edu/mag/ACE.html
	http://www.srl.caltech.edu/ACE/ASC/
STEREO:	stereo.gsfc.nasa.gov, stereo-ssc.nascom.nasa.gov
CACTUS:	http://sidc.oma.be/cactus/
GOES:	www.osd.noaa.gov/GOES/
Big Bear:	www.bbso.njit.edu
Mauna Loa:	http://www2.hao.ucar.edu/mlso/mlso-home-page
SST:	http://www.solarphysics.kva.se/
SEEDS:	http://spaceweather.gmu.edu/seeds/
ARTEMIS:	http://cesam.lam.fr/lascomission/ARTEMIS/
Radar and Ionosonde:	
Superdarn:	http://center.stelab.nagoya-u.ac.jp/hokkaido/site1/intro_e.html
	http://super-darn.jhuapl.edu/
	http://vt.superdarn.org/tiki-index.php?page=DaViT+TEC+Four+Plot
	http://vt.superdarn.org/tiki-index.php
MIT:	http://madrigal.haystack.mit.edu/madrigal/
	http://www.haystack.mit.edu/atm/mho/instruments/isr/index.html
ISRIM:	http://madrigal.haystack.edu/models/
SRI:	http://isr.sri.com/about.htm
	http://isr.sri.com/madrigal/
	ftp://isr.sri.com/pub/radar_data/summaryplots/
EISCAT:	https://www.eiscat.se/about/whatiseiscat_new
	https://www.eiscat.se/rtg/rtg.cgi
	https://www.eiscat.se/madrigal/
	https://www.eiscat3d.se/science
Ionosonde:	http://www.digisonde.com/instrument-description.html
GIRO:	http://umlcar.uml.edu/DIDBase,_http://spase.info/SMWG/Observatory/GIRO
CADI:	http://chain.physics.unb.ca
Sodankylä Geoph. Obs.:	www.sgo.fi
IRF:	http://www.irf.se/~ionogram/ionogram/plots/dayplots/
Tromsø:	http://www.tgo.uit.no/ionosonde/ , http://www.qinetiq.com/

Auroral Oval:

DMSP:	ngdc.noaa.gov/eog/dmsp
	space.jpl.nasa.gov/msl/Programs/dmsp
	www.losangeles.af.mil
	http://sd-www.jhuapl.edu/Aurora/spectrogram/spectrogram_displays.html
	http://cedarweb.hao.ucar.edu/wiki/index.php/Main_Page,
	http://cedarweb.hao.ucar.edu/wiki/index.php/DMSP:Main
	cindispace.utdallas.edu
OVATION:	http://sd-www.jhuapl.edu/Aurora/ovation_live
	http://www.swpc.noaa.gov/ovation
	http://sd-www.jhuapl.edu/Aurora/ovation/datasets.html
POES:	http://swpc.noaa.gov/pmap.index.html
SVALTRACKII:	kho.unis.no
Aurora Tracker:	fox.phys.uit.no/AFFECTS

TEC/Scintillation:

NMA:	www.kartverket.no
Global TEC/ JPL:	http://iono.jpl.nasa.gov//latest_rti_global.html
Bath University:	http://www.bath.ac.uk/elec-eng/invert/iono/rti_3d.html
MIT Global TEC:	http://madrigal.haystack.mit.edu/cgi-bin/madrigal/gSimpleUIAccessData.py
CHAIN:	ftp://chain.physics.unb.ca/
ESWUA:	http://www.eswua.ingv.it/ingv/

Space Weather:

NMA:	sesolstorm.kartverket.no
NRS:	www.romsenter.no
Uni Alaska:	gse.gi.alaska.edu
NOAA:	www.sec.noaa.gov, www.swpc.noaa.com,
	http://www.swpc.noaa.gov/SWN/index.html
STD:	www.spacew.com, http://solar.uleth.ca/
SIDC	sidc.oma.be
Aurora Watch:	http://www.york.ac.uk/news-and-events/news/2000/aurorawatch
IPS:	www.ips.gov.au/space_weather
GSC/NRCAN:	http://www.spaceweather.gc.ca/index-eng.php

Geomagnetic

WDC:	http://wdc.kugi.kyoto-u.ac.jp/dstae/ http://wdc.kugi.kyoto-u.ac.jp/index.html.
	http://wdc.kugi.kyoto-u.ac.jp/wdc/Sec1.html
	http://wdc.kugi.kyoto-u.ac.jp/aedir/ae2/onAEindex.html
GFZ, Potsdam:	http://www-app3.gfz-potsdam.de/kp_index/description.html
OMNI:	http://omniweb.gsfc.nasa.gov
IMAGE:	http://www.space.fmi.fi/image/, http://space.fmi.fi/image/beta/
	http://www.geo.fmi.fi/cgi-bin/imagecgi/electrojet
SAMNET:	http://spears.lancs.ac.uk/samnet/
IRF:	www.irf.se/allsky/dasc

Images and other resources:

www.uio.no/studier/emner/matnat/fys/Fys/3610/h08/undervisningsmateriale/compendium/magnetometer, 2008
www.fujifilmusa.com/shared/bin/S2_Brochure.pdf
http://download.hao.ucar.edu/d5/mlso/log/event/mlso.daily_and_events.2003
http://science.gsfc.nasa.gov/671/staff/bios/cs/Nelson_Reginald/Chapter1.pdf
http://www.unc.edu/~rowlett/units/scales/solar_flares.htm
www.moveable-type.co.uk/scripts/gis-faq5.1.html
www.swpc.noaa.gov/ace/ace_rtsw_data.htm
http://sunearthday.nasa.gov/2007/multimedia/gal_004.php
http://sohowww.nascom.nasa.gov/gallery/images/large/mdi20031028_prev.jpg
http://www.kis.uni-freiburg.de/index.php?id=513&L=1&id=513
http://solarscience.msfc.nasa.gov/dynamo.shtml
http://www.solarphysics.kva.se
www.nasa.gov/topics/solarsystem/features/solar_plasma.html
http://trace.lmsal.com/POD/images/T171_0602_14UT.gif
http://www.nasa.gov/images/content/611128main_cme-112611_full.jpg
http://www.onr.navy.mil/focus/spacesciences/satellites/orbit2.htm
http://www.geo-orbit.org/sizepgs/geodef.html
http://sohodata.nascom.nasa.gov/cgi-bin/data_query
http://www.ssg.sr.unh.edu/mag/ACE.html
http://vt.superdarn.org/tiki-index.php?page=Radar+Overview
http://www.haystack.edu/atm/mho/index.html
http://blog.eiscat3d.org/2012/04
http://umlcar.uml.edu/DPS.htm;
http://www.digisonde.com/instrument-description.html
http://www.britannica.com/EBchecked/media/1171/The-substorm-wedge-current-is-a-field-aligned-current-system
http://www.nasa.gov/mission_pages/themis/auroras/substorm_history.html
http://roma2.rm.ingv.it/en/themes/11/ionospheric_scintillation.
http://www.faa.gov/about/office_org/headquarters_offices/ato/service_units/techops/navservices/gnss/gpshttp://glonass-iac.ru/en
http://spaceinimages.esa.int/Images/2000/12/Galileo
http://oceanservice.noaa.gov/education/kits/geodesy/media/supp_geo09b4.html
http://www.gpspassion.com/pics/geoideb.gif
http://www.ips.gov.au/Images/Satellite/Ionospheric%20Scintillation/dwn_S4_latest.png
www.springer.com/cda/content/.../cda.../9789400745575-c2.pdf
www.springer.com/cda/content/.../cda.../9780387209753-c1.pdf
http://www-ssg.sr.unh.edu/tof/Smart/Students/lees/periods.html
*http://silas.psfc.mit.edu/intro*plasma/chap2.html*
*http://silas.psfc.mit.edu/intro*plasma/chap2.html*
http://roma2.rm.ingv.it/en/themes/7/the_earth-s_main_field.
http://www.igpp.ucla.edu/public/THEMIS/SCI/Pubs/Nuggets/FTE_nugget/first_figure%5B1%5D.bmp
http://www.igpp.ucla.edu/public/THEMIS/SCI/Pubs/Nuggets/gabrielse/gabrielse.html(http://www.igpp.ucla.edu/public/THEMIS/SCI/Pubs/Nuggets/gabrielse/gabrielse.html
http://www.propagation.gatech.edu/ECE6390/project/Fall2011/group5/website/ssp/sat/env/res/FigureE5.gif
http://solarphysics.livingreviews.org/Articles/lrsp-2007-1/fig_4.html
http://global.britannica.com/EBchecked/topic/106159/Chapman-Ferraro-current-system
http://www-ssc.igpp.ucla.edu/personnel/russell/papers/magsphere/msphere06.gif
http://www-spof.gsfc.nasa.cov/Education/wtail.html
http://www.physics.usyd.edu.au/~cairns/teaching/lecture14/node4.html

http://plasma.physics.swarthmore.edu/ssx/faq.html
https://wiki.oulu.fi/display/SpaceWiki/Ionospheric+convection
www.measurement.dees.unict.it/rtd_ fluxgate.html
http://space.fmi.fi/image/beta/?page=map
http://www.space.fmi.fi/image/bear/bear_ej.html
http://space.fmi.fi/image/beta/?page=il_index

Appendix

MATLAB CODE

Solar Wind:

```
clc;
clear;

% Loading datasets from ACE 20.November 2003:

SWE = 'ACE_SWEPAM_Data2.dat';
MFI = 'ACE_MAG_Data2.dat';

d = load(MFI);
d(d <= -999) = nan;
day_mag     = d(:,1);
hour_mag    = d(:,2);
minute_mag  = d(:,3);
seconds_mag = d(:,4);
B_total     = d(:,5);
Bx          = d(:,6);
By          = d(:,7);
Bz          = d(:,8);
time_mag =  datenum(0,0,0,hour_mag,minute_mag,seconds_mag);

d = load(SWE);
d(d <= -9999) = nan;
day_swe     = d(:, 1);
hour_swe    = d(:, 2);
minute_swe  = d(:, 3);
seconds_swe = d(:, 4);
H_dens      = d(:, 5);
temp        = d(:, 6);
speed       = d(:, 7);
Vx          = d(:, 8);
Vy          = d(:, 9);
Vz          = d(:,10);
time_swe = datenum(0,0,0,hour_swe,minute_swe,seconds_swe);


%%%Solar wind velocity measured at ACE.%%%
%Removing errors in measurements and replacing with closest approximate
%value

N = numel(Vx);
for i = 1:N
 if(isnan(Vx(i)))
   for j = 1:N
    if( (i-j >= 1) & not(isnan(Vx(i-j))) ), Vx(i) = Vx(i-j); break; end
    if( (i+j <= N) & not(isnan(Vx(i+j))) ), Vx(i) = Vx(i+j); break; end
   end
 end
end
% plots
figure(2);
plot(time_swe, -Vx);
datetick('x');
xlabel('Time [hours]');
```

```
ylabel('Velocity [km/s]');
title('Solar Wind Velocity');

Vx_avg= mean(Vx);
%Average velocity of Vx-component Vx=-557.27 km/s

%%% MAG %%%
figure(3);
subplot(4,1,1);
plot(time_mag,Bx);
datetick;
xlabel('time[hours]')
ylabel('Bx [nT]');
title('Variations in IMF Measured at ACE');
subplot(4,1,2);
plot(time_mag,By);
datetick;
xlabel('time[hour]')
ylabel('By [nT]');
subplot(4,1,3);
plot(time_mag,Bz);
datetick;
xlabel('time[hours]')
ylabel('Bz [nT]');
subplot(4,1,4);
plot(time_mag,B_total);
datetick('x');
xlabel('time[hours]');ylabel('Btotal[nT]');

%%%Proton Density%%%

N = numel(H_dens);
for i = 1:N
 if(isnan(H_dens(i)))
   for j = 1:N
    if( (i-j >= 1) & not(isnan(H_dens(i-j))) ), H_dens(i) = H_dens(i-j);
break; end
    if( (i+j <= N) & not(isnan(H_dens(i+j))) ), H_dens(i) = H_dens(i+j);
break; end
   end
 end
end

 figure(4);
 %plot(4,1,1);
 plot(time_swe,H_dens)
 datetick('x');
 xlabel('time[hours]');
 ylabel('density[cm^-3]');
 title('Variations in Proton Density');

H_dens_avg=mean(H_dens);
 % Mean density: H_avg=12.313/cm^3.

%%%Calculation of distance between ACE-satellite and Magnetopause:%%%
%ACE is located in Lagrange point 1 (L1),
%1.5 million km from the center of the Earth.
%Distance from Earth center to L1 is ca. 235.5 Earth radii.
L1=235.5;
%Approximate mean standoff distance:
```

```
Xm_avg=mean(Xm); %Xm_avg =8.9061RE
% Stand-off-distance calculated:
Xm=107.4.*(H_dens.*Vx.^2).^(-1/6);
%Mean distance between Ace and MP:
ACE_MP_dist=L1-Xm_avg;
% ACE-MP=226.6 Earth radii.
%Time delay from ACE to MP. Distandce divided by mean velocity yields:
Delay=((ACE_MP_dist.*6370)./abs(Vx_avg))./60;
%time delay = 43.17min.
```

Visible Satellites

```
% Load data for Oslo. The same program is used for all stations!
d = load('osls3240_simpler.ZON');

% Put data into variables (just to make the code below easier to handle and
read)
satId = d(:,1);
t = d(:, 6);

% Make plot of all satellites
% Loop over satellites
for sat = 1:32
 % Select satellite number "sat"
 r = (satId == sat);
 % If there is no data for that satellite, skip to next iteration of loop
 if(sum(r) == 0), continue, end

 % Plot time-of-visibility
 plot(t(r), zeros(1,numel(t(r))) + sat, '*')
 hold on
end
hold off
ylim([0 33])
grid
xlabel('Time (hour-of-day)')
ylabel('Satellite Id')

 For the evening plot of BERGEN, the same program is used with adjusted
time scales:
% Load data
d = load('Brgs3240_kveld.txt');
satId = d(:,1);
t = d(:, 6);
for sat = 1:32
 % Select satellite number "sat"
 r = (satId == sat);
 % If there is no data for that satellite, skip to next iteration of loop
 if(sum(r) == 0), continue, end
 % Plot time-of-visibility
 plot(t(r), zeros(1,numel(t(r))) + sat, '*')
 hold on
end
hold off
ylim([0 33])
grid
xlabel('Time (hour-of-day)')
ylabel('Satellite Id')
```

Elevation plots

```
% Load data for Oslo. Same program is used for all stations.
d = load('osls3240_simpler.ZON');
recName = 'osls';

% Put data into variables (just to make the code below easier to handle and
read)
satId = d(:,1);
latitude = d(:, 5);
t = d(:, 6);

% Prepare figure for combined plot
figure(100), clf, cla, hold on


% Make plot of all satellites
% Loop over satellites
for sat = 1:32
 % Select satellite number "sat"
 r = (satId == sat);
 % If there is no data for that satellite, skip to next iteration of loop
 if(sum(r) == 0), continue, end

 % Plot latitude, one plot per satellite
 figure(sat)
 plot(t(r), latitude(r), 'x')
 grid
 xlim([0 24])
 xlabel('Time (hour-of-day)')
 ylabel('Latitude (degrees)')
 title(['Receiver ' recName ', satellite ' num2str(sat)])

 % Plot latitude, combined plot
 figure(100)
 plot(t(r), latitude(r), 'x')
end

figure(100)
hold off
grid
xlim([0 24])
xlabel('Time (hour-of-day)')
ylabel('Latitude (degrees)')
title(['Receiver ' recName])
```

DST

```
clc; clear;

% Plotting the hourly values of the Dst-index from
% http://wdc.kugi.kyoto-u.ac.jp/dstae/index.html for Nov. 20 2003:
% Using datas from Nov. 19, 19:00UT to Nov. 21, 09:00UT.
Dst = 'Dst_data_2.txt';

d = load(Dst);

year_dst     = d(:,1);
month_dst    = d(:,2);
day_dst      = d(:,3);
hour_dst     = d(:,4);
minute_dst   = d(:,5);
seconds_dst  = d(:,6);
Dst_total    = d(:,7);

date_dst = datenum(0,0,day_dst,hour_dst,minute_dst,seconds_dst);
plot(date_dst,Dst_total);
datetick('x');
```

Haversine:

```
%Great circle formula /Haversine) for calculating the shortest distance on
a spherical
%shell. Using the geographical coordinates of start and stop destination.
phi2=69.6;                 %defining the latitudes of Tromsø
phi1=42.6;                  % and Millstone Hill

Lat2=phi2.*pi./180;         %coversion from degrees to radians
Lat1=phi1.*pi./180;

dlat=Lat2-Lat1;
dla=dlat./2;

lambda2=19.2;             % defining the longitudes of Tromsø
lambda1=288.5;               %and Millstone Hill.
Lon2=lambda2.*pi./180;       %converting from degrees to radians
Lon1=lambda1.*pi./180;
dlong=Lon2-Lon1;
dlo=dlong./2;
R_E=6371;                 % mean Earth radius in km.
%calculating the great circle distance d straight forward:
a=(sin(dla)).^2 +cos(Lat1).*cos(Lat2).*(sin(dlo)).^2;
 c=2*asin(min(1,sqrt(a)));
d=R_E*c  %d=5.6548e3km.
% distance from Millstone Hill to Eiscat Tromsø is approximately:
%5600 km.

%Formula was found at: www.moveable-type.co.uk/scripts/gis-faq5.1.html
```

Correlation Plots:

```
%Inserting the values into a matrix for plotting and calculation of
correlation coefficient.

%Number of cycle slips as a function of phase scintillation.
d=[0.45 900; 0.8 1400; 0.45 50; 0.7 900; 0.6 1300; 0.4 250; 0.75 1300; 0.75
1800; 0.6 350;];
plotmatrix(d);
corrcoef(d); %correlation coefficient is 0.7749

%phase scintillation as a function of ROTI.

d=[3.0 0.45;4.0 0.8;2.0 0.45;4.5 0.7;7.0 0.6;3.0 0.4;5.5 0.75;7.0 0.75;5.0
0.6;];
plotmatrix(d);
corrcoef(d)  % correlation coefficient is 0.6274

%phase scintillation as function of VTEC

d=[12.5 900; 25 1400; 40 50; 15 900; 15 1300; 20 250; 22 1300; 45 1800; 25
350];
plotmatrix(d);
corrcoef(d)% correlation coefficient is 0.0634
```

IPPs

The IPPs for Bergen receiver station at 08:00UT. In order to make the OVATION/IPP/RTIM plots the coordinates for the IPPs were extracted for the selected time of day.

```
sites = [  % Format: siteId  longitude  latitude
0  5.27  60.12 ;
];

IPPs = {  % Format: siteId  satIdStr  longitude  latitude
0  'GPS03'  5.11043  76.6216 ;
0  'GPS08'  11.7411  60.5046 ;
0  'GPS09'  -10.7106  54.971 ;
0  'GPS10'  3.33773  53.9061 ;
0  'GPS15'  -4.35311  67.4632 ;
0  'GPS18'  -5.41092  64.7098 ;
0  'GPS21'  -12.7326  61.4033 ;
0  'GPS26'  2.8319  59.9272 ;
0  'GPS27'  26.0117  60.9856 ;
0  'GPS28'  8.95923  58.6729 ;
0  'GPS29'  4.80285  59.3872 ;
0  'GPS31'  16.6683  66.7524 ;
};
```